UNIVERSITY OF CALIFORNIA, SAN DIEGO
SAN DIEGO STATE UNIVERSITY

Bifunctional Agents for MRI, PET and Fluorescence Imaging and Study of Nanoparticles Formed from Water Oxidation Catalysts

A dissertation submitted in partial satisfaction of the

requirements for the degree Doctor of Philosophy in

Chemistry

by

Marie-Caline Z. Abadjian

Committee in charge:

University of California, San Diego

Professor Timothy Bertram
Professor Karen Christman
Professor Nathan Gianneschi

San Diego State University

Professor Douglas B. Grotjahn, Chair
Professor Thomas Cole
Professor Usha Sinha

2014

The dissertation of Marie-Caline Z. Abadjian is approved and it is acceptable in quality and form for publication on microfilm and electronically.

Chair

University of California, San Diego

San Diego State University

2014

DEDICATION

I would like to dedicate this work to my family and specifically my parents, Zareh and Lena Abadjian. Without their encouragement and backing, I would not have been able to achieve what I have done nor become who I am now. Even though they minimally understood my research and even doubted my career at times, they have been supportive throughout my schooling. This degree belongs to them just as much as it does to me.

TABLE OF CONTENTS

LIST OF TABLES

LIST OF FIGURES

ACKNOWLEDGEMENTS

I am very fortunate to have met and learned from the people that crossed my path in graduate school. First off, I would like to thank the Grotjahn lab as whole. We have supported each other scientifically and personally over the years and continue to do so when we graduate and move on. To Derek Brown, Hai Tran, Robert Wilson and Stewart Polk who entered SDSU at the same time as I did, even after you joined different labs and graduated you were just as connected as when we started. I especially want to thank Derek and Hai for their emotional support at the some pretty personally low points. In my year of classes at UCSD, Michelle Biglarian, Michael Doud, Travis Blane, David Schmit and Marcel Hetu were always around to vent to and study with. I don't think I would have survived the classes without you all. To the core group that I have worked with the most: Dr. Reji Nair, Dr. Gülin Erdogan, Dr. Casey Larsen, David Marelius, Jayneil Kamdar, Jessica Lamonte/Martin, Dr. Zephen Specht, David Catrone, Adria Lombardo, Farhana Barmare, Erik Paulson, Melinda Pope and Michael Heberlein. Goodness, we are a fun lab!

A special thank you to Christie Schulte, who took me under her wing when I first started and made me feel at home in my new "lab home." I also am grateful to have known and worked alongside with Dr. Valentin Miranda, Dr. Sara Cortes-Llamas, Dr. Derek Butler and Xi Zeng. Their knowledge and experience has always been of value, and I loved learning from them.

I would also like to thank my undergraduates whom I have had the chance to influence while a graduate student: Andrea Rodriguez, Christoff van Niekerk, Marly De Gracia, Evan Darrow, and Paul Gracia. I am so proud of them all and where they have

gone. My little chicks are off in the world doing amazing things.

All the rest of the Grotjahn lab that I had a chance to work with: Thomas Cao, Lily Cao, Khoi Le, Ariana Perez, Maulen Utiliyev, Swetha Neravetla, Ruth Mendez, Ian Neel, Paul Lee, Elijah Kragulj, Joanna Cuevas, Alice Lu, Michael Tran, Robert Vasquez, and Patrick Brklycica, Annaliese Dang. I am quite lucky to have met and at times worked with these skilled graduate students: Isabelle Lerario, James Caldwell, Norm Zhu, Spencer Swarts, Gloria Hincapie, David Zillman, Melissa Lokensgard, Lee Wang, Scott Burley, Tim Montgomery, Michael Barker, Erin Singh, Robert Sellers, Eddie Pan, Jenny Van, Manna, Eric Miller and Ryan Barker.

I cannot forget the extraordinary people that make this program and department function. Thank you: LeRoy Lafferty for all the NMR help; Curtis Moore for encouraging me to grow better crystals; Arnie Rheingold for teaching me about crystallography; Dr. Cole for being so supportive; Ken Long for the magic he does behind the scenes; and to Irene Occhiello and Gayle Anderson for keep our department running.

Chapter I.2: I would like to thank Christie Schulte who took me under her wing when I first joined the lab and started this project on the synthetic route to make compound **5** and **12**. I would like to thank Sara Cortes-Llamas for assistance and guidance on the Moshers' acid testing. I would also like to thank Andrea Rodriguez for her initial studies to make the *t*-butyl ester azide (entries 1 through 7).

Chapter I.3: I thank the Pittsburgh NMR Center for Biomedical Research which is supported by grant P41EB 001977 from the National Institutes of Health. I also thank my collaborating authors at UPMC (Zhihua Huang, Raghvendra S. Sengar, Archana

Nigam, Douglas M. Potter, and Erik C. Wiener) for their work on our published paper (*Investigative Radiology* **2010**, *45*, 10, 641).

Chapter I.4: Support of the NIH (R01 DK078500-01) is acknowledged. At SDSU, we thank Dr. LeRoy Lafferty for his assistance with NMR experiments. L.V.E. thanks the ARC Programs of the French Community of Belgium, the FNRS (Fonds National de la Recherche Scientifique), the support and sponsorship concerted by COST Actions (D38 and TD1004).

Chapter I.5: I would like to thank our collaborators at Carnegie Mellon University, Brigitte, Marcel Bruchez, Yi Wang, Alan Waggner, Erik Wiener. Kevin Hitchens. I thank Virgil Simplaceanu and Kevin Hitchens for their helpful advice and the Pittsburgh NMR Center for Biomedical Research.

Chapter I.6: I would like to thank all the members of our lab's dendrimer subgroup for helpful conversations related to this project.

Chapter II: I would like to thank our collaborators at the University of Pittsburgh: Erik Wiener and Carolyn Anderson for the opportunity to work on this project, and Dexing Zeng for his patience, guidance and starting material for this project. I especially thank Josh Swider for mass spectrometry analysis of some key samples.

Chapter III: Synthesis of catalysts and testing was done by several members of our group, who are named as co-authors on our joint publication. In particular: synthesis of catalysts, NMR studies of reactions, powder X-ray diffraction, oxygen measurements, and some UV-vis measurements were done by these colleagues.

Lastly, but not by any means least, I would like to thank Doug for all his guidance

and teachings. His patience, knowledge, experience, and never ending excitement about chemistry continues to motivate me. He was right there with me helping me ride the highest highs when chemistry went right, and pushing me onward and forward when chemistry and I ran into brick walls. Because of him I will always make sure my presentations and structures are in the same font and size; to use at least two forms of characterization to identify a compound; always think about all possible side reactions; and if the reaction didn't work, raise the temperature.

VITA

2014 Ph.D. Chemistry
University of California, San Diego, CA & San Diego State University, CA

2009 M.A., Organic Chemistry
San Diego State University, CA

2002 B.S., Chemistry concentration in Biochemistry
University of California, Irvine, CA

PUBLICATIONS

Wiener, E. C.; **Abadjian, M.-C.;** Raghvendra, S.; van der Elst, V.; Van Niekerk, C.; Douglas, B. G.; Leung, P. Y.; Schulte, C.; Moore, C. E.; Rheingold, A. "Bifunctional Chelates Optimized for Molecular MRI". *Inorganic Chemistry* (**2014**), 53(13), 6554-6568.

Grotjahn, D. B.; Brown, D. B.; Martin, J. K.; Marelius, D. C.; **Abadjian, M.-C.**; Tran, H. N.; Kalyuzhny, G.; Vecchio, K. S.; Specht, Z. G.; Cortes-Llamas, S. A. "Evolution of Iridium-Based Molecular Catalysts during Water Oxidation with Ceric Ammonium Nitrate" *Journal of the American Chemical Society* (**2011**), *133*(47), 19024-19027.

Huang, Z.; Raghvendra, S.; Nigam, A.; **Abadjian, M.-C.**; Potter, D. M.; Grotjahn, D.B.; Wiener, E. C. "A fluorinated dendrimer-based nanotechnology platform: new contrast agents for high field imaging" *Investigative Radiology* (**2010**), *45*(10), 641-654.

ORAL PRESENTATIONS

Abadjian, M.-C.; Van Niekerk, C.; Raghvendra, S.; Ferdani, R.; Anderson, C. J.; Douglas, B. G.; Wiener, E. C. "Bifunctional Imaging Agents for MRI and PET" Poster presentation at Gordon Conference: Metals in Medicine, Proctor Academy, Andover, New Hampshire, June 24-29, 2012.

POSTER PRESENTATIONS

Abadjian, M.-C.; Douglas, B. G.; Raghvendra, S.; Wiener, E. C.; Ferdani, R.; Anderson, C. J.; "Bifunctional macrocyclic chelators for metals in medicinal imaging" Poster presentation at 40th International Coordination Chemistry Conference, Valencia, Spain, Sept. 8-13, 2012.

Abadjian, M.-C.; Van Niekerk, C.; Raghvendra, S.; Ferdani, R.; Anderson, C. J.; Douglas, B. G.; Wiener, E. C. "Bifunctional Imaging Agents for MRI and PET" Poster presentation at Gordon Conference: Metals in Medicine, Proctor Academy, Andover, New Hampshire, June 24-29, 2012.

Abadjian, M.-C.; Ferdani, R.; Douglas, B. G.; Anderson, C. J.; Wiener, E. C.

“Multifunctional PET tracer based on a pendant-armed cross-bridged tetraazamacrocycle scaffold” Poster presentation at 243rd ACS National Meeting, San Diego, CA, March 25-29, 2012, ORGN-784.

Abadjian, M.-C.; Van Niekerk, C.; Douglas, B. G.; Wiener, E. C**.** “Gd-based MRI Contrast Agents: Syntheses to Broaden Applications” Poster presentation at 2012 Student Research Symposium, San Diego CA, March 9- 10, 2012. 252-CHEM-31.

Abadjian, M.-C.; Van Niekerk, C.; Douglas, B. G.; Wiener, E. C**.** “Clickable bifunctional DOTA and DOTMA analogs” Poster presentation at 241st ACS National Meeting, Anaheim, CA, March 27-31, 2011, ORGN-142.

Abadjian, M.-C.; Leung, S.; Schulte, C.; Grotjahn, D. B.; Wiener, E. C. “Bifunctional DOTA and DOTMA analogs: Synthesis, characterization, and coordination to gadolinium” Poster presentation at 238th ACS National Meeting, Washington, DC, August 16-20, 2009, INOR-792.

Abadjian, M.-C.; Leung, S.; Schulte, C.; Grotjahn, D. B.; Wiener, E. C.
“Synthesis of bifunctional DOTA and DOTMA analogs” Poster presentation at 236th ACS National Meeting, Philadelphia, PA, August 17-21, 2008, ORGN-135.

Abadjian, M.-C.; Metzke, M.; Guan, Z. “Novel Biomaterials for Cell Transfection and Extracellular Matrices” Poster presentation at Undergraduate Research Opportunities Program Symposium, 2006, Irvine, CA. Chem. 121.

Abadjian, M.-C.; Metzke, M.; Guan, Z. “Synthesis of Gene Delivery Vectors for Transfection Studies” Poster presentation at Undergraduate Research Opportunities Program Symposium, 2005, Irvine, CA. Chem. 162.

AWARDS

June 2012 Travel Award for Gordon Research Conference: Metals in Medicine.

Spring 2011 Instructionally Related Activities (IRA) Student Travel Fund for 241th meeting.

Fall 2009 IRA Student Travel Fund for 238th ACS (American Chemical Society) National meeting.

Fall 2008 ACS Division of Organic Chemistry Travel Award for 236th ACS National meeting.

Summer 2005 Allergan Undergraduate Research Fellowship.

2004 Undergraduate Research Opportunities Award at UC-Irvine Program.

MAJOR FIELDS OF STUDY

Major Field: Chemistry (Organic and Inorganic)

Studies in Synthesis and Applications of Imaging Agents

Professor Douglas B. Grotjahn

ABSTRACT OF THE DISSERTATION

Bifunctional Agents for MRI, PET and Fluorescence Imaging

and
Study of Nanoparticles Formed from Water Oxidation Catalysts

by

Marie-Caline Z. Abadjian

Doctor of Philosophy in Chemistry

University of California, San Diego, 2014

San Diego State University, 2014

Professor Douglas B. Grotjahn, Chair

The work is divided into four parts: (1) MRI contrast agents are designed to enhance T_1 relaxivity by coupling them to dendrimers, the precise structure of which can be controlled through synthesis. Cyclen is used as a starting scaffold for the synthesis of bifunctional Gd-DOTA and Gd-DOTMA analogues. One unique side chain on the macrocycle contains an azide moiety that can be clicked to an alkyne-containing core, making a first-generation dendrimer with the potential to improve MRI efficiency. (2) PET tracers are designed to specifically coordinate ^{64}Cu, a positron source, while containing clickable side arms. A functionalized cross-bridge tetraazamacrocycle with two identical azide-bearing side arms can be clicked to alkynyl amino acid, which provides several advantages with respect to applications. (3) Using the results of part 1, MRI-fluorescence imaging agents are constructed. Preliminary tests determine their

efficiency as bimodal agents. (4) My contributions to a separate project to investigate the fate of water oxidation catalysts under acidic conditions are described.

We have synthesized and characterized four novel bifunctional MRI imaging agents to date. Preliminary studies show successful clicking of these complexes to form dendrimers. We are also currently synthesizing and optimizing a unique bifunctional PET tracer. Future work includes, but is not limited to, optimization of syntheses, full characterization of the bifunctional PET tracer, theoretical calculations of expected T_1 relaxivities of bifunctional MRI contrast agents, imaging cells in tissue-like matrices for MRI-fluorescence agents, and designing more robust water oxidation catalysts.

CHAPTER I

Optimizing Gd(III)-based Contrast Agents for Magnetic Resonance Imaging (MRI)

I.1. Introduction to Magnetic Resonance Imaging (MRI)

I.1.1. MRI technique

Magnetic resonance imaging (MRI) is a nuclear medicine imaging technique that can reconstruct three-dimensional images of various structures and tissues in the body. The MRI instrument exposes the body to strong magnetic fields (0.2 – 3.0 Tesla) and then applies a radiofrequency pulse sequence, similar to that used in nuclear magnetic resonance (NMR) spectrometers for laboratory research samples. The pulse causes water protons to be excited. After the pulse stops, relaxation occurs, and position-dependent resonance frequencies are emitted, detected and reconstructed into an image. Figure I.1.1 shows quality of images that can be obtained from MRI.

Figure I.1.1. MR image of my left knee post ACL tear. Images taken at Sharp Rees-Stealy (Mira Mesa) **Medical** Group.

Significant advances in the MRI field include functional MRI (fMRI);[1,2] dynamic contrast enhancement (DCE) MRI[3,4] as a marker of changing vascular endothelial growth

factor[1,2] in cancer; imaging receptor expression;[7-13] stem cell tracking;[14-18] transporter systems;[19-22] using choline[23-25] as a marker for the PI3K pathway;[26-28] the use of intracellular sodium[29,30] for imaging cell division;[31] and blood oxygen level monitoring.[32-35]To better visualize disease and physiological processes, MRI has been improved by integrating other imaging techniques, using external or internal markers. In an effort to provide efficient imaging to diagnose disease and assess treatments, imaging agents are employed to enhance signal-to-noise, which indirectly can be manipulated to enhance the image generated from the signals. MRI contrast agents (CAs), as known as dyes, can improve the contrast of structures or fluids within the body during imaging by improving sensitivity and/or specificity by shortening water proton relaxation times. Over the past 80 years, starting with X-rays, noninvasive imaging methodology and instrumentation has advanced along with technology, and MRI has similarly advanced since it was proposed ~40 years ago, but the design and development of MRI contrast agents have progressed more slowly.

I.1.2. Relaxivity (r_1)

The sensitivity of some of the advances mentioned above depends on the imaging agent's efficiency (relaxivity) at the level of the individual ion or entire molecule. Relaxivity is calculated as the change in relaxation rate (1/T) per unit concentration of Gd (III) ion ($mM^{-1}s^{-1}$). The effects of two relaxation mechanisms are described by T_1 (spin-lattice or longitudinal relaxation time), and T_2 (spin-spin or transverse relaxation time). The relaxivities corresponding to T_1 and T_2 are denoted r_1 and r_2, respectively. Higher relaxivities are the hallmark of more efficient CAs, resulting in lower doses of CA and/or

increased detectabiliy for low expression targets. The most common type of MRI CA uses dipole-dipole interactions between a paramagnetic ion and protons of the directly coordinated water molecule or molecules (Figure I.1.2). The efficiency of a contrast agent can be optimized by synthetically changing variables in three categories (inner,[36-39] second[40] and outer sphere[41,42] contributions). The inner sphere contribution depends on the number of water molecules directly coordinated to the metal ion (q), the time that the water molecules remain coordinated to the ion (the water residence time, τ_M), the number of unpaired electron (or spin quantum number, S), the distance between the metal ion dipole and dipole of the interest (r), the electronic relaxation time (τ_S), and a measure of rotational diffusion or the rotational correlation time (τ_R), Figure I.1.2. The second sphere contribution depends on similar variables, which are associated with the second coordination sphere. The outer sphere contribution depends on the number of unpaired electrons or spin quantum number (S), the electronic relaxation time (τ_S), the distance between the metal ion dipole and dipole of the interest (r), and the relative diffusion coefficient D such that r^2/D is the translational correlation time (τ_D).

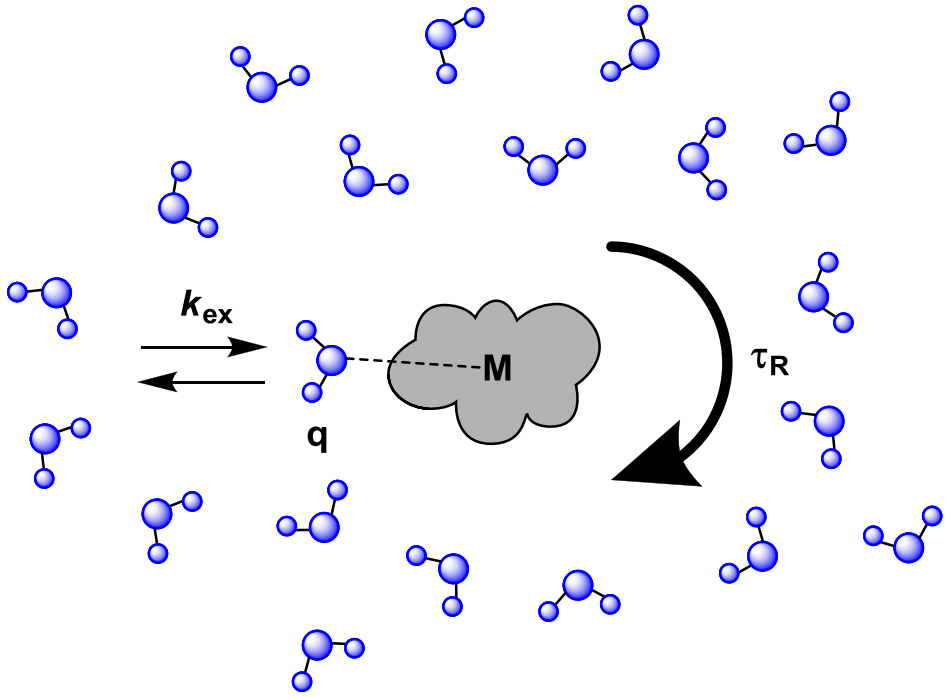

Figure I.1.2. Schematic representing some factors affecting relaxivity for a paramagnetic chelate complex in water. The gray shape with M represents the metal complex.

Based on the type of tissue being imaged, there are three common parameters that can be used to image and modify CA efficiency; spin density (ρ), longitudinal relaxation time (T_1) or transverse relaxation time (T_2). For T_1-based CAs with long electronic relaxation times, such as those containing Gd(III), the best method to increase the efficiency of a CA is to increase the rotational correlation time (τ_R) by making the molecule bigger to slow its tumbling in solution.[36] Another factor that can be synthetically optimized is increasing the water exchange rate (k_{ex}) by making it easier for water molecules to access and directly bind to the paramagnetic metal coordination site.

I.1.3. MRI Contrast Agents (CAs)

The subtle relaxation time differences of environment-sensitive NMR resonances are the basis of MRI. To overcome the poor sensitivity of magnetic resonance techniques,

high concentrations of nuclei are needed for detection, which in living systems can present a special challenge. Water protons are ideal because of their high concentration (110 M in pure water, and water comprises 70% w/ w of a living body); high natural isotopic abundance of 99.98%; and high gyromagnetic ratio. Because of low sensitivity, MRI requires relatively long acquisition times (around tens of minutes). This disadvantage of MRI can be overcome by using CAs, because they allow for shorter acquisition time by decreasing the relaxation time of water protons.

Most contrast agents used in clinical MRI are paramagnetic metal complexes or superparamagnetic clusters, since both have been shown to shorten relaxation times of water coordinated to the CA versus bulk water found in the system.[38,39] The CAs cause differences in distribution of water proton relaxation rates. The effect on water proton relaxation times is used to indirectly detect the CAs. As part of categorizing the abilty of CAs, to perform detection a quantity known as relaxivity, which is proton relaxation rate per unit concentration of CA, is used. The closer the water molecules are to a paramagnetic metal, the shorter the relaxation time which increases relaxivity, giving a stronger signal to reconstruct an image. For instance, the paramagnetic[43,44] and superparamagnetic[45,46] CAs relaxivities change with cellular accumulation, and are affected by the water exchange rate within different tissue and cellular compartments. Biological, metabolic, and molecular processes, such as vascular endothelial growth factor-induced angiogenesis,[47] can be quantified using the relaxivity of CAs used in MRI. The *in vivo* relaxivity relies on several biological factors and is not consistent throughout the tissue or organism being imaged. Depending on what kind of tissue being imaged, there are different magnetic

metal sources for contrast agents (T_1 versus T_2 CAs). The use of CAs requires a sufficient concentration of the imaging agent at the desired target. To achieve detection, a number of approaches have been used including delivery of relatively large numbers of paramagnetic or superparamagnetic ions [Gd(III), Mn(II), and Fe(III)] in the form of polymeric drug delivery systems[48,49] and/or nanoparticles,[50-53] or a smaller number of more highly efficient agents, or a combination of the two.[54-56]

I.1.4. Commercially used MRI CAs

Of the three paramagnetic metals previously mentioned, gadolinium(III) has the largest magnetic moment and 7 unpaired electrons compared to 5 unpaired electrons for manganese(III) and iron(III). Gadolinium(III) also has been shown to have faster electronic relaxation rates of water protons and many clinically used CAs are Gd(III)-based complexes. These complexes ideally are biocompatible, have a long retention time in the body for imaging and/or accumulation at target site, and are the appropriate size for bioavailability and degradation/removal pathway.

Generally, Gd(III)-based CAs are removed from the body by filteration through the kidneys. Free, unchelated Gd(III) is highly toxic and can cause nephrogenic systemic fibrosis/nephrogenic fibrosing dermopathy (NSF/NFD), which broadly affects skin elasticity making the skin rigid.[57] Free Gd(III) ions are comparable in size and charge to calcium ions and are sequestered within the bone and liver, where they can inhibit calcium channels effecting numerous cellular processes. Therefore, Gd(III)-based CAs must be comprised of Gd(III) stabilized in chelate complexes. Most clinical CAs use cyclic or acyclic poly(aminocarboxylate) ligands to chelate gadolinium (Figure I.1.3),

rendering the Gd(III) ion inert as long as the complex is kinetically stable which is crucial to prevent free metal from interacting with endogenous compounds and to ensure rapid renal excretion.[58]

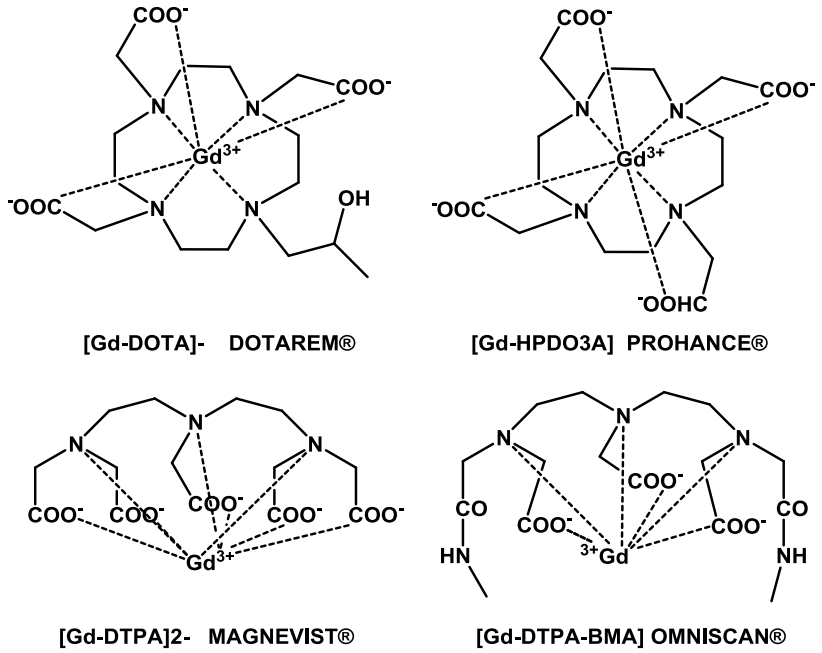

Figure I.1.3. Representative clinically used Gd(III)-based contrast agents for MRI. DOTA = 1,4,7,10-tetraazacyclododecane-1,4,7,10- tetraacetic acid; HPDO3A = 10-(2-hydroxypropyl)-1,4,7-tetraazacyclododecane-1,4,7-triacetic acid; DTPA = diethylenetriamine pentaacetic acid; DTPA-BMA = 5,8-Bis(carboxymethyl)-11-[2-(methylamino)-2-oxoethyl]-3-oxo-2,5,8,11-tetraazatridecan-13-oic acid.

Gadolinium can accommodate from 8 to 9 ligands; typical MRI contrast agents feature Gd(III) with nine coordination sites. To act as an efficient CAs, the chelate should have a balance between open coordination sites for water to exchange and enough ligands to keep Gd(III) complexes intact until excretion. There are a variety of clinically available Gd(III)-based CAs. Some chelates have 8 or 7 ligands which allows for one or two water molecules to coordinate to Gd(III), respectively. Most chelates fall into two groups according to structure: macrocyclic like DOTA or HPDO3A or linear like DTPA

or DTPA-BMA. Due to the chelate effect, macrocyclic chelates tend to be give more stable Gd(III) complexes than linear chelates. The overall charge of CAs is another consideration, since the charged complex will tend to accumulate or be directed to certain areas of the body. Gadolinium has a 3+ charge and generally Gd(III) chelates have -3 or -4 charges leading to Gd(III)-based CAs with either an overall neutral charge or negative charge.

I.1.5. Bifunctional MRI CAs

Taking into account the variables mentioned to make efficient Gd(III)-based CAs, many groups have worked on optimization by designing numerous chelates coupled to a variety of macromolecular structures to increase relaxivity.[59] Some examples of macromolecular structures being studied include linear polymers,[60,61] dendrimers,[62] micelles,[63] proteins,[64] nanotubes,[65] and nanoparticles.[66] There is also research being done on targeted Gd(III)-based CAs that aim to localize in or around certain tissue types by coupling Gd(III)-based CAs to targeting agents for example antibodies[67] or peptide receptors.[68] A synthetic challenge for Gd(III)-based CAs is the creation of a bifunctional chelating system that has all of the following favorable properties: (1) rapid water exchange that allows highly efficient relaxation and increased sensitivity, (2) tight Gd(III) binding, and (3) easy covalent attachment to a desired structure while maintaining the properties that allow highly efficient relaxation and increased sensitivity. This thesis describes a novel versatile bifunctional Gd(III)-based contrast agent that can be selectively linked through click chemistry or peptide coupling, depending on the need, to a molecule of interest rather than using the carboxylate-active ester or isothiocyanate groups, which are commonly used and commercially available. A contrast agent that is

connected to other units resulting in an efficient imaging, targeting and therapeutic agent would be a trifecta of medicinal treatment. There are several groups working on bifunctional[69] and trifunctional[70] MRI contrast agents, but none have made their debut on the commercial market.

I.1.6. Scope of this work

We designed bifunctional Gd(III)-based CAs for MRI. Compared to commercially used CAs (Figure I.1.3), we choose to use cyclen as a scaffold with the intention to make derivatives of 1,4,7,10-tetraazacyclododecane-1,4,7,10- tetraacetic acid (DOTA) and (1*R*,4*R*,7*R*,10*R*)-α, α', α'', α''''-tetramethyl-1,4,7,10-tetraaza-cyclododecane-1,4,7,10-tetraacetic acid (DOTMA). We set out to make two chelates for Gd(III) ion. Both chelates are octadentate, leaving one coordination site for water to bind Gd(III) but one of the nitrogens has a unique moiety that has a handle that can either be an azide or amine for further coupling to targeting molecules, Figure I.1.4. A compromise was made in choosing an octadentate chelate for greater projected inertness of Gd(III) in exchange for more than one open coordination site for water. By combining the stability of a macrocycle, the magnetic moment of Gd(III), and the coupling potential of azides or amines, we expected to develop an efficient MRI contrast agent that could be especially versatile. This Chapter presents the study and applications of these novel bifunctional Gd(III)-based MRI CAs.

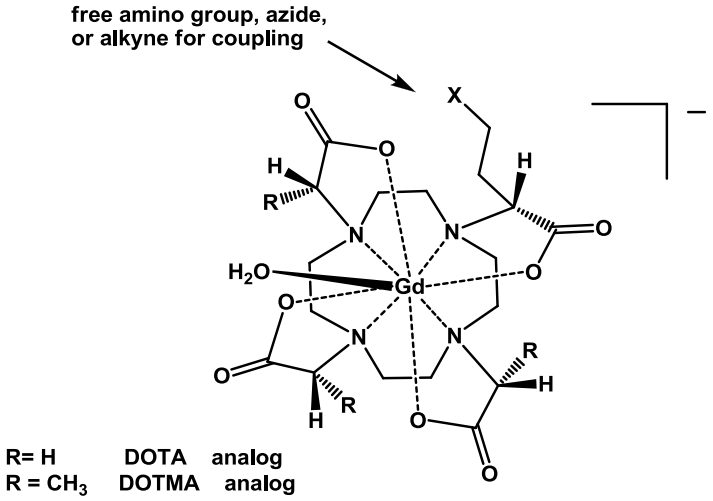

Figure I.1.4. Design of novel Gd(III)-based MRI CAs using DOTA and DOTMA as scaffolds. DOTA = 1,4,7,10-tetraazacyclododecane-1,4,7,10- tetraacetic acid; DOTMA = (1*R*,4*R*,7*R*,10*R*)-α, α', α'', α''''-tetramethyl-1,4,7,10-tetraaza cyclododecane-1,4,7,10-tetraacetic acid.

Section I.2. describes and fully characterizes key homochiral intermediate **5** needed to make the structures shown in Figure I.1.5 and a few variations of it for further synthetic applications.

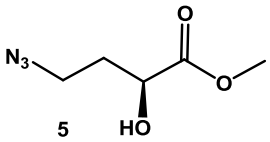

Figure I.1.5. Compound **5**, key compound for coupling MRI CAs.

Section I.3. aims to develop a directly ^{19}F-detected magnetic resonance imaging (MRI) contrast agent for use with high fields. A new bifunctional DOTA chelate was prepared and characterized. Using the chelators made in this thesis, two methods for reducing the ^{19}F longitudinal relaxation time were applied: (*a*) increasing the dendrimer size by increasing the generation, and (*b*) covalent and noncovalent introduction of Gd(III)-chelates. The investigations of imaging on rats suggest potential importance of the dendrimers in ^{19}F MRI applications, Figure I.1.6.

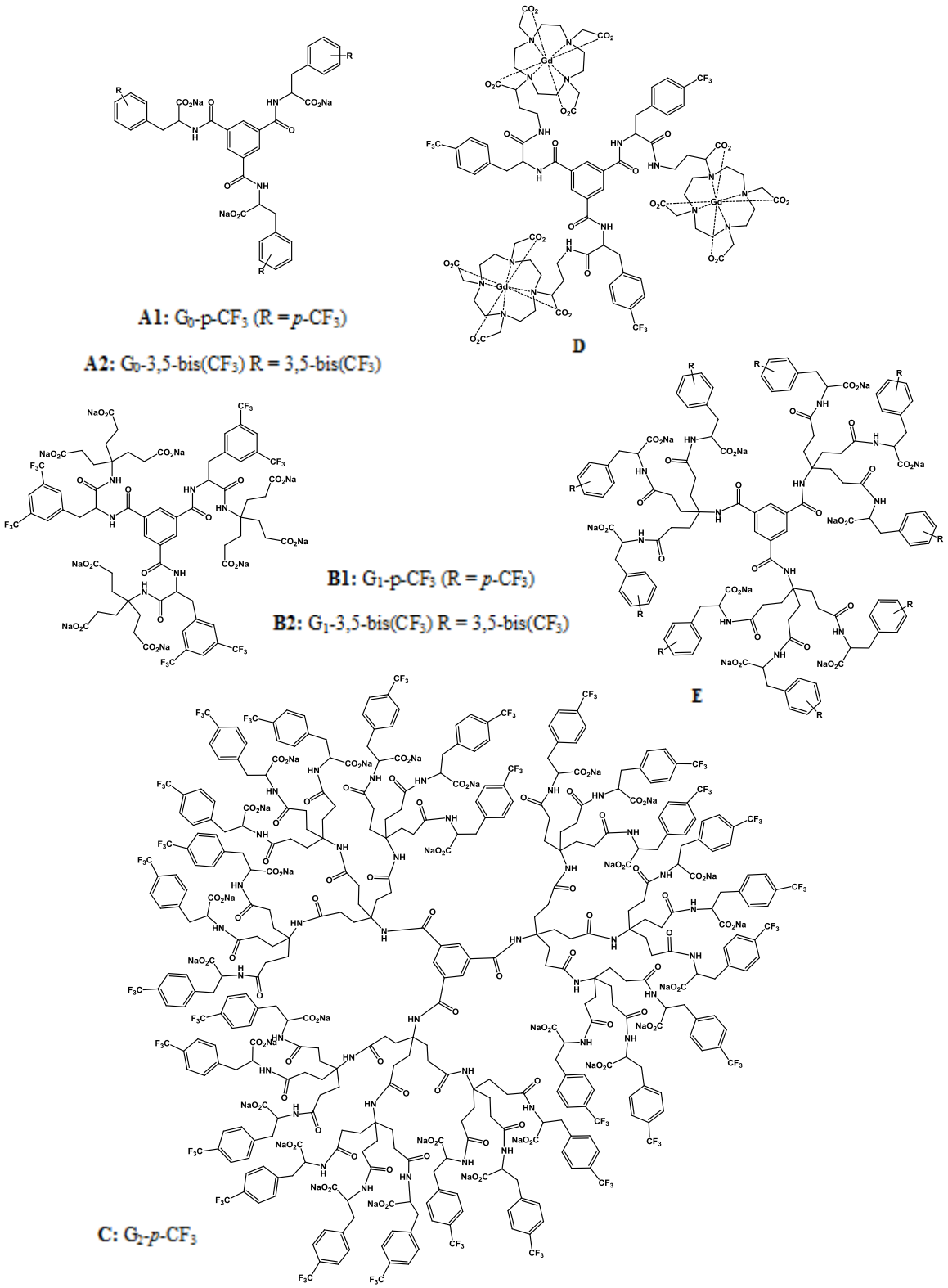

Figure I.1.6. Structure of dendrimers. (**A1**) G_0-p-CF_3, (**A2**) G_0-3,5-bis(CF_3), (**B1**) G_1-p-CF_3, (**B2**) G_1-3,5-bis(CF_3), (**C**) G_2-p-CF_3, (**D**) G_0-p-CF_3-Gd(III)-DOTA, (**E**) G_0-3,5-bis(CF_3)-BA.

Section I.4. reports the concise synthesis and characterization of several new enantiopure bifunctional derivatives of DOTMA (and their DOTA analogs as controls), that can be covalently attached to a contrast agent delivery system using either click or peptide coupling chemistry, Figure I.1.7. Gd-complexes of these derivatives can be attached to delivery systems while maintaining optimal water residence time for increased molecular imaging sensitivity. Long chain biotin (LC-biotin) derivatives of the Eu(III) and Gd(III) chelates associated with avidin are used to demonstrate higher efficiencies. Variable temperature relaxometry, ^{17}O NMR, and NMRD used on the complexes and biotin-avidin adducts measure the influence of water residence time and rotational correlation time on constrained and unconstrained systems. The Gd(III)-DOTMA derivative has a shorter water residence time than the Gd(III)-DOTA derivative. Compared to the constrained Gd(III)-DOTA derivatives, the rotationally constrained Gd(III)-DOTMA derivative has ~40% higher relaxivity at 37 ^{o}C, which could increase its sensitivity as a MRI agent as well as reduce the dose of the targeting agent.

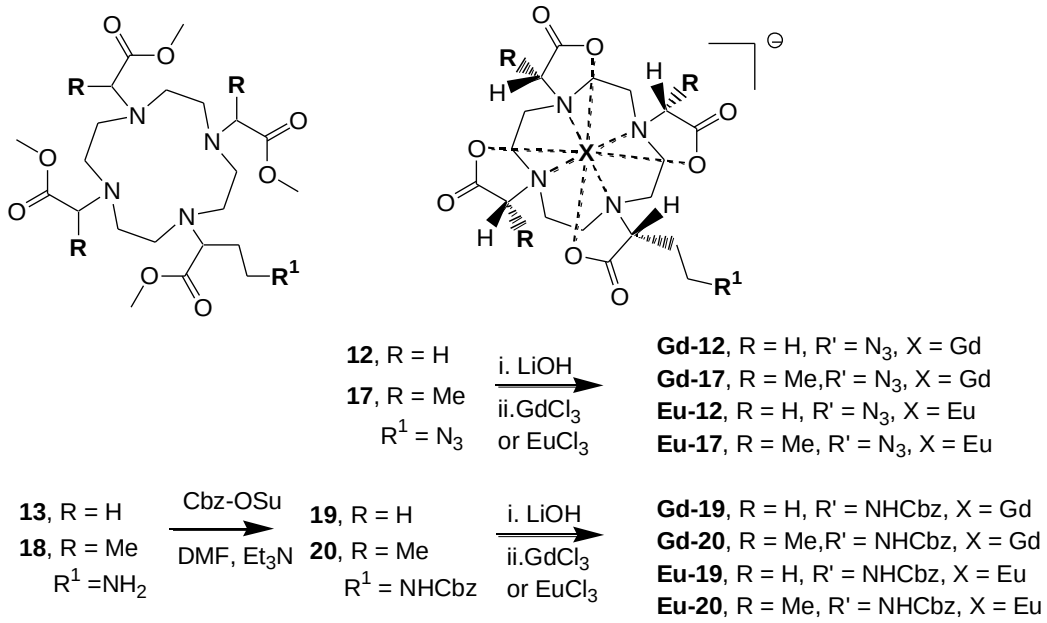

Figure I.1.7. Synthesis of N_3 and Cbz model complexes M-12, M-17, M-19 and M-20 (M = Eu, Gd).

Section I.5. describes development of four derivatives (**2a,b** and **3a,b**) to compare and evaluate these constructs as dual modality imaging probes for fluorescence and MRI diagnostic imaging, Figure I.1.8. The bifunctional molecules in this section are comprised of a DOTA or DOTMA derivative that coordinate gadolinium tightly and contain a linker to malachite green for fluorescence imaging capabilities.

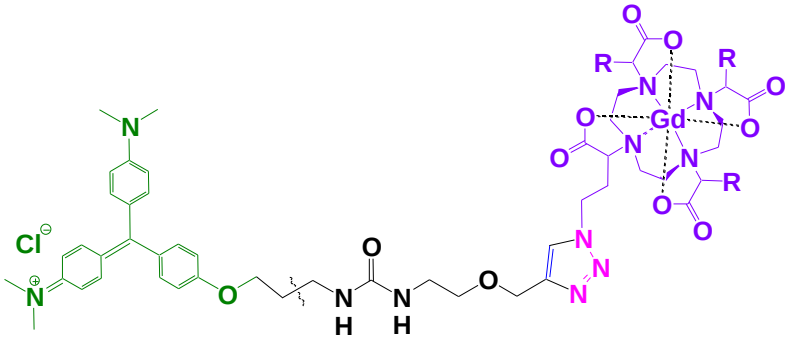

Gd-23, MG-2p-(Gd-DOTA), R = H

Gd-24, MG-2p-(Gd-DOTMA), R = Me

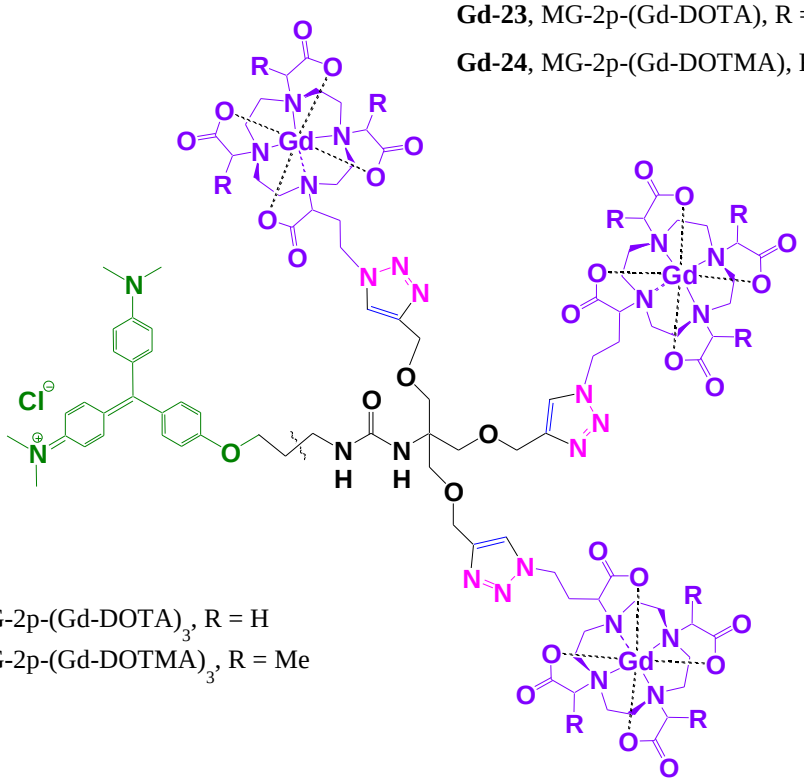

Gd-25, MG-2p-(Gd-DOTA)$_3$, R = H

Gd-26, MG-2p-(Gd-DOTMA)$_3$, R = Me

Figure I.1.8. Dual modal imaging agents (combining **Gd-23**, **Gd-24**, **Gd-25** & **Gd-26**) MRI and fluorescence capabilities.

Section I.6. discusses use of the azide-bearing chelators in click reactions. Macrocyclic chelators attached to targeting molecules have the potential to be used in theranostics. The advantageous capabilities of being an imaging tool as well as an agent for targeted radiotherapy or in the case of nanoparticles, a drug delivery vehicle for a cytotoxic agent, is attractive synthetically and in medicinal applications. In this work,

copper-catalyzed azide-alkyne cycloaddition (CuAAC) is used to form a triazole linkage between the imaging agent and the targeting compound of interest, Figure I.1.9. Click reactions are attractive since they are facile, give good yields and are performed under mild conditions. In an effort to increase the number of bound water molecules on the Gd contrast agent, we envisioned making a dendrimer decorated with Gd-contrast agents.

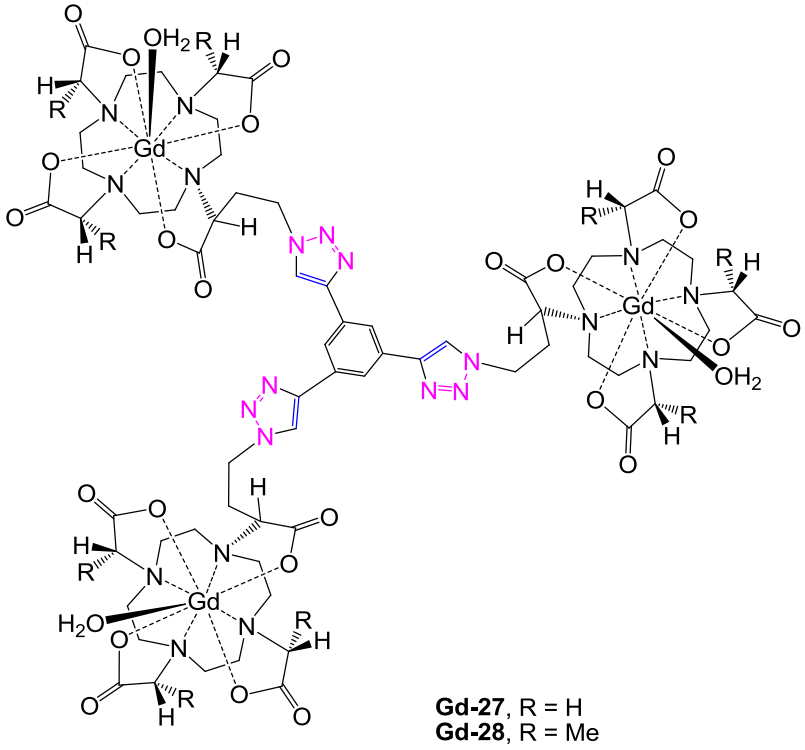

Figure I.1.9. Novel MRI dendrimer contrast agents, **Gd-27** and **Gd-28**.

I.1.8 References

[1] Ogawa, S.; Tank, D. W.; Menon, R.; Ellermann, J. M.; Kim, S. G.; Merkle, H.; Ugurbil, K. *Proc. Nat. Acad. Sci. USA* **1992,** *89*, 5951.

[2] Kwong, K. K.; Belliveau, J. W.; Chesler, D. A.; Goldberg, I. E.; Weisskoff, R. M.; Poncelet, B. P.; Kennedy, D. N.; Hoppel, B. E.; Cohen, M. S.; Turner, R.; Cheng, H. M.; Brady, T. J.; Rosen, B. R. *Proc. Nat. Acad. Sci. USA* **1992,** *89*, 5675.

[3] Tofts, P. S.; Brix, G.; Buckley, D. L.; Evelhoch, J. L.; Henderson, E.; Knopp, M. V.; Larsson, H. B.; Lee, T. Y.; Mayr, N. A.; Parker, G. J.; Port, R. E.; Taylor, J.; Weisskoff, R. M. *J. Magn. Reson. Imaging* **1999**, *10*, 223.

[4] Huang, W.; Li, X.; Morris, E. A.; Tudorica, L. A.; Seshan, V. E.; Rooney, W. D.; Tagge, I.; Wang, Y.; Xu, J.; Springer, C. S., Jr. *Proc. Nat. Acad. Sci. USA* **2008**, *105*, 17943.

[5] Keunen, O.; Johansson, M.; Oudin, A.; Sanzey, M.; Rahim, S. A.; Fack, F.; Thorsen, F.; Taxt, T.; Bartos, M.; Jirik, R.; Miletic, H.; Wang, J.; Stieber, D.; Stuhr, L.; Moen, I.; Rygh, C. B.; Bjerkvig, R.; Niclou, S. P. *Proc. Nat. Acad. Sci. USA* **2011**, *108*, 3749.

[6] de Groot, J. F.; Lamborn, K. R.; Chang, S. M.; Gilbert, M. R.; Cloughesy, T. F.; Aldape, K.; Yao, J.; Jackson, E. F.; Lieberman, F.; Robins, H. I.; Mehta, M. P.; Lassman, A. B.; Deangelis, L. M.; Yung, W. K. A.; Chen, A.; Prados, M. D.; Wen, P. Y. *J. Clin. Oncol.* **2011**, *29*, 2689.

[7] Gallez, B.; Lacour, V.; Demeure, R.; Debuyst, R.; Dejehet, F.; De Keyser, J. L.; Dumont, P. *Magn. Reson. Imaging* **1994**, *12*, 61.

[8] Josephson, L.; Groman, E. V.; Menz, E.; Lewis, J. M.; Bengele, H. *Mag. Res. Imaging* **1990**, *8*, 637.

[9] Konda, S. D.; Aref, M.; Brechbiel, M.; Wiener, E. C. *Invest. Radiol.* **2000**, *35*, 50.

[10] Reimer, P.; Weissleder, R.; Lee, A. S.; Buettner, S.; Wittenberg, J.; Brady, T. J. *Radiology* **1991**, *178*, 769.

[11] Schaffer, B. K.; Linker, C.; Papisov, M.; Tsai, E.; Nossiff, N.; Shibata, T.; Bogdanov, A., Jr.; Brady, T. J.; Weissleder, R. *Magn. Reson. Imaging* **1993**, *11*, 411.

[12] Sipkins, D. A.; Cheresh, D. A.; Kazemi, M. R.; Nevin, L. M.; Bednarski, M. D.; Li, K. C. *Nature Med.* **1998**, *4*, 623.

[13] Vera, D. R.; Buonocore, M. H.; Wisner, E. R.; Katzberg, R. W.; Stadalnik, R. C. *Acad. Radiol.* **1995**, *2*, 497.

[14] Bulte, J. W. M.; Douglas, T.; Witwer, B.; Zhang, S. C.; Strable, E.; Lewis, B. K.; Zywicke, H.; Miller, B.; van Gelderen, P.; Moskowitz, B. M.; Duncan, I. D.; Frank, J. A. *Nature Biotechnol.* **2001**, *19*, 1141.

[15] Hinds, K. A.; Hill, J. M.; Shapiro, E. M.; Laukkanen, M. O.; Silva, A. C.; Combs, C. A.; Varney, T. R.; Balaban, R. S.; Koretsky, A. P.; Dunbar, C. E. *Blood* **2003**, *102*, 867.

[16] Kraitchman, D. L.; Heldman, A. W.; Atalar, E.; Amado, L. C.; Martin, B. J.; Pittenger, M. F.; Hare, J. M.; Bulte, J. W. M. *Circulation* **2003**, *107*, 2290.

[17] Modo, M.; Cash, D.; Mellodew, K.; Williams, S. C. R.; Fraser, S. E.; Meade, T. J.; Price, J.; Hodges, H. *Neuroimage* **2002**, *17*, 803.

[18] Bulte, J. W. M. *AJR Am. J. Roentgenol.* **2009**, *193*, 314.

[19] Lauffer, R. B.; Greif, W. L.; Stark, D. D.; Vincent, A. C.; Saini, S.; Wedeen, V. J.; Brady, T. J. *J. Comput. Assist. Tomogr.* **1985**, *9*, 431.

[20] Lauffer, R. B.; Vincent, A. C.; Padmanabhan, S.; Villringer, A.; Saini, S.; Elmaleh, D. R.; Brady, T. *J. Magn. Reson. Med.* **1987**, *4*, 582.

[21] Geninatti Crich, S.; Cabella, C.; Barge, A.; Belfiore, S.; Ghirelli, C.; Lattuada, L.; Lanzardo, S.; Mortillaro, A.; Tei, L.; Visigalli, M.; Forni, G.; Aime, S. *J. Med. Chem.* **2006**, *49*, 4926.

[22] Stefania, R.; Tei, L.; Barge, A.; Geninatti Crich, S.; Szabo, I.; Cabella, C.; Cravotto, G.; Aime, S. *Chem. Eur. J.* **2009**, *15*, 76.

[23] Beloueche-Babari, M.; Chung, Y. L.; Al-Saffar, N. M. S.; Falck-Miniotis, M.; Leach, M. O. *Brit. J. Cancer* **2010**, *102*, 1.

[24] Remy, C.; Von Kienlin, M.; Lotito, S.; Francois, A.; Benabid, A. L.; Decorps, M. *Magn. Reson. Med.* **1989**, *9*, 395.

[25] Weiner, M. W.; Hetherington, H.; Hubesch, B.; Karczmar, G.; Massie, B.; Maudsley, A.; Meyerhoff, D. J.; Sappey-Marinier, D.; Schaefer, S.; Twieg, D. B.; Matson, G. B. *NMR Biomed.* **1989**, *2*, 290.

[26] Al-Saffar, N. M. S.; Jackson, L. E.; Raynaud, F. I.; Clarke, P. A.; Ramirez de Molina, A.; Lacal, J. C.; Workman, P.; Leach, M. O. *Cancer Res.* **2010**, *70*, 5507.

[27] Glunde, K.; Bhujwalla, Z. M. *Semin. Oncol.* **2011**, *38*, 26.

[28] Koul, D.; Shen, R.; Kim, Y.-W.; Kondo, Y.; Lu, Y.; Bankson, J.; Ronen, S. M.; Kirkpatrick, D. L.; Powis, G.; Yung, W. K. A. *Neuro-oncol.* **2010**, *12*, 559.

[29] Ouwerkerk, R. *Methods Mol. Biol.* **2011**, *711*, 175.

[30] Perman, W. H.; Turski, P. A.; Houston, L. W.; Glover, G. H.; Hayes, C. E. *Radiology* **1986**, *160*, 811.

[31] Boada, F. E.; Tanase, C.; Davis, D.; Walter, K.; Torres-Trejo, A.; Couce, M.; Hamilton, R.; Kondziolka, D.; Bartynski, W.; Lieberman, F. *Conf. Proc. IEEE Eng. Med. Biol. Soc.* **2004**, *7*, 5238.

[32] Kwong, K. K.; Belliveau, J. W.; Chesler, D. A.; Goldberg, I. E.; Weisskoff, R. M.; Poncelet, B. P.; Kennedy, D. N.; Hoppel, B. E.; Cohen, M. S.; Turner, R.; Cheng, H.-m.; Brady, T. J.; Rosen, B. R. *Proc. Nat. Acad. Sci. USA* **1992**, *89*, 5675.

[33] Menon, R. S.; Ogawa, S.; Kim, S. G.; Ellermann, J. M.; Merkle, H.; Tank, D. W.; Ugurbil, K. *Invest. Radiol.* **1992**, *27 Suppl 2*, S47.

[34] Ogawa, S.; Lee, T. M.; Kay, A. R.; Tank, D. W. *Proc. Nat. Acad. Sci. USA* **1990**, *87*, 9868.

[35] Ogawa, S.; Lee, T. M.; Nayak, A. S.; Glynn, P. *Magn. Reson. Med.* **1990**, *14*, 68.

[36] Burton, D. R.; Forsen, S.; Franek, F.; Novotny, J. *FEBS Lett.* **1979**, *102*, 249.

[37] Koenig, S. H. & Brown, R. D., 3rd *Magn. Reson. Med.* **1984**, *1*, 478.

[38] Lauffer, R. B. *Chem. Rev*. **1987**, *87*, 901.

[39] Caravan P., Ellison J. J., McMurry T. J., et al. *Chem Rev*. **1999**, *99*, 2293.

[40] Jacques, V.; Dumas, S.; Sun, W. C.; Troughton, J. S.; Greenfield, M. T.; Caravan, P. *Invest. Radiol.* **2010**, *45*, 613.

[41] Freed, J. *J. Chem. Phys.* **1978**, *68*, 4034.

[42] Koenig, S. H.; Kellar, K. E. *Magn. Reson. Med.* **1995**, *34*, 227.

[43] Donahue, K. M.; Weisskoff, R. M.; Chesler, D. A. et al. *Magn. Reson. Med*. **1996**, *36*, 858.

[44] Crich, S. G.; Biancone, L.; Cantaluppi, V. et al. *Magn. Reson. Med*. **2004**, *51*, 938.

[45] Mandeville, J. B.; Moore, J.; Chesler, D. A. et al. *Magn. Reson. Med*. **1997**, *37*, 885.

[46] Billotey, C.; Wilhelm, C.; Devaud, M. et al. *Magn. Reson. Med*. **2003**, *49*, 646.

[47] Aref, M.; Brechbiel, M.; Wiener, E.C. *Invest. Radiol*. **2002**, *37*, 178.

[48] Manabe, Y.; Longley, C.; Furmanski, P. *Biochim. Biophys. Acta* **1986**, *883*, 460.

[49] Shreve, P.; Aisen, A. M. *Magn. Reson. Med.* **1986**, *3*, 336.

[50] Josephson, L.; Groman, E. V.; Menz, E.; Lewis, J. M.; Bengele, H. *Magn. Reson. Imaging* **1990**, *8*, 637; Reimer, P.; Weissleder, R.; Lee, A. S.; Buettner, S.; Wittenberg, J.; Brady, T. J. *Radiology* **1991**, *178*, 769.

[51] Reimer, P.; Weissleder, R.; Lee, A. S.; Buettner, S.; Wittenberg, J.; Brady, T. J. *Radiology* **1991**, *178*, 769.

[52] Schaffer, B. K.; Linker, C.; Papisov, M.; Tsai, E.; Nossiff, N.; Shibata, T.; Bogdanov, A., Jr.; Brady, T. J.; Weissleder, R. *Magn. Reson. Imaging* **1993**, *11*, 411.

[53] Sipkins, D. A.; Cheresh, D. A.; Kazemi, M. R.; Nevin, L. M.; Bednarski, M. D.; Li, K. C. *Nature Med.* **1998**, *4*, 623.

[54] Konda, S. D.; Aref, M.; Brechbiel, M.; Wiener, E. C. *Invest. Radiol.* **2000**, *35*, 50.

[55] Wiener, E.; Tomalia, D.; Lauterbur, P. C. *Proc. Soc. Magn. Reson. Med.* **1990**, 1106.

[56] Wiener, E. C.; Brechbiel, M. W.; Brothers, H.; Magin, R. L.; Gansow, O. A.; Tomalia, D. A.; Lauterbur, P. C. *Magn. Reson. Med.* **1994**, *31*, 1.

[57] (a) Ersoy, H.; Rybicki, F. J. *J. Magn. Reson. Imaging* **2007,** *26*, 1190-1197; (b) Grobner, T. *Nephrol., Dial., Transplant.* **2006,** *21*, 1104.

[58] Oksendal, A. N.; Hals, P. A. *J. Magn. Reson. Imaging* **1993,** *3*, 157.

[59] (a) *Magn. Res. Med.* **1999**, *31*, 1; (b) *J. Drug Targeting* **2008**, *16*, 329.; (c) *J. Inorg. Biochem.* **2011**, *105*, 250; (d) *J. Contr. Rel.* **2009**, *136*, 14; (e) *J. Nanobiotech.* **2010,** *6*, 32; (f) *J. Inorg. Biochem.* **2011,** *105*, 250.

[60] Tóth, É.; Helm, L.; Kellar, K. E.; Merbach, A. E. *Chem.- Eur. J.* **1999,** *5*, 1202.

[61] (a) Tóth, É.; van Uffelen, I.; Helm, L.; Merbach, A. E.; Ladd, D.; Briley-Sæbø, K.; Kellar, K. E. *Magn. Reson. Chem.* **1998,** *36*, S125; (b) Dunand, F. A.; Tóth, É.; Hollister, R.; Merbach, A. E. *J. Biol. Inorg. Chem.* **2001,** *6*, 247; (c) Yan, G. P.; Zhuo, R. X.; Xu, M. Y.; Zhang, X.; Li, L. Y. *Polymer International* **2002,** *51*, 892; (d) Duarte, M. G.; Gil, M. H.; Peters, J. A.; Colet, J. M.; Vander Elst, L.; Muller, R. N.; Geraldes, C. F. G. C. *Bioconjugate Chem.* **2001,** *12*, 170.

[62] (a) Tóth, É.; Pubanz, D.; Vauthey, S.; Helm, L.; Merbach, A. E. *Chem.- Eur. J.* **1996,** *2*, 1607; (b) Wiener, E. C.; Brechbiel, M. W.; Brothers, H.; Magin, R. L.; Gansow, O. A.; Tomalia, D. A.; Lauterbur, P. C. *Magn. Reson. Med.* **1994,** *31*, 1; (c) Margerum, L. D.; Campion, B. K.; Koo, M.; Shargill, N.; Lai, J. J.; Marumoto, A.; Sontum, P. C. *J. Alloys Compd.* **1997,** *249*, 185; (d) Bryant, L. H.; Brechbiel, M. W.; Wu, C. C.; Bulte, J. W. M.; Herynek, V.; Frank, J. A. *J. Magn. Reson. Imaging* **1999,** *9*, 348; (e) Nicolle, G. M.;

Tóth, É.; Schmitt-Willich, H.; Radüchel, B.; Merbach, A. E. *Chem.- Eur. J.* **2002,** *8*, 1040.

[63] (a) André, J. P.; Tóth, É.; Fischer, H.; Seelig, A.; Mäcke, H. R.; Merbach, A. E. *Chem. Eur. J.* **1999,** *5*, 2977; (b) Nicolle, G. M.; Tóth, É.; Eisenwiener, K. P.; Macke, H. R.; Merbach, A. E. *J. Biol. Inorg. Chem.* **2002,** *7*, 757; (c) Hovland, R.; Aasen, A. J.; Klaveness, J. *Org. Biomol. Chem.* **2003,** *1*, 1707; (d) Accardo, A.; Tesauro, D.; Roscigno, P.; Gianolio, E.; Paduano, L.; D'Errico, G.; Pedone, C.; Morelli, G. *J. Am. Chem. Soc.* **2004,** *126*, 3097; (e) Kimpe, K.; Parac-Vogt, T. N.; Laurent, S.; Pierart, C.; Vander Elst, L.; Muller, R. N.; Binnemans, K. *Eur. J. Inorg. Chem.* **2003**, 3021.

[64] (a) Aime, S.; Fasano, M.; Terreno, E.; Botta, M. In *The Chemistry of Contrast Agents in Medical Magnetic Resonance Imaging;* Merbach, A. E.; Tóth, É. Eds.; John Wiley & Sons Ltd.: Chichester, 2001; pp. 193-241; (b) Aime, S.; Botta, M.; Fasano, M.; Crich, S. G.; Terreno, E. *J. Biol. Inorg. Chem.* **1996,** *1*, 312; (c) Caravan, P.; Cloutier, N. J.; Greenfield, M. T.; McDermid, S. A.; Dunham, S. U.; Bulte, J. W. M.; Amedio, J. C.; Looby, R. J.; Supkowski, R. M.; Horrocks, W. D.; McMurry, T. J.; Lauffer, R. B. *J. Am. Chem. Soc.* **2002,** *124*, 3152; (d) Lauffer, R. B.; Parmelee, D. J.; Dunham, S. U.; Ouellet, H. S.; Dolan, R. P.; Witte, S.; McMurry, T. J.; Walovitch, R. C. *Radiology* **1998,** *207*, 529.

[65] (a) Hartman, K. B.; Laus, S.; Bolskar, R. D.; Muthupillai, R.; Helm, L.; Tóth, É.; Merbach, A. E.; Wilson, L. J. *Nano Lett.* **2008,** *8*, 415; (b) Tran, L. A.; Krishnamurthy, R.; Muthupillai, R.; da Graça Cabreira-Hansen, M.; Willerson, J. T.; Perin, E. C.; Wilson, L. J. *Biomaterials* **2010,** *31*, 9482.

[66] (a) Moriggi, L.; Cannizzo, C.; Dumas, E.; Mayer, C. R.; Ulianov, A.; Helm, L. *J. Am. Chem. Soc.* **2009,** *131*, 10828; (b) Park, J.-A.; Kim, H.-K.; Kim, J.-H.; Jeong, S.-W.; Jung, J.-C.; Lee, G.-H.; Lee, J.; Chang, Y.; Kim, T.-J. *Bioorg. Med. Chem. Lett.* **2010,** *20*, 2287.

[67] (a) Unger, E. C.; Totty, W. G.; Neufeld, D. M.; Otsuka, F. L.; Murphy, W. A.; Welch, M. S.; Connett, J. M.; Philpott, G. W. *Invest. Radiol.* **1985,** *20*, 693; (b) Sipkins, D. A.; Cheresh, D. A.; Kazemi, M. R.; Nevin, L. M.; Bednarski, M. D.; Li, K. C. P. *Nat. Med.* **1998,** *4*, 62; (c) Anderson, S. A.; Rader, R. K.; Westlin, W. F.; Null, C.; Jackson, D.; Lanza, C. M.; Wickline, S. A.; Kotyk, J. J. *Magn. Reson. Med.* **2000,** *44*, 433.

[68] (a) Abiraj, K.; Jaccard, H.; Kretzschmar, M.; Helm, L.; Maecke, H. R. *Chem. Commun.* **2008**, 3248; (b) Sturzu, A.; Kalbacher, H.; Echner, H.; Klose, U.; Gharabaghi, A.; Heckl, S. *Amino Acids* **2010,** *38*, 1415.

[69] (a) Luo, Kui; Liu, Gang; He, Bin; Wu, Yao; Gong, Qingyong; Song, Bin; Ai, Hua; Gu, Zhongwei *Biomaterials* **2011**, *32*, 2575; (b) Kundu, Amitava; Peterlik, Herwig; Krssak, Martin; Bytzek, Anna K.; Pashkunova-Martic, Irena; Arion, Vladimir B.; Helbich, Thomas H.; Keppler, Bernhard K. *J. Inorg. Biochem.* **2011,** *105*, 250.

[70] (a) te Boekhorst, B. C. M.; Bovens, S. M.; van de Kolk, C. W. A.; Cramer, M. J. M.; Doevendans, P. A. F. M.; ten Hove, M.; van der Weerd, L.; Poelmann, R.; Strijkers, G. J.; Pasterkamp, G.; et al *NMR Biomed*. **2010**, *23*, 939.; (b) Morisco, A.; Accardo, A.; Gianolio, E.; Tesauro, D.; Benedetti, E.; Morelli, G. *J. Peptide Sci.* **2009**, *15*, 242.

I. 2. Synthesis of Homochiral (*S*)-4-Azido-2-hydroxy-butyric Acid Derivatives

I.2.1. Introduction

Figure I.2.1 shows the derivatives to be made, so that we can make chelates capable of acting as a ligand to metals such as copper or gadolinium, but with a coupling arm for further chemistry. The linking part was designed include a carboxylate, so as to be similar to the other three arms, derived from its deprotection from either a methyl ester or *tert*-butyl (*t*-butyl) ester. The coupling end of the linker needed to be versatile, and usable under a variety of coupling conditions. We chose to use an azide because of its popular usage in coupling through click chemistry[1] or, after reducing to a primary amine, peptide coupling. In addition to synthesizing a bifunctional moiety with coupling and coordinating abilities, the chirality of the compound was also important. For the MRI project (Section I.4.), the chirality of the ligand influences the relaxivity of the Gd(III)-based MRI contrast agent.[2] In regards to the PET project (Chapter II), the chirality may be of interest concerning binding affinity.[3]

Initially the unique moiety was design for our MRI projects based on the 1,4,7,10-tetraazacyclododecane-1,4,7,10- tetraacetic acid (DOTA) and (1*R*,4*R*,7*R*,10*R*)-α, α', α'', α''''-tetramethyl-1,4,7,10-tetraaza cyclododecane-1,4,7,10-tetraacetic acid (DOTMA) chelates. We looked for a way to design the coordinating part of our linker to be similar to the acetic acid ligands of DOTA with room to attach the azide, Figure I.2.1.

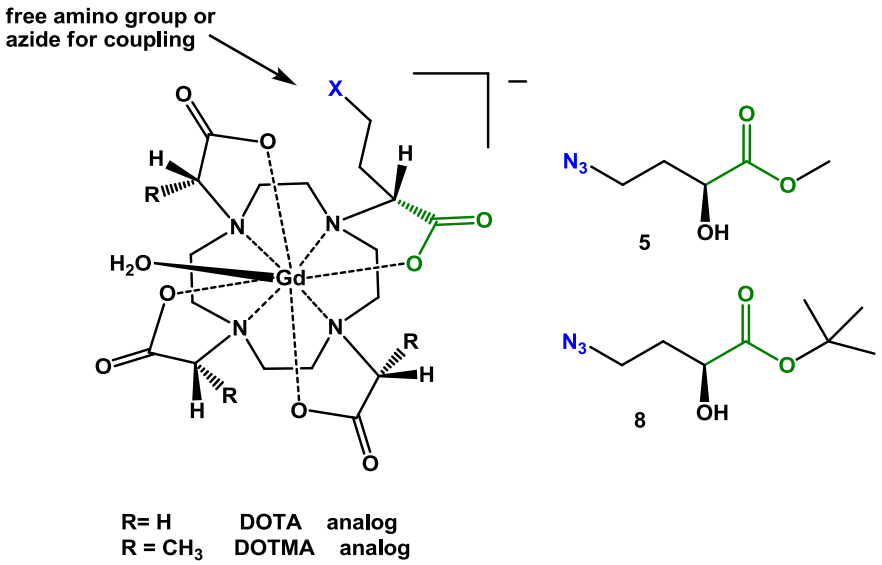

Figure I.2.1. Relationship of **5** and **8** to the DOTA/DOTMA chelators for Gd(III)-based MRI contrast agents. The blue X represents the coupling part of the moiety, either a primary amine or azide. The green atoms represent the coordinating ligand in similar strength and length as the other coordinating carboxylates. Compound **5** is the methyl ester azide; compound **8**, the *t*-butyl ester azide.

Racemic **5** was known,[4] and synthesis of the (*R*)-enantiomer was described,[5] but we needed the (*S*)-antipode **5** to match the chirality of lactic-acid derived arms in the DOTMA analog. Nakatani *et al.* made **5** on small scale, but we needed the compound on larger scale. Thus we used a modified and optimized version of their synthesis starting from the relatively cheap starting material (L-malic acid) and ending with **5** on multi-gram scale in high enantiomeric and product purity, Figure I.2.1. The methyl ester was easier to synthesize, purify and isolate than the *t*-butyl ester analog (compound **8**). The *t*-butyl ester version is attractive because one could avoid base-mediated deprotections in biological applications of the resulting imaging agents. The journey of synthesizing and optimizing compound **5** and attempts at other linker moieties (Figure I.2.1) will be discussed.

I.2.2. Experimental section

General: Unless specified, all the reactions were done in oven-dried or flame dried glassware in an atmosphere of dry argon or nitrogen gas using standard Schlenk techniques. The anhydrous solvents were purchased from Acros and Aldrich chemical companies and used in the reactions without further purification. The stains used to visualize the TLC plates (aluminum backed 200 μm silica) were Hanessian's Stain [$CeSO_4$ (5 g) and $(NH_4)Mo_7O_{24}{\cdot}4H_2O$ (25 g) dissolved in water (450 mL) and concentrated sulfuric acid (50 mL)], and potassium permanganate stain [$KMnO_4$ (1.5 g) and K_2CO_3 (10 g) dissolved in 10% NaOH (1.25 mL) in water (200 mL)]. A UV lamp with two wavelengths, long-wave (336 nm) and short-wave (254 nm).

Caution: Although we did not observe any unusual decompositions of the azides reported, organic azides can be explosive materials and should be handled with care.

^{1}H, ^{13}C, ^{23}Na and ^{19}F NMR spectra were recorded using Bruker ACP-500 or Varian spectrometers at 30 ^{o}C or room temperature. ^{1}H, ^{13}C and ^{19}F NMR chemical shifts are reported in ppm referenced to residual solvent resonances (^{1}H NMR: δ 7.27 for $CHCl_3$ in $CDCl_3$, and 3.31 for CHD_2OD in CD_3OD. ^{13}C NMR: δ 77.23 for $CDCl_3$ and 49.15 for CD_3OD. ^{19}F NMR: -76.55 for CF_3COOD). Deuterated solvents for NMR were obtained from Cambridge Isotope Laboratories and were used without purification. Electrospray ionization Mass spectra (ESI MS) were collected on a Micromass Quattro II, triple quadrupole mass spectrometer using both negative and positive ionization modes. Elemental analyses were performed at NuMega Resonance Labs, San Diego, CA. LCMS spectra were recorded on Agilent Technologies 6330 Ion Trap instrument. HR- ESI-TOF

analyses were performed at Scripps Center for Metabolomics and Mass Spectrometry, La Jolla, CA. IR spectra were obtained on a Nicolet Nexus 670 FT-IR Instrument using KBr pellets.

*Synthesis of (3-oxo-1,4-dioxa-spiro[4.5]dec-2-yl)-acetic acid (**1**).*

To a dry flask was added L-(-)-malic acid (20.130 g, 149.15 mmol) dissolved in dry diethyl ether 200 ml. To this solution was added cyclohexanone (23.2 mL, 223.7 mmol) dissolved in dry diethyl ether 100 mL. The solution was cooled to 0 ºC, under nitrogen. Trifluoroborane etherate (28.4 mL, 223.7 mmol) was added dropwise over 10 min. to the cold solution. The reaction stirred at room temperature under nitrogen overnight. The reaction was checked for completion by TLC (1:10 diethyl ether to hexanes) and developed in Hanessian's stain giving a product spot with a R_f = 0.30. The reaction solution was washed with 10% NaOAc (3 x 100 mL), Et_2O (1 x 100 mL), and brine (1 x 100 mL). The organic layer was collected and dried over $MgSO_4$, and concentrated under vacuum. The tan solid was recrystralized twice with hot hexanes, affording an off-white solid (28.760 g, crude yield 90%).^{1}H NMR ($CDCl_3$, 399.8 MHz): δ 10.42 (br s, 1H), 4.72 (dd, $^3J_{HH}$= 6.4 Hz, $^3J_{HH}$= 6.4 Hz, 1H), 2.91 (dddd, J_{HH}= 4.0, 6.4, 6.8, 17.2 Hz, 2H), 1.86-1.79 (m, 2H), 1.78-1.57 (m, 6H), 1.54-1.36 (m, 2H).

*Synthesis of 3-(2-hydroxy-ethyl)-1,4-dioxa-spiro[4.5] decan-2-one (**2**).*

To a dry three-neck flask equipped with stir bar, nitrogen inlet, addition funnel was added a solution THF (15 mL), borane dimethyl sulfide complex (2.8 mL, 28 mmol), and trimethyl borate (3.2 mL, 28 mmol). The solution was cooled to 0 ºC, under

nitrogen. Compound **1** (3.0245 g, 14.1 mmol) was dissolved in dry THF (5.0 mL) and transferred to the additional funnel via cannula then added dropwise over 10 min. to the cold solution. The reaction stirred for one hour at 0ºC, under nitrogen; analysis of an aliquot by TLC (1:1 hexanes to ethyl acetate) using Hanessian's stain showed a product spot with a R_f = 0.36. The reaction was then worked up by adding MeOH (2 x 90 mL) slowly while stirring. The solution was then concentrated under vacuum to give a faint yellow oil (2.6788 g, crude yield 95%). ^{1}H NMR ($CDCl_3$, 399.8 MHz): δ 4.51 (dd, $^3J_{HH}$= 8.0 Hz, $^3J_{HH}$= 8.0 Hz, 1H), 3.79-3.68 (m, 2H), 2.10-2.02 (m, 1H), 1.94-1.86 (m, 1H), 1.84-1.54 (m, 10H).

*Synthesis of methanesulfonic acid 2-(3-oxo-1,4-dioxa-spiro[4.5]dec-2-yl)-ethyl ester (**3**).*

To a dry flask was added compound **2** (11.215 g, 55.9 mmol) dissolved in dry DCM (60 mL). The solution was cooled to 0 ºC, under nitrogen to which was added N,N-diisopropylethylamine (9.1358 g, 70.7 mmol) dropwise over 10 min. and then methanesulfonyl chloride (6.8038g, 59.4 mmol) was added dropwise over 10 min. The sides of the flask were washed down with dry DCM (40 mL) and the reaction stirred on ice for one hour. Analysis of an aliquot by TLC (2:1 hexanes to ethyl acetate, spots visualized using Hanessian's stain) showed a product spot with a R_f = 0.41. To the reaction solution was added 5% $NaHPO_4$ 100 mL, and was then extracted with DCM (3 x 100 mL). The organic phases were combined and washed with brine (1 x 100 mL). The organic layer was collected and dried over $MgSO_4$ filtered, and the filtrate was concentrated under vacuum. The oil was further dried by adding benzene (100 mL) and concentrating under vacuum to yield a yellowish oil (15.645 g, crude yield 101%). ^{1}H

NMR ($CDCl_3$, 399.8 MHz): δ 4.51 (dd, $^3J_{HH}$= 7.4 Hz, $^3J_{HH}$= 4.9 Hz, 1H), 4.47-4.28 (m, 2H), 3.01 (s, 3H), 2.36-2.24 (m, 1H), 2.19-2.06 (m, 1H), 1.88-1.54 (m, 8H), 1.53-1.34 (m, 2H). ^{13}C NMR ($CDCl_3$, 100.5 MHz): δ 170.8, 111.3, 69.8, 65.0, 38.0, 37.1, 35.7, 32.0, 27.7, 25.1, 23.7.

To a dry flask was added compound **2** (11.2154 g, 55.9 mmol) dissolved in dry DCM (60 mL). The solution under nitrogen was cooled to 0ºC, and N,N-diisopropylethylamine (9.1358 g, 70.7 mmol) was added dropwise over 10 min followed by methanesulfonyl chloride (6.8038 g, 59.4 mmol) dropwise over 10 min. The sides of the flask were washed down with dry DCM (40 mL) and the reaction stirred on ice for 1 h. Analysis of an aliquot by TLC showed product R_f = 0.41 (hexanes-ethyl acetate, 2:1, developed in Hanessian's stain). To the reaction solution was added 5% $NaHPO_4$ (100 mL), and the aqueous phase was then extracted with DCM (3 ×100 mL). The organic phases were combined and washed with brine (1×100 mL). The organic layer was collected over anhydrous $MgSO_4$, filtered, and the filtrate was concentrated under vacuum. The oil was further dried by adding benzene (100 mL) and concentrating under vacuum to yield a yellowish oil (15.6447g, crude yield 101%). ^1H NMR ($CDCl_3$, 399.8 MHz): δ 4.51 (dd, $^3J_{HH}$= 7.4 Hz, $^3J_{HH}$= 4.9 Hz, 1H), 4.47-4.28 (m, 2H), 3.01 (s, 3H), 2.36-2.24 (m, 1H), 2.19-2.06 (m, 1H), 1.88-1.54 (m, 8H), 1.53-1.34 (m, 2H). ^{13}C (^1H) NMR ($CDCl_3$, 100.5 MHz): δ 170.8, 111.3, 69.8, 65.0, 38.0, 37.1, 35.7, 32.0, 27.7, 25.1, 23.7.

*Synthesis of 3(2-azido-ethyl)-1,4-dioxa-spiro[4.5] decan-2-one (**4**).*

To a flask was added compound **3** (3.7536 g, 13.5 mmol) dissolved in dry DMF

(13 mL). Sodium azide (1.1462 g, 17.5 mmol) was then added to the flask. The sides of the flask were rinsed down with dry DMF (3 mL). The reaction was stirred overnight under nitrogen at 70 ºC. An aliquot was removed and analyzed by TLC (2:1 hexanes to ethyl acetate and visualized using Hanessian's stain) showing a product with a R_f = 0.77. The reaction was then cooled to room temperature. To the solution was added petroleum ether (50 mL). The reaction was extracted with petroleum ether (5 x 50 mL) and the combined organic phases were washed with deionized water (50 mL). The organic layer was collected and dried over $MgSO_4$, filtered and filtrate concentrated under vacuum to afford a yellow oil (2.5422 g, crude yield 84%). ^{1}H NMR ($CDCl_3$, 399.8 MHz): δ 4.40 (dd, $^3J_{HH}$= 7.6 Hz, $^3J_{HH}$= 4.5 Hz, 1H), 3.57-3.39 (m, 2H), 2.15-2.01 (m, 1H,), 1.95-1.83 (m, 1H), 1.83-1.70 (m, 2H), 1.70-1.48 (m, 6H), 1.48-1.25 (m, 2H).

To a flask was added compound **3** (3.7536 g, 13.50 mmol) dissolved in dry DMF (13 mL). Sodium azide (1.1462 g, 17.55 mmol) was then added to the flask. The sides of the flask were rinsed down with dry DMF (3 mL). The reaction was stirred overnight under nitrogen at 70 ºC. An aliquot was analyzed by TLC showing product R_f = 0.77 (hexanes-ethyl acetate, 2:1, visualized using Hanessian's stain). The reaction was then cooled to room temperature. To the solution was added petroleum ether (50 mL). The reaction was extracted with petroleum ether (5×50 mL) and combined organic fractions washed with deionized water (50 mL). The organic layer was collected and dried over anhydrous $MgSO_4$, filtered and filtrate concentrated under vacuum to afford a yellow oil (2.5422 g, crude yield 84%). ^{1}H NMR ($CDCl_3$, 399.8 MHz): δ 4.40 (dd, $^3J_{HH}$= 7.6 Hz, $^3J_{HH}$= 4.5 Hz, 1H), 3.57-3.39 (m, 2H), 2.15-2.01 (m, 1H,), 1.95-1.83 (m, 1H), 1.83-1.70

(m, 2H), 1.70-1.48 (m, 6H), 1.48-1.25 (m, 2H).

*Synthesis of 4-azido-2-hydroxy-butyric acid methyl ester (**5**).*

To a dry flask was added compound **4** (9.3342 g, 41.47 mmol) dissolved in MeOH (50 mL). The solution was cooled to 0ºC, under nitrogen. A solution of sodium methoxide (1.1529g, 20.73 mmol) dissolved in MeOH (30 mL) was cooled to 0 ºC before being added dropwise over 5 min. into the reaction flask. The reaction stirred for 30 min in an ice bath. The reaction was checked for completion by TLC (2:1 hexanes to ethyl acetate), using Hanessian's stain which showed a product spot with a R_f = 0.49. Dowex 50x8 H^+ resin (actual mass not noted) was added to the solution until the pH reached 7.0. The resin was then filtered off and the filtrate concentrated under vacuum. The crude product was purified by silica gel chromatography (hexanes/ EtOAc 2.5/1), affording a clear oil (2.9318 g, 43%). ^{1}H NMR ($CDCl_3$, 399.8 MHz): δ 4.30 (dd, , J_{HH}= 4.1, 7.6 Hz, 1H), 3.82 (s, 3H), 3.55-3.42 (m, 2H), 3.05-2.84 (br s, 1H), 2.09 (dddd, J_{HH}= 4.1, 6.6, 7.4, 14.1 Hz, 1H), 1.90 (tdd, J_{HH}= 6.3, 7.8, 12.5 Hz, 1H). ^{13}C (^{1}H) NMR ($CDCl_3$, 150.8 MHz): δ 174.7, 67.42, 52.26, 46.93, 32.82.

*Synthesis of 4-azido-2-trifluoromethanesulfonyloxy-butyric acid methyl ester (**6a**).*

To a dry flask was added compound **5** (0.7214 g, 4.53 mmol) dissolved in dry DCM (8 mL) at 0ºC, under nitrogen. To this solution was added N,N-diisopropylethylamine (0.6634 g, 5.13 mmol) dissolved in dry DCM (8 mL). Trifluoromethanesulfonic anhydride (1.3422 g, 4.76 mmol) was then added to the reaction dropwise over 10 min. The reaction stirred for one hour at 0 ºC, under nitrogen.

The reaction was checked for completion by TLC (2:1 hexanes to ethyl acetate), developing the plate in Hanessian's stain to see a product spot with a R_f = 0.70. The reaction solution was then concentrated under vacuum and pentanes 100mL was added. The precipitate that formed was filtered off and the filtrate concentrated under vacuum to yield a yellowish oil (1.2300 g, crude yield 93%). ^{1}H NMR ($CDCl_3$, 399.8 MHz): δ 5.27 (dd, J_{HH}= 5.2, 7.2 Hz, 1H), 3.89 (s, 3H), 3.59 (m, 2H), 2.29-2.23 (m, 2H). ^{19}F NMR (CD_3OD, 399.8 MHz): δ -74.8 (s).

*Synthesis of 4-azido-2-(4-nitro-benzenesulfonyloxy)-butyric acid methyl ester (**6b**).*

To a dry flask was added compound **5** (4.2483 g, 26.70 mmol) dissolved in dry DCM (130 mL). The solution was cooled to 0 ºC, under nitrogen to which was added triethylamine (7.4 mL, 53 mmol). A solution of 4-dimethylamine pyridine (0.4447 g, 3.64 mmol) dissolved in dry DCM (10mL) was added dropwise over 5 min and a solution of 4-nitrobenzenesulfonyl chloride (8.1471 g, 36.76 mmol) dissolved in dry DCM (10 mL) was added dropwise over 10 min. The reaction stirred on ice under nitrogen overnight. An aliquot was taken and checked for completion by TLC (2:1 hexanes to ethyl acetate, visualization using Hanessian's stain) to show a product spot with a R_f = 0.47. The reaction was extracted with Na_2CO_3 (2 x 100 mL), 1M HCl (2 x 100 mL); the aqueous layer was extracted with DCM (1 x 100 mL), and combined organic phases were washed deionized water (1 x 100 mL) and dried over Na_2SO_4, filtered and the filterate was concentrated under vacuum. The crude product was purified by silica gel chromatography (hexanes/EtOAc 4/1) affording a light yellow oil (3.9400 g, 43%).^{1}H NMR ($CDCl_3$, 399.8 MHz): δ 8.42-8.38 (m, 2H), 5.13 (dd, J_{HH}= 8.4, 8.4 Hz, 1H), 3.70 (s, 1H), 3.51-

3.44 (m, 1H), 3.40-3.34 (m, 1H), 2.20-2.04 (m, 2H). ^{13}C NMR ($CDCl_3$, 150.8 MHz): δ 168.0, 150.8, 141.6, 129.3, 124.2, 75.4, 52.8, 46.1, 31.2. See Appendix Figure A.1.

*Conversion of methyl ester to alpha-hydroxy acid (**7**).*

To a dry scintillation vial was added compound **5** (1.0101 g, 6.347 mmol) followed by THF (2.3 mL) to make a solution. A solution of LiOH-H_2O (0.5696 g, 13.57 mmol) was made from 3.3/1 deionized water to THF in another scintillation vial. The mixture was shaken and added to the compound **5** vial. The reaction was stirred for 24 h and checked for completion by TLC (2:1 hexane to ethyl acetate) and developed in Hanessian's stain. A new spot with an of R_f = 0.95 appeared and the pH of reaction was pH ~11. Then H^+ Dowex resin (5.4903 g) was added to the reaction vial until pH reached ~2. After filtration, the filtrate was concentrated by rotary evaporation to give an oil (0.8013 g, crude yield of 87%). ^{1}H NMR ($CDCl_3$, 399.8 MHz): δ 4.40 (dd, J_{HH}= 7.9, 4.0 Hz, 1H), 3.57 (t, J_{HH}= 6.5 Hz, 2H), 2.17 (dddd, J_{HH}= 4.1, 6.9, 7.2, 14.1 Hz, 1H), 1.98 (tdd, J_{HH} = 7.8, 8.0, 14.1 Hz, 1H).

*Conversion of alpha-hydroxy acid to 4-azido-2-hydroxy-butyric acid tert-butyl ester (**8**).*

To a dry flask was added compound **7** (0.1522 g, 1.23 mmol) dissolved in *t*-BuOAc (7 mL). Solution was cooled to 0 ºC, under nitrogen. Trifluoromethansulfonic acid (10.9 µL, 0.123 mmol) was added to the solution and stirred for 23.5 h as the ice bath warmed to room temperature. The reaction was checked by TLC (100% ethyl acetate) and Hanessian's stain, showing a new spots with R_f = 0.65 and 0.98. Triethylamine (34 µL, 0.2456 mmol) was added to the solution and stirred for 5 min, pH

~6. To the solution DCM (5 mL) and $NaHCO_3$ (5 mL) was added and stirred for 4 min, then transferred to a separatory funnel. Organic phase was extracted with DCM which was washed with $NaHCO_3$ and deionized H_2O. Organic layer was dried over Na_2SO_4, filtered and concentrated by rotary evaporation to give an oil (0.0221 g, crude yield of 8.9%). ^{1}H NMR ($CDCl_3$, 399.8 MHz): δ 4.32 (dd, $^3J_{HH}$= 7.8 Hz, $^3J_{HH}$= 4.1 Hz, 1H), 3.54-3.50 (m, 2H), 1.71 (m, 1H), 1.66 (m, 1H) (note: it was not determined which of these peaks belonged to the desired product).

I.2.3. Results and discussion

The L-(-)-malic acid diol groups were protected to give **1** (crude yield 90%). The carboxylic acid on the other end was reduced to give primary alcohol **2** (crude yield 95%). Compound **2** was mesylated to give **3** which provided a better leaving group for the next step. Sodium azide was used for S_n2 chemistry yielding compound **4** (crude yield 84%). The cyclohexanone protecting group was removed using sodium methoxide in methanol to give retained stereochemistry to the chiral carbon in compound **5**, Figure I.2.2.

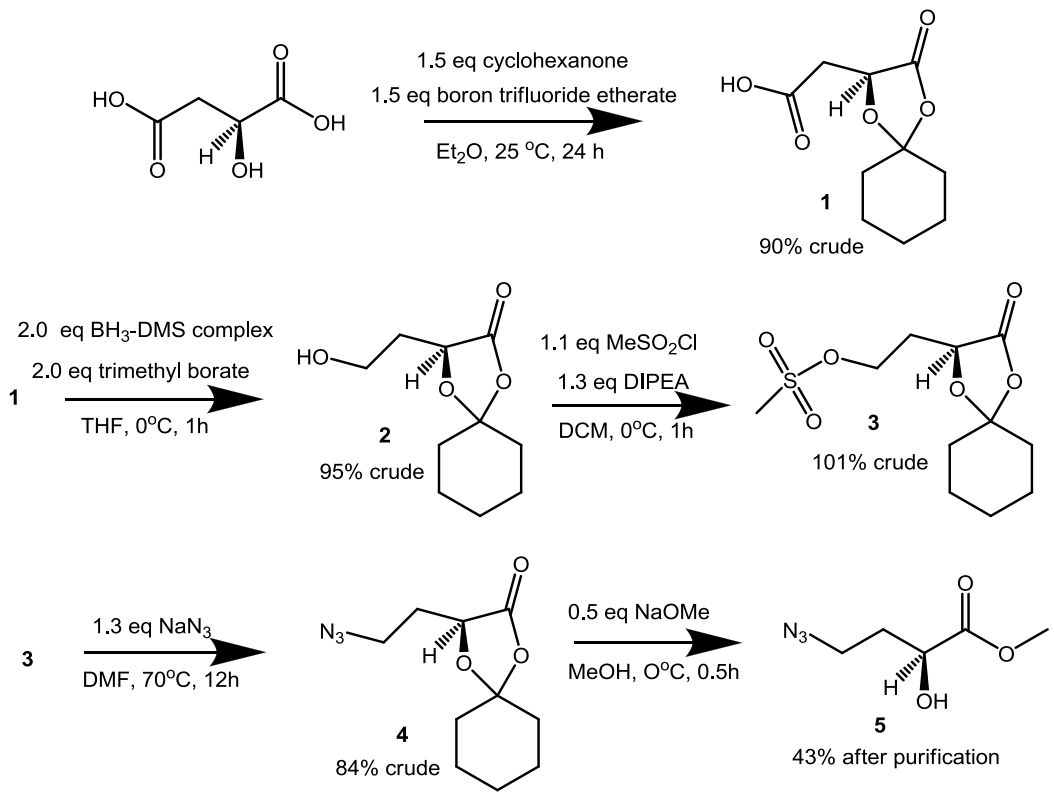

Figure I.2.2. Synthesis of chiral compound **5**.

The reagents and steps used were modified versions of literature procedure.[6] The compound was purified by normal phase chromatography to yield 43% clean product from **4**, Figure I.2.2. The synthesis of compound **5** in 31.2% overall yield in 5 steps is also reported in our published paper; *Investigative Radiology* (**2010**), *45*(10), 641.

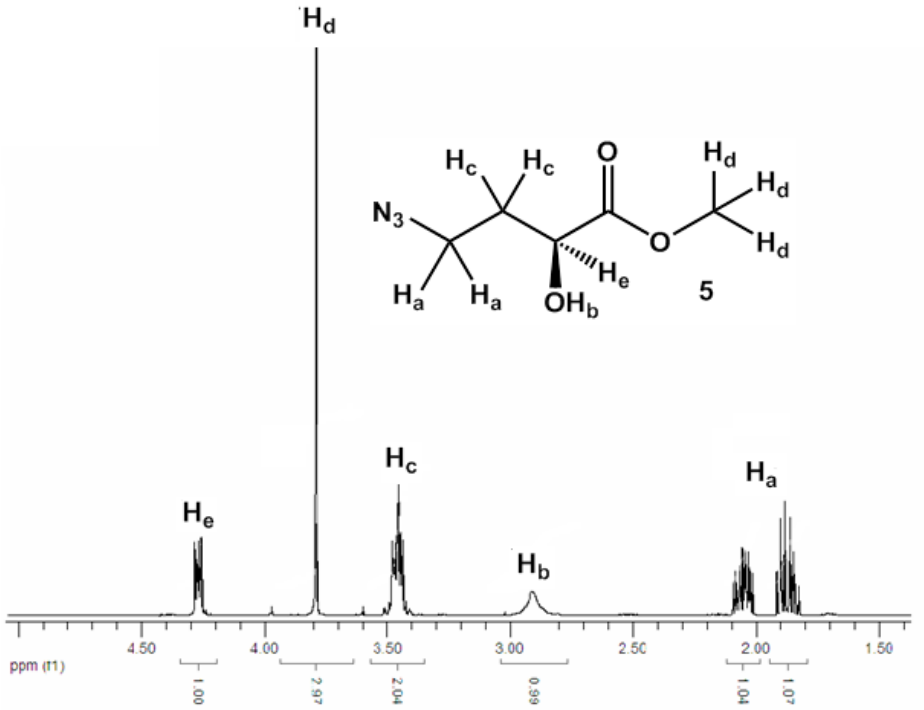

Figure I.2.3. Proton spectrum of purified compound **5** ($CDCl_3$, 399.8 MHz), peaks assigned.

Since possible enantiomers would not be distinguished from each other in proton NMR, compound **5** was further analyzed by Moshers' acid derivatization[7] to verify stereochemical purity. Mosher's acid, α-methoxy-α-trifluoromethylphenylacetate (MTPA) was used to make diastereomers of compound **5**. The diastereomers can be detected and quantified by ^{1}H and ^{19}F NMR, Figure I.2.3. Because we had neither a racemic sample of **5**, nor its (*R*) enantiomer, we used (*R*+*S*)-MTPA and (*S*)-MTPA to compare chirality and determine purity of compound **5**. If compound **5** was not enantiomerically pure (*R* and *S* present), then two sets of peaks should be seen in ^{1}H and ^{19}F NMR when reacted with (*S*)-MTPA to make two diastereomers (*R*,*S* and *S*,*S*), Figure I.2.4. In addition, mixing compound **5** (if **5** was a mixture of *R* and *S* enantiomers) with (*R*+*S*)-MTPA would result in four products but only two are visible by NMR (*R*,*S* and *R*,*R* or *S*,*S* and *S*,*R*), Figure I.2.4. Based on analysis of the ^{19}F NMR peaks (CF_3) and the

proton NMR spectral data for the chiral proton (~4.3 ppm for the starting compound **5**), only one set of new ^{1}H NMR peaks were observed from the (*S*)-MTPA test and only two sets of peaks from (*R*+*S*)-MTPA test. The ^{19}F NMR revealed the presence of one enantiomer of compound **5**. The derivatization with racemic MTPA tells us where to look for peaks for the "wrong" diastereomer of the ester, if it is present. The estimated limit of detection for the wrong diastereomer was 0.5 %, hence it was determined that compound **5** is enantiomerically pure to 99.5%. Based on the synthetic route, compound **5** can be deduced to be the (*S*)-enantiomer. It is important to confirm the chiral purity for better understanding of further chemistry with this compound.

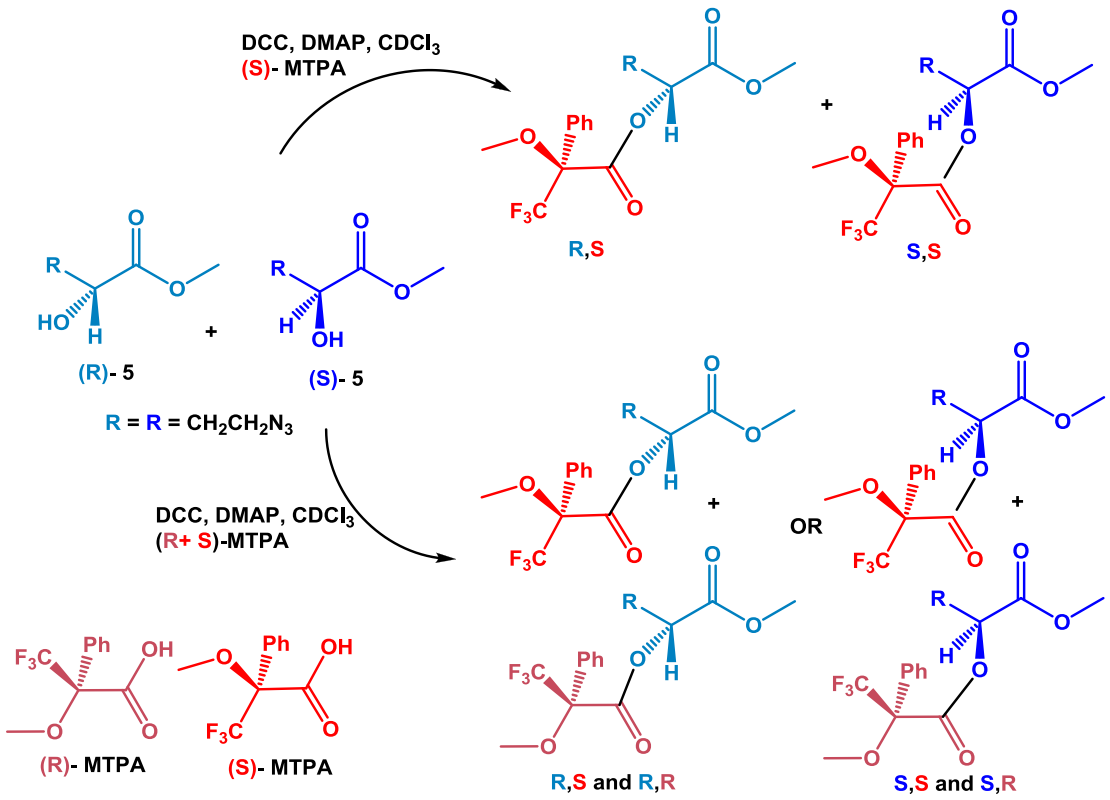

Figure I.2.4. Mosher's acid test with compound **5** + (*S*)-MTPA and compound **5** + (*R* + *S*)-MTPA. Coloring denotes stereochemistry of chiral carbons of starting material and products.

To use compound **5** as an alkylating agent, the hydroxyl group must be converted to a better leaving group. A short study was done to compare different leaving groups for alkylation of the cyclen derived macrocycle for MRI contrast agent projects that would retain the stereochemistry of the chiral carbon. The leaving groups tested were triflate and nosylate.[8] The alkylating agents (**6a** and **6b**) were synthesized under dry conditions, Figure I.2.5. Even after some optimization, it became clear that the nosylate (**6b**) took significantly more time (~12 h) to make from the alcohol compared to the triflate (**6a**) (~1 h). More importantly, in alkylation reactions (not shown), the triflate (**6a**) alkylated compound **11** (see section I.3) to give purified product in 64% yield in ~3 h, whereas the nosylate (**6b**) alkylated the same nucleophile in ~62% yield (as determined by NMR spectroscopy) after ~ 3 months! Taking into consideration the time need to synthesize the alkylation agent and to complete the alkylation reaction, the triflate alkylating agent (**6a**) was used for further reactions.

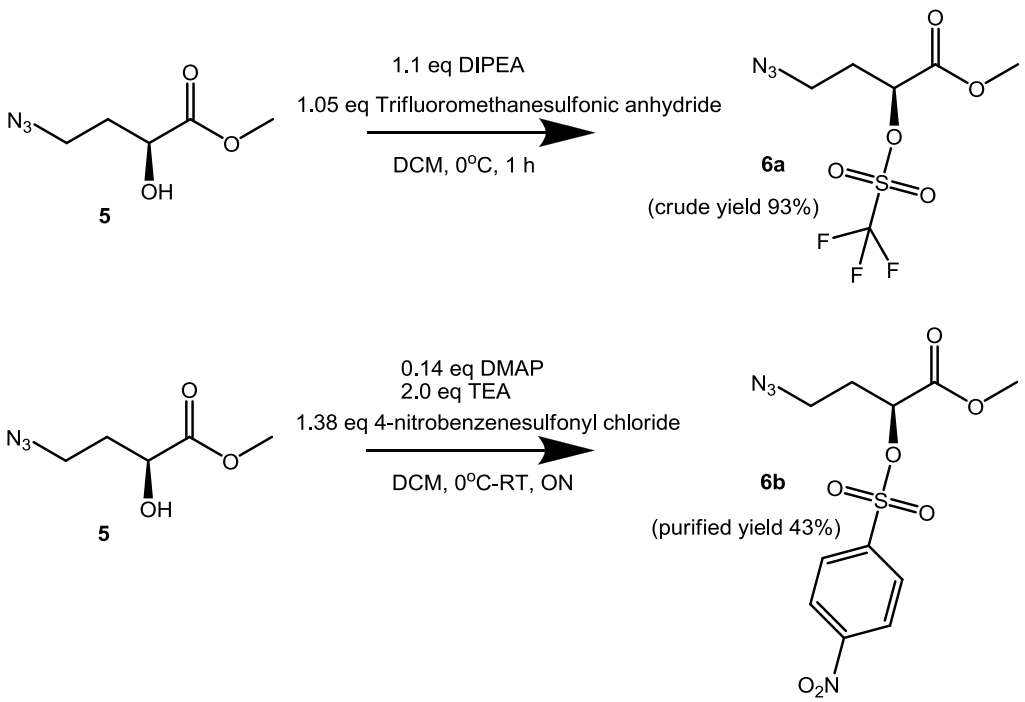

Figure I.2.5. Synthesis of alkylation agents from compound 5 with either a triflate (**6a**) or nosylate (**6b**) leaving group.

Methyl ester **5** was available in respectable overall yields and large enough scale. But for biological applications, the *t*-butyl ester became of greater interest because it can be deprotected using acid, which is often favored in the presence of proteins over basic conditions used for deprotection of methyl esters. Since compound **5** was synthesized and stored in gram quantities, we sought to deprotect the methyl ester to give compound **7** and reprotect the acid with a *t*-butyl ester (**8**) or interchange protecting groups from compound **4**, Figure I.2.6.

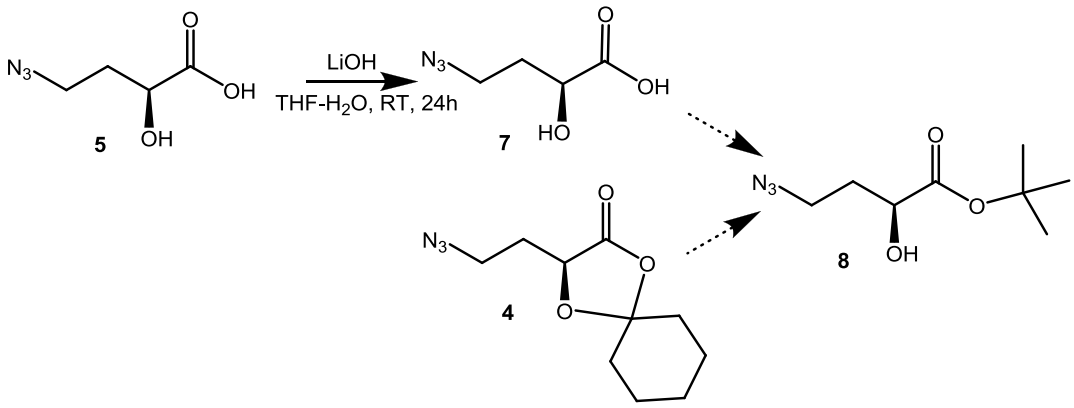

Figure I.2.6. Synthetic scheme for making the *t*-butyl ester azide (**8**) from compound **5** or compound **4**.

Several attempts were made to synthesize the *t*-butyl ester azide. Using literature procedures,[9] a variety of conditions were used to try to synthesize compound **8**. In entry 1 of table I.2.1., compound **4** and LiO*t*Bu was used instead of NaOMe, but no reaction was observed over 2 days and the reaction was thus abandoned. The cyclohexane ring and *t*-butoxide were likely too sterically hindered to react. Entries 2-6 involve acid **7** and *t*-butyl acetate in the presence of triflic acid at various reaction times. The reactions did not go to completion, as determined by TLC and NMR spetcroscopy. Even after 24 hours, only 9% crude yield was obtained and after purification only 1.8% was isolated. In entry 7, a large excess of *t*BuOAc was heated to push the reaction forward, but TLC and NMR data did not show significant progression of the reaction. The reaction of entry 8 used isobutylene in a sealed container. The reaction appeared to generate product by NMR but upon workup, the crude yellowish oil gave mostly starting material and other side products. Another method to make the *t*-butyl ester is by make a copper-DIC complex with *t*-butanol[10] and the starting material. The reaction of entry 9 gave 11.6% crude yield; unfortunately upon purification, the product could not be detected by NMR. The *t*-butyl ester has proved to be challenging to synthesize as well as purify. Not only do the

reaction conditions need to be optimized but also the workup steps. Research toward making **9** is still ongoing; one route to be explored is conversion of **4** using either *t*-BuOAc, *t*-BuOH or perhaps isobutylene under acidic conditions, used by Nakatani et al. to convert **4** to the methyl ester.

Table I.2.1. Attempts at making the *t*-butyl ester azide, compound **8**. Solvent THF unless otherwise specified. Starting material was **7** except for entry 1 in which **4** was used.

Entry #	Reagents (equiv)*	Temp.	Time	Yield	Comments
1	LiO*t*Bu (1.0)	RT	2 d	Not isolated	Reaction time too long
2	*t*BuOAc (20) triflic acid (0.1)	RT	9 h	Not isolated	Lost reaction to spill
3	*t*BuOAc (20) triflic acid (0.1)	RT	11 h	4.80% crude	Extraction workup
4	*t*BuOAc (20) triflic acid (0.1)	RT	13 h	Not isolated	Extraction workup, not clean extraction
5	*t*BuOAc (20) triflic acid (0.1)	RT	24 h	8.90% crude	Extraction workup
6	*t*BuOAc (20) triflic acid (0.1)	RT	24 h	1.80% Purified	Still had starting material after extraction. Silica column.
7	*t*BuOAc (60) triflic acid (0.1)	RT -> 30^{o}C	9 h	Not isolated	Extraction workup
8	conc. H_2SO_4 (0.2) isobutylene (3.0)	-5 ^{o}C-> RT	16 h	60.4% crude	Extraction workup, mostly starting material and side products
9	*t*BuOH (1.2) Cu-DIC (1.0)	RT	6 h	11.6% crude	Starting material and product detected, Extraction workup

*Equiv = equivalent of reagent with respect to starting material.
Solvent used was tetrahydrofuran except for entry 9.

I.2.4. Conclusions

Compound **5** was made enantiomerically pure (*S*, >99.5%) and after optimization, on a large scale (>20 g). The *t*-butyl ester azide (**8**) was made in minute quantities but the reaction and workup still need to be optimized. In using **5** for alkylation reactions,

conversion to the triflate was found to be superior compared to nosylate. While research continues to make the *t*-butyl ester azide (**8**), the methyl ester azide (**5**) has been used in several projects with great success.

I.2.5 Acknowledgements

I would like to thank Christie Schulte who took me under her wing when I first joined the lab and started this project on the synthetic route to make compound **5**. I would like to thank Sara Cortes-Llamas for assistance and guidance on the Moshers' acid testing. I would also like to thank Andrea Rodriguez for her initial studies to make the *t*-butyl ester azide (entries 1 through 7).

I.2.6. References

[1] (a) Meldal, M.; Tornøe, C. *Chem. Rev*. **2008**, *108*, 2952; (b) Liang, L.; Astruc, D. *Coord. Chem. Rev*. **2011**, *255*, 2933; (c) Hein, J.; Fokin, V. *Chem. Soc. Rev*., **2010**, *39*, 1302; (d) Kolb, H. & Sharpless, K. *DDT* **2003** *8*, 1128.

[2] (a) Brittain, H.; Desreux, J. *Inorg. Chem.* **1984**, *23*, 4459; (b) Shukla, R. B.; Kumar, K.; Weber, R.; Zhang, X.; Tweedle, M. *Acta Radiol. Suppl.* **1997**, *412*, 121; (c) Dunand, F. A.; Dickins, R. S.; Parker, D.; Merbach, A. E. *Chem. Eur. J.* **2001**, *7*, 5160; (d) Aime, S.; Botta, M.; Garda, Z.; Kucera, B. E.; Tircso, G.; Young, V. G.; Woods, M. *Inorg. Chem.* **2011**, *50*, 7955.

[3] (a) Wiese, C.; Maestrup, E. G.; Schepmann, D.; Grimme, S.; Humpf, H.-U.; Brust, P.; Wuensch, B. *Chirality* **2011**, *23*, 148; (b) Green, M. A.; Mathias, C. J.; Hsiao, Y.-M. Abstracts of Papers, 235th ACS National Meeting, New Orleans, LA, United States, April 6-10, 2008 (2008), MEDI-158.

[4] (a) Haskell, T. H.; Rodebaugh, R.; Plessas, N.; Watson, D.; Westland, R. D. *Carbohydr. Res.* **1973**, *28*, 263; (b)Hashimoto, N.; Takahashi, K.; Nakama, C.; Ogino, Y.; Sakai, F.; Nishimura, T.; Eiki, J. *PCT Int. Appl.* (**2006**), WO 2006049304 A1 20060511.

[5] Nakatani, S.; Ikura, M.; Yamamoto, S.; Nishita, Y.; Itadani, S.; Habashita, H.; Sugiura, T.; Ogawa, K.; Ohno, H.; Takahashi, K. et al *Bioorg. Med. Chem.* **2006**, *14*, 5402.

[6] (a) Kanth, J. V. B.; Periasamy, M. *J. Org. Chem.* **1991,** *56*, 5964; (b) McKennon , M. J.; Meyers, A. I.; Drauz, K.; Schwarm, M. *J. Org. Chem.* **1993,** *58*, 3568; (c) Hanessian, S.; Tehim, A.; Chen, P. *J. Org Chem.* **1993**, *58*, 7768; (d) Nakatani, S.; Ikura, M.; Yamamoto, S.; Nishita, Y.; Itadani, S.; Habashita, H.; Sugiura, T.; Ogawa, K.; Ohno, H.; Takahashi, K.; et al. *Bioorg. Med. Chem*. **2006**, *14*, 5402; (e) Dutton, F. E.; Lee, B. H.; Johnson, S. S.; Coscarelli, E. M.; Lee, P. H. *J. Med. Chem*. **2003**, *11*, 2057; (f) Brown, H. C.; Ravindran, N. *Inorg. Chem.* **1977**, *16*, 2938; (g) Young, D. E.; McAchran, G. E.; Shore, S. G. *J. Am. Chem. Soc.* **1966**, *88*, 4390.

[7] (a) Dale, J.A.; Mosher, H. S. *J. Am. Chem. Soc.* **1973**, *95*, 512; (b) Dale, J. A. et al. *J. Org. Chem.* **1969**, *34*, 2543.

[8] Di Gioia, M. L.; Leggio, A.; Liguori, A.; Perri, F. *J. Org. Chem.* **2007**, *72*, 3723.

[9] (a) Anderson, G. W.; Callahan, F. M. *J. Am. Chem. Soc.* **1988**, *82*, 3359; (b) Johnson, W.S. et al. *Org. Synth. , Coll. Vol. IV, **1963**, 261*; (c) Anderson, G.W. & Callahan, F. M. *J. Am. Chem. Soc.* **1960,** 82, 3359; (d) Kurkin, A. V.; Belov, D. S.; Yurovskaya, M. A. *Chem. Heterocycl. Compd.* **2008**, *44*, 1123; (e) Conroy, T.; Guo, J. T.; Linington, R. G.; Hunt, N. H.; Payne, R. J. *Chem.- Eur.. J.* **2011**, *17*, 13544.

[10] Conroy, T.; Guo, J.-T.; Hunt, N. H.; Payne, R. J. *Org. Lett.* **2010**, *12*, 5576.

I.3. A Fluorinated Dendrimer-Based Nanotechnology Platform New Contrast Agents for High Field Imaging

I.3.1. Introduction

Higher MRI field strengths (3–11.7 T) are becoming more common, and therefore these new directly detectable CAs of this section will be immensely useful for quantitative MRI methods.

Taking this into consideration, fluorine is a quite attractive nuclide because ^{19}F has the following properties:[1] (1) 100% natural abundance meaning high sensitivity, (2) a wide chemical shift range that is sensitive to its local environment, (3) similar magnetic moment to that of protons, and (4) negligible background signal in living organisms. A few disadvantages of using ^{19}F are the long longitudinal relaxation time (T_1) and its nuclear anisotropy.

Even though these disadvantages exist, ^{19}F MRI has been used in a variety of applications such as metabolism, tumor growth, blood flow, and protease activity detection.[2] Fluorine-rich large molecules, which have nanometer dimensions or larger, are being used for molecular and cellular imaging at wide MRI field strengths (1.5 and 11.7T).[3] Some of these ^{19}F MRI CAs have been used to quantify receptor expression.[3d] The perfluorocarbon emulsion-based nanoparticles have ^{19}F concentrations of 12.14 M but diameters between 100-250 nm, thus are too big to enter capillaries, restricting applications for targeting within the vasculature or labeling of cells for cell tracking.

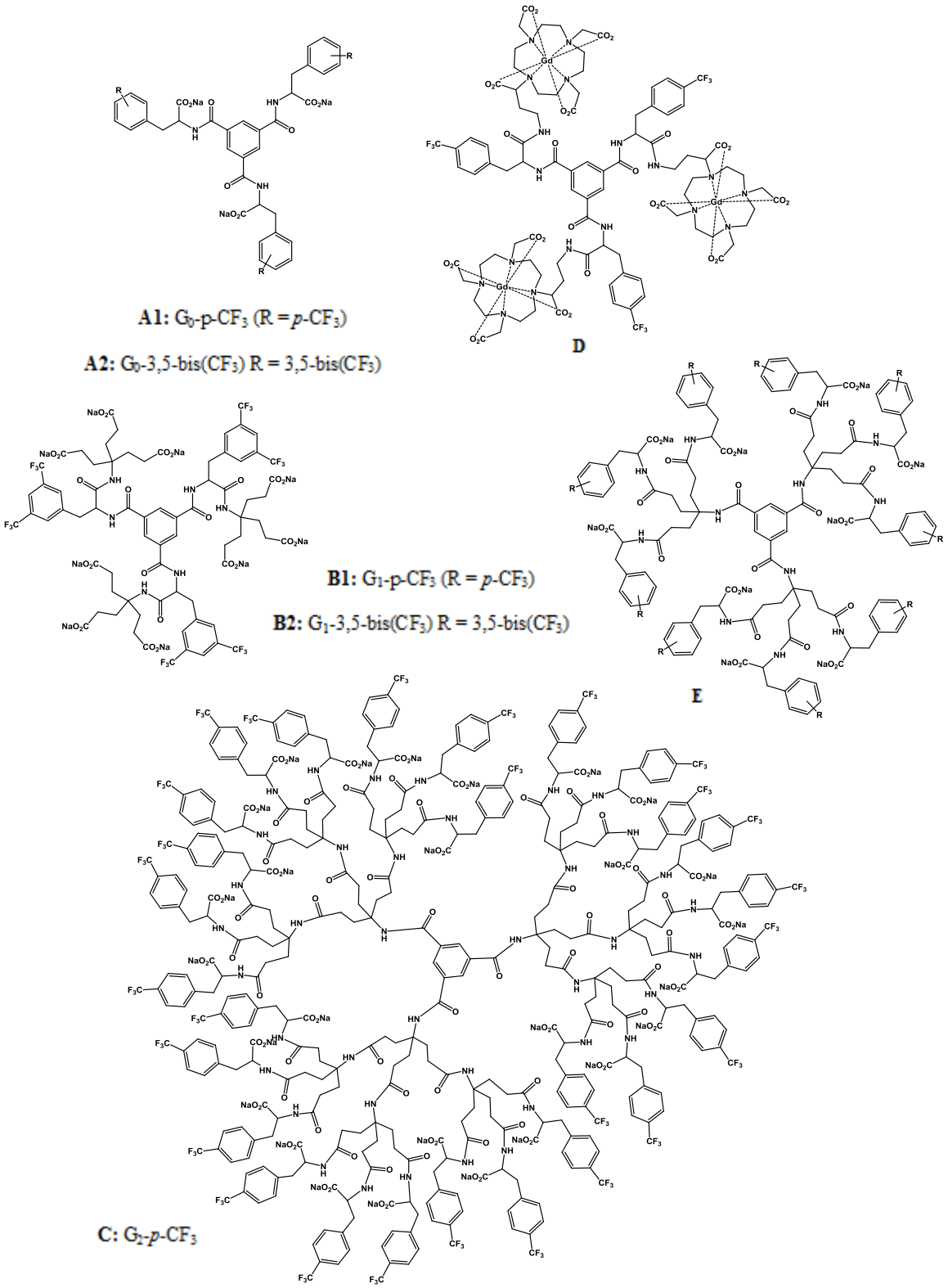

Figure I.3.1. Structure of dendrimers. (**A1**) G_0-p-CF_3, (**A2**) G_0-3,5-bis(CF_3), (**B1**) G_1-p-CF_3, (**B2**) G_1-3,5-bis(CF_3), (**C**) G_2-p-CF_3, (**D**) G_0-p-CF_3-Gd(III)-DOTA, (**E**) G_0-3,5-bis(CF_3)-BA.

We envisioned dendrimers (Figure I.3.1) containing many equivalent fluorines as nanoscale agents for ^{19}F MRI, the size and shape of which could be controlled by choosing the correct structures to synthesize. Dendrimers are well-defined polymers with useful characteristics: (1) monodisperse units that are similar in size to biological building blocks; (2) well-defined spacing including interior void space where small molecules could be encapsulated; and (3) a large number of reactive functional groups on the surface that could provide attachment points for other molecules of interest. Dendrimers make possible the preparation of nanoscale biomaterials with specific properties[4-8] and applications including drug and gene delivery,[8-10] molecular and cellular imaging,[11-14] and tissue engineering. This section describes efforts to solve problems facing direct MRI using ^{19}F with a new dendrimer-based nanotechnology platform, methods for reducing T_1, synthesis of a new bifunctional chelate, toxicity studies, and in vivo images.

I.3.2 Experimental section

See Section I.2.2. for general experimental methods not covered here. Sephadex G25 and Superdex 30PG were purchased from GE Healthcare. Silica gel chromatography was done manually using flash silica.

Gadolinium concentration was measured by inductively coupled argon plasma (ICP) mass spectrometry (University of Illinois at Urbana-Champaign {UIUC}, Illinois Sustainability Technology Center, Division of the Institute of Natural Resource Sustainability). The sample (0.0500 mL), was added to Optima grade nitric acid (0.500 mL) and heated to 80 ^{o}C in a closed vial overnight. The solution was left for 7 weeks

before being shipped to UIUC. Samples were also measured by ICP-OES (San Diego State University, Ecology Analytical Facility).

X-ray crystallography:

After purification of **12-NaOTf** by chromatography, the compounds was crystallized and data acquired and analyzed by the Small Molecule X-ray Crystallography facility at the University of California, San Diego. Compound **12-NaOTf** was crystallized by slow evaporation of CH_2Cl_2.

*Synthesis of **11**.*

Formylcyclen hydrate (**10**) was prepared according to D. D. Dischino, E. J. Delaney, J. E. Emswiler, G. T. Gaughan, J. S. Prasad, S. K. Srivastava and M. F. Tweedle, *Inorg. Chem.*, **1991**, *30*, 1265–1269 and J. Platzek, P. Blaszkiewicz, H. Gries, P. Luger, G.Michl, A.Müller-Fahrnow, B. Radüchel and D. Sülzle, *Inorg. Chem.*, **1997**, *36*, 6086–6093; S. I. Kang, R. S. Ranganathan, J. E. Emswiler, K. Kumar, J. Z. Gougoutas, M. F. Malley, M. F. Tweedle, *Inorg. Chem.* **1993** *32*, 2912-2918. A sample of **10** (7.71 g, 35.3 mmol) was taken up in CH_2Cl_2 (30 mL). In this preparation, some solid was seen. The solution was filtered through a polyethylene frit in a syringe into the reaction flask, and the frit rinsed with CH_2Cl_2 (2×10 mL). Additional CH_2Cl_2 (20 mL) was added to make a 0.5 M solution of substrate and the flask chilled in an ice bath. Anhydrous sodium carbonate (22.47 g, 212.0 mmol) was added, followed by methyl bromoacetate (17.66 g, 115.4 mmol) in portions over 10 min. The ice bath was allowed to melt as the reaction mixture was well stirred. After 52 h, an aliquot was removed from the supernatant, solvent was removed using a nitrogen stream, and the residue analyzed

in CD_3OD by ^1H NMR spectroscopy, showing complete disappearance of the formylcyclen signal at 8.12 ppm and the appearance of one major (>97%) singlet at 8.05 ppm. After a total of 68 h reaction time, the mixture was filtered through a glass frit, and the fine powdery filter cake rinsed with CH_2Cl_2 (4×100 mL). (In another attempt using potassium carbonate as base, the reaction was much slower, less clean, and also at this point, much harder to filter.) The cloudy combined filtrates were poured into crushed ice and water (150 cc) and the resulting mixture shaken in a separatory funnel. The CH_2Cl_2 layer was washed with ice water (150 mL). The CH_2Cl_2 layer was stirred over anhydrous Na_2CO_3 (10 g) for 5 min before the mixture was filtered and the filtrate concentrated by rotary evaporation, leaving a clear oil (15.79 g) containing intermediate and some methyl bromoacetate. ^1H NMR (CD_3OD, 499.9 MHz) δ 8.03 (s, 1H), 3.69 (s, 3H), 3.68 (s, 3H), 3.67 (s, 3H), 3.55 (app t, $J \approx 5$, 2H), 3.52 (t, $J = 5.5$, 2H), 3.48 (s, 2H), 3.42 (s, 2H), 3.39 (s, 2H), 3.01 (t, $J = 5.5$, 2H), 2.84 (t, $J = 5.5$, 2H), 2.78-2.82 (m, 2H), 2.73-2.77 (m, 2H), 2.67-2.73 (m, 4H).

The crude product was dissolved in methanol (140 mL), and the resulting solution (0.25 M in reactant) stirred as the flask was chilled in ice. Triflic acid (11.04 g, 73.6 mmol, 2.08 equiv relative to **10**) was added over 5 min. (In some preparations, a granular precipitate of the di-triflate salt of the intermediate formed, which on heating dissolved.) After an additional 5 min, the mixture was heated in a 62 ^oC oil bath for 51 h before being cooled to room temperature and concentrated by rotary evaporation. The residue was stored under vacuum for 3 d, leaving **11** (24.25 g, 35.2 mmol if pure, 100%) as crispy foam, which quickly turns sticky on exposure to moisture in air, making elemental

analysis difficult. ^{1}H NMR (CD_3OD, 599.8 MHz) δ 4.31 (s, 2H), 3.87 (s, 3H), 3.73 (s, 6H), 3.66 (d, *J* = 18.2, 2H), 3.56-3.61 (m, 4H?, partially overlapping with other signals), 3.56 (d, *J* = 18.2, 2H), 3.30-3.36 (m, 2H?, partially overlapping with solvent C*H*D_2OD signal), 3.24 (ddd, *J* = 3.5, 7.0, 13.8, 2H), 3.10-3.16 (m, 4H), 3.03-3.10 (m, 2H), 2.81 (ddd, *J* = 3.5, 7.0, 14.7, 2H). $^{13}C\{^{1}H\}$ NMR (CD_3OD, 150.8 MHz) δ 174.3 and 168.4 (about 2 : 1 intensity), 121.9 (q, *J* = 318.7), 55.5, 54.0, 53.9, 53.6, 53.0, 51.0, 50.0, 43.7.

*Synthesis of **12-NaOTf**.*

Ester-azide-alcohol **5** (7.768 g, 48.8 mmol) was dissolved in benzene (30 mL) in a 250 mL Schlenk flask and the resulting solution concentrated by rotary evaporation before a septum was placed on the neck. The residue was stirred as the contents of the flask were subjected to four cycles of evacuation and filling with nitrogen. Dry CH_2Cl_2 (60 mL) was added by syringe, and the flask was placed in an ice bath. Dry *i*-Pr_2NEt (8.3438 g, 64.6 mmol) was added by syringe. Over 38 min, Tf_2O (14.1023 g, 50.0 mmol) was added dropwise or in small portions from a syringe. The mixture was clear and orangish-brown. Using a gastight syringe, 65 min after the first Tf_2O had been added, a 50 µL aliquot was removed and quickly added to dry $CDCl_3$ (0.6 mL) in an NMR tube. Analysis by ^{19}F NMR spectroscopy showed singlets at -74.8 and -78.5 ppm for **6a** and triflate ion, respectively, almost no detectable peak at -71.7 (Tf_2O). Analysis by ^{1}H spectroscopy showed a singlet at 3.87 ppm (CH_3O_2C of product, 3.0 units) and a small multiplet at 4.29 ppm (C*H*OH of reactant **5**, 0.04 units), indicating that approximately 4% of alcohol **5** remained. An additional portion of Tf_2O (0.4756 g, 1.69 mmol) was added 80 min after the beginning the first Tf_2O addition. Another 30 min elapsed before the solution of triflate **6a** was added to the other reactant solution, prepared as follows:

Meanwhile, in a separate flask under nitrogen, to salt **11** (31.75 g, derived from 45.9 mmol of formylcyclen **10**) was added CH_2Cl_2 (60 mL) and dry *i*-Pr_2NEt (29.15 g, 225.5 mmol). In this preparation, getting all of the material to dissolve required some vigorous swirling and stirring of the mixture, whereas in other cases all material went into solution easily. The flask was chilled in ice and the solution of triflate ester **6a** was added via cannula over 7 min. After an additional 9 min the ice bath was removed and the mixture was allowed to warm to ambient temperature. After an additional 140 min, using a gastight syringe, a 50 µL aliquot was removed and quickly added to dry $CDCl_3$ (0.6 mL) in an NMR tube. Analysis by ^{19}F NMR spectroscopy showed one major singlet at -78.5 ppm (triflate ion) and a very minor peak at -74.8 (**6a**). The flask was chilled in ice and ice-cold NaOH (16 g) in water (100 mL) was added. The aqueous phase was extracted with CH_2Cl_2 (2×100 mL). Each CH_2Cl_2 layer was washed in turn with water (125 mL). The combined CH_2Cl_2 phases were stored over anhydrous sodium carbonate, filtered, and the filtrate concentrated. The residue was stored under vacuum for 3 h, leaving 34.06 g of brownish solid. A sample (79.6 mg) was dissolved in CD_3OD (0.7 mL). ^{23}Na NMR (CD_3OD, 105.7 MHz) δ 6.3 (br s). Addition of NaOTf (18.1 mg, 0.105 mmol) led to the appearance of a second ^{23}Na NMR signal: δ 6.3 (br s, integral 45.7 units), -3.3 (slightly br s, integral 54.3 units). The crude product was purified by silica gel chromatography (gradient from DCM to acetonitrile; product elutes with acetonitrile-DCM, 0.4:1), affording a beige foam-like solid (27.35 g, 39.0 mmol, 85% overall yield from formylcyclen **10**). The sample from this preparation contained small amounts of impurity showing aliphatic CH peaks in the NMR (probably some *i*-Pr_2NEt derivative) but preparations from other reactions did not. ^1H NMR (CD_3OD, 399.8 MHz): δ 3.80 (s,

3H), 3.77 (s, 3H), 3.76 (s, 6H), 3.74-3.68 (m, 1H), 3.68-3.46 (m, 5H), 3.20-3.07 (br m, 3H), 3.07-2.89 (m, 4H), 2.83-2.60 (br m, 4H), 2.48-2.36 (br m, 1H), 2.36-2.20 (m, 4H), 2.20-2.05 (m, 3H), 2.03-1.86 (m, 2H). $^{13}C(^{1}H)$ NMR (CD_3OD, 599.8 MHz): δ 177.4, 176.2, 176.1, 175.9, 59.6, 56.1, 54.2, 54.0, 53.3, 52.9, 51.4, 45.8, 24.7. ^{23}Na NMR (CD_3OD, 399.8 MHz): δ 6.3 (br s). ^{19}F NMR (CD_3OD, 399.8 MHz): δ -80.0 (s). Anal. Calcd. for $C_{22}H_{39}N_7O_8 + CF_3NaO_3S$ (701.65): C, 39.37; H, 5.60; N, 13.97. Found: C, 39.44; H, 5.23; N, 13.91. ESI-HRMS *m/z* 530.2936 (calculated for $C_{22}H_{40}O_8N_7$ = 530.2933). XRD data for **12-NaOTf** is included in the Appendix Table A.1-A.5. Similar Na^+ complexes like **12-NaOTf** have been previously reported.[15]

*Isolation of sodium-free material that may contain **12** from column purification of compound **12-NaOTf**.*

After column purification of compound **12-NaOTf**, the column was flushed with 100% methanol and the eluent collected and concentrated, leaving 1.0922 g of an amber foam-like solid. The proton NMR spectrum was complex, and the fluorine NMR spectrum showed one peak at ~ -80.13 ppm but there were no peaks in the sodium NMR spectrum. We suspected that perhaps there might be some portion of **12** that lost Na^+ on the column, becoming a much more basic (and polar) free tetra-amine. By TLC (40% ACN/DCM), there were spots near the baseline, but no spot with the same R_f as that of Na^+ adduct **12**. To the eluent was added sodium trifluoromethanesulfonate (1.02 equiv) in DCM, and the TLC (same conditions) showed three spots, one of which had the same R_f as compound **12**. In the ^{23}Na NMR spectrum, free sodium triflate appears around 3.28 ppm (minor peak) and sodium triflate bound to compound **12** appears as a broad peak

around 6.27 ppm. The equilibrium seemed to favor **12**. Several methanol-eluted samples from columns run have been saved and compound **12** may be salvaged by adding sodium trifluoromethanesulfonate and repurifying. *Synthesis of **13***.

Methanol (250 mL) was added to a mixture of **12** (12.96 g, 18.5 mmol) and Pd on carbon (5%, 1.29 g) in a 1 L flask so as to wet the catalyst as quickly as possible. The mixture was stirred as the flask was placed in an ice bath. After 10 min, TfOH (2.868 g, 19.1 mmol) was added over 1 min. The ice bath was removed and hydrogen was bubbled slowly through the mixture for 9 h. The mixture was stirred an additional 38 h under static hydrogen atmosphere, hydrogen gas being bubbled through the mixture once for 5 min in the middle of this time period. The mixture was filtered through Celite and the filter cake rinsed with methanol (4 x 100 mL). Combined filtrates were concentrated by rotary evaporation and the syrupy residue stored under vacuum for 2 weeks, leaving **13** (15.17 g) as crispy foam, which quickly turns sticky on exposure to moisture in air, making elemental analysis difficult. The NMR data suggest the presence of two species in CD_3OD solution, likely a mixture of the structure shown (with Na^+ associated with the macrocycle, δ_{Na} = 6.5 ppm) along with free solvated Na^+ (δ_{Na} = -3.4 ppm) and the sodium-free macrocycle. ^{1}H NMR (CD_3OD, 399.8 MHz): δ 3.81 (s, 3H), 3.79-3.74 (m, 9H), 3.69-3.63 (m, 1H), 3.63-3.40 (m, 4H), 3.27-3.08 (m, 5H), 3.08-2.90 (m, 5H), 2.84-2.57 (m, 4H), 2.48-2.19 (m, 5H), 2.19-1.30 (m, 6H). ^{13}C(^{1}H) NMR (CD_3OD, 599.8 MHz): δ 176.6, 176.1, 175.9, 175.1, 174.0, 173.4, 60.5, 56.0, 54.2, 53.9, 52.8, 50.6, 47.0, 45.7, 40.1, 39.3, 29.6, 26.9, 23.2, 19.8. ^{23}Na NMR (CD_3OD, 105.8 MHz): δ 6.5 (br s), -3.4 (s). ^{19}F NMR (CD_3OD, 376.1 MHz): δ -79.7 (s).

I.3.3. Results and discussion

Synthesis. A single NMR signal would be optimal for directly detectable CAs. We designed new fluorine-rich molecules in which all ^{19}F nuclei are magnetically equivalent. . Dendrimers containing phenylalanine moieties bearing one CF_3 group are termed Type I with 9, 27, and 81 ^{19}F atoms for generations 0 (**A1**), 1 (**B1**), and 2, (**C**) respectively. Dendrimers that contain the 3,5-bis(trifluoromethyl)-phenylalanine are termed Type II which contain twice the amount of fluorines (**A2**, **B2**). The dendrimers in Figure I.3.1 were made using the convergent method where appropriate dendrons (Figure I.3.2) are first synthesized and then coupled to a core. Dendrons were prepared at UPMC by coupling 3 equivalents of the fluorinated amino acid to the 3 carboxylic acids of the repeat branch unit. The dendron was then deprotected at the amine and either coupled to another branch unit (increasing the generation, G) or used directly.

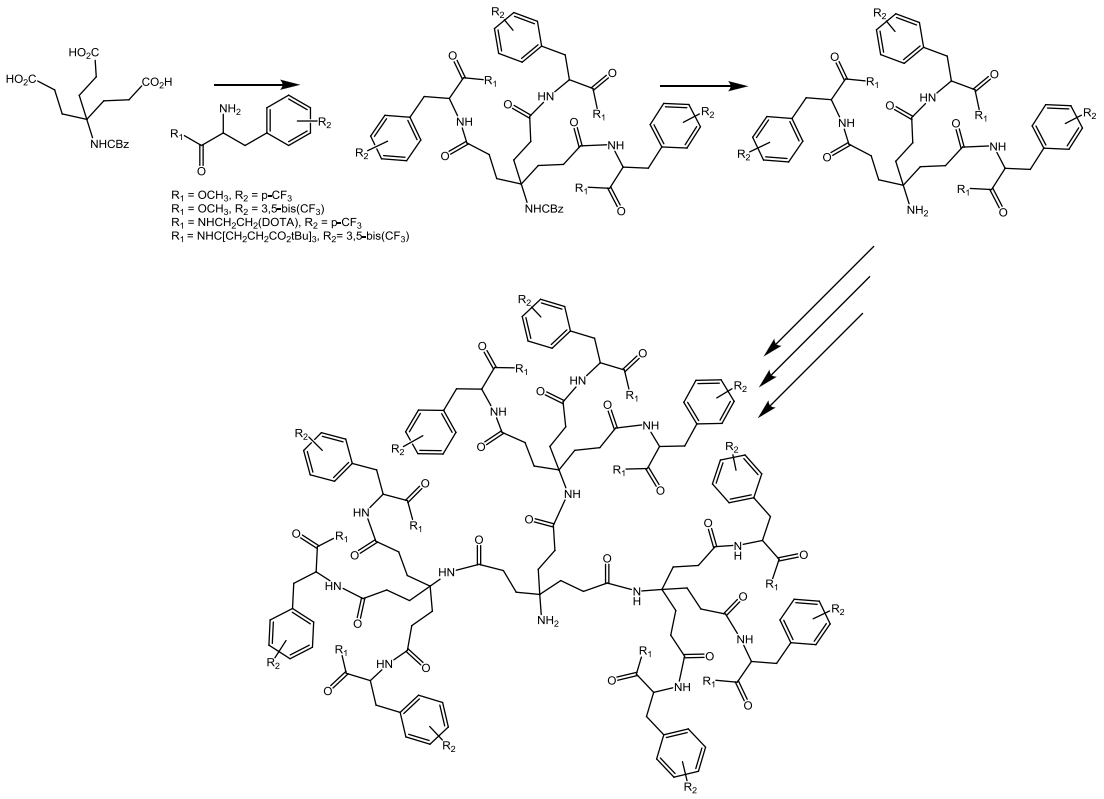

Figure I.3.2. Synthesis of dendrons.

Synthesis of the novel bifunctional DOTA analogs was done at SDSU. The precursor **5** was made by adapting various literature synthetic procedures to give an enantiomerically pure compound in 5 steps from malic acid as described in section I.1. A cyclen derivative with one nitrogen protected by deactivation as an *N*-formyl group gave precursor **10**.[16,17] Alkylation of **10** with slightly more than 3 equivalents of methyl bromoacetate in the presence of carbonate base gave clean tri-alkylation. The *N*-formyl group was subsequently removed in warm acidic methanol yielding **11** quantitatively. Triflic acid was used rather than more commonly used acids, because in a subsequent synthetic step we wanted to avoid the presence of nucleophilic ions such as chloride, which could react with the triflate ester of **5** and cause unwanted inversion at the reacting carbon. A titration of compound **11** was done to determine the number of acidic

hydrogens. There were two inflection points on the Figure I.3.3 indicating two acidic hydrogens, meaning that two moles of strong acid (dry HCl or triflic acid) were likely sufficient to catalyze the deprotection. Several attempts were made to neutralize compound **11** with Amberjet OH 4400 (strong anion exchange resin) at varying equivalencies (1.5, 4.0, 5.0, 7.2, 10.5 equiv) to give the free base version, but they all failed in that low yields of isolated product were obtained, likely due to unusual solubility. This was not detrimental to the synthesis since the triflate salt could be used without neutralization to go onto the next step.

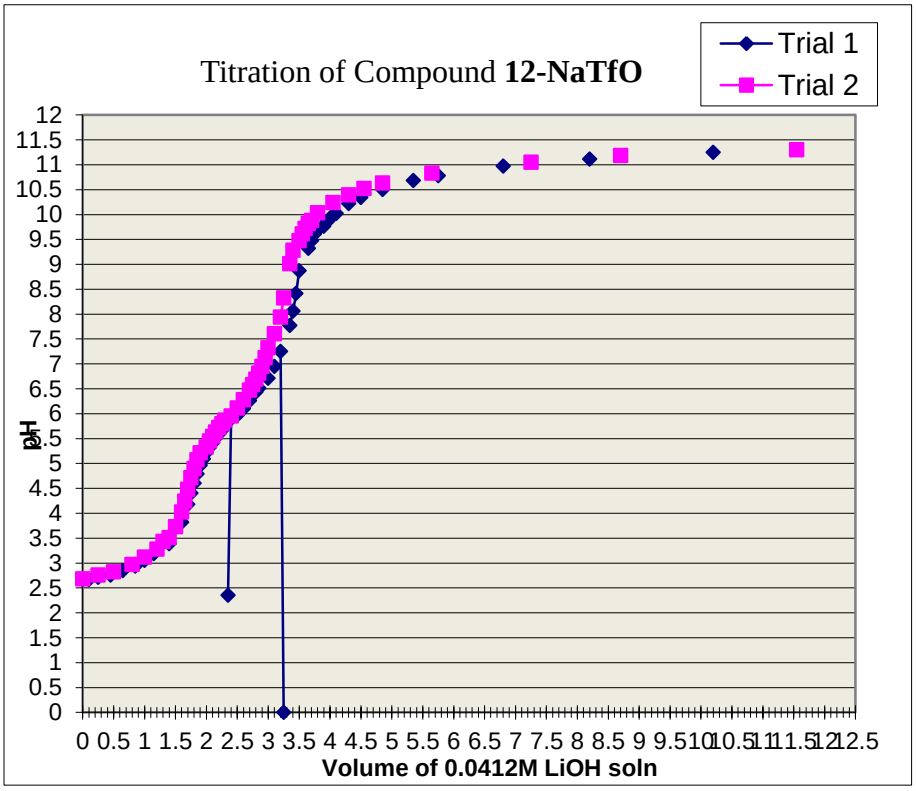

Figure I.3.3. Titration of Compound **12-NaTfO** with 0.0412 M LiOH.

Precursor **5** was converted to triflate ester **6a**, which could be isolated but was used *in situ*. Compound **9** was then added to a freshly prepared mixture of excess *i*-Pr_2NEt and the di(triflate) salt **11**. Alkylation of **11** with **6a** took place within 2-3 h. The

workup was done with aqueous sodium carbonate and a normal phase silica column chromatography gave **12-NaOTf** in 64% to 85% overall yield from compound **10**. Interestingly, we eventually concluded that both triflate and sodium ions were present by NMR in **12-NaOTf** even after purification. We tried to remove the sodium ion by using different carbonate bases (Cs_2CO_3 and Li_2CO_3, independently) during work up, which gave sodium-free crude product (as suggested by lack of significant peak in the ^{23}Na NMR spectrum) but after silica gel chromatography, the sodium and triflate ions had appeared! We concluded that the sodium ion was being leached off the silica column and somehow associated with the product during the chromatography. The ^{23}Na NMR spectrum of **12-NaOTf** in CD_3OD shows a large peak (~95%) for **12-NaOTf** and a smaller peak (~5%). The larger peak increases upon addition of NaOTf, suggesting that only a minor amount of sodium ion dissociates from the neutral ligand **12-NaOTf**. There is literature precedent showing similar association of sodium ion into macrocycles derived from cyclen.[15] We were able to isolate a small amount of sodium-free macrocycle **12** from the column used to purify **12-NaOTf**, by flushing the column with 100% methanol.

Fluorobenzene was used to quantify how much triflate was associated with the purified compound **12-NaOTf**. A known amount of fluorobenzene was added to known amount of compound **12-NaOTf**, and the ratios were calculated in triplicate using ^{19}F and ^{1}H NMR spectroscopies. The ^{19}F NMR spectrum showed two peaks (one for fluorobenzene and the other for triflate from compound **12-NaOTf**) showing the ratio between the fluorobenzene and triflate. The ^{1}H NMR spectrum was used to find the ratio of compound **12** to fluorobenzene. The ratio of triflate to compound **12** was found to be

1.03 ± 0.16 (Appendix Table A.6).

To have a more bio-friendly anion, we tried to exchange the triflate anion with hydroxide using Amberjet OH 4400 and used ^{19}F NMR to check for the presence or absence of triflate. Various equivalencies of anion exchange resin were used at different contact times in either methanol or DCM, see Table I.3.1. Unfortunately, the anion exchange resin did not remove the triflate ion. There were two instances where no triflate ion was detected, but there was also no compound **12** detected, suggesting the compound **12** remained associated with the resin.

Table I.3.1. Using anion exchange resin to remove triflate ion from compound **12**.

Entry	Resin	Equivalents*	Contact time	Solvent	^{19}F NMR†	^{1}H NMR‡
1	Amberjet OH^-	0.84	< 30 s	Methanol	yes	yes
2	Amberjet OH^-	3.5	4 min.	Methanol	no	no
3	Amberjet OH^-	3.5	6 min.	Methanol	yes	no
4	Amberjet CO_3^{2-}	3.5	7 min.	Methanol	no	no
5	Amberjet OH^-	0.90	< 30 s	DCM	yes	yes
6	Amberjet OH^-	1.2	1 min.	DCM	yes	yes
7	Amberjet OH^-	1.2	3 min.	DCM	yes	yes
8	Amberjet OH^-	1.2	30 min.	DCM	yes	yes

* Equivalents of anion from exchange resin to **12-NaOTf**.
† ^{19}F NMR spectroscopy used to detect presence of triflate; yes = triflate detected, no = no triflate detected
‡ ^{1}H NMR spectroscopy used to detect presence of **12-NaOTf**; yes = **12-NaOTf** detected, no = **12-NaOTf** not detected.

Although the triflate anion could not be removed/exchanged, the experiments

performed further support the characterization of this chelate. After elemental analysis, ^{23}Na,^{19}F and ^{1}H NMR spectroscopy, and X-ray crystallography (Figure I.3.4 and Figure I.3.5), the structure and ions associated with compound **12** were confidently assigned. There were two molecules per unit cell, molecule (**12'**) and molecule (**12"**), that crystallized. The distances of the nitrogens to the sodium are very similar in both molecules, Table I.3.2. And they both have a longer distance N(1)-Na(1) and N(1')-Na(1') compared to the others. The distances between coordinated carboxylate O to the center sodium are very close in molecule (12') and a little more varied in molecule (12'') especially the O(1')-Na(1') distance.

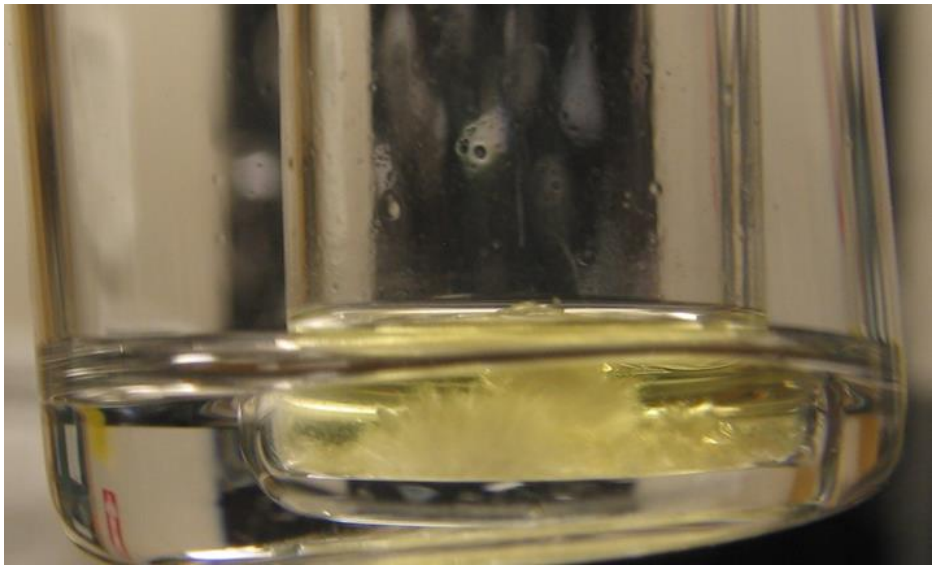

Figure I.3.4. Crystals of compound **12-NaOTf**.

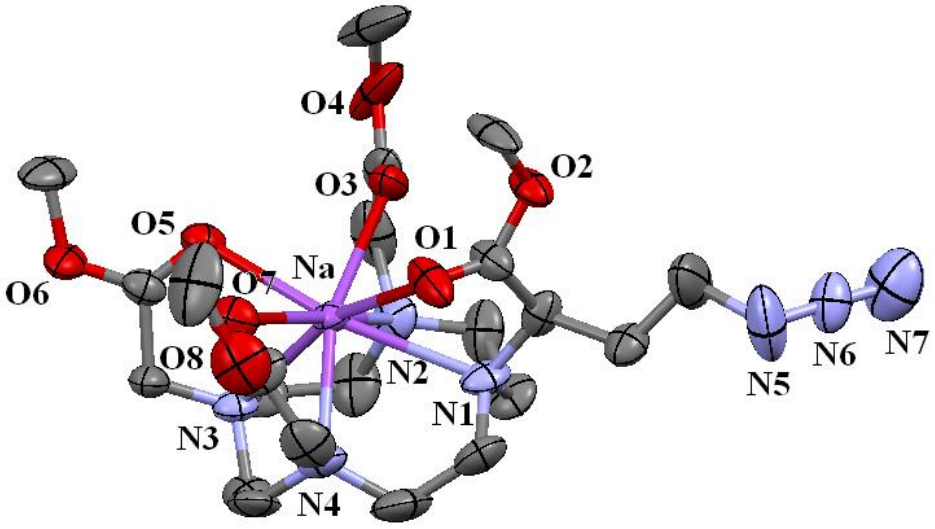

Figure I.3.5. Thermal ellipsoid plot of **12-NaOTf** drawn at 35% probability level. Hydrogen atoms and triflate counter ion were omitted for clarity.

Table I.3.2. Bond distances between sodium ion and surrounding nitrogens and oxygens for both molecules (**12-NaOTf'** and **12-NaOTf"**) found in unit cell.

Bond in molecule 12-NaOTf'	**Bond length(Å)**	**Bond in molecule 12-NaOTf"**	**Bond length(Å)**
N(1)-Na(1)	2.590	N(1')-Na(1')	2.642
N(2)-Na(1)	2.550	N(2')-Na(1')	2.500
N(3)-Na(1)	2.555	N(3')-Na(1')	2.551
N(4)-Na(1)	2.549	N(4')-Na(1')	2.511
O(1)-Na(1)	2.531	O(1')-Na(1')	2.823
O(2)-Na(1)	2.534	O(2')-Na(1')	2.419
O(3)-Na(1)	2.522	O(3')-Na(1')	2.557
O(4)-Na(1)	2.557	O(4')-Na(1')	2.380

The reduction of the azide moiety of **12-NaOTf** gave the amine salt **13** as a hygroscopic foam. One mole of triflic acid was added before reduction of the azide, because previous work in the Grotjahn lab had shown that without acidification, the amino group being formed would attack the nearby methyl ester, forming a lactam.[18]

Because the hydrogenation reaction is quantitative, the average yield for each of the 4 steps is ~95% making the overall synthesis (Figure I.3.6) very efficient, all the more so because only one column chromatography is used.

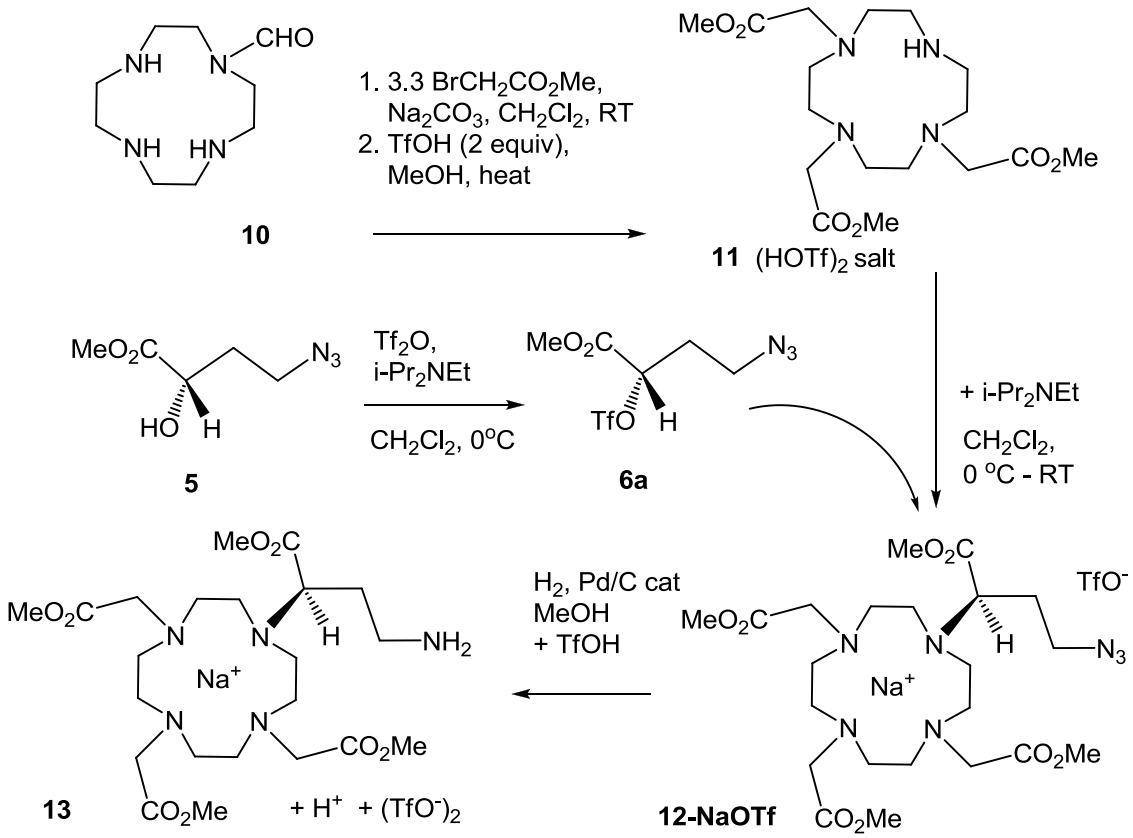

Figure I.3.6. Synthesis of bifunctional chelates **12-NaOTf** and **13**.

At University of Pittsburgh Medical Center (UPMC), our collaborators used the amino side chain group on **13** to produce dendrimer **D** in 2 steps, which itself was complexed with 3 Gd(III) in 2 steps to give dendrimer **D-Gd**, Figure I.3.7.

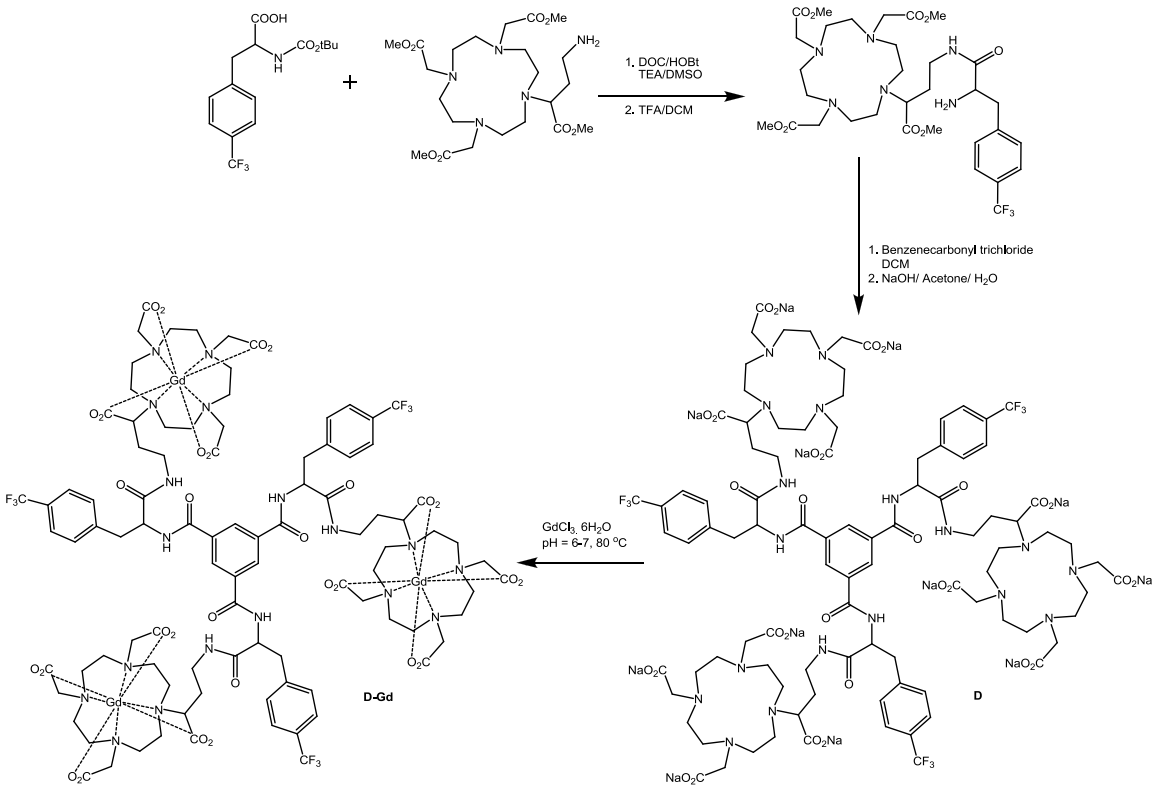

Figure I.3.7. Synthesis of dendrimer chelates **D** and **D-Gd**.

Relaxivity properties. The ^{19}F NMR spectra of the dendrimers (Figure I.3.8) showed only one sharp peak, validating our design. Notably, the dendrimers show a much narrower ^{19}F peak than do perfluorcarbon nanoparticles.[9,11] The narrowness of the peak results from the high symmetry of the dendrimer and the resulting magnetic equivalence of the ^{19}F nuclei, that will result in maximum signal-to-noise ratio when imaging.

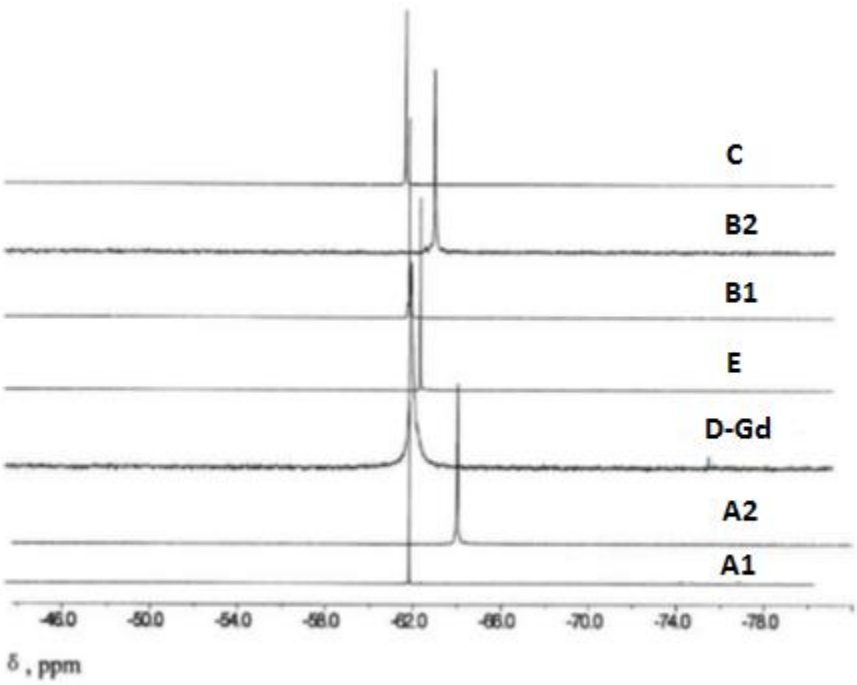

Figure I.3.8. ^{19}F NMR spectra of the dendrimers.

Using pulsed field gradient diffusion ordered NMR spectroscopy (DOSY) at 300 K and D_2O as solvent, the hydrodynamic radius of the dendrimers was determined at Carnegie Mellon University (CMU). As the generation number of the dendrimers increases, the hydrodynamic radius increases as shown in Table I.3.3 (comparing entries 1, 2, and 3 as well as 4 and 5). The sizes of the dendrimers are mostly less than 3 nm, which are about 2 orders of magnitude smaller than perfluorocarbon nanoparticles (~200 nm).[9,11] These smaller sizes are intended to enable the dendrimer nanoparticles to move into soft tissue and be removed through the kidneys.

Table I.3 3. Size and ^{19}F Nuclear magnetic resonance (NMR) relaxation times (T_1) of the dendrimers.

		Size Measured by 1H NMR*		T_1 (s)	
	Compound	**Diffusion Coefficient (cm^2s^{-1})**	**Hydro-dynamic Radii (nm)**	**11.7 T†**	**7 T‡**
1	G_0-*p*-CF_3 (**A1**)	2.49 (±0.31) x10^{-10}	0.86 (±0.10)	1.056	1.176
2	G_1-*p*-CF_3 (**A2**)	1.67 (±0.12) x 10^{-10}	1.26 (±0.09)	0.867	0.740
3	G_2-*p*-CF_3 (**C**)	1.21 (±0.05) x 10^{-10}	1.74 (±0.07)	0.708	/
4	G_0-3,5-bis(CF_3) (**A2**)	2.34 (±0.31) x 10^{-10}	0.91 (±0.11)	0.907	0.925
5	G_1-3,5-bis(CF_3) (**B2**)	1.54 (±0.16) x 10^{-10}	1.38 (±0.14)	0.882	/
6	G_0-3,5-bis(CF_3)-BA (**E**)	/	/	0.911	1.036§
7	G_0-*p*-CF_3-DOTA (**D**)¶	/	/	0.860	0.528
8	G_0-*p*-CF_3-Gd(III)-DOTA (**D-Gd**)	/	/	0.140	/

*^1H NMR data were obtained in D_2O at 298K.
†T_1 data were obtained at 310K using ^{19}F NMR spectroscopy at 11.7 T. The solutions for the measurement are 50 mM potassium phosphate buffer with pH = 7.4, except that the solution for dendrimer **D-Gd** is HEPES buffer with pH = 7.
‡Data obtained at 310K using ^{19}F MR imaging at 7 T. Solutions were prepared in 50 mM potassium phosphate buffer with pH = 7.4.
§Solution was prepared in water.
¶Dendrimer **D** is the precursor to **D-Gd**, without gadolinium (III).

Typically, fluorine atoms have long longitudinal relaxation times (T_1). Similar to other nuclei, if the size of the dendrimer is increased then the rotational correlation time of the nuclei would reduce the longitudinal relaxation time (T_1). This was found to be true for our dendrimers as can be seen in Table I.3.3. The type I dendrimer ^{19}F T_1 at 11.7 T reduced from 1.056 to 0.708 seconds from an almost two-fold increase in hydrodynamic radius (G = 0 to G = 2).

Following the observation of decreasing T_1 with increasing hydrodynamic radius,

additional increases of the hydrodynamic radius were attempted to decrease T_1 further. For this dendrimer, **D** was made (Figure I.3.7) by attaching 3 chelates to the outer surface of dendrimer **A1**. The new bifunctional DOTA chelate **13** (Figure I.3.6) was designed and made to synthesize **D** and **D-Gd**.

Dendrimer **D** was found to have a significantly shorter ^{19}F T_1 value than its parent dendrimer **A1**, 0.860 versus 1.056 seconds respectively (Table I.3.3). The chelate insertion to the generation 0 dendrimer adds about the same number of atoms as going to the next generation dendrimer. This should have a similar observed hydrodynamic radius as a generation 1 (G_1) dendrimer. The ^{19}F T_1 of G_0 DOTA dendrimer (**D**) is comparable to G_1 derivative without the DOTA chelate (G_1-*p*-CH_3, **A2**), 0.860 versus 0.867 seconds (Table I.3.3). Therefore, substitutes to the surface of a type I dendrimer appears to reduce T_1, which is consistent when increasing dendrimer size.

Studies of the type II dendrimers display different trends. There is only a small decrease in ^{19}F T_1 (0.911 versus 0.882) when comparing generation G_0 to G_1 (**A2**-**B2**), respectively. The ^{19}F T_1 did not decrease when a Behera's amine was added to the surface of a G_0 type II dendrimer (**E**). By increasing the generation from 0 to 1, the reduction in ^{19}F T_1 is much smaller for type II dendrimers compared to type I, and even adding a dendron to the surface does not give the same reduction in ^{19}F T_1. It is possible that the solvation effects of 3,5-bis(CF_3) group might cause a larger hydrodynamic radius.

For fluorine species, 0.708 seconds is a short T_1 but it is still relatively long for imaging or short repetition time pulse sequences. At these T_1 values, imaging would require long acquisition times and / or a higher concentrations of CAs. If the T_1 could be

shorter, this would allow for shorter repetition times without compromising on signal intensity. Increasing the hydrodynamic radius is one method to reduce T_1, but an alternative would be to insert a gadolinium ion close to the ^{19}F nucleus and employ dipole-dipole interactions to reduce the T_1. Dendrimer **D-Gd** was made where Gd(III) is complexed to the chelates on the surface of dendrimer **D**. In Table I.3.3, the ^{19}F T_1 significantly decreased from 0.86 to 0.14 seconds for dendrimer **D** and **D-Gd**, respectively.

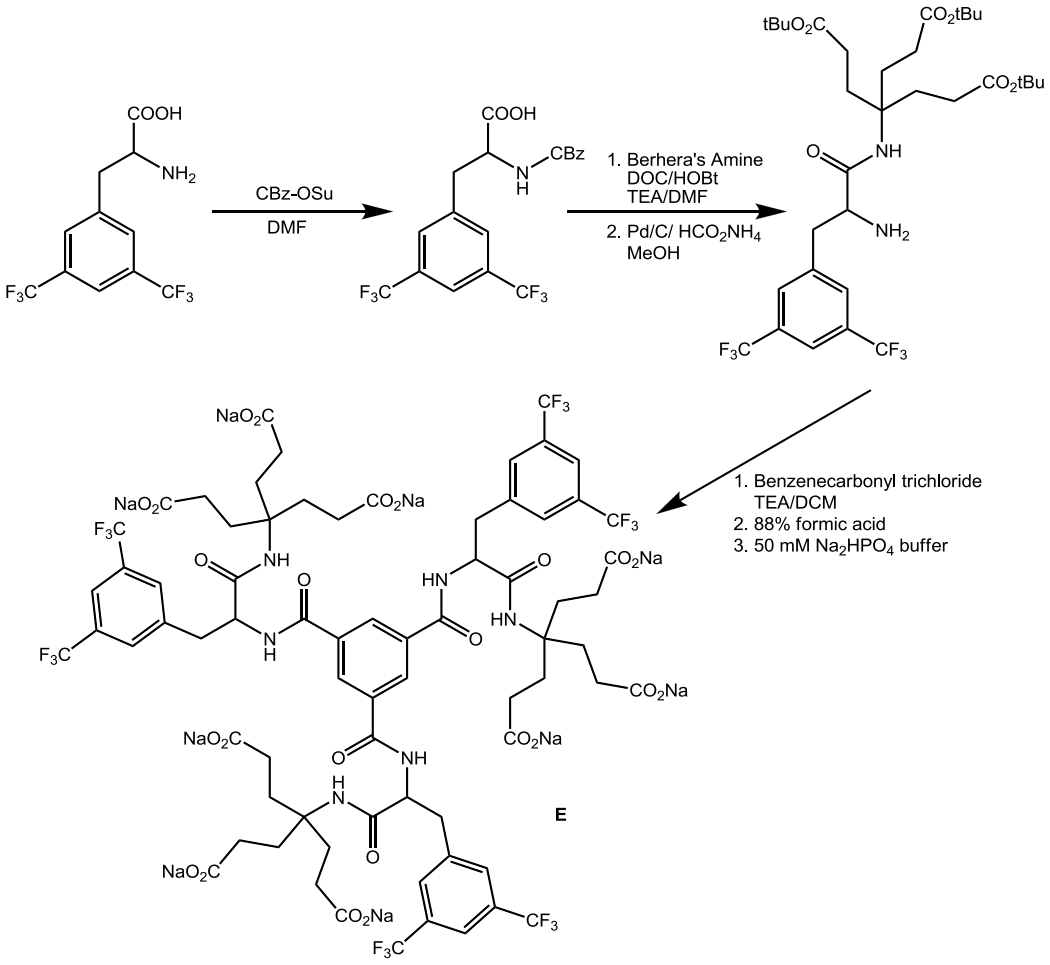

Figure I.3.9. Synthesis of nontoxic dendrimer **E**.

It has been shown that dipole-dipole interactions reduce the T_1 and that the

noncovalently attached Gd(III) CAs can enhance fluorine relaxation.[19,20] It is also known that dendrimers can act as hosts to guest molecules. This led us to consider combining MRI CAs with type II fluorine-rich dendrimers. Therefore, fluorine-rich dendrimer **E** (Figure I.3.9) was mixed with ProHance (Gd(III)-HPDO3A, Bracco Diagnostics Inc, Princeton, NJ). Quite notably, the ^{19}F T_1 at 11.7 T decreased from 911 to 17 ms for a solution of dendrimer **E** with 15 mM ProHance. In Figure I.3.9, there is a jump in the trendline at 1:1 molar ratio of Gd(III) CA to amino acid (15 mM each). The slope of the lines give relaxivity; the first 7 and last 4 data points give 3.69 and 4.82 $(mM*s)^{-1}$ with adjusted R^2 values of 0.9989 and 0.9990, respectively, Figure I.3.10. The increase in relaxivity may be due to interactions between the electronegative CF_3 groups with the secondary coordination sphere through hydrogen bonding to water in the inner coordination sphere. This kind of hydrogen bonding influencing relaxivity has been reported with a fluoride substituent for fluoromethemoglobin.[21]

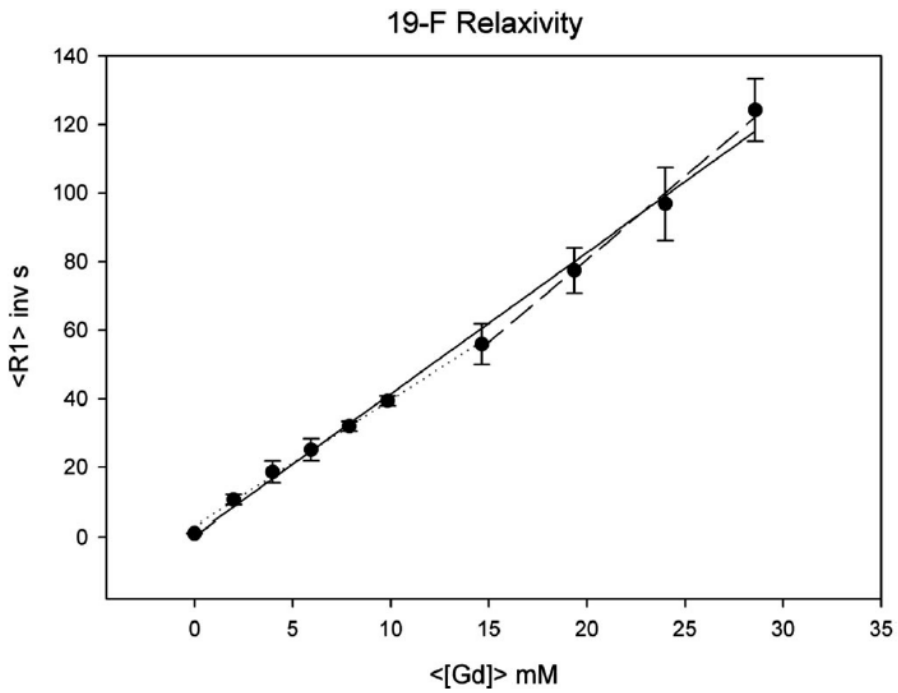

Figure I.3.10.[19]F NMR relaxation rate of the dendrimer **E** at 11.7 T and 300 K in HEPES buffer (pH = 7) as a function of Prohance [Gd] concentration. Error bars represent standard deviation based on n = 3 experiments.

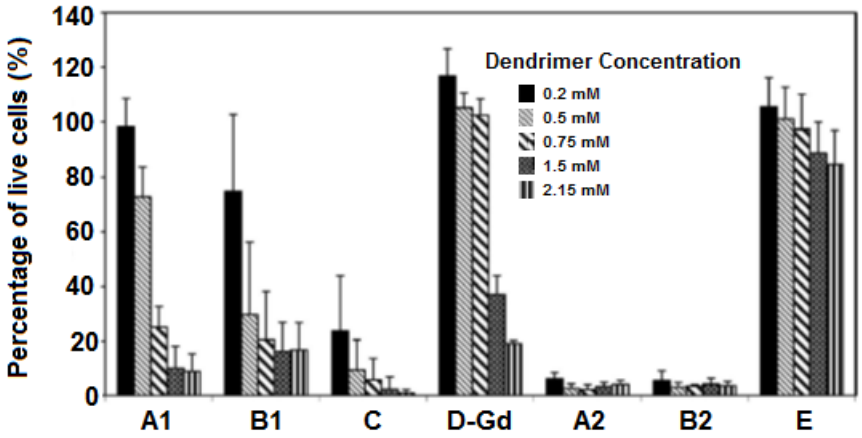

Figure I.3.11. Cytotoxicity response of the dendrimers as a function of concentration; from left column to right column for each dendrimer 0.2 (solid), 0.5, 0.75, 1.5, and 2.15 (vertical stripes) mM. Error bars represent standard deviation based on n = 3 experiments.

Toxicity studies. Besides increasing the hydrodynamic radius, the dendrimer toxicity can be reduced by shielding the CF_3 groups by adding a surface layer (dendrimer

E versus **B2**). At UPMC, cytotoxicity was tested on the dendrimers using the MTT assay on human KB cells. The type I dendrimers with the p-trifluoromethylphenylalanine on the surface were found to be toxic (Figure I.3.11). The toxicity found for type I dendrimers increased with generations and appears to be linked to the CF_3 concentration. Type II dendrimers (3,5-bis(CF_3)-phenylalanine) showed higher toxicity than type I dendrimer. For dendrimer **A2**, the percentage of living cells are as follows: 8.5, 0.6, 0.2, 1.7, and 2.3 at dendrimer concentrations of 0.2, 0.5, 0.75, 1.5, and 2.15 mM ([^{19}F] of 1.2, 3.0, 4.5, 9.0, and 12.9 mM), respectively. For type I dendrimer A1 (generation 0), the percentage of living cells are as follows: 93.5, 66.2, 31.4, 18.9, and 14.9 at dendrimer concentrations of 0.2, 0.5, 0.75, 1.5, and 2.15 mM ([^{19}F] of 0.6, 1.5, 2.25, 4.5, and 6.45 mM), respectively.

One method to reduce the toxicity of the dendrimer is to mask the aromatic-CF_3 groups by placing them further into the interior core of the dendrimer; thus, large hydrophilic groups were coupled to the surface of dendrimers (**D-Gd** or **E**). Shielding the CF_3 groups from the surface might inhibit the fluorine groups on the dendrimer from interacting on cellular components and/or decrease hydrophobicity. From the cytotoxicity data collected (Figure I.3.11), the type I and II dendrimers that either had Gd(III)-chelate (**D-Gd**) or Behera's amine group on the surface (**E**) were significantly less toxic than their parent dendrimers (**A1** or **A2**). For dendrimer **E**, the percentages of living cells are as follows: 105.5, 101.0, 97.4, 88.8, and 84.7 at concentrations of 0.2, 0.5, 0.75, 1.5, and 2.15 mM, respectively.

Table I.3.4. A comparison of best treatment for **E** or **D-Gd** with compounds **A1**, **A2**, **B1**, **B2**, and **C**.

Dendrimer Dose (mM)	*P*, Compound E	*P*, Compound D-Gd
0.2	0.22	0.044
0.5	0.020	0.010
0.75	0.0030	0.00058
1.5	0.0024	0.013
2.15	0.0036	0.34

Using the min test, which identified the best treatment, dendrimer **E** was compared with dendrimers **A1**, **A2**, **B1**, **B2**, and **C**. Dendrimer **E** was shown to be significantly better at four highest doses (min test used 2-sample, one-sided *t* tests with an unequal variance at each dose).

Dendrimer **D-Gd** was compared to **A1**, **A2**, **B1**, **B2**, and **C** and was also found to be significantly better at four highest doses (Table I.3.4). The dose response curves are dependent on the experiment, and the comparison is not straightforward. Therefore, the results from these experiments at one dose are not independent to other doses. Because the comparison depends on the dose chosen, dendrimers were compared at each dose. Toxicity was reduced for both dendrimers when the CF_3 groups were buried into the interior of the dendrimers. At the four highest concentrations, dendrimer E was less toxic than **A1**, **A2**, **B1**, **B2**, and **C**. At the four lowest concentrations, dendrimer **D-Gd** was less toxic than **A1**, **A2**, **B1**, **B2**, and **C.** Using the min test, dendrimer **E** was found to be significantly less toxic at the two highest concentrations when compared to **A1**, **A2**, **B1**, **B2**, **C**, and **D-Gd** (Table I.3.5). Notably, dendrimer **E** was the least toxic of all the dendrimers tested at the two highest doses including **D-Gd** and was found to be a better treatment at these doses.

Table I.3.5. A comparison of best treatment for **E** with compounds **A1**, **A2**, **B1**, **B2**, **C** and **D-Gd**.

Dendrimer E Dose (mM)	*P*
0.2	0.87
0.5	0.68
0.75	0.70
1.5	0.0021
2.15	0.0056

Currently there are no known dendrimers with carboxylic acid on the surface that have shown toxicity at physiological pH.[22] Hydrophobic compounds have been known to be toxic, and octanol-water partition coefficient (P) was used to measure the biological effect of these dendrimers. Dendrimer toxicity was studied using the 1-octanol and phosphate buffer partition coefficients. The logP values for the dendrimers are as follows: - 0.8 ± 0.1, - 2.61 ± 0.05, - 1.81 ± 0.02, and - 3.2 ± 0.1 for **A2**, **B1**, **D-Gd**, and **E**, respectively. As predicted the least hydrophobic dendrimer (**E**) was found to be the least toxic, and the most hydrophobic dendrimer (**A2**) was the most toxic. The toxicities of dendrimers **B2** and **D-Gd** did not correspond to their hydrophobicity.

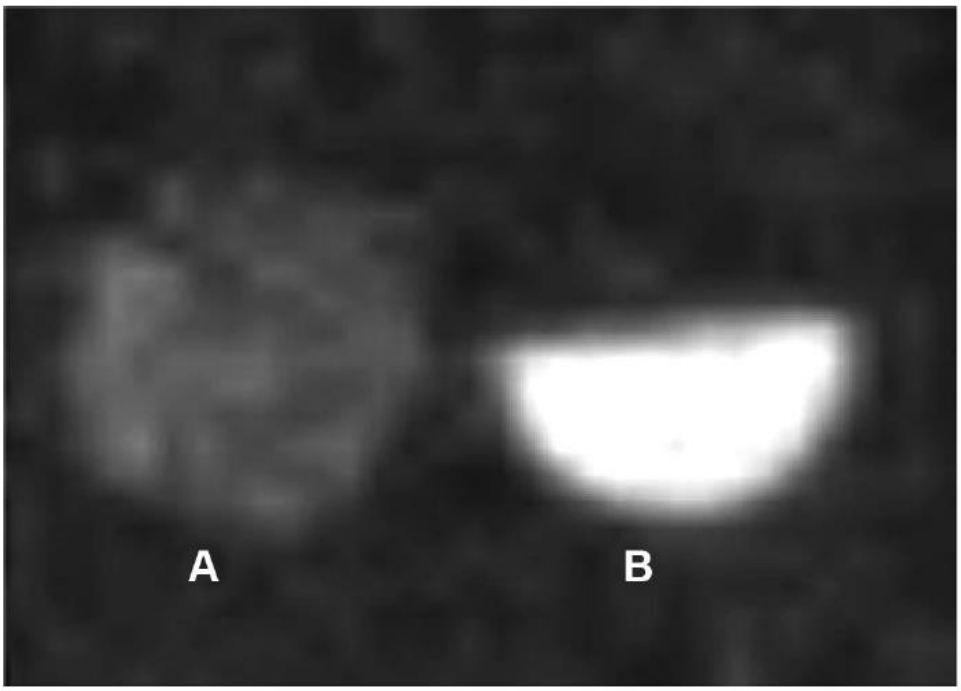

Figure I.3.12. ^{19}F MRI phantom imaging of dendrimer **E** at 7 Tesla. A, 4 mL solution of 6.0 mM dendrimer in water and (B) is a 2 mL mixture of 9.0 mM dendrimer and 4.95 mM ProHance.

Imaging studies. At UPMC, phantom images were prepared to test the applicability of these dendrimers as MRI CAs. The dendrimers were dissolved in water and imaged at 7 Tesla using dual ^{1}H and ^{19} F radiofrequency coil. The relaxation times (T_1) at 7 T and 11.7 T have similar data patterns T_1, decreases with increasing dendrimer size (Table I.3.3). The T_1 and signal intensity for dendrimer **E** with buried CF_3 groups were studied for their efficiency as exogenous Gd(III) CAs, because the data in Figure I.3.10 and its predicted filterability by the kidneys. Images of two aqueous solutions of dendrimer **E** were taken without and with exogenous Gd(III) CA added, Figure I.3.12 A and B, respectively. By adding exogenous Gd(III) CA to dendrimer **E** decreased the ^{19}F T_1 from 1036 to 35 ms, which is consistent with observed data at 11.7 T. Higher signal intensities in images acquired with short repetition times gave this decrease in T_1 (Figure

I.3.12). The addition of exogenous Gd(III) CA with dendrimer **E** decreased the ^{19}F T_1 at 7 T which resulted in significantly higher signal intensities for lower repetition times.

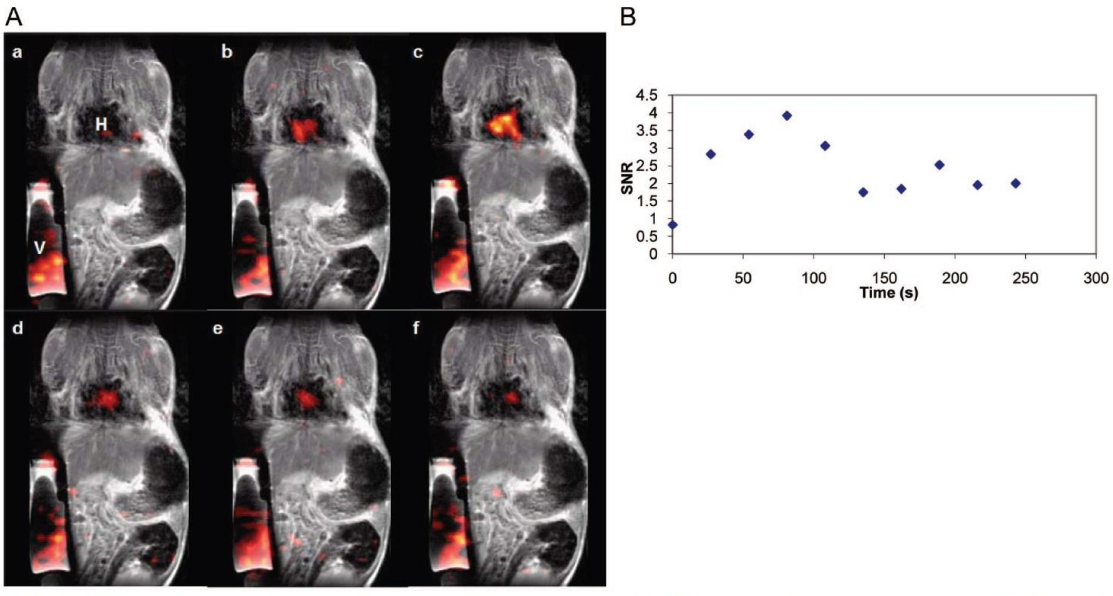

Figure I.3.13. In vivo Dynamic Contrast Enhancement MRI of dendrimer **E** (mixture of 0.19 M dendrimer **E** with 0.086 M Prohance aqueous solution, the dose used was 0.65 mmol dendrimer/ kg animal weight and 0.3 ProHance/ kg animal weight) in the rat. A, each FLASH-2D ^{19}F image (pseudo color) is collected in 27 seconds, the animal heart is clearly seen because of the intravenous injection of dendrimer solution. The gray style underlay is an anatomic ^{1}H image. Heart (H) and fiduciary (a vial V containing dendrimer) are indicated on the image. (a) before injection, (b) 0 seconds after injection, (c) 27 seconds after injection, (d) 54 seconds after injection, (e) 81 seconds after injection, (f) 108 seconds after injection. B, Signal to Noise enhancement due to the ^{19}F signal in the heart as a function of time.

Dendrimer **E** should not be toxic *in vivo* from the biocompatibility data. Dendrimer **E** was selected for *in vivo* studies over **D-Gd** based on the biocompatibility data, the statistical analysis that showed dendrimer **E** to be the best treatment over all the other dendrimers, and dendrimer **E** has twice the number of ^{19}F than dendrimer **D-Gd**. At UPMC, in vivo ^{19}F MR imaging was done on a healthy rat model to show fast imaging of Gd(III) CA and dendrimer **E** coinjected. An anatomic whole body ^{1}H image was collected first, then via tail-vein injection, a bolus of dendrimer **E** and ProHance (Gd(III)

CA) was given and simultaneous acquisition of ^{19}F images (FLASH-2D sequence, acquisition time = 27 s/image). The ^{19}F images were superimposed over the ^{1}H images to clearly see the contrast in the heart generated from dendrimer **E**, Figure I.3.14. Figure I.3.13B shows the percent contrast enhancement as a result of ^{19}F signal over time. In Figure I.3.14, similar results were obtained with the FLASH-3D protocol (acquisition time = 1m 7 s/ image; isotropical resultion = 3.125 mm/ voxel).

The dose used in these studies (0.65 mmol/ kg dendrimer and 11.7 mmol/ kg ^{19}F) is similar to the perfluorocarbon emulsions and relatively low compared to other fluorine-rich imaging agents. Waters et al.[12] used a targeted perfluorocarbon emulsion in mice (1 mL/ kg) which is equivalent to 11.7 mmol/ kg fluorine (perfluorocarbon emulsions[9] were ~11.7 M in ^{19}F). Another group designed a ^{19}F imaging agent with 27 identical ^{19}F nuclei (^{19}FIT)[7]; they injected mice with 2.2 and 1.1 mmol/ kg, equivalent to 60 and 30 mmol/ kg ^{19}F. The doses used by others are around 4- 2 times higher in imaging agent and 5- 2.8 higher in ^{19}F content. Since our dendrimers have a branching multiplicity of 3, the next generation dendrimer can be kept at a constant dose and increase the ^{19}F dose by 3 or the ^{19}F dose can be constant and decrease the dendrimer dose by 3. For our dendrimers, the number of ^{19}F nuclei can be calculated by the following equation: $(3 \times 3^{G}) \times 6$, where G is the generation number (the core and branch multiplicities are 3 each and 6 ^{19}F per amino acid). With respect to the amino acid, the G_0 dendrimer had 18 identical ^{19}F compared to 27 for reported literature.[7]

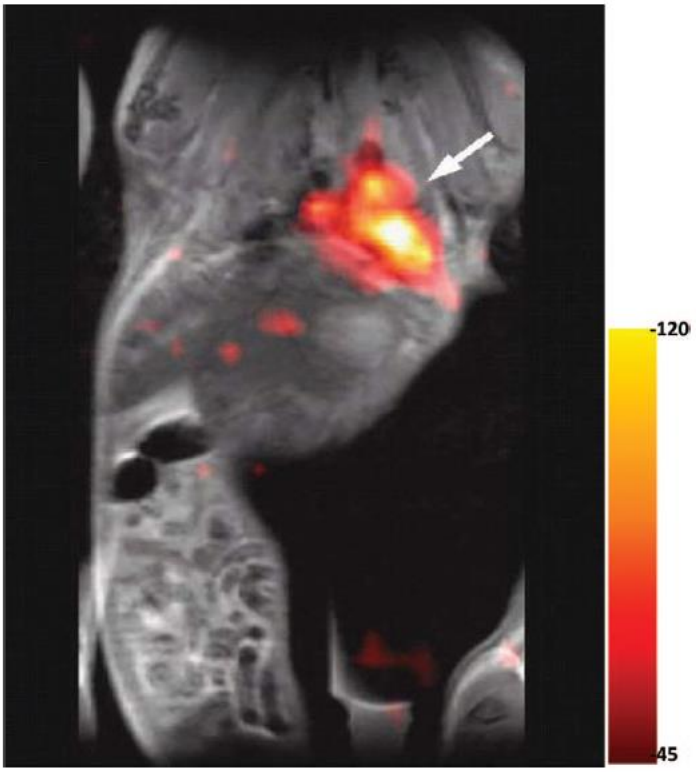

Figure I.3.14. A 2D representation of a FLASH-3D ^{19}F image (pseudo color) of Go-3,5-bis(CF_3)-BA dendrimer (**E**) (doped with Prohance) in the rat showing contrast from fluorine (in red, indicated by arrow) in rat. Image was collected in 1 minute 7 seconds, which clearly shows fast imaging of heart. The gray style underlay is an anatomic ^{1}H image.

I.3.4. Conclusion

We have shown the preparation, characterization, and use of a new bifunctional DOTA chelate, in preparation and characterization of a novel fluorinated dendrimer-based nanotechnology platform for direct-detection ^{19}F MRI. Directly detectable CAs for human MRI are increasingly common at higher field strengths (3, 7, 9.4, and 11.7 Tesla).Through robust chemical synthesis, the physical and chemical properties of our novel fluorine-rich dendrimers can be controlled. Future studies using these nanoscale ^{19}F MRI CAs involve evaluating their efficacy in clinical and biochemical settings. We predict that such fluorine-rich dendrimers will have a wide application in

research and clinical settings for molecular and cellular imaging, due to the precise synthetic control in making these dendrimers. Moreover, dendrimers like **D-Gd** have the potential to be used for ratiometric imaging which provides a method to accurately determine Gd(III) concentration through techniques that do not assume the equivalence of *in vitro* and *in vivo* Gd(III) ion relaxivity.

I.3.5. Acknowledgements

I thank the Pittsburgh NMR Center for Biomedical Research which is supported by grant P41EB 001977 from the National Institutes of Health. I also thank my collaborating authors at UPMC (Zhihua Huang, Raghvendra S. Sengar, Archana Nigam, Douglas M. Potter, and Erik C. Wiener) for their work on our published paper (*Investigative Radiology* **2010**, *45*, 10, 641).

I.3.6. References

[1] Yu, J.; Kodibagkar, V. D.; Cui, W. et al. *Curr Med Chem*. **2005**, *12*, 819.

[2] (a) Schlemmer, H. P.; Becker, M.; Bachert, P. et al. *Cancer Res*. **1999**, *59*, 2363; (b) Wolf, W.; Presant C. A.; Waluch, V. *Adv. Drug Deliv. Rev*. **2000**, *41*, 55; (c) Eleff, S. M.; Schnall, M. D.; Ligetti, L. et al. *Magn. Reson. Med*. **1988**, *7*, 412; (d) Mizukami, S.; Takikawa, R.; Sugihara, F. et al. *J. Am. Chem. Soc*. **2008**, *130*, 794.

[3] (a) Huang, Z,; Sengar, R.; Arbujas, N. et al. *Mol. Imaging*. **2006**, *4*, 330; (b) Jiang, Z. X.; Liu, X.; Jeong, E. K. et al. *Angew. Chem. Int. Ed. Engl*. **2009**, *48*, 4755; (c) Janjic, J. M.; Srinivas, M.; Kadayakkara, D.K. et al. *J. Am. Chem. Soc*. **2008**,*130*, 2832; (d) Morawski AM, Winter PM, Yu X, et al. *Magn. Reson. Med*. **2004**, *52*, 1255; (e) Caruthers, S. D.; Neubauer, A. M.; Hockett, F. D. et al. *Invest. Radiol*. **2006**, *41*, 305; (f) Ahrens, E. T.; Flores, R.; Xu, H. et al. *Nature Biotech.* **2005**, *23*, 983; (g) Waters, E. A.; Chen, J.; Yang, X. et al. *Magn. Reson. Med*. **2008**, *60*, 1232.

[4] Tomalia, D. A.; Naylor A. M.; Goddard, W. A. *Angew. Chem. Int. Ed. Engl*. **1990**, *29*, 138.

[5] Tomalia, D. A.; Reyna, L. A.; Svenson, S. *Biochem. Soc. Trans*. **2007**, *35*, 61.

[6] Grayson, S. M.& Frechet, J. M. *Chem. Rev*. **2001**, *101*, 3819.

[7] Lee, C. C.; Mackay, J. A.; Frechet, J. M. et al. *Nat. Biotech*. **2005**, *23*, 1517.

[8] Allen, T. M. & Cullis, P. R. *Science*. **2004**, *303*, 1818.

[9] Esfand, R. & Tomalia, D. A. *Drug. Discov. Today*. **2001**, *6*, 427.

[10] Svenson, S. & Tomalia, D. A. *Adv. Drug Deliv. Rev*. **2005**, *57*, 2106.

[11] Stiriba, S.; Frey, H.; Haag, R. *Angew. Chem. Int. Ed. Engl*. **2002**, *41*, 1329.

[12] Wiener EC, Brechbiel MW, Brothers H, et al. *Magn. Reson. Med*. 1994;31:1.

[13] Wiener, E. & Narayanan, V. V. *Advances in Dendritic Macromolecules.* (**2002**) Vol. 5. New York, NY: Elsevier.

[14] Wiener, E. C.; Konda, S.; Shadron, A. et al. *Invest. Radiol*. **1997**, *32*, 748.

[15] (a) Moore, Dennis A. PCT Int. Appl. (**2007**), WO 2007106546; (b) Xu, J.; Sun, G.; Rossin, R.; Hagooly, A.; Li, Z.; Fukukawa, K.; Messmore, B. W.; Moore, D. A.; Welch, M. J.; Hawker, C. J.; Wooley, K. L. *Macromolecules* (Washington, DC) **2007**, *40*, 2971.

[16] Dischino, D.D.; Delaney, E. J.; Emswiler, J. E. et al.: *Inorg. Chem*. **1991**, *30*, 1265.

[17] Platzek, J.; Blaszkiewicz, P.; Gries, H. et al. *Inorg. Chem*. **1997**, *36*, 6086.

[18] D. Grotjahn, unpublished results.

[19] Lee, H.; Price, R. R.; Holburn, G. E. et al. *J. Magn. Reson. Imaging.* **1994**, *4*, 609.

[20] Gong, B.; Gill, M.; Washburn, D. B. et al. *J.Magn. Reson. Imaging*. **1991**, *9*, 101.

[21] Aime, S.; Fasano, F.; Paoletti, S. et al. *Magn. Reson. Med*. **1995**, *33*, 827.

[22] Lide D. *Handbook of Chemistry and Physics.* 84th ed. Boca Raton, FL: CRC Press; 2003:16–43.

I.4. Study of Properties of Bifunctional Chelates DOTA and DOTMA derivatives for Optimized for Molecular MRI

I.4.1. Introduction

Coupling MRI contrast agents to larger macromolecular structures has been shown to increase the rotational correlation time and the relaxivity.[1-4] Initial studies coupled monofunctional chelates to macromolecules by forming a amide bond with one of the the chelating carboxylates and an amine on the macromolecule. Increases in observed relaxivities were significantly less than expected Lauffer et al.[3] used variable temperature relaxivity studies to predict that the relaxivity gains from increasing the rotational correlation time were limited by the long water residence time. Others[5]using the same method had also found that generally Gd(III) chelates coupled through amide ligands showed water residence times that were long enough to negate the relaxivity gains from increasing rotational correlation time. Direct measurement of water oxygen exhange rate by Gonzalez et al.[6] affirmed the long water residence times for the bis-methyl-amide derivative of DTPA complexed to Gd(III) (2325 ns at 25 °C), Gd(III)-DTPA (244 ns) and Gd(III)-DOTA (208 ns).

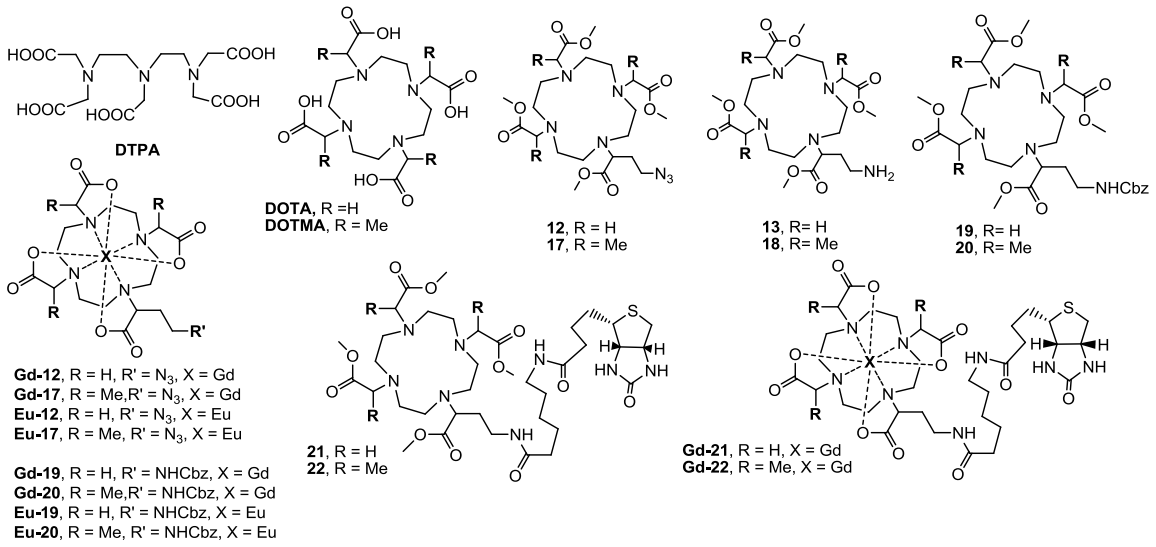

Figure I.4.1. Known (DTPA, DOTA, DOTMA) chelators for Gd(III) and novel bifunctional compounds (**12**, **13**, **17**, **18**, **19**, **20**, **21**, **22**) made in this study.

The ideal water residence time to amplify the relaxivity by increasing the rotational correlation time of Gd(III) contrast agents was predicted to be between 10-60 ns.[3,7] The water residence time by direct measurements of Gd(III) complexes with either DTPA,[8] DOTA[8] (Figure I.4.1) or their amide[6] derivatives previously mentioned verify that their water residence times are greater than 200 ns. Direct measurements along with variable temperature relaxometry measurments support that the water residence times of Gd(III)-DTPA and Gd(III)-DOTA limits the improvements in relaxivity when increasing rotational correlation time.[7,9-12]

The DOTA chelate exists in two conformational isomers with different water residence times and relaxivity properties, Figure I.4.2. Modifications in the structure of DOTA or its analogs, for example adding a methyl group to each acetate (DOTMA) such that the complex is homochiral (Gd(III)-*R,R,R,R,*-DOTMA, **Gd-17**) or fusing cyclohexyl rings to the backbone, results in faster water exchange rates meaning shorter water

residence times and higher relaxivities for rotationally constrained systems. These higher relaxivities stem from the relative population of isomers shifting to the one(s) with faster water exchange.[13-16]

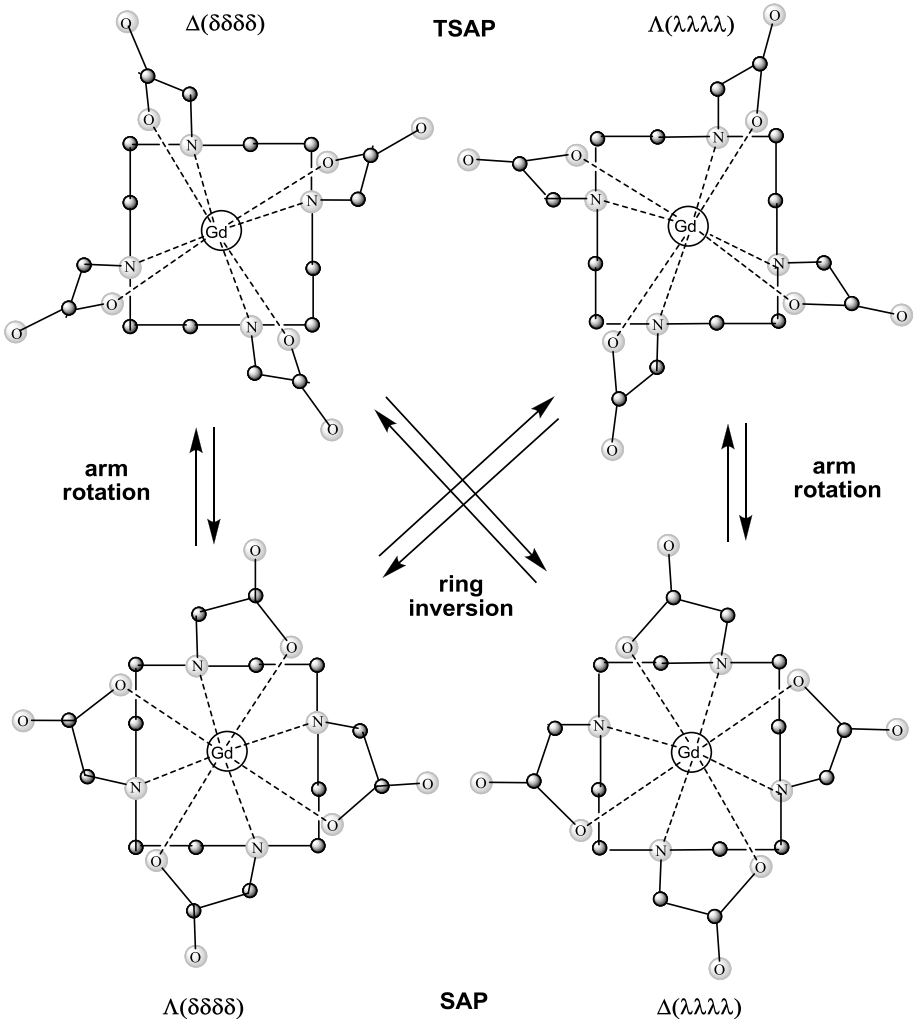

Figure I.4.2. Isomers of DOTA chelates for Gd(III).

Contrast agents made from Gd(III)-DOTMA should be more efficient and show higher relaxivities compared to agents based on Gd(III)-DOTA, yet previous methods coupled macrocycles using one of the carboxylates to form an amide linkage which has been shown to result in longer water residence times and lower relaxivities. For this

reason, we designed new bifunctional derivatives of DOTA and DOTMA (Figure I.4.1) where the tetracarboxylate chelating arms are left intact. Derivatives contain an azide-bearing coupling arm (**12** and **17**, respectively) that can be coupled to alkynes using click chemistry[17] (not shown in this work) or an amine-bearing (**13** and **18**, respectively) for coupling to carboxylic acids using standard amide formation, as shown here and in Section I.3.

Commerically available bifunctional imaging agents exist, but commonly use carboxylate-active ester or isothiocyanate groups for covalent attachement which compromises one or more of the chelating carboxylates thus disrupting the ideal coordination geometry favored by homochiral DOTMA resulting in a less effective agent. In this work we present the synthessi of **12**, **17** and **13, 18**, and derivatization of **13, 18** with either a Cbz group or biotinylated chain.

The chelates for the low molecular weight rapidly rotating models were derivatized at the amino group to establish bifunctionality as well as prevent the free amine from wrapping around and coordinating to the Gd(III). The benzyl carbamate protecting group (Cbz) was used for amino derivatives.

Complexation of new bifunctional DOTA and DOTMA agents to Gd(III) allowed us to find the water residence time and relaxivity measurements of low molecular weight and macromolecular complexes of the amine derivatives. The ideal water residence time varies as a function of the field strength. The DOTMA-based complexes of **17** have shown ideal water residence times and significantly higher relativities (greater than 40%) when rotationally constrained by avidin-biotin binding compared to the Gd(III)-DOTA

derivative. These higher relativities are predicted to enable potentially lower doses of CA to be used and/or allow lower CA concentrations to be detected, making the CA more efficient.

I.4.2. Experimental

General: Unless specified, all the reactions were done in oven-dried or flame dried glassware in an atmosphere of dry nitrogen or argon gas using standard Schlenk techniques. The anhydrous solvents were either purchased from Acros and Aldrich chemical companies and used in the reactions without further purification, or dried in-house (CH_2Cl_2 distilled from CaH_2). All work up and chromatographic purifications of compounds were done in air using reagent grade solvents. Column chromatography was done manually using flash silica. HiTrap™ SP HP columns purchased from GE Healthcare® were used for ion-exchange chromatography. The stains used to visualize the TLC plates (aluminum backed 200 μm silica) were Hanessian's Stain [$CeSO_4$ (5 g) and $(NH_4)Mo_7O_{24}{\cdot}4H_2O$ (25 g) dissolved in water (450 mL) and concentrated sulfuric acid (50 mL)], and potassium permanganate stain [$KMnO_4$ (1.5 g) and K_2CO_3 (10 g) dissolved in 10% NaOH (1.25 mL) in water (200 mL)]. A UV lamp with two wavelengths, long-wave (336 nm) and short-wave (254 nm).

Caution: Although we did not observe any unusual decompositions of the azides reported, organic azides can be explosive materials and should be handled with care.

^{1}H, ^{13}C, ^{23}Na and ^{19}F NMR spectra were recorded using Bruker ACP-500 or Varian spectrometers at 30 ^{o}C or room temperature. ^{1}H, ^{13}C and ^{19}F NMR chemical shifts are reported in ppm referenced to residual solvent resonances (^{1}H NMR: δ 7.27 for C*H*Cl_3 in

$CDCl_3$, and 3.31 for C*H*D_2OD in CD_3OD. ^{13}C NMR: δ 77.23 for *C*DCl_3 and 49.15 for *C*D_3OD. ^{19}F NMR: -76.55 for CF_3COOH). Deuterated solvents for NMR were obtained from Cambridge Isotope Laboratories and were used without purification. Electrospray ionization Mass spectra (ESI MS) were collected on a Micromass Quattro II, triple quadrupole mass spectrometer using both negative and positive ionization modes. Elemental analyses were performed at NuMega Resonance Labs, San Diego, CA. LCMS spectra were recorded on Agilent Technologies 6330 Ion Trap instrument. HR- ESI-TOF analyses were performed at Scripps Center for Metabolomics and Mass Spectrometry, La Jolla, CA. IR spectra were obtained on a Nicolet Nexus 670 FT-IR Instrument using KBr pellets.

Gadolinium concentration was measured by inductively coupled argon plasma (ICP) mass spectrometry (University of Illinois at Urbana-Champaign {UIUC}, Illinois Sustainability Technology Center, Division of the Institute of Natural Resource Sustainability). The sample (0.0500 mL), was added to Optima grade nitric acid (0.500 mL) and heated to 80 ^oC in a closed vial overnight. The solution was left for 7 weeks before being shipped to UIUC. Samples were also measured by ICP-OES (San Diego State University, Ecology Analytical Facility).

X-ray crystallography:

After purification of **12-NaOTf** and **17-NaOTf** by chromatography, the compounds were crystallized and data acquired and analyzed by the Small Molecule X-ray Crystallography facility at the University of California, San Diego. Compound **12-**

NaOTf was crystallized by slow evaporation of CH_2Cl_2, whereas **17-NaOTf** was crystallized by vapor diffusion of diethyl ether into a CH_2Cl_2 solution at -10 °C.

Compound **5** and Compound **12-NaOTf** (DOTA-N_3) described in sections I.2. and I.3., respectively.

*Synthesis of **14**.*[18]

To a dry 3-neck flask was added triflic anhydride (13.7469 g, 48.72 mmol, 1.03 equiv relative to (*S*)-methyl lactate) and dry CH_2Cl_2 (15 mL). An addition funnel was placed on the 3-neck flask and filled with (*S*)-methyl lactate (4.9040 g, 47.10 mmol), dry *N*,*N*-diisopropylethylamine (6.3931 g, 49.46 mmol) and dry CH_2Cl_2 (5 mL). The contents of the addition funnel were added dropwise under nitrogen to the reaction mixture as the flask was cooled in an ice bath over a period of 10 min before the bath was allowed to warm to room temperature. Reaction completion was monitored by analysis of aliquots by proton and fluorine NMR. The proton NMR showed 2.1% of unreacted alcohol in reaction mixture. The crude reaction mixture was used directly in the next step without further purification. ^{1}H NMR of an aliquot (CD_3OD, 399.8 MHz) showing peaks for **14**: δ 5.25 (q, *J* = 7.0, 1H), 3.86 (s, 3H), 1.72 (d, *J* = 7.0, 3H). ^{19}F NMR ($CDCl_3$, 376.1 MHz): δ -75.2 (s) triflate on **14** and -78.4 (s) free triflate ion.

*Synthesis of **15**.*

A sample of **10**[19,20] (3.44 g, 15.68 mmol) was taken up in CH_2Cl_2 (40 mL) and the resulting solution dried over molecular sieves (beads, grade 512 type 4 Å, 4-8 mesh) overnight. The flask was then chilled in an ice bath under nitrogen. Dry (distilled from

CaH_2) *N*,*N*-diisopropylethylamine (12.47 g, 96.48 mmol) was added dropwise, followed by the reaction mixture described above, containing **14** (47.10 mmol assuming 100% yield) via cannula, and the reaction flask was rinsed with CH_2Cl_2 (3 mL) to complete the transfer of alkylating agent. After 3 h, an aliquot was removed from the supernatant, solvent was removed using a nitrogen stream, and the residue was analyzed in CD_3OD by ^1H NMR spectroscopy, showing complete disappearance of the formylcyclen signal at 8.12 ppm and the appearance of one major (>92%) singlet at 8.02 ppm. After a total of 4 h reaction time, the mixture was filtered through a Büchner funnel containing Whatman filter paper (No. 40) to remove molecular sieves and the solids were rinsed with cold CH_2Cl_2 (50 mL). The combined CH_2Cl_2 filtrates were washed with ice water (100 mL). The CH_2Cl_2 phase was washed with 3% NaOH (3 x 100 mL). The aqueous layers were combined and back-extracted with CH_2Cl_2 (100 mL). All organic layers were combined and washed with brine (100 mL) and dried over Na_2SO_4. The mixture was filtered and the filtrate concentrated by rotary evaporation, leaving an amber oil (8.21 g) containing intermediate **15** and some **14**. For **15** in the mixture: ^1H NMR (CD_3OD, 399.8 MHz) δ 8.02 (s, 1H), 4.17 (ddd, *J* = 5.3, 8.4, 14.0, 1H), 3.89 (ddd, *J* = 4.2, 9.3, 13.7 1H), 3.678 (s, 3H), 3.671 (s, 6H) [In addition, COSY spectra suggests additional peaks overlap peaks in this region], 3.585 and 3.583 (two q, each with *J* = 7.0, total 2H), 3.47 (td, *J* = 5.2, 14.3 1H), 2.95- 2.81 (m, 7H), 2.75 (td, *J* = 5.1, 14.2, 2H), 2.69- 2.62 (m, 3H), 2.50-2.38 (m, 2H), 1.258 (d, *J* = 7.0, 3H), 1.250 (d, *J* = 7.2, 3H), 1.215 (d, *J* = 7.2, 3H). $^{13}C\{^1H\}$ NMR (CD_3OD, 100.5 MHz): δ 175.7, 175.6, 175.5, 165.5, 61.2, 60.0, 57.2, 53.8, 51.9, 51.8, 51.7, 51.6, 51.3, 51.1, 51.0, 50.2, 44.0, 15.7, 15.6, 15.2. ^{19}F NMR (CD_3OD, 376.1 MHz): δ -80.1 (s). ESI-MS *m*/*z* 459.2 (*M* + H), 481.3 (*M* + Na), (calculated for *M* =

$C_{21}H_{38}O_7N_4$, 458.27). There were no peaks visible in the ^{23}Na NMR spectrum. In addition, minor peaks in the ^{1}H and ^{13}C NMR spectra are present for DOTMA or its Na^+ OTf^- adduct, an undesired side-product. There was also evidence of a minor presence of DOTMA by ESI-MS *m*/*z* 539.3 (*M* + Na) , (calculated for *M* = $C_{24}H_{44}O_8N_4$, 516.32).

The crude product was dissolved in methanol (100 mL), and the resulting solution stirred as the flask was chilled in ice. Triflic acid (5.09 g, 33.9 mmol, 2.0 equiv relative to the amount of **10** used; the yield of intermediate **14** was assumed to be 100%) was added over 5 min. After an additional 5 min, the mixture was allowed to warm to room temperature then heated in a 60 ^{o}C oil bath for 7 h before being cooled to room temperature and concentrated by rotary evaporation. The residue was stored under vacuum for 10 h, leaving **15** (26.26 g, 33.9 mmol, 100%) as crispy beige foam, which quickly turns sticky on exposure to moisture in air.. ^{1}H NMR (CD_3OD, 399.8 MHz, digital resolution = 0.20 Hz) δ 5.48 (s, 1H), 4.66 (q, *J* = 7.2, 1H), 4.37 (q, *J* = 7.0, 1H), 3.85 (s, 3H), 3.73 (s, 3H), 3.66 (s, 3H), 3.95-3.56 (m, 6H?, partially overlapping with other signals and partially hidden quartet at 3.72 ppm), 3.29-3.22 (m, 4H), 3.15-2.95 (m, 6H), 2.84-2.60 (m, 3H), 1.64 (d, *J* = 7.2 3H), 1.37 (d, *J* = 7.1, 3H), 1.36 (d, *J* = 6.8, 3H). $^{13}C\{^{1}H\}$ NMR (CD_3OD, 100.5 MHz) δ 176.7, 176.5, 171.4, 121.9 (q, *J* = 318.6), 60.8, 56.5, 56.0, 55.7, 54.1, 53.2, 53.2, 48.8, 48.4, 46.3, 44.6, 44.3, 44.1, 44.0, 42.6. ^{19}F NMR (CD_3OD, 376.1 MHz): δ -79.9 (s). ^{23}Na NMR (CD_3OD, 376.1 MHz): δ -3.4 (s).

*Synthesis of **17**.*

Triflic anhydride (4.8468 g, 17.2 mmol) was added to a dry 3-neck flask containing dry CH_2Cl_2 (15 mL). Ester-azide-alcohol **5** (2.497 g, 15.7 mmol) and dry *i*-

Pr_2NEt (2.2375 g, 17.3 mmol) were added dropwise over 10 min using an addition funnel. The mixture was transparent pale brown. Using a gastight syringe, 90 min after the first Tf_2O had been added, a 50 µL aliquot was removed and quickly added to dry $CDCl_3$ (0.6 mL) in an NMR tube. Analysis by ^{19}F NMR spectroscopy showed singlets at -74.6 and -78.4 ppm for **6a** and triflate ion, respectively, and almost no detectable peak at -79.2 (Tf_2O). Analysis by ^{1}H spectroscopy showed a singlet at 3.89 ppm (CH_3O_2C of product, 3.0 units) and a small singlet at 3.83 (CH_3O_2C of reactant **5**, 0.10 units), indicating that approximately 10% of alcohol **5** remained. An additional portion of Tf_2O (0.5985 g, 2.12 mmol) was added 120 min after the beginning the first Tf_2O addition. Another 6.5 h elapsed before the solution of triflate **6a,** which was kept in the freezer, was added to the other reactant solution, prepared as follows: in a separate flask under nitrogen, to salt **15** (26.26 g, derived from 15.68 mmol of formylcyclen **10**) was added CH_2Cl_2 (80 mL) and dry *i*-Pr_2NEt (10.52 g, 81.4 mmol). The flask was chilled in ice and the solution of triflate ester **6a** was added via cannula over 7 min. After an additional 8 min the ice bath was removed and the mixture was allowed to warm to ambient temperature. After an additional 6 h, using a gastight syringe, a 50 µL aliquot was removed and quickly added to dry $CDCl_3$ (0.6 mL) in an NMR tube. Analysis by ^{19}F NMR spectroscopy showed one major singlet at -80.1 ppm (triflate ion) and a very minor peak at -76.8 (**6a**). The flask was chilled in ice and an ice-cold solution of NaOH (6 g) in water (50 mL) was added. The aqueous phase was extracted with CH_2Cl_2 (2 × 50 mL). The combined CH_2Cl_2 phases were concentrated by rotary evaporation and the residue stored under vacuum for 5 h, leaving a brownish solid (10.98 g). Analysis by ^{19}F NMR spectroscopy showed singlets at -76.8 and -80.1 ppm, for **6a** and product, respectively.

The crude product was purified by silica gel chromatography (gradient from CH_2Cl_2 to acetonitrile; product elutes with acetonitrile-CH_2Cl_2, 0.4:1), affording a beige foam-like solid (total 6.076 g, 8.170 mmol, 52% overall yield from formylcyclen **10,** with 5% DOTMA-NaTfO calculated from NMR spectra (not shown)). ^{1}H NMR (CD_3OD, 399.8 MHz, digital resolution = 0.20 Hz): δ 3.84-3.80 (m, 4H), 3.78 (s, 3H), 3.76 (s, 3H), 3.75 (s, 3H), 3.74 (s, 3H), 3.73-3.67 (m, 2H), 3.65-3.63 (m, 1H), 3.57-3.50 (m, 1H), 3.11-2.07 (m, 4H), 2.75-2.65 (m, 4H), 2.43-2.38 (m, 4H), 2.00-1.91 (m, 2H), 1.26 (d, *J* =7.0, 3H), 1.25 (d, *J* = 7.1, 6H). $^{13}C\{^{1}H\}$ NMR (CD_3OD, 599.8 MHz): δ 178.4, 178.2, 178.2, 177.4, 59.6, 57.8, 57.8, 57.8, 53.2, 53.1, 53.0, 51.6, 48.5, 46.0, 45.9, 45.9, 45.9, 24.6, 7.83, 7.80. ^{23}Na NMR (CD_3OD, 399.8 MHz): δ 6.6 (br s) and -3.4 (sharper s) in a ratio of 98 to 2, respectively, based on integration of NMR peaks. ^{19}F NMR (CD_3OD, 399.8 MHz): δ -79.9 (s). ESI-LCMS *m*/*z* 572.3 (*M* + H) (calculated for *M* + = $C_{25}H_{45}O_8N_7$ = 571.33). Anal. Calcd. for $C_{25}H_{45}N_7O_8$ + CF_3NaO_3S (743.73): C, 41.99; H, 6.10; N, 13.18. Found: C, 41.70; H, 5.93; N, 13.58. IR (KBr): 3442.9 br, 2956.4 s, 2845.7 s, 2099.2 s, 1728.2 s, minor peaks at 2360.4, 1637.5.

See Appendix Table A.7-A.11 for XRD data for **17-NaOTf**. For examples of Na^+ complexes like **17-NaOTf**, see references.[21,22]

*Synthesis of **18** (isolated product formulated as monohydrate)*:

To a round bottom flask containing **17** (7.53 g, contained 7% DOTMA-NaOTf, 10.12 mmol if 100% pure) was added 5% palladium on carbon (0.7530 g) along with MeOH (150 mL) under nitrogen. The mixture was put in an ice bath and TfOH (1.5781 g, 10.515 mmol) was added over 10 min. Hydrogen gas was bubbled gently through the

mixture for 6 h. The vent needle was then removed and reaction kept under hydrogen gas overnight. The mixture was then filtered through Celite pad into a tared flask. The Celite pad was rinsed with MeOH (2 x 50 mL). The filtrate was concentrated by rotary evaporation and then put under vacuum for 4 days, affording a pale orange syrup (8.85 g, 10.20 mmol, 100.8%, quantitative yield). ^{1}H NMR (CD_3OD, 599.6 MHz): (the δ 3.8- 3.6 region includes signal from DOTMA) δ 3.80 (s, 3H), 3.75 (s, 3H), 3.74 (s, 6H), 3.67-3.65 (m, 1H), 3.34-3..31 (m, 4H; likely 2H, but obscured by solvent signal), 3.14-3.06 (m, 1H), 3.02 (t of narrow multiplet, $J \approx 14.0$, 5H), 2.77 (tdd, J = 13.7, 5.0, 2.7, 2H), 2.69 (tdd, J = 13.7, 6.5, 2.6, 3H), 2.44-2.39 (m, 5H), 2.29-2.20, (m, 4H), 2.09-1.98 (m. 2H), 1.27 (d, J = 7.3, 3H), 1.25 (d, J = 7.0, 8H, 6H from **18** as well as signal from DOTMA). ^{13}C{^{1}H} NMR (CD_3OD, 599.8 MHz): δ 178.4, 178.2, 178.2, 178.1, 176.7, 60.6, 57.7(t), 53.4, 53.0, 48.8, 48.5, 45.9, 40.2, 23.3, 7.8. ^{23}Na NMR (CD_3OD, 105.7 MHz): δ 6.6 (br s), -3.4 (s). ^{19}F NMR (CD_3OD, 376.1 MHz): δ -79.9 (s). Anal. Calcd. for $C_{27}H_{48}F_6N_5NaO_{14}S_2$ (867.81): C, 37.37; H, 5.58; N, 8.07. Found: C, 36.71; H, 5.78; N, 7.57. Calcd. for $C_{27}H_{48}F_6N_5NaO_{14}S_2 + H_2O$ (885.82): C, 36.61; H, 5.69; N, 7.91.

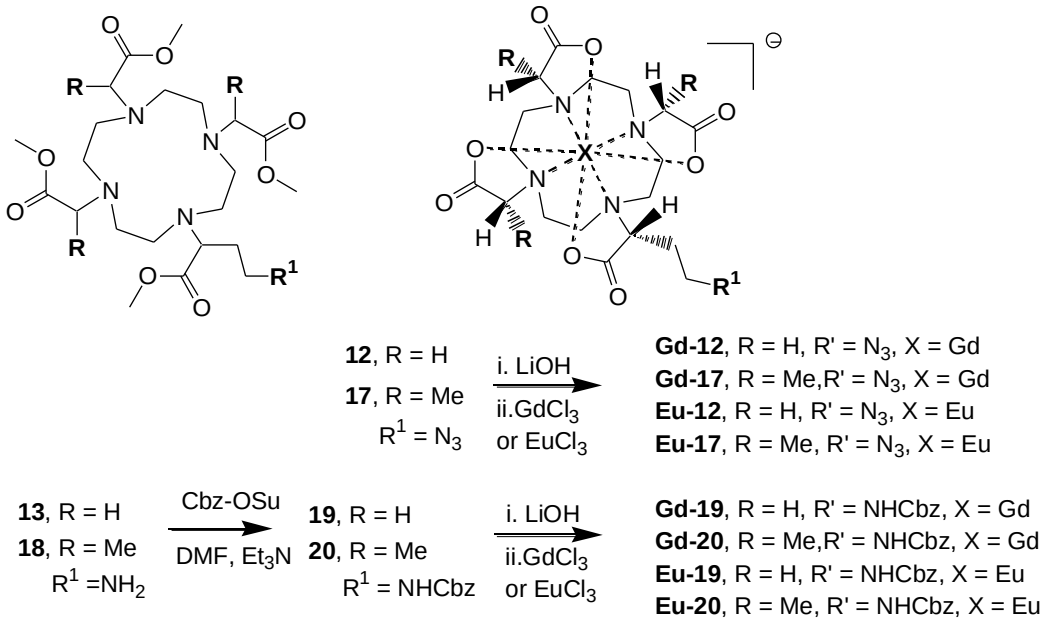

Figure I.4.3. Synthesis of N_3 and Cbz model complexes M-12, M-17, M-19 and M-20 (M = Eu, Gd).

General method for the synthesis of gadolinium and europium complexes of N_3-DOTA and N_3-DOTMA chelates (experiments done by Raghvendra Sengar at UPMC): Complexes **Gd-12**, **Gd-17**, **Eu-12** and **Eu-17** (Figure I.4.3):

In an open flask, N_3-ester chelate (**12** or **17**, 1.00 mmol, 1.0 equiv) was dissolved in tetrahydrofuran (15 mL) followed by the addition of water (4 mL). To the above mixture was added $LiOH \cdot H_2O$ (6.0 molar equiv) while stirring at 0 ^oC. The reaction was brought to room temperature and stirring was continued overnight (16 h). The reaction could be monitored by IR [before addition of LiOH: 2100.5 cm^{-1} (N_3), 1733.4 cm^{-1} (C=O); after LiOH: 2092.2 cm^{-1} (N_3), 1595.3 cm^{-1} (carboxylate)]. Once complete, the reaction mixture was concentrated by rotary evaporation and storage under oil pump vacuum. The crude hydrolysis product was further used without purification and the yield assumed to be 100%; the solid (1.0 equiv from **12** or **17** starting material) was dissolved

in water (40 mL) and $GdCl_3 \cdot 6H_2O$ or $EuCl_3 \cdot 6H_2O$ (1.1 molar equiv) was added at room temperature. The pH was adjusted to 7 using 1 M HCl and the mixture was stirred overnight at 80 ^oC, under nitrogen. Completion was determined by ESI-MS (direct injection). The solution was then concentrated by freeze-drying and the residue dried over phosphorus pentoxide in a desiccator for at least 2 d. Yields could not be calculated because of the uncertain composition of the complexes' counter ions (X) as well as other ions accumulated during the synthesis. Even after attempts at purification using ion exchange columns, elemental analyses tended to give low values, which others have noted for lanthanide-DOTA complexes.[23,24] Since the purification of complexes Gd-12, Gd-17, Eu-12 and Eu-17 was not trivial, analogous complexes (Gd-19, Gd-20, Eu-19 and Eu-20) were purified after functionalization with Cbz group.

[Gd(DOTA- N_3)]X (**Gd-12**) was obtained (0.6601 g) from the starting ester-chelate **12** (0.4516 g, 0.6436 mmol). ^{23}Na NMR (CD_3OD, 105.7 MHz): δ -2.10 (br s). ^{19}F NMR (CD_3OD, 376.1 MHz): δ -80.11 (s). ^{7}Li NMR (CD_3OD, 155.4 MHz): δ -0.39 (br s). ICP-OES (Gd at 342.247 and 335.047 nm); 143.5-145.2 ppm, expected 215.6 ppm (if all material was only Gd-DOTA-N_3 anion). HRMS (ESI-TOF) of Gd-DOTA-N_3 : *m*/*z* 651.1130 *(M* + Na + H), (calculated *m*/*z* for (*M* + Na + H) = $(^{12}C)_{18}(^{1}H)_{27}(^{158}Gd)(^{14}N)_7(^{16}O)_8$, 651.1138).

[Gd(DOTMA- N_3)]X (**Gd-17**) was obtained (0.7033 g) from the starting ester-chelate **17** (0.4628 g, 0.6223 mmol). ^{23}Na NMR (CD_3OD, 105.7 MHz): δ 0.08 (s). ^{19}F NMR (CD_3OD, 376.1 MHz): δ -78.80 (s). ^{7}Li NMR (CD_3OD, 155.4 MHz): δ 0.12 (s). ICP-OES(Gd at 342.247 and 335.047 nm); 204.1-207.7 ppm, expected 284.0 ppm (if all

material was only Gd-DOTMA-N_3 anion._HRMS (ESI-TOF) of Gd-DOTMA-N_3 : *m*/*z* 671.1777 *(M* + 2H), (calculated *m*/*z* for *(M* + 2H) = $(^{12}C)_{21}(^{1}H)_{33}(^{158}Gd)(^{14}N)_7(^{16}O)_8$, 671.1788).

[Eu(DOTA- N_3)]X (**Eu-12**) was obtained (1.7075 g) was obtained from the starting ester-chelate **12** (1.0020 g, 1.4281 mmol). ^{23}Na NMR (CD_3OD, 105.7 MHz): δ -0.42 (br s). ^{19}F NMR (CD_3OD, 376.1 MHz): δ -79.99 (s). ^{7}Li NMR (CD_3OD, 155.4 MHz): δ 0.00 (br s). ESI-MS(+): *m*/2*z* 318.5 (*M* + 2Li) (calculated *m*/*z* for *M* = $C_{18}H_{27}EuN_7O_8$, 622.11).

[Eu(DOTMA- N_3)]X (**Eu-17**) (0.5507 g) was obtained from the starting ester-chelate **17** (0.3478 g, 0.4676 mmol). ^{23}Na NMR (CD_3OD, 105.7 MHz): δ 0.15 (s). ^{19}F NMR (CD_3OD, 376.1 MHz): δ -78.76 (s). ^{7}Li NMR (CD_3OD, 155.4 MHz): δ 0.12 (s). ESI-MS(+): *m*/*z* 666.4 (*M* + 2H); ESI-MS(-): *m*/*z* 664.1 (*M*); (calculated *m*/*z* for *M* = $C_{21}H_{33}GdN_7O_8$, 664.16).

*General method for the synthesis of Cbz-protected esters **19** and **20** (experiments done by Raghvendra Sengar at UPMC)*:

A round bottom flask was charged with tetraester amine (**13** or **18**, 2.4 mmol) and *N*-(benzyloxycarbonyloxy)succinimide (910 mg, 3.66 mmol) and CH_2Cl_2 (80 mL) was added. The flask was kept on an ice-bath and the mixture was stirred for 15 min before the addition of triethylamine (1.3 mL, 9.7 mmol). The ice-bath was removed and the reaction mixture was stirred at room temperature for overnight. Solvent was removed by rotary-evaporation and the remaining residue was dissolved in methylene chloride (50

mL) and washed with water (3 × 20 mL). The organic layer was separated, dried over anhydrous sodium sulfate, filtered, and evaporated to give a light yellow gummy mass. The compound was purified using normal phase silica chromatography and a solvent gradient of CH_2Cl_2 in methanol (from 0 to 80% methanol).

DOTA-Cbz-ester **19**: (1.24 g, 81%) was obtained from the starting ester-chelate **13** (1.21 g, 2.4 mmol). ^{1}H NMR (DMSO-d_6, 500 MHz): δ 7.44-7.20 (m, 5H), 5.01 (s, 2H), 3.87-3.44 (m, 16H), 3.37-2.77 (m, 16H), 2.76-2.56 (m, 2H), 2.31-1.82 (m, 3H), 1.80-1.62 (m, 1H), 1.27-1.08 (m, 4H). ESI-MS (+): 638.59 (M+H, 100%) [M = $C_{30}H_{47}N_5O_{10}$, 637.72].

DOTMA-Cbz-ester **20**: (1.23 g, 74%) was obtained from the starting ester-chelate **18** (1.34 g, 2.45 mmol). ^{1}H NMR ($CDCl_3$, 500 MHz): δ 7.42-7.23 (m, 5H), 6.50 (s, 1H), 5.09 (s, 2H), 3.77-3.59 (m, 12H), 3.58-3.23 (m, 6H), 3.19-3.01 (m, 2H), 2.99-2.32 (m, 14H), 2.11-1.68 (m, 2H), 1.32-1.11 (m, 9H). ESI-MS (+): 680.31 (M+H, 100%), 546.28 (M-Cbz+H, 55%) [M = $C_{33}H_{53}N_5O_{10}$, 679.4].

*General method for the synthesis of gadolinium and europium complexes of Cbz-DOTA and Cbz-DOTMA chelates (experiments done by Raghvendra Sengar at UPMC): Complexes **Gd-19**, **Gd-20**, **Eu-19** and **Eu-20**.*

In an open flask, Cbz-ester chelate (**19** or **20**, 1.00 mmol) was dissolved in a mixture of tetrahydrofuran (6 mL) and MeOH (3 mL) followed by the addition of water (2 mL). An aqueous solution of $LiOH{\cdot}H_2O$ (230 mg in 1 mL water, 5.45 mmol) was added to the above mixture while stirring at 0 ^{o}C. The reaction was brought to room

temperature and stirring was continued overnight. The mixture was concentrated and redissolved in water (4 mL) followed by adjusting the pH ~ 7 using 0.5 M HCl. Water was removed by freeze-drying and the remaining solid was checked by ^{1}H NMR spectroscopy to confirm the absence of OMe-signals. The crude hydrolysis product was further used without purification; the solid was dissolved in water (20 mL) and a 1 M aqueous solution of $GdCl_3 \cdot 6H_2O$ or $EuCl_3 \cdot 6H_2O$ (1 mL, 1.00 mmol) was added at room temperature. The pH was adjusted to 7 and maintained by adding a 1.0 M solution of LiOH during the course of the reaction. The mixture was stirred overnight at 65 ^{o}C. Solvent was removed by freeze-drying and the remaining solid was purified over reverse phase C18 silica using methanol and water (0% to 100%) as eluents. Fractions containing desired compounds were identified by thin layer chromatography and mass spectral analysis. An aqueous solution of Gd-compounds were further passed through a HiTrap™ SP HP column, which removed lithium ions.

Li[Gd(DOTA-Cbz)] (**Gd-19**) was obtained (255 mg, 38%) from the starting ester-chelate **19** (630 mg, 0.91 mmol). ESI-MS(-): 735.26 (M-Li, 100%) (calculated *m*/*z* for *M* = $C_{26}H_{35}GdLiN_5O_{10}$, 742.18].

Li[Gd(DOTMA-Cbz)] (**Gd-20**) was obtained (313 mg, 47%) from the starting ester-chelate **20** (580 mg, 0.85 mmol). ESI-MS(-): 777.20 (M-Li, 100%). ESI-MS(+): 791.24 (M+2Li, 100%) (calculated *m*/*z* for *M* = $C_{29}H_{41}GdLiN_5O_{10}$, 784.23).

Li[Eu(DOTA-Cbz)] (**Eu-19**) (68 mg, 32% yield) was obtained from the starting ester-chelate **19** (185 mg, 0.27 mmol). ESI-MS(+): 738.21 (M + H, 100%) (calculated *m*/*z* for *M* = $C_{26}H_{35}EuLiN_5O_{10}$, 737.18).

Li[Eu(DOTMA-Cbz)] (**Eu-20**) (125 mg, 68% yield) was obtained from the starting ester-chelate **20** (160 mg, 0.24 mmol). ESI-MS(+): 780.24 (M + H, 74%), 786.15 (M + Li, 100%) (calculated *m*/*z* for *M* = $C_{29}H_{42}EuLiN_5O_{10}$, 779.22).

In order to create rotationally constrained chelates with increased rotational correlation times, a biotin moiety for avidin binding was added as outlined in Figure I.4.4.

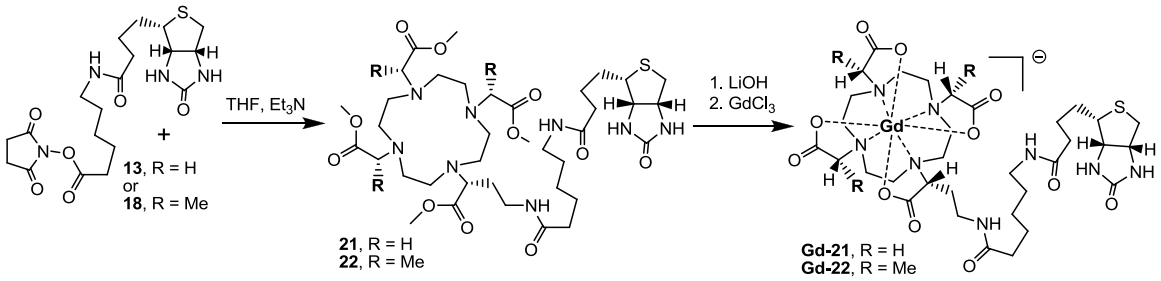

Figure I.4.4. Synthesis of biotin-chelate conjugates **Gd-21** and **Gd-22**.

General method for the synthesis of biotinylated chelate esters **21** and **22** (experiments done by Raghvendra Sengar at UPMC):

A round bottom flask was charged with ester-chelate (**13** or **18**, 0.15 mmol) and biotinamidohexanoic (LC-biotin) acid NHS-ester (60 mg, 0.13 mmol) followed by the addition of tetrahydrofuran (5 mL). The flask was kept on an ice bath and the mixture was stirred for 15 min before the addition of triethylamine (150 µL, 1.1 mmol). The ice-bath was removed and the reaction mixture was stirred at room temperature for 16 h. The solvent was removed in a rotary evaporator and the remaining residue was dissolved in CH_2Cl_2 (20 mL), and washed with water (3 × 5 mL). The organic layer was separated, dried over anhydrous sodium sulfate, filtered, and evaporated to give an off-white solid.

The compound was purified using SiO_2 and a gradient of CH_2Cl_2 in methanol (from 0 to 80% methanol).

21 (86 mg, 74%) was obtained from **13** (78 mg, 0.155 mmol). ^{1}H NMR ($CDCl_3$, 500 MHz): δ 7.29 (t, 1H, *J* = 5.2 Hz), 6.88 (t, 1H, *J* = 5.3 Hz), 6.01 (s, 1H), 5.69 (s, 1H), 4.54-4.48 (m, 1H), 4.36-4.29 (m, 1H), 3.81-3.69 (m, 12H), 3.58-3.52 (m, 1H), 3.51-3.34 (m, 3H), 3.24-3.12 (m, 5H), 3.11-2.81 (m, 8H), 2.79-2.70 (m, 1H), 2.65-2.01 (m, 16H), 1.96-1.71 (m, 3H), 1.70-1.28 (m, 11H). ESI-MS(+): 843.60 (M+H, 10%), 865.64 (M+Na, 100%) (calculated *m*/*z* for *M* = $C_{38}H_{66}N_8O_{11}S$, 842.46).

22 (62 mg, 53%) was obtained from **18** (86 mg, 0.157 mmol). ^{1}H NMR ($CDCl_3$, 500 MHz): δ 7.31 (m, 1H), 6.82 (m, 1H), 5.92 (s, 1H), 5.47 (s, 1H), 4.51 (m, 1H), 4.34 (m, 1H), 3.85-3.61 (m, 15H), 3.55-3.41 (m, 2H), 3.40-3.32 (m, 1H), 3.28-3.11 (m, 4H), 3.01-2.82 (m, 5H), 2.79-2.69 (m, 1H), 2.61-2.44 (m, 4H), 2.44-2.13 (m, 11H), 2.02-1.29 (m, 15H), 1.29-1.13 (m, 9H). ESI-MS(+): 907.68 (M+Na, 100%) (calculated *m*/*z* for *M* = $C_{41}H_{72}N_8O_{11}S$, 884.50).

General method for the synthesis of gadolinium complexes of biotin-chelate ***Gd-21*** *and* ***Gd-22*** *(experiments done by Raghvendra Sengar at UPMC)*:

In an open flask, biotin-tetraester derivative **21** or **22** (0.1 mmol) was dissolved in a mixture of tetrahydrofuran (2 mL) and MeOH (1 mL) followed by the addition of water (0.5 mL). An aqueous solution of $LiOH{\cdot}H_2O$ (21.5 mg in 0.5 mL water, 0.5 mmol) was added to the above mixture while stirring at 0 ^{o}C. The reaction was brought to room temperature and stirring was continued overnight. The mixture was concentrated and

redissolved in water (4 mL) followed by adjusting the pH to ~ 7 using 0.5 M HCl. Water was completely removed by freeze-drying and the remaining solid was checked by ^{1}H NMR spectroscopy to confirm the absence of OMe-signals. The crude hydrolysis product was further used without purification; the solid was dissolved in water (5 mL) and a 1 M aqueous solution of $GdCl_3$ (115 µL, 0.12 mmol) was added at room temperature. The pH was adjusted to 7 and maintained by adding a 1.0 M solution of LiOH during the course of the reaction. The mixture was stirred for 40 h at 55 ^{o}C. The solvent was removed by freeze-drying and the remaining solid was purified over reverse phase C18 silica using methanol and water (0% to 100%) as eluents. Fractions containing desired salts **Gd-21** or **Gd-22** were identified by thin layer chromatography and mass spectral analysis. Aqueous solutions of Gd salts were further passed through a HiTrap™ SP HP column.

Gd-21 (40 mg, 42% yield) was obtained from the starting ester-chelate **21** (86 mg, 0.1 mmol). ESI-MS(-): 940.30 (M-Li, 100%). ESI-MS(+): 942.10 (M-Li+2H, 100%) [M = $C_{34}H_{54}Gd_1Li_1N_8O_{11}S_1$, 946.30]. ESI-HRMS(-): 942.4705 (M-Li+2H, 96%), 964.4579 (M-Li+H+Na, 100%) (calculated *m*/*z* for *M* = $C_{34}H_{54}Gd_1Li_1N_8O_{11}S_1$, 947.3034).

Gd-22 (37 mg, 53% yield) was obtained from the starting ester-chelate **22** (62 mg, 0.07 mmol). ESI-MS(-): 982.3 (M-Li, 100%). ESI-MS(+): 984.3 (M-Li+2H, 100%) [calculated *m*/*z* for *M* = $C_{37}H_{60}Gd_1Li_1N_8O_{11}S_1$, 989.35). ESI-HRMS(+): 990.3564 (M+H, 100%) (calculated *m*/*z* for *M* = $C_{37}H_{60}Gd_1Li_1N_8O_{11}S_1$, 989.3503).

Oxygen-17 NMR measurements (experiments done by Erik Wiener and Luce Vander Elst at University of Mons):

Nuclear magnetic resonance measurements of ^{17}O were performed as described by Laurent et al.[25] Solutions of **Gd-19** and **Gd-20** were prepared in distilled water (pH 6.5-7.0) at concentrations of 23 mM. Solutions (0.35 mL) were transferred to 5 mm o.d. NMR tubes and ^{17}O NMR measurements were made at 11.7 T in a Bruker AVANCE-500 spectrometer (Bruker, Karsruhe, Germany). The temperature was regulated by air or nitrogen flow controlled by a Bruker BVT 3200 unit. ^{17}O transverse relaxation times of distilled water (pH = 6.5–7) were measured using a CPMG sequence and a subsequent two parameters fit of the data points. The 90° and 180° pulse lengths were 27.5 and 55 μs, respectively. The ^{17}O T_2 values of water in the solutions of complexes were obtained from linewidth measurements. All spectra were proton decoupled. Data are presented as the reduced transverse relaxation rate ($1/T_2^R = 55.55/(q*[complex]*1/T_2^p)$, where [complex] is the molar concentration of the complex, q is the number of inner sphere coordinated water molecules, and $1/T_2^p$ is the paramagnetic transverse relaxation rate. Data analysis and treatment was performed as described by Vander Elst, et al.,[26] Muller, et al.,[27] and Laurent, et al.[28]

Proton Nuclear Magnetic Relaxation Dispersion (NMRD) Measurements (experiments done by Erik Wiener and Luce Vander Elst at University of Mons):

Proton NMRD measurements were made over a magnetic field range of 0.47 mT to 1.0 T on a Stelar Spin fast field cycling (FFC) NMR relaxometer (Stelar, Mede (PV), Italy). Three different solutions of each complex were prepared in 50 mM HEPES buffer, pH = 7.35, with 150 mM NaCl. Measurements were performed on 0.800 mL samples in 10 mm o.d. NMR tubes. Additional relaxation rates were measured at 20 and 60 MHz on

a Bruker Minispec mq-20 and mq60 at temperatures specified in Figure I.4.12 and matching temperatures used for all samples.

Avidin-Biotin Complexation (ABC) (experiments done by Erik Wiener and Luce Vander Elst at University of Mons):

Three separate sample concentrations of **21** and **22** were prepared with avidin. In separated tubes a solution of 50 mM HEPES, pH = 7.35, with 150 mM NaCl was added to six tubes containing avidin for final concentrations of 0.22 mM. Chelates were added such that [chelate] : [avidin] never exceeded 3.2 (in other words were always less than 4 to prevent saturation of avidin) at concentrations of 0.553, 0.692, and 0.700 mM Gd(III) for **21** and 0.267, 0.315, 0.448 mM Gd(III) for **22**. The lower concentrations of **22** versus **21** used would not be responsible for changes in the slope because the plot is linear.

*Model reaction of DMF with **14**:*

To a dry J. Young resealable NMR tube was added **14** (0.0184 g, 0.07791mmol, 1.0 equiv) and dry DMF (0.0107 g, 0.14639 mmol, 1.88 equiv) and CD_2Cl_2 was added until the total volume was ~0.55 mL. The NMR tube was left at room temperature. Proton and fluorine NMR spectra were acquired at different time points (11 min, 1.2 h, 2.2 h, 3.2 h, 6.5 h, 19.7 h, and 7 d) to monitor the evolution and stability of product/s formed. ^{19}F NMR (CD_2Cl_2, 376.1 MHz): δ -79.1 (s) for the free triflate of the product and -75.7 (s) for the covalently bound triflate of the starting material. As time elapsed the peak at δ -75.7 decreased as a peak at δ -79.1 increased. After 1.3 h, integration of the ^{19}F NMR peaks showed that 77% of the fluorine is in the free triflate ion. After 19.7 h had passed

the only ^{19}F NMR peak was the one at δ -79.1 ppm, showing complete consumption of **9**. For the intermediate compound **A** in the reaction mixture: ^{1}H NMR (CD_2Cl_2, 399.8 MHz): δ 8.93 (s, 1H), 7.96 (s, 1H), 5.55 (q, *J* = 7.0, 1H), 3.82 (s, 3H), 3.50 (s, 3H), 3.29 (s, 3H), 1.73 (d, *J* = 7.0, 3H). ^{13}C NMR (CD_2Cl_2, 399.8 MHz): δ 167.9, 160.5, 121.2 (q, *J* = 320.1) 81.7, 54.0, 42.6, 37.2, 17.3. ^{19}F NMR (CD_2Cl_2, 399.8 MHz): δ -79.2 (s).

After 22 d, product formed appears to be stable as seen by the proton NMR spectrum. To test our proposed hydrolysis hypothesis, in the glovebox deoxygenated water (5.5 µL, 0.30 mmol, 1.2 equiv) was added to the reaction mixture in the NMR tube. The reaction was monitored by proton NMR spectroscopy, showing that after 25 min the proton peaks corresponding to **A** were not detectable and only the peaks for hydrolysis products were seen, indicating that the hydrolysis occurred relatively quickly, which supports the notion that trialkylation of compound **10** to form **15** is accompanied by some overalkylation and loss of the formyl group, leading to the formation of small amounts of DOTMA-NaOTf. For the hydrolysis mixture: ^{1}H NMR (CD_2Cl_2, 399.8 MHz): δ 8.07 (s, 1H), 5.19 (q, *J* = 7.0, 1H), 3.72 (s, 3H), 1.49 (d, *J* = 7.0, 3H); in addition, peaks for residual excess DMF were seen at 7.96 (s, 1H), 2.92 (s, 3H), 2.82 (s, 3H) and a broad peak for water at 4.60 ppm. ^{13}C NMR (CD_2Cl_2, 399.8 MHz): δ 171.1, (163.1, DMF carbonyl carbon), 160.6, 68.6, 52.8, 36.9, 36.0, 31.7, 17.3. ^{19}F NMR (CD_2Cl_2, 399.8 MHz): δ -79.1 (s).

I.4.3. Results and Discussion

Synthesis.We have prepared four new bifunctional chelates (**12-**, **17-**, **13-**, and **18-NaOTf**) and characterized them by NMR, X-ray crystallography and mass spectroscopy

and effectively complexed them to Gd(III) to make novel MRI contrast agents. For each chelate (DOTA and DOTMA), two pragmatic functional groups (N_3, **12**, **17**) and (NH_2, **13**, **18**) were designed for coupling to either terminal alkynes through click chemistry or carboxylic acids using amide bond formation.

The syntheses of **12-** and **17-NaOTf** were designed to minimize the number of purification steps, and make distinctive use of triflate as a counterion for several reasons. Our previous work[29] with the triflate leaving group from **14** showed that it could be displaced by S_N2 with high constancy, and since the reaction rates are relatively fast with amine nucleophiles, subsequent epimerization of the new chiral center was diminished.[18] Although HCl could be used in the deprotection of **10**, the chloride counterion present could interfere with the subsequent alkylation by **9**, because chloride could displace the triflate group. Theortically, the HCl salt could be neutralized and isolated from the free amine for further alkylation, but in practice, we recovered higher overall yields when using the procedure shown with trific acid. Other leaving groups were tried (other sulfonates, halides) but did not give satifactory results. Published work also showed that despite the ability to isolate and even distill compound **14**, isolation by either of these methods tended to lower the enatiomeric purity of **14** and its alkylation products.[18] Therefore, rather than isolating or storing triflate electrophiles **9** and **14**, they were both made fresh and used as mixtures.

According to literature,[19,20] *N*-formylcyclen was a suitable mono-protected cyclen derivative[30] which was reported as the monohydrate. In our prior work,[29] the trialkylation of **10** with the primary halide $BrCH_2CO_2tBu$ and subsequent *N*-deprotection was

achieved without incident. In this work, at some point the formyl protecting group was lost during the alkylation step resulting in undesired DOTMA product. A model reaction using DMF (Figure I.4.5) was done to test this hypothesis. Compound **14** and dry DMF were combined in CD_2Cl_2 under dry conditions in a resealable NMR tube, allowing for in situ monitoring of reaction progress without having to disturb the reaction by removing aliquots. With a half-life of about 1 h, a stable intermediate formed (compound **A**) as evidenced by proton and fluorine NMR spectral data. The methine proton on the chiral carbon appeared at 5.55 ppm, the formyl proton 8.93 ppm, and a fluorine peak for free triflate ion at -79.1 ppm. Upon addition of water, **A** quickly hydrolysed to **B**, as shown by proton and fluorine NMR data. The proton on the chiral carbon shifted upfield to 5.19 ppm, the formyl proton shifted upfield to 8.07 ppm, whereas in ^{19}F NMR spectra the free triflate ion signal remained at -79.1 ppm.

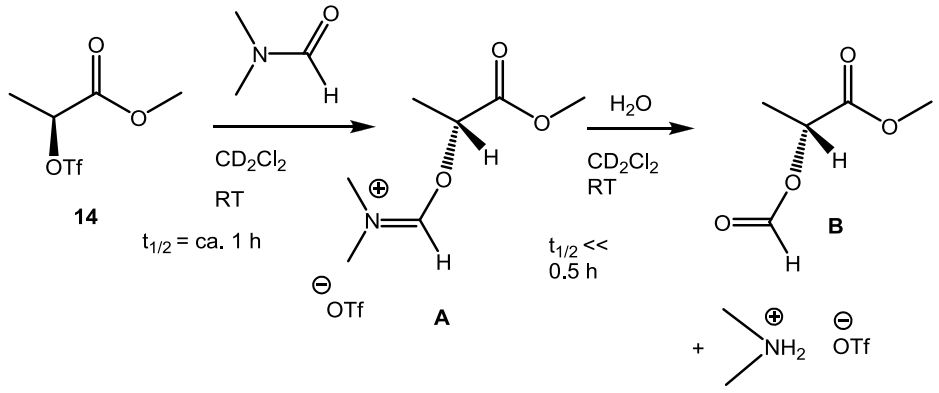

Figure I.4.5. Model reactions showing feasibility of deprotection of N-formyl group by **14** and water.

The model reaction shown in Figure I.4.5 showed how the formyl group loss could be due to incomplete drying of the alkylation reaction; DMF was rapidly alkylated and the resulting iminium ion swiftly underwent hydrolysis. We hypothesized that the

water from compound **10** (monohydrate) and/or wet methanol facilitated the untimely loss of the *N*-formyl group which allowed a fourth alkylation event, resulting in the DOTMA-NaOTf adduct. Based on this model, we then dried the formylcyclen in dry DCM over molecular sieves overnight prior to alkylation, which reduced the side product to below 10%, though we could not prevent its formation entirely. Literature does provide examples of similar formamide alkylations[31,32] as well as subsequent hydrolyses.[33-35] The reaction progression of the trialkylation of **10** (Figure I.4.6) was followed by taking aliquots analyzed by ^{1}H NMR spectroscopy. The disappearance of the formyl resonance for **10** and any peaks other than intermediate **14** were monitored. The following deprotection of the *N*-formyl group needed only two equivalents of acid in methanol, resulting compound **16** as a triflate salt in quantitative yield.

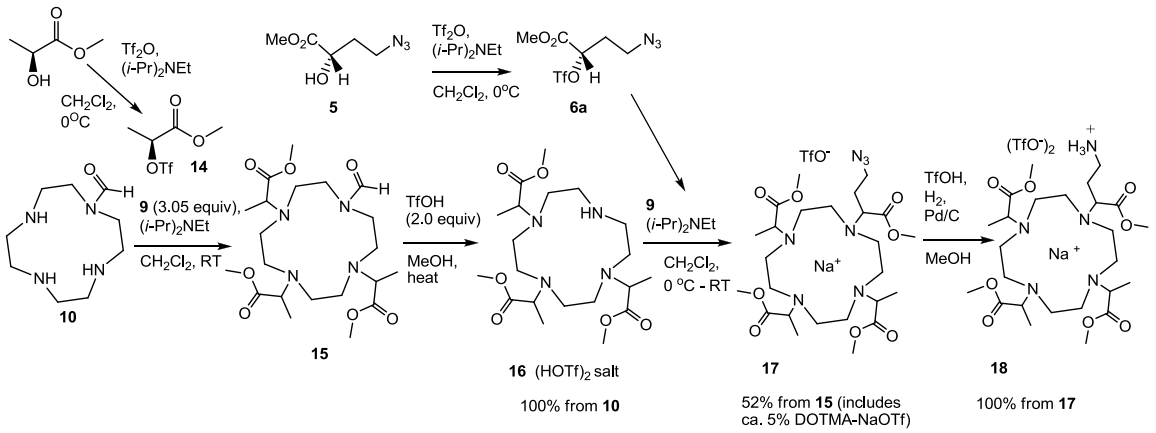

Figure I.4.6. Synthesis of **17** and amine analog **18**.

The alkylation of compound **16** was made in situ using freshly prepared **6a** to give **17-NaOTf**, which was purified by column chromatography using CH_2Cl_2-CH_3CN. Since the ^{23}Na and ^{19}F NMR spectra showed strong peaks, the structure of **17-NaOTf** as a NaOTf adduct was very likely and ultimately verified by NMR, elemental analysis and

X-ray crystallography (Figure I.4.8). Compound **17-NaOTf** was crystallized by vapor diffusion of diethyl ether into a CH_2Cl_2 solution at -10°C, Figure I.4.7.

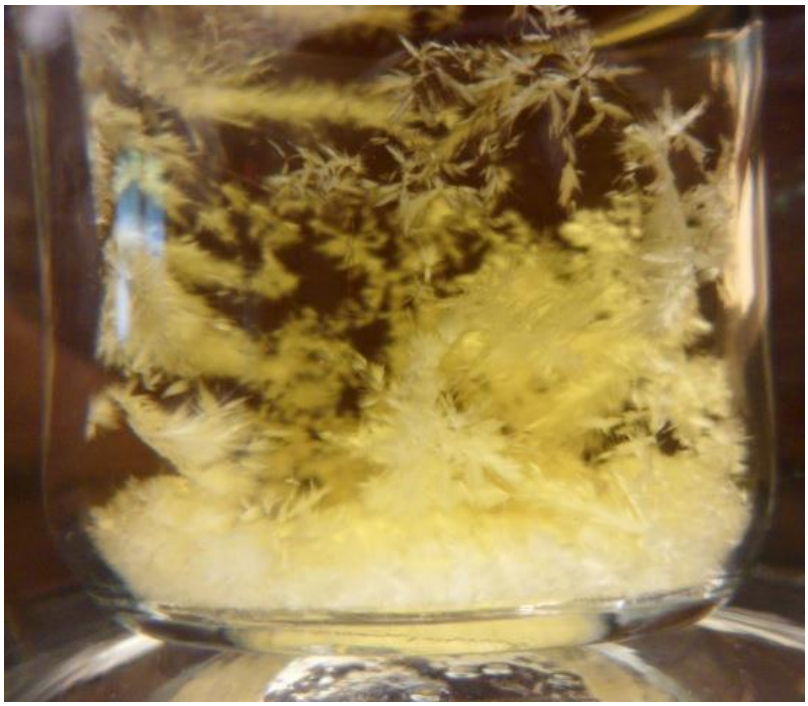

Figure I.4.7. Crystals of compound **17-NaOTf**.

The X-ray data showed that the azide analogs (**12-NaOTf** and **17-NaOTf**) had a sodium cation coordinated within the macrocycle, balanced by an outer-sphere triflate counterion. As in the synthesis of **12-NaOTf** (the DOTA analog), these ions were present and detected by NMR even after purification by liquid chromatography and crystallization! There is literature precedent of similar macrocycles[21,22,36] that contain a sodium ion coordinated by the ring nitrogens and carbonyl-containing arms. The average bond distances between Na-O and Na-N of **12-NaOTf** were 2.540(8) Å and 2.556(7) Å respectively. And the average bond distances between Na-O and Na-N of **17-NaOTf**

(Figure I.4.8) were 2.502(7) Å and 2.562(7) Å, respectively. These bond distances fall reasonably within the average range of distances found for similar crystal structures (CCDC search results: Na-O: 2.513(30) Å and Na-N: 2.622(7) Å). Among the four molecules that for the unit cell in the crystal structure of **17-NaOTf**, a trend exists where the Na-N bond was longest for the nitrogen with the side chain containing the $-CH_2CH_2N_3$ moiety, possibly due to steric effects. In contrast, only one of the two molecules in the units cell of **12-NaOTf** had a significantly longer Na-O and Na-N distance (2.823(11) Å and 2.642(11) Å, respectively) on the nitrogen and oxygen that are part of the azide moiety. However, the azide moiety does not significantly alter the macrocycle conformation by disrupting chelation by the ester oxygens or ring nitrogens as shown by the crystallographic data for **12-NaOTf** and **17-NaOTf.**

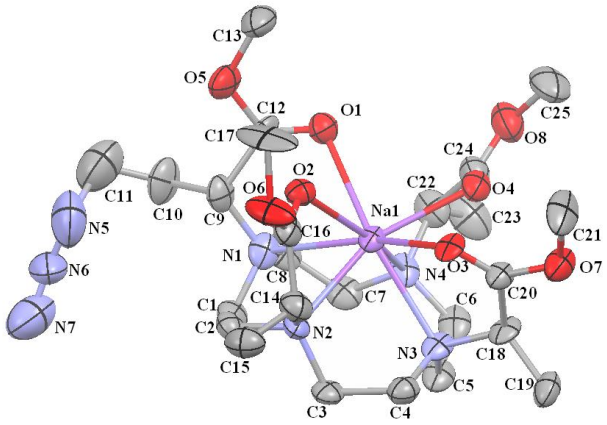

Figure I.4.8. Thermal ellipsoid plot of **17-NaOTf** drawn at 35% probability level. Hydrogen atoms and triflate counter ion were omitted for clarity.

After careful analysis of bulk samples of the product by ^{1}H and ^{13}C NMR spectroscopy, a second minor (5-10%) compound was determined to be present. It was identified as the NaOTf adduct of the tetramethyl ester of DOTMA, which most likely formed from the loss of the *N*-formyl group of **10** or **14**. The DOTMA impuity was used

in following experiments, since the presence of the impurity did not interfere with the next step of conjugation because it lacked a reactive side chain group.

The hydrogenation of the azide in Figure I.4.6 progressed well in the presence of one added equivalent of TfOH, so as to prevent the amine formed during hydrogentation from attacking the ester of the unique side chain and forming the unwanted lactam. Triethylamine was used to neutralize the resulting triflate salts of **18-NaOTf** and then acylated by an external reagent, such as biotinamidohexanoic acid of Cbz NHS-esters (Figure I.4.6 and **6a**) forming **19**, **20**, **21** or **22.** The subsequent hydrolysis using LiOH and water-THF mixtures, followed by complexation with Gd(III) or Eu(III) at a slightly acidic pH resulted in amine-acylated chelates for further study.

The difference between the water residence times of Gd(III) complexes of DOTA and DOTMA stems from the differences of the relative populations of the conformational isomers, square antiprismatic (SAP) and twisted square antiprismatic (TSAP). The TSAP isomer exchanges more quickly than the SAP isomer. DOTMA is created via alpha subsitiution of the acetate carms attached to the four nitrogens on DOTA, making four chiral centers which favors the TSAP isomer. The homochiral diastereomer of DOTMA (either the *R*,*R*,*R*,*R* or the *S*,*S*,*S*,*S* enantiomer) has the highest TSAP/SAP ratio.[13,15,16] By using ^{1}H NMR spectroscopy of Eu(III) complexes, Wood et al.[16] could differentiate the various diastereomers and determine the relative TSAP/SAP ratio. We also used proton NMR of the Eu(III) complexes of the Cbz derivatives (**Eu-19** and **Eu-20**), Figure I.4.9. The proton NMR spectrum of **Eu-20** (Figure I.4.9B) is consistant with an *R*,*R*,*R*,*R* configuration, even with the unique amino butyric arm breaking the symmetry, which

causes the four distinctive m_{ax} peaks to be seen between δ 18 and 20 ppm. These peaks are comparable to the four axial peaks that were observed for the *R*,*R*,*R*,*S* isomer of Eu(III)-DOTMA where the *R*-configured center breaks the symmetry.[16] Our NMR data for **Eu-20** show the presence of either stereisomer (*R*,*R*,*R*,*R* or *S*,*S*,*S*,*S*), but independently do not differeniate between the two possibilities. Nevertheless, what does discrimiate between the possible stereoisomers is the synthetic starting materials and known S_N2 inversion. Our synthetic design of compound **18** ensured the product to yield the *R*,*R*,*R*,*R* enantiomer. The crystal structures of the intermediate **17-NaOTf** demonstrates that it is in the *R*,*R*,*R*,*R* configuration, just as the structure of **12-NaOTf** show its single stereocenter in the *R* configuration. However, the one forewarning is that the configuration assignments are rigorously proven only for the single crystals analyzed. In the case of **17-NaOTf**, which has four stereogenic centers, a more rigorous analysis is possibile: a bulk sample (50-100 mg) was analyzed by ^{13}C NMR with particular attention to the carbonyl region (δ 178.5 to 178.0 ppm). There was a minor peak for DOTMA-NaOTf at 178.1 ppm, and four major singlets (178.3, 178.2, 178.2, and 177.4 ppm) for the product. Based on our findings, we conlude that there are no other diastereomers present in greater than 3% (our estimated limit of detection) concentration, because if another diastereomer were present, its carbonyl peaks would be overlapping with those observed.

The DOTMA derivative **Eu-20** (Figure I.4.9B) has a much higher TSAP/SAP ratio than the DOTA derivative **Eu-19** (Figure I.4.9A). It is interesting to note that only two sets of peaks are observed demonstrating that the base deprotection of the methyl esters did not significantly epimerize the chiral centers. If the chiral centers had

epimerized there would have been up to 16 stereoisomers (!) and a large number of peaks in the axial region (downfield of δ 15 ppm). The high TSAP/SAP ratio for **Eu-20** indicates that the conformational properties of the macrocycle or its complexes are not detectably changed by the unique side chain of the novel derivative **20**. Woods et al.[16] expected the conformational behavior of Eu(III) and Gd(III) complexes would be equivalent in their analysis, so we also used the same reasonable assumption. Based on their Eu(III) complexes, the bifunctional Gd(III)-DOTMA derivatives are predicted to have a shorter water residence time than their Gd(III)-DOTA analogs.

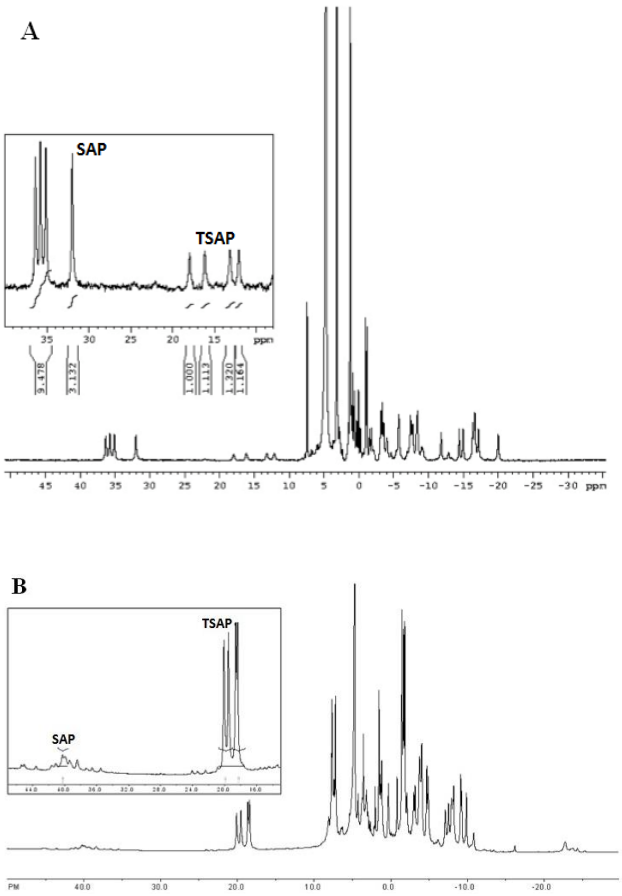

Figure I.4.9. Proton NMR of Eu-Cbz-chelates showing the SAP/TSAP ratio. Upper: **Eu-19**; lower: **Eu-20**.

Looking at other literature on bifunctional chelators based on cyclen, a 1992 paper[37] by Renn and Meares titled "Large Scale Synthesis" of a bifunctional DOTA analog in "up to 10 g" quantities in a linear nine-step reaction with an overall yield of 5.6%. Several of their purification steps required a reverse-phase HPLC which is not inexpensive. Meares' work required a synthetically challenging cyclen ring substitution with a *para*-nitrobenzyl group, whereas our approach can use commercially available cyclen. Others[38-40] have also reported on the synthesis of the *para*-nitrobenzyl DOTMA analog with studies on the structure and dynamics of their lanthanide complexes, but to date, there are no reports on the use of the bifunctional nature of these DOTMA derivatives. In contrast, we report the synthesis of an arm-substition to a cyclen scaffold resulting in biofunctional DOTMA analogs on a similar scale ~ 10 g, but in only five steps! Conversion of cyclen to the azide derivative (**17-NaOTf**) was successfully accomplished with an overall yield of 40% with only one chromatography step. In addition as discussed below, we hypothesized that macromolecular DOTMA agents would have higher relaxivity than DOTA analogs was correct, in appreciation to our ability to conjugate the new DOTMA derivatives without compromising water residence times.

Relaxivity properties: We used ^{17}O NMR to measure the reduced transverse relaxation rate of the water molecules in the inner coordination sphere of the complexes as a function of temperature (Figure I.4.10) to verify the proton NMR data and calculate the actual water residence time. According to literature,[15] "the water-exchange rate is definitely independent of the solution structure for both the SAP and TSAP isomers, and,

hence, the overall water exchange only depends on the SAP/ TSAP isomeric ratio." Looking at the proton NMR spectra, the SAP/ TSAP ratio is significantly greater for **Eu-19** relative to **Eu-20**. The water residence time for the **Gd-19** (101 ns) at 37 ^{o}C is approximately 2.5 times longer than that of **Gd-20** (42 ns), which is consistent with the larger SAP/ TSAP ratio. We could not measure water residence time of **21** and **22** directly because the concentrations need for ^{17}O experiments were relatively high and our amount of sample was limited. Also the chemical change going from **19** and **20** to **21** and **22** is far enough from Gd(III) that it should have no effect on the water residence time.

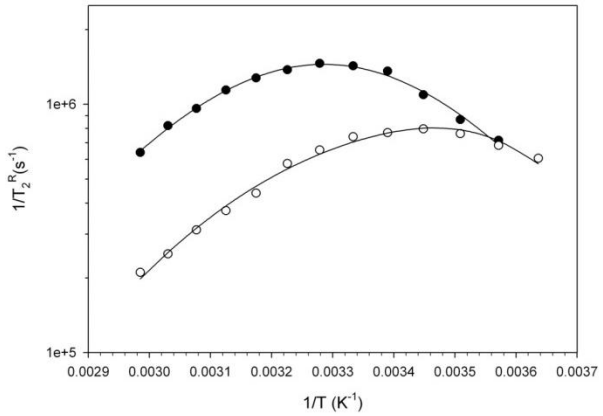

Figure I.4.10. ^{17}O NMR measurement of the reduced transverse relaxation time as a function of temperature: **Gd-19** (filled circles) and **Gd-20** (open circles).

The analysis of the data at 37 °C demonstrated that the new DOTA analog **Gd-19** (100.8 ns) had a longer water residence time than the new DOTMA analog **Gd-20** (41.6 ns), Table I.4.1. The rotational correlation time and water residence time increase as the temperature decreases, which typically have opposite effect on relaxivity. When relaxivity is not limited by long water residence times, decreasing the temperature with the subsequent increase in rotational correlation time increases the relaxivity of rapidly rotating complexes. If the water residence time limits the relaxivity, decreasing the

temperature will result in a decrease in relaxivity. The water coordination number was not measured for the Eu complexes, but the Solomon-Bloembergen-Morgan calculations done are standard procedure in this field, but it is known that having multiple parameters make the analysis less accurate than reducing parameters.[41]

Table I.4.1. Parameters obtained by the theoretical analysis of the ^{17}O NMR experimental data.

	τ_M^{310} (ns)	τ_V^{298} (ps)	$\Delta H^{\ddagger}$ (kJ mol^{-1})	B x 10^{20} (s^{-2})	E_V (kJ mol^{-1})	A/ħ x 10^6 (Rad s^{-1})	$\Delta S^{\ddagger}$ (J mol^{-1} K^{-1})
Gd-19	100.8 ±4.7	4.86 ±0.56	54.1 ±0.52	1.99 ±0.229	0.102 ±19	-2.95± 0.203	63.3 ± 2.2
Gd-20	41.6 ±5.2	5.23 ±0.40	63.1 ±0.198	6.37 ±0.493	8.12 ±3.98	-3.0± 0.146	99.7± 0.407

To analyze the temperature dependence on the relaxivity of **Gd-19** and **Gd-20**, we used variable temperature relaxometry, Figure I.4.11. At 37 ^oC the relaxivities of the two chelates are nearly equal, which is expected for related Gd(III) systems with one inner sphere water molecule where rotational correlation time influences the relaxivity. Both chelates display increasing relaxivities as the temperature decreases from 37 to 15 ^oC. There is an increase in relaxivity for both chelates when the temperature decreases until about 10 ^oC. It is interesting to note, from 15 to 3 ^oC the relaxivity of **Gd-19** levels off while the relaxivity of **Gd-20** continues to increase, Figure I.4.11. From the τ_M data in Table I.4.1, we would expect the relaxivity of **Gd-19** to level off and **Gd-20** to continue to increase. In regard to **Gd-20** where the data are clearer from the smaller error bars, the value at 2.5 ^oC is larger than the values at 10 ^oC and at all other higher temperatures. The graphs of Figure I.4.11 are independent for each other. Since the average of the data

points would not change significantly with smaller error bars, the general curves of the graphs would still show that as temperature decreases, relaxivity levels off.

The relaxivities at 25 and 37 ^{o}C should be similar for Gd(III)-Cbz-chelate complexes with a small molecular size considering the difference in water residence times. But the relaxivity values should differ when there is an increase in rotational correlation times. Hence, we increased the rotational correlation time by decreasing the temperature. By decreasing the temperature, the relaxivity would increase if the chelate was limited by the rotational correlation time. If the relaxivity of the chelate were limited by the water residence time, then decreasing the temperature would decrease the relaxivity. The relaxivity of **Gd-19** levels off since the associated increase in relaxivity with increasing rotational correlation time is now counteracted by the decrease in relaxivity associated with increasing water residence time. The water residence time of **Gd-20** at 37 ^{o}C is lower than that of **Gd-19**; even when lowering the temperature to 3 ^{o}C, the water residence time did not reach a value that offset the changes in relaxivity associated with increasing the rotational correlation time. Studies done on the Cbz derivatives **19** and **20** provided preliminary data for the further investigation of derivatives **21** and **22**.

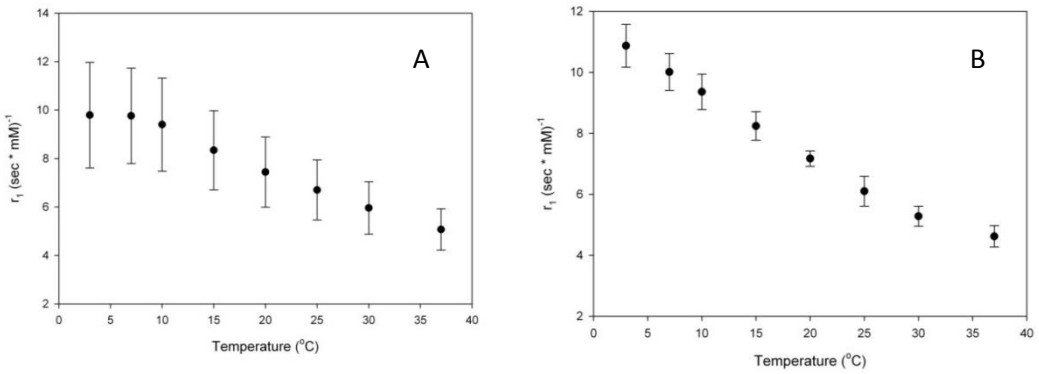

Figure I.4.11. Variable temperature relaxometry at 0.47 T showing dependence of relaxivity on temperature. A: **Gd-19**; B: **Gd-20**. Note that graph A and B are independent of each other; the large error bars in A does not take away from the general curve of the graph. Note that for standard errors apply for the concentrations used and were calculated using Sigmaplot.

The data for the Cbz derivatives (**Gd-19** and **Gd-20**) predict that the relaxivity of rotationally constrained analogs of **19** with the ethylamino linker are limited by water residence time in addition to rotationally constrained analogs of **20** should have higher relaxivities. In other words, based on data from the short water residence time and variable temperature relaxometry, the rotationally constrained Gd(III)-DOTMA derivative should have a significantly higher relaxivity that a rotationally constrained Gd(III)-DOTA derivative.

Chelates can be rotationally contrained by increasing the viscosity[14] or attaching chelate to a macromolecule covalently or noncovalently.[3,4,42] We decided to increase the rotational correlation time of our two types of chelates by noncovalently attaching them to avidin through avidin-biotin complexation (ABC). The ABC was first done with a derivative of Gd(III)-diethylenetriaminepentaacetate (Gd(III)-DTPA) by Langereis et al.,[43] and later by Geninatti Crich et al.[44] Biotin is known to bind to avidin and streptavidin with extremely high binding constant; each avidin has four biotin binding

sites. To test our hypothesis, biotinylated derivatives of the two chelates (**Gd-21** and **Gd-22**) were made and used in ABC reaction which increases the rotational correlation time or rotationally constrains the two compounds. The biotinylated analogs (**Gd-21** and **Gd-22**) are rapidly rotating small molecules and have essentially the same relaxivities and similar NMRD profiles, Figure I.4.12. This result is expected since the rotational correlation time dominates the influence on relaxivity for small Gd(III)-chelates with these water residence times. Adding avidin to the bionylated analogs results in binding which increases the rotational correlation time and thus greatly increases the relaxivity; values **Gd-22** increased significantly more than for **Gd-21**. In the high field region of the NMRD profile, **Gd-21 + avidin** and **Gd-22 + avidin** show the characteristic peaks of the relaxivity, which is typical for slowly rotating complexes.[3] These characteristic peaks of higher relaxivity across all magnetic field strengths for **Gd-22 + avidin** relative to **Gd-21 + avidin** are consistent with the well-accepted observation that water residence time limits the relaxivity of constrained Gd(III)-DTPA and Gd(III)-DOTA chelate systems and the shorter water residence times on the new DOTMA derivative, **Gd-22**.

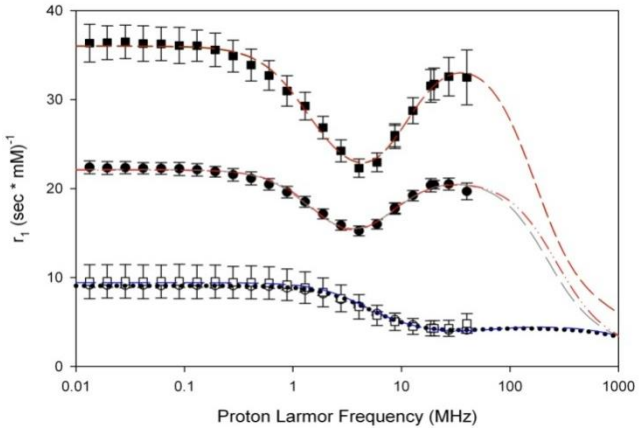

Figure I.4.12. NMRD profiles of **Gd-21** (circles) and **Gd-22** (squares) with (filled) and without (open) avidin at 37 ^{o}C, showing the effects of biotin-avidin binding on relaxivity.

After gathering the results from the variable temperature relaxometry, the calculated water residence times of the Cbz derivatives **Gd-19** and **Gd-20** and the NMRD profiles of biotinylated derivatives **Gd-21** and **Gd-22**, we predicted that the relaxivity of the rotationally constrained **Gd-21 + avidin** might be limited by the water residence time while that of the **Gd-22 + avidin** might be dominated by the rotational correlation time. The long chain (LC) derivative of biotin was used which contains biotin and an aminohexanoic acid chain. The long chain ensures that biotin is allowed unimpeded access to avidin binding sites, such that the affinity of the biotin conjugate would be equal to that of biotin itself. Commerically available LC-biotin from Thermo Scientific (e.g., EZ-Link Sulfo –NHS-LC-Biotin) are designed for similar binding studies. The long chain also has the potential to introduce unwanted rotational freedom along the chain linking the chelate to the protein. The potential segmental motions may result in shorter overall rotational correlation times. To determine if further increases in the rotational correlation time increased the relaxivity, we conducted variable temperature relaxometry experiments on the **Gd-21 + avidin** and **Gd-21 + avidin**, Figure I.4.13.

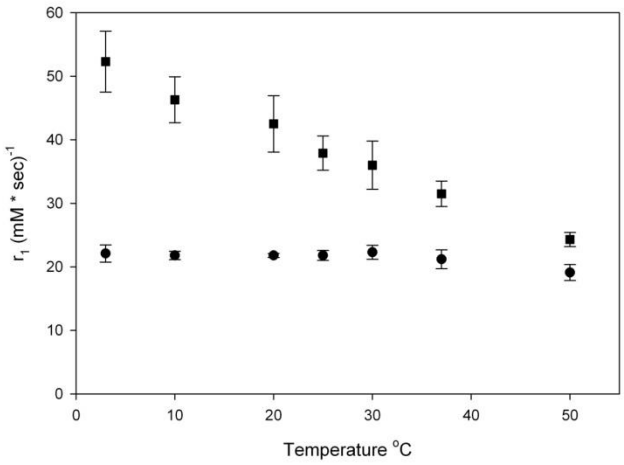

Figure I.4.13. Variable temperature relaxometry of **Gd-21** (filled circles) and **Gd-22** (filled squares) with avidin at 0.47 T. Note that for a given temperature, each **Gd-22** value is significantly different from the **Gd-21** value at $P < 0.001$. Among **Gd-21** values, the 50 °C value is significantly different ($P \leq 0.001$) from all others, and the 3 °C value is significantly different ($P \leq 0.001$) than all others except the 10 °C value. Other groups of values significantly different ($P \leq 0.001$): 37 °C and 3, 10, 20 °C; 30 °C and 3 and 10 °C; 25 °C and 3 and 10 °C.

At 20 MHz, the relaxivity of **Gd-21 + avidin** was not effected by decreasing the temperature (50 to 3 °C) and remained constant. At the same field strength, the relaxivity of **Gd-22 + avidin** almost doubled with decreasing temperature, Figure I.4.13. Analysis of the repeated measurements variance gave $P \leq 0.001$ and a power of the test with alpha equal to 0.050 : 1.000. To isolate the groups that differ from one another, we used the Holm-Sidak method for pairwise multiple comparison. At all temperatures, except 50 °C, the **Gd-22 + avidin** relaxivities significantly differed from the relaxivities at all temperatures of **Gd-21** with $P \leq 0.001$. At 50 °C, the **Gd-22 + avidin** value was not significantly different from the relaxivities of **Gd-21+ avidin** at 3, 10, 20, 25, 30, 37, and 50 °C. The **Gd-21+ avidin** did not exhibit significant differences in relaxivities at any temperature. The relaxivities of **Gd-22 + avidin** at all temperatures differed significantly,

$P \leq 0.001$, except the relaxivities at 3 and 10; 10 and 20; 20 and 25; 20 and 30; 25 and 30; 25 and 37; 30 and 37 ^{o}C.

The data collected that the water residence time limits the relaxivity of rotationally constrained DOTA complexes (e.g., **Gd-21 + avidin**) is consistent with other reports. It has been shown that the water residence time limits relaxivity of a generation 6 ammonia core polyamidoamine dendrimer with an isothiocyanatobenzyl-DOTA derivative having a linker attached to a ring carbon.[7] Relaxivity increases from 25 to 32 $(s * mM)^{-1}$ when the temperature is increased from 5 to 35 ^{o}C. This increase in relaxivity related to decreasing water residence time (resulted from increasing the temperature) that counteracts and outweighs the decrease in relaxivity related to decreasing the rotational correlation time (resulted from increasing the temperature). When the relaxivity increases with increasing temperature, the water residence time becomes dominant. Bryant et al.[45] reported using the same chelate attached to ethylene diamine core polyamindoamine dendrimers that relaxivity levels off near generation 7. At 20 MHz and 23 ^{o}C, the relaxivities for generations 5, 7, 9, and 10 are 30, 35, 36, and 36 $(s * mM)^{-1}$, respectively. These values are similar to relaxivity obtained for the generation 6 ammonia core by our collaborators.[7] Others reported dendrimers that also have similar relaxivities.[14] Tweedle's group used viscous solution to create rotationally constrained Gd(III)-DOTA systems which reduced the rotational correlation time and resulted in relaxivity values of 35 $(s * mM)^{-1}$. Using the experimental values for the water residence time, the theoretical values caluclated with Solomon-Bloembergen-Morgan theory coincided well with the experimental values. The theoretical data suggested that the water

residence time would limit the relaxivity of rotationally constrained Gd(III)-DOTA systems. Our results show that water residence time limits the relaxivity of the Gd(III)-DOTA derivative (**Gd-21**), but the greatest relaxivity observed for **Gd-21 + avidin** is significantly lower 22 $(s * mM)^{-1}$ compared to those reported by other systems[45] [30 to 36 $(s * mM)^{-1}$], Table I.4.2. The lower relaxivity could be due to the longer water residence time possibly caused by the binding of the chelate with avidin. Analogous to other biotin-avidin systems (Table I.4.2), the **Gd-21 + avidin** relaxivity is comparable.

Some reported relaxivity values for highly constrained DOTMA derivatives in viscous solution [58 $(s * mM)^{-1}$][7] are higher than the relaxivity of **Gd-22 + avidin** [32 ± 2 $(s * mM)^{-1}$ at 37 ^{o}C]. Nonetheless, our data at a lower temperature (3 ^{o}C) gave a relaxivity of 52 ± 5 $(s * mM)^{-1}$, which shows the effects of increased rotational correlation time. The lower relaxivity of **Gd-22 + avidin** could be due to the segmental motions from the long chain version of the biotin. Perhaps using a shorter biotin linker or direct linkage to biotin might give higher relaxivities. The relaxivity data for the rotationally constrained **Gd-22 + avidin** are consistent with those reported in literature. The long chain Gd(III)-DOTA derivative (**Gd-21**) has a significantly lower relaxivity due to the lack of steric effects from the CH_3 groups on the ligand arms. The CH_3 groups on the ligand arms of **Gd-22** could be interfering with the water residence time and/or reducing the number of inner sphere water molecules which would not emerge in the case of **Gd-21** and avidin.

Table I.4.2 . Comparison of relaxivities (r_1) of selected compounds similar to those in this work.

Compound	r_1 (mM^{-1} s^{-1})	Tesla	Temp (C°)	Ref.
Gd(III)-DTPA	4.2	0.47	35	[5]
Gd(III)-DOTA	3.4	0.47	37	[46]
Gd(III)-DOTMA	4.2	0.47	40	[47]
G = 5 PAMAM (Gd-DOTA)	30	0.59	35	[7]
G= 6 PAMAM (Gd-DOTA)	31	0.59	35	[7]
G = 7 PAMAM (Gd-DOTA)	34	0.59	25	[7]
G=10 PAMAM (Gd-DOTA)	36	0.47	23	[7]
Biotinylated Gd-DTPA	6.1 ± 0.2	1.5	20	[5]
(Biotinylated) **Gd-21**	8.7	0.47	37	this work
(Biotinylated) **Gd-22**	8.7	0.47	37	this work
Avidin- biotinylated GdL1/Av (DOTA)	18.1	0.47	25	[48]
Avidin- biotinylated GdL2/Av (DOTA)	17.4	0.47	25	[48]
Avidin-biotinylated Gd-DTPA	17.5 ± 0.3	1.5	20	[5]
Avidin-biotinylated **Gd-21**	22	0.47	20	this work
Avidin-biotinylated **Gd-22**	45	0.47	20	this work

Similarly to the –OH groups on polyethylene glycol, avidin is a highly glycosylated protein and the hydroxyl groups may reduce relaxivity.[49,50] The NMRD profile fitting let the water residence time float instead of fixing it to a value for Gd(III)-

DOTA-Cbz, measured by ^{17}O NMR giving a long water residence time relative to our measured DOTA derivative (**Gd-19**), 408 vs 101 ns, respectively. By letting the water residence time float during the NMRD fitting process, this value is about 10 times the value calculated for **Gd-22 + avidin** (45 ns). We cannot disregard using either model since both fitting methods, letting the water residence time float or fixing it to the values measure by ^{17}O NMR, give reasonable values. Letting the water residence time float provides similar rotational correlation times, and using fixed water residence times yields different correlation times. A change in correlation time could stem from protein-chelate interactions which is a second possibility that cannot be eliminated.[51,52] From the variable temperature NMRD data (Figure I.4.12), the constant relaxivity observed for binding of **Gd-21** to avidin supports the increase in water residence time to longer values. A decrease in the relaxivity associated with a decrease in temperature would be expected and was observed with a generation 6 ammonia core PAMAM dendrimer coated with a Gd(III)-DOTA surface.[7] It is unclear how to differentiate between changes in rotational correlation time or in water residence time associated with binding of the chelate to avidin. This underscores a major problem with multiparameter NMRD profile fits; commonly there are multiple solutions that give similar quality of fits. The most reasonable parameter values obtained are merely estimates and lack accuracy. Since fits begin with an assigned value for the distance between the water proton and metal ion, large errors can arise in the values of the parameters.[53] Typically proton-metal distances are taken from X-ray crystallographic data, and it is known that solution structures and crystal structures can diverge significantly. For water proton-metal distances, a relatively small error can cause significantly larger deviation in the five fitted parameters due to the

inverse 6^{th} power relationship, $1/r^6$, of the water proton-metal distance. Even though the quantitative accuracy of the fits is always questionable, qualitative conclusions can be extrapolated from the NMRD profile fits, specifically when comparing analogous chelates.

Four novel bifunctional chelates (**12-**, **17-**, **13-**, and **18-NaOTf**) are presented for future studies of their lanthanide complexes for imaging. These bifunctional octadentate chelates were designed to coordinate Gd(III) while sustaining and enhancing contrast properties and accessibilty for further chemistry at the unique azide/amine moiety. Data collected on these complexes show that the constrained derivative of **Gd-22** had higher relaxivity than constrained derivative of **Gd-21** caused by the a larger TSAP/SAP ratio. Furthermore, the relaxivity of **Gd-22** is dominated by the rotational correlation time whereas **Gd-21** is affected by the water residence time.

I.4.4. Conclusions

Concise and efficient syntheses of new bifunctional chelates are reported here, notably including those containing four stereogenic centers derived from a chiral pool. The conformations and MRI relevant properties were obtained using Gd(III) and Eu(III) complexation. A notable finding for the novel bifunctional materials, comparing the DOTA- and DOTMA- derived chelates, is that the Gd(III)-DOTMA complex has a shorter water residence time, and when rotationally constrained, it has essentially 40% higher relaxivity at 37 ^{o}C than the constrained conventional Gd(III)-DOTA chelates. The higher relaxivity has the potential to enhance the sensitivity of molecular imaging and/ or reduce the dose of targeted agents. The azide functionalized chelates, N_3-DOTA

(deprotected **12**) and N_3-DOTMA (deprotected **17**), are applicable with click chemistry for future couplng to target molecules.[17] In summary, we show that macromolecular DOTMA imaging agents indeed have higher relaxivity than DOTA derivatives, due to the ability to covalently couple the new DOTMA derivatives without compromising water exchange rates. These new bifunctional compounds are foreseen to be practical because of the ability to couple the ideal DOTMA derivatives using either azide or amine functionality, without disturbing favorable relaxivity properties.

I.4.5. Acknowledgements

Support of the NIH (R01 DK078500-01) is acknowledged. At SDSU, we thank Dr. LeRoy Lafferty for his assistance with NMR experiments. L.V.E. thanks the ARC Programs of the French Community of Belgium, the FNRS (Fonds National de la Recherche Scientifique), the support and sponsorship concerted by COST Actions (D38 and TD1004).

I.4.6. References

[1] Wiener, E.; Tomalia, D.; Lauterbur, P. C. *Proc. Soc. Magn. Reson. Med.* **1990**, 1106.

[2] Wiener, E. C.; Brechbiel, M. W.; Brothers, H.; Magin, R. L.; Gansow, O. A.; Tomalia, D. A.; Lauterbur, P. C. *Magn. Reson. Med.* **1994**, *31*, 1.

[3] Lauffer, R. B. *Chem. Rev. (Washington, D. C.)* **1987**, *87*, 901.

[4] Lauffer, R. B.; Brady, T. J.; Brown, R. D., 3rd; Baglin, C.; Koenig, S. H. *Magn. Reson. Med.* **1986**, *3*, 541.

[5] Aime, S.; Botta, M.; Fasano; Paoletti, S.; Anelli, P. L.; Uggeri, F.; Virtuani, M. *Inorg. Chem.* **1994**, *33*, 4707.

[6] González, G.; Powell, D. H.; Tissières, V.; Merbach, A. *J. Phys. Chem.* **1994**, *98*, 53.

[7] Wiener, E.; Narayanan, V. *Adv. Dendritic Macromol.* **2002**, *5*, 129.

[8] Micskei, K.; Helm, L.; Brucher, E.; Merbach, A. *Inorg. Chem.* **1993**, *32*, 3844.

[9] Aime, S.; Gianolio, E.; Longo, D.; Pagliarin, R.; Lovazzano, C.; Sisti, M. *ChemBioChem.* **2005**, *6*, 818.

[10] Schuehle, D. T.; Polasek, M.; Lukes, I.; Chauvin, T.; Tóth, É.; Schatz, J.; Hanefeld, U.; Stuart, M. C. A.; Peters, J. A. *Dalton Trans.* **2010**, *39*, 185.

[11] Tei, L.; Gugliotta, G.; Baranyai, Z.; Botta, M. *Dalton Trans.* **2009**, *44*, 9712.

[12] Dumas, S.; Jacques, V.; Sun, W.-C.; Troughton, J. S.; Welch, J. T.; Chasse, J. M.; Schmitt-Wilich, H.; Caravan, P. *Invest. Radiol.* **2010**, *45*, 600.

[13] Brittain, H.; Desreux, J. *Inorg. Chem.* **1984**, *23*, 4459.

[14] Shukla, R. B.; Kumar, K.; Weber, R.; Zhang, X.; Tweedle, M. *Acta Radiol. Suppl.* **1997**, *412*, 121.

[15] Dunand, F. A.; Dickins, R. S.; Parker, D.; Merbach, A. E. *Chem. Eur. J.* **2001**, *7*, 5160.

[16] Aime, S.; Botta, M.; Garda, Z.; Kucera, B. E.; Tircso, G.; Young, V. G.; Woods, M. *Inorg. Chem.* **2011**, *50*, 7955.

[17] Mastarone, D. J.; Harrison, V. S. R.; Eckermann, A. L.; Parigi, G.; Luchinat, C.; Meade, T. J. *J. Am. Chem. Soc.* **2011**, *133*, 5329.

[18] Effenberger, F.; Burkard, U.; Willfahrt, J. *Liebigs Ann. Chem.* **1986**, 314.

[19] Dischino, D. D.; Delaney, E. J.; Emswiler, J. E.; Gaughan, G. T.; Prasad, J. S.; Srivastava, S. K.; Tweedle, M. F. *Inorg. Chem.* **1991**, *30*, 1265.

[20] Platzek, J.; Blaszkiewicz, P.; Gries, H.; Luger, P.; Michl, G.; Müller-Fahrnow, A.; Radüchel, B.; Sülzle, D. *Inorg. Chem.* **1997**, *36*, 6086.

[21] Moore, D. A. PCT Int. Appl. WO 2007106546 A2, 2007.

[22] Xu, J.; Sun, G.; Rossin, R.; Hagooly, A.; Li, Z.; Fukukawa, K.-i.; Messmore, B. W.; Moore, D. A.; Welch, M. J.; Hawker, C. J.; Wooley, K. L. *Macromolecules (Washington, DC)* **2007**, *40*, 2971.

[23] Faulkner, S.& Pope, S. J. A. *J. Am. Chem. Soc.* **2003**, *125*, 10526.

[24] Pershagen, E.; Nordholm, J.; Borbas, K. E. *J. Am. Chem. Soc.* **2012**, *134*, 9832.

[25] Laurent, S.; Vander Elst, L.; Muller, R. *Contrast Media Mol. Imaging* **2006**, *1*, 128.

[26] Vander Elst, L.; Maton, F.; Laurent, S.; Seghi, F.; Chapelle, F.; Muller, R. N. *Magn. Reson. Med.* **1997**, *38*, 604.

[27] Muller, R.; Raduchel, B.; Laurent, S.; Platzek, J.; Pierart, C.; Mareski, P.; Vander Elst, L. *Eur. J. Inorg. Chem.* **1999**, 1949.

[28] Laurent, S.; Vander Elst, L.; Houze, S.; Guerit, N.; Muller, R. N. *Helv. Chim. Acta* **2000**, *83*, 394.

[29] Huang, Z.; Sengar, R. S.; Nigam, A.; Abadjian, M.-C.; Potter, D. M.; Grotjahn, D. B.; Wiener, E. C. *Invest. Radiol.* **2010**, *45*, 641.

[30] Suchy, M.; Hudson, R. H. E. *Eur. J. Org. Chem.* **2008**, 4847.

[31] Hafner, K.; Vöpel, K. H.; Ploss, G.; König, C. *Org. Synth., Coll. Vol. 5* **1973**, 431.

[32] Abramson, S.; Berkovich-Berger, D.; Dagan, S.; Goldberg, I.; Golender, L.; Grabarnik, M. N.; Lemcoff, G.; Weinman, S.; Fuchs, B. *Eur. J. Org. Chem.* **2007**, *12*, 1957.

[33] Feenstra, R. W.; Stokkingreef, E. H. M.; Nivard, R. J. F.; Ottenheijm., H. C. J. *Tetrahedron* **1988**, *44*, 5583.

[34] Knorr, R.; Löw, P.; Hassel, P.; Bronberger, H. *J. Org. Chem.* **1984**, *49*, 1288.

[35] Alder, R. W.; Blake, M. E.; Bufali, S.; Butts, C. P.; Orpen, A. G.; Schütz, J.; Williams, S. J. *J. Chem. Soc., Perkin Trans. 1* **2001**, 1586.

[36] (a) Tsukube, H.; Mizutani, Y.; Shinoda, S.; Okazaki, T.; Tadokoro, M.; Hori, K. *Inorg. Chem.* **1999**, *38*, 3506; (b) Kumar, K.; Chang, C. A.; Francesconi, L. C.; Dischino, D. D.; Malley, M. F.; Gougoutas, J. Z.; Tweedle, M. F. *Inorg. Chem.* **1994**, *33*, 3567; (c) Dickins, R. S.; Howard, J. A. K.; Moloney, J. M.; Parker, D.; Peacock, R. D.; Siligardi, G. *Chem. Commun. (Cambridge)* **1997**, 1747; (d) Dickens, R. S.; Howard, J. A. K.; Maupin, C. L.; Moloney, J. M.; Parker, D.; Peacock, R. D.; Riehl, J. P.; Siligardi, G. *New J. Chem.* **1998**, *22*, 891; (e) Shinoda, S.; Nishimura, T.; Tadokoro, M.; Tsukube, H. *J. Org. Chem.* **2001**, *66*, 6104; (f) Govenlock, L. J.; Howard, J. A. K.; Moloney, J. M.; Parker, D.; Peacock, R. D.; Siligardi, G. *J. Chem. Soc., Perkin Trans. 2* **1999**, 2415; (g) Gunnlaugsson, T.; Brougham, D. F.; Fanning, A.-M.; Nieuwenhuyzen, M.; O'Brien, J. E.; Romain., V. *Org. Lett.* **2004**, *6*, 4805; (h) Tsukube, H.; Mizutani, Y.; Shinoda, S.; Tadokoro, M.; Hori, K. *Tetra. Lett.* **1997**, *38*, 5021.

[37] Renn, O. & Meares, C. F. *Bioconjugate Chem.* **1992**, *3*, 563.

[38] Woods, M.; Kovacs, Z.; Zhang, S.; Sherry, A. D. *Angew. Chem., Int. Ed.* **2003**, *42*, 5889.

[39] Woods, M.; Botta, M.; Avedano, S.; Wang, J.; Sherry, A. D. *Dalton Trans.* **2005**, 3829.

[40] (a) Tircso, G.; Webber, B. C.; Kucera, B. E.; Young, V. G.; Woods, M. *Inorg. Chem.* **2011**, *50*, 7966; (b) Webber, B.; Woods, M. *Inorg. Chem.* **2012**, *51*, 8576.

[41] Dunand, Frank A.; Borel, Alain; Merbach, Andre E. *JACS* **2002**, *124*(4), 710.

[42] Koenig, S. H.; Brown, R. D., 3rd *Magn. Reson. Med.* **1984**, *1*, 478.

[43] Langereis, S.; Kooistra, H.-A. T.; van Genderen, M. H.; Meijer, E. W. *Org. Biomol. Chem.* **2004**, *2*, 1271.

[44] Geninatti Crich, S.; Barge, A.; Battistini, E.; Cabella, C.; Coluccia, S.; Longo, D.; Mainero, V.; Tarone, G.; Aime, S. *J. Biol. Inorg. Chem.* **2005**, *10*, 78.

[45] Bryant, L. H., Jr.; Brechbiel, M. W.; Wu, C.; Bulte, J. W.; Herynek, V.; Frank, J. A. *J. Magn. Reson. Imaging* **1999**, *9*, 348.

[46] Meyer, D.; Schaefer, M.; Doucet, D. *Invest. Radiol. (Suppl. 1)* **1992**, *25*, S53.

[47] Ranganathan, R. S.; Raju, N.; Fan, H.; Zhang, X.; Tweedle, M. F.; Desreux, J. F.; Jacques, V. *Inorg. Chem.* **2002**, *41*, 6856.

[48] Tei, L.; Barge, A.; Geninatti Crich, S.; Pagliarin, R.; Negri, V.; Ramella, D.; Cravotto, G.; Aime, S. *Chem.Eur. J.* **2010**, *16*, 8080.

[49] Manjappa, A.S.; Chaudhari, K.R.; Venkataraju, M. P. et al. *J. Controlled Release* **2011**, *150*, 2.

[50] Hermanson, G. *Bioconjugate Techniques*, (**2008**) (2nd ed). Academic Press; London.

[51] Aime, S.; Barge, A.; Botta, M.; Terreno, E. *Met. Ions Biol. Syst.* **2003**, *40*, 643.

[52] Aime, S.; Gianolio, E.; Terreno, E.; Giovenzana, G. B.; Pagliarin, R.; Sisti, M.; Palmisano, G.; Botta, M.; Lowe, M. P.; Parker, D. *J. Biol. Inorg. Chem.* **2000**, *5*, 488.

[53] Avedano, S.; Botta, M.; Haigh, J. S.; Longo, D. L.; Woods, M. *Inorg. Chem.* **2013**, *52* , 8436.

I.5. Bimodal Imaging: MRI and Fluorescence Imaging Agents

I.5.1. Introduction

Advances in MRI contrast agents (CAs) include attaching them to other imaging agents to make bimodal imaging agents. Combining MRI CAs and fluorophores into one molecule aim to take advantage of the high resolution of MRI and the high sensitivity of fluorescence,[1] Table I.5.1. MRI has already been established as an indispensable technique to diagnosis illness and diseases. Fluorescence imaging has also been shown to be a powerful technique for in vitro and in vivo imaging because of its exceptional sensitivity and selectivity.[2] Near-infrared (NIR) fluorescence agents are more common considering that the excitation/emission of NIR (650- 900 nm) can penetrate 2-3 mm in tissue without being absorbed by the blood.[3] MRI/fluorescent bimodal imaging agents have been shown to elucidate cellular mechanisms such as cellular tracking,[4] enzyme degradation,[5] and cellular uptake.[6]

Table I.5.1. Key features of MRI and fluorescence techniques.

Technique	Resolution	Time (image acquisition)	Target
MRI	100-100 µM	Minutes to hours	Anatomical, physiological, molecular
Fluorescence	2-3 mm	Seconds to minutes	Physiological, molecular

Table adapted from ref.[7]

The project summarized in this section aims to develop robust syntheses of bimodal imaging agents for cellular imaging agents and potentially medicinal applications. As discussed in previous sections, the Gd(III)-based MRI contrast agent DOTA is commonly used in the clinical setting. Also discussed was the derivative of DOTMA, that has been shown to enhance MRI signal because of shorter water proton

relaxation times, but because of the need for four identical stereogenic centers DOTMA is harder to make. The bimodal imaging agents in this project are comprised of a DOTA or DOTMA derivative that will coordinate gadolinium tightly and contain an azide to click[8] to our collaborators' fluorescent dye, derivatives of malachite green.

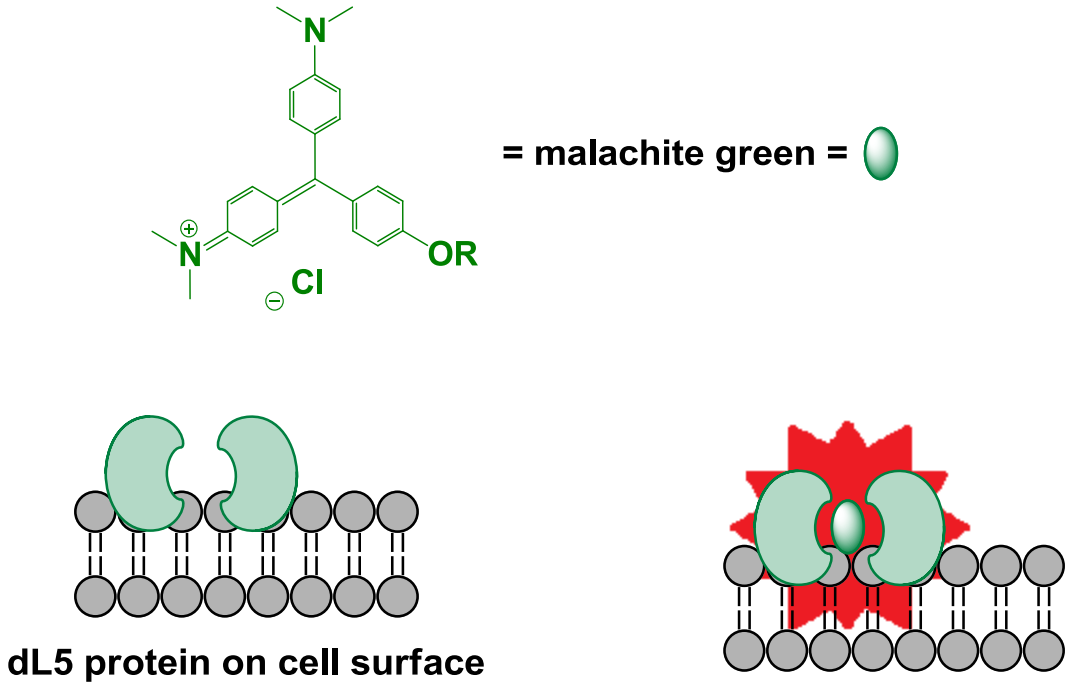

Figure I.5.1. Derivatives of the fluorescent dye, malachite green, interacting with protein dL5. On binding, fluorescence is possible (excitation max. ~634 nm; emission max. ~667 nm).

Our collaborators at Carngie Mellon Unversity (CMU), Dr. Alan Waggoner, Dr. Marcel Bruchez and Dr. Brigitte Schmidt, have a unique fluorescent dye with exceptional properties. Their malachite green dye derivative fluoresces upon binding to a fluorogen activation protein (FAP), dL5,[9] Figure I.5.1. When the malachite green (MG) dye is unbound to dL5 protein, it is essentially non-fluorescent. Upon binding to dL5 protein, the MG fluoresces with a notably high extinction coefficient (ε = 110,000 M^{-1} cm^{-1}).[10]

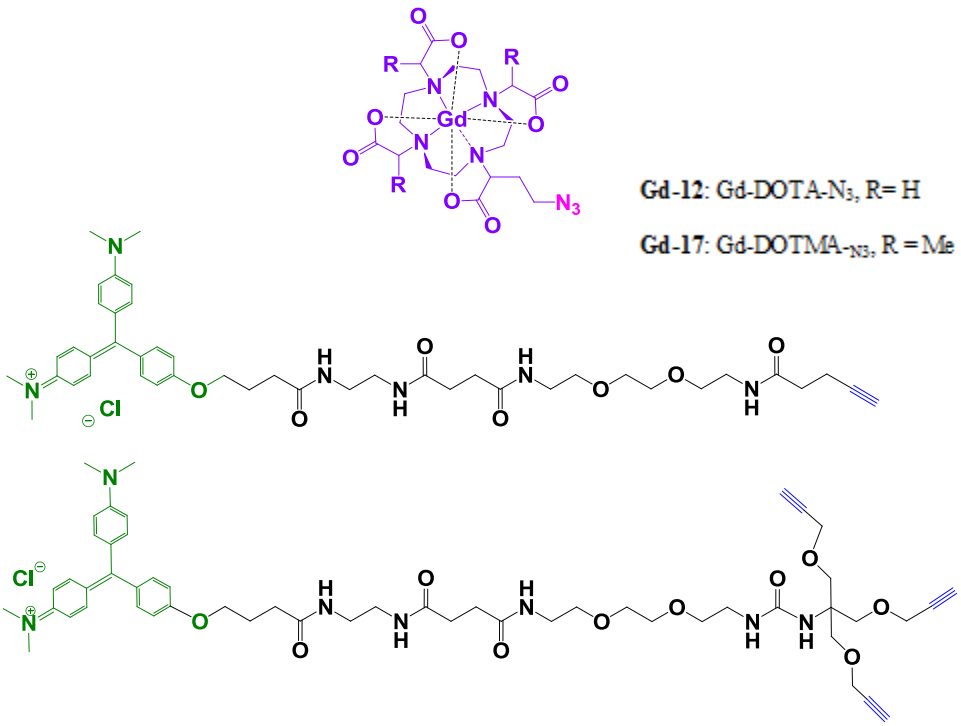

Figure I.5.2. Fluorescent malachite green dyes (MG-2p) for clicking to **Gd-12** and **Gd-17**.

Brigitte had a set of malachite green dyes with a linker (2p) bearing either one or three terminal alkynes, Figure I.5.2. The linker has been shown by their lab (unpublished data) to not hinder binding to the dL5 protein and even improve the dye's photostability. The 2p linker also aids aqueous solubility, and the lack of steric hindrance around dthe alkyne(s) should facilitate click reactions. We aimed to compare not only the DOTA and DOTMA MR imaging agents (**Gd-12** and **Gd-17**) with malachite green dye (MG-2p) but also different dye:Gd(III) imaging agent ratios (1:1 and 1:3).

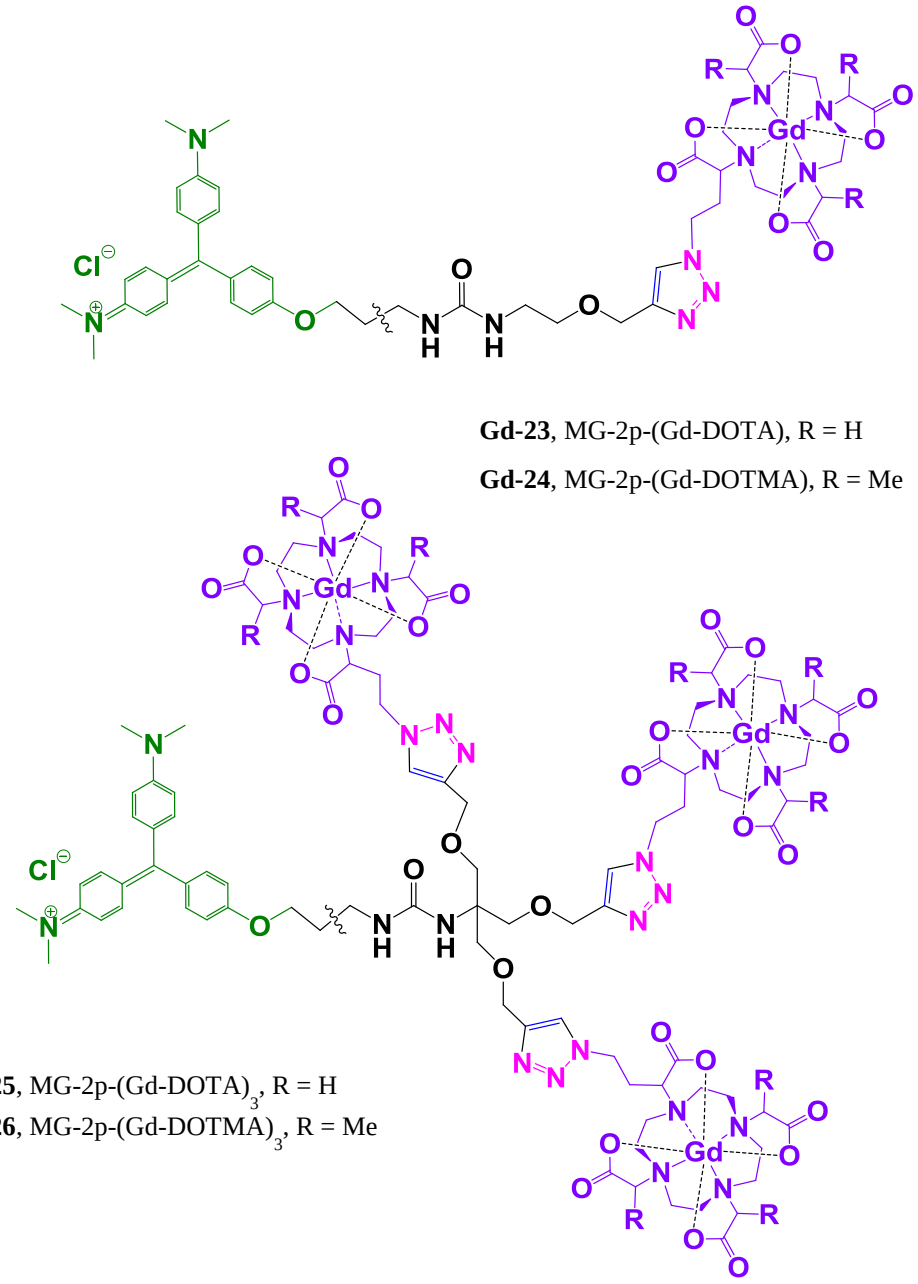

Gd-23, MG-2p-(Gd-DOTA), R = H

Gd-24, MG-2p-(Gd-DOTMA), R = Me

Gd-25, MG-2p-(Gd-DOTA)$_3$, R = H

Gd-26, MG-2p-(Gd-DOTMA)$_3$, R = Me

Figure I.5.3. Four new constructs of bimodal MRI and fluorescence imaging, (**Gd-23**, **Gd-24**, **Gd-25** and **Gd-26**).

The bifunctional MRI contrast agents containing an azide moiety (**Gd-12** and **Gd-17**) were made as discussed in sections I.3. and I.4. The four constructs from those MRI contrast agents (Gd complexed **23, 24, 25** and **26**) were synthesized at CMU during my productive visit in November 2013, Figure I.5.3. A major challenge in developing

bimodal MRI/fluorescent imaging agents is finding the balance between the relatively low detection sensitivity (mM) of the CA and the single molecule detection capability of fluorescence imaging. In March 2014, testing and imaging of these four constructs (Gd complexed **23, 24, 25** and **26**) were performed to compare and evaluate these constructs as bimodal imaging agents for fluorescence and MRI diagnostic imaging.

I.5.2. Experimental section

*Synthesis of **Gd-12** and **Gd-17** are described in detail in sections I.3 and I.4.*

*General method for the click reacton between **Gd-12** and **Gd-17** with alkyne **MG-2p** dyes to make **Gd-23**, **Gd-24**, **Gd-25** and **Gd-26** (experiments done with Dr. Brigitte Schimdt, CMU):*

In an open flask, MG-2p-(alkyne)$_3$, (0.021 mmol, 1.0 equiv per alkyne) was dissolved in a mixture of water (1 mL) and MeOH or EtOH (1 mL) [MeOH was used for reactions with **Gd-12** and EtOH was used for reactions with **Gd-17**]. Gd(III)-based MRI agent azide **Gd-12** or **Gd-17** (0.090 mmol, 1.5 equiv per alkyne) was dissolved in water (1 mL) and added to the solution of **MG-2p** alkyne. A solution of $CuSO_4$ (0.19 mmol, 3.1 equiv with respect to MG-2p-alkyne) and water (250 µL) was added to the reaction mixture. Argon gas was bubbled into the reaction mixture for 10 minutes. Sodium ascorbate (0.21 mmol, 3.2 equiv with respect to MG-2p-alkyne) was then added with a flow of argon over flask opening. The reaction flask was then put in a 60 °C oil bath and stirred overnight. The reaction was monitored by TLC (1/1 MeOH/$CHCl_3$) and ESI-MS of aliquots. Upon reaction completion, the reaction was passed through a Bio-Rad P-2

column (10% EtOH in water) and further purified by reverse phase chromatography (20-50% EtOH in water). All samples were sent for mass spectrometry analysis.

dL5 binding assay

General method binding assay of constructs (**Gd-23**, **Gd-24**, **Gd-26**, & **MG-2p**) with dL5 protein (experiments done with Yi Wang, CMU):

Samples were prepared in triplicates. Samples were prepared in Eppendorf tubes at a ratio of 1.0 µM construct or MG-2p (control) to 10 µM dL5 protein using PBS+ (Thermo Scientific Prod# 8409400, Pluronic F-127) for a final volume of 250 µL. Samples were put on a shaker at room temperature for 3 hours. Samples were transferred to a plate (ThermoFisher Scientific – Nunclon 96 flat bottom black polystyrol plate). The excitation wavelength started at 400 nm and stepwise increase by 2 nm to 670 nm. Emission wavelength: 700 nm.

T_1 and T_2 measurements

Proton longitudinal (T_1) and transversal (T_2) relaxation time measurements were performed on a Bruker Minispec mq20 NMR analyzer. A minimum of 16 data points were taken for T_1 and 200 data points for T_2 per measurement for each sample. Three separate concentrations of each sample (total volume 200 µL) in 50 mM HEPES buffer were prepared and measured at constant temperature (37 °C).

Relaxivity measurements

Relaxivity values (r_1 or r_2) were calculated from the T_1 or T_2 recorded values, respectively. The concentrations of sample with respect to Gd(III) were plotted versus $1/T_1$ or $1/T_2$. The slope of the linear plot gave the relaxivity.

MR Imaging

Samples were prepared in phosphate buffered saline and imaged on a 7 T and 4.7 T Bruker BioSpin MRI GmbH. Samples' temperatures were maintained at 37°C using an automated forced warm air circulator. Image acquisition and processing were achieved by using ParaVision 4.0 software (Bruker Biospin).

I.5.3. Results and discussion

At CMU, the four derivatives (Gd complexed **23, 24, 25** and **26**) were made from **Gd-12** or **Gd-17** with **MG-2p** linker bearing either one or three terminal alkynes. The click reaction was monitored by TLC and MS. Purification of the desired product was straightforward but tedious since two purification columns were involved.

Three of the four constructs (**Gd-23**, **Gd-24**, and **Gd-26**) were assayed against the dL5 protein at different concentration in triplicates to find accurate binding on and off constants (**Gd-25** had not been made at this point). This study was to determine of the presence of either one or three Gd(III)-based macrocyclic chelates (DOTA and DOTMA versions) hindered MG-2p binding to dL5 protein by measuring the constructs' K_d (dissociation constant), absorption and emission spectrum, Figure I.5.4. The controls consisted of the constructs and MG-2p without dL5 protein. The K_d measurements along with the spectroscopic data showed that the constructs were just as good as the control MG-2p. There is a blue shift in the emission spectra that could indicate slightly stronger binding to dL5 protein compared to MG-2p.

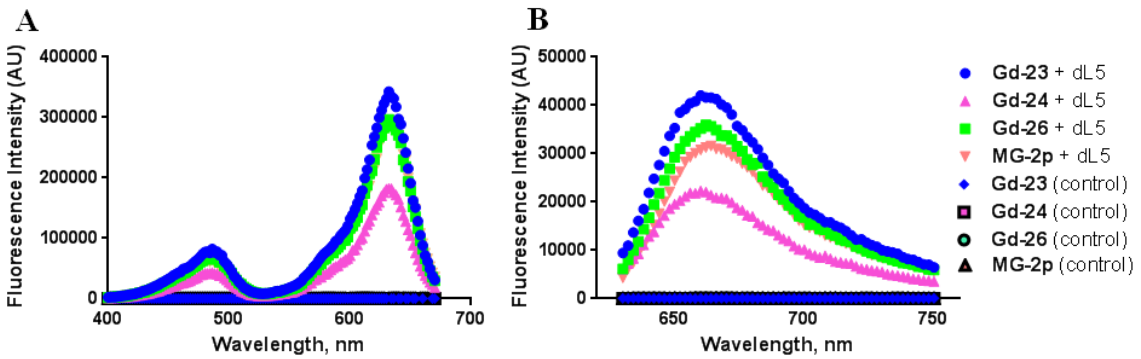

Figure I.5.4. dL5 binding assay. A: absorption spectra; B: emission spectra. Controls had no dL5 protein present giving no absorption or emission which was expected.

We have established that the presence of either one or three Gd(III)-based macrocyclic chelates (DOTA and DOTMA versions) does not affect the binding of MG-2p to dL5 protein. Measurements were taken with a Minispec 20 MHz (0.47 T) to compare the relaxivities of all four constructs (per Gd), Table I.5.2. It was found that there was not a significant different in relaxivity between having one or three Gd(III) chelates in both the DOTA (entry 3 & 4) and DOTMA (entry 5 & 6) case. The difference in relaxivities is seen when the constructs are made bigger (slower tumbling in solution) by binding to dL5 protein (entry 7 & 8). The increase in relaxivity for the DOTA version 7.6 and 9.0 mM^{-1} s^{-1} per Gd (entry 4 & 7) is comparable to the DOTMA version 9.5 and 12.6 mM^{-1} s^{-1} per Gd (entry 6 & 8).

Table I.5.2. Relaxivity measurements of constructs at different field strengths.

Entry	Compound	r_1 ($mM^{-1} s^{-1}$) per complex	r_1 ($mM^{-1} s^{-1}$) per Gd
1	**Gd(III)-DOTA** [a]	-	3.4
2	**Gd(III)-DOTMA** [b]	-	4.2
3	**Gd-23** [c]	7.4	7.4
4	**Gd-24** [c]	22.8	7.6 ± 0.2
5	**Gd-25** [c]	-	9.5
6	**Gd-26** [c]	28.7	9.5
7	**Gd-24 + dL5** [d]	27.1	9.0
8	**Gd-26 + dL5** [d]	38.0	12.6
9	**Gd-24 + dL5** [e]	13.8	4.6
10	**Gd-26 + dL5** [e]	22.2	7.4
11	**Gd-24 + dL5** [f]	8.0	2.6
12	**Gd-26 + dL5** [f]	16.1	5.4

a: 0.47 T (20 MHz) at 37 °C;[11] b: 0.47 T (20 MHz) at 40 °C; [12] c: Millipore water, 0.47 T (20 MHz) at 37 °C; d: PBS, 0.47 T (20 MHz) at 37 °C; e: PBS, 4.7 T (200 MHz) at 37 °C; f: PBS, 7.0 T (298 MHz) at 37 °C.

Relaxivity measurements were also obtained at higher field strengths 200 MHz (4.7 T) and 298 MHz (7.0 T), Table I.5.2. Similar differences were seen in relaxivities between the **Gd-24** and **Gd-26** with dL5 protein: 4.6 & 7.4 (entry 9 & 10) and 2.6 & 5.4 (entry 11 & 12). It is interesting to note that although relaxivity decreases with increasing field strength, the DOTMA version, **Gd-26**, maintains higher relaxivities than the DOTA

version, **Gd-24**.

Imaging on the new constructs bound to dL5 protein was done at CMU's Pittsburgh NMR Center for Biomedical Research. Under the direction of Kevin Hitchens, samples were prepared for imaging on at 4.7 and 7.0 T instruments.

Table I.5. 3. Table of images obtained from **Gd-24** and **Gd-26** constructs bound to dL5 protein at 37 °C.

Construct	Conc. (μM)	4.7 T	7.0 T
Gd-26 + dL5	10	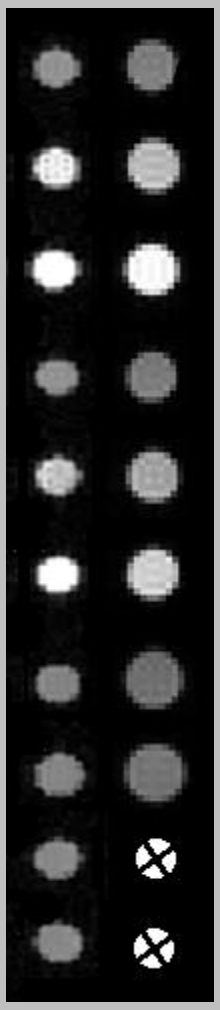	
Gd-26 + dL5	50		
Gd-26 + dL5	150		
Gd-24 + dL5	10		
Gd-24 + dL5	50		
Gd-24 + dL5	150		
MG-2p + dL5	5		
MG-2p + dL5	20		
dL5	20		
PBS	1x		

The relaxivities were calculated from T_1 relaxation times from images obtained, Table I.5.3. The relaxation rates were normalized to compare samples among each other, Figure I.5.5. In all cases, the DOTMA versions had a faster relaxation time compared to the DOTA versions. This study also revealed the detection limit of the constructs, 50 -10 µM per Gd.

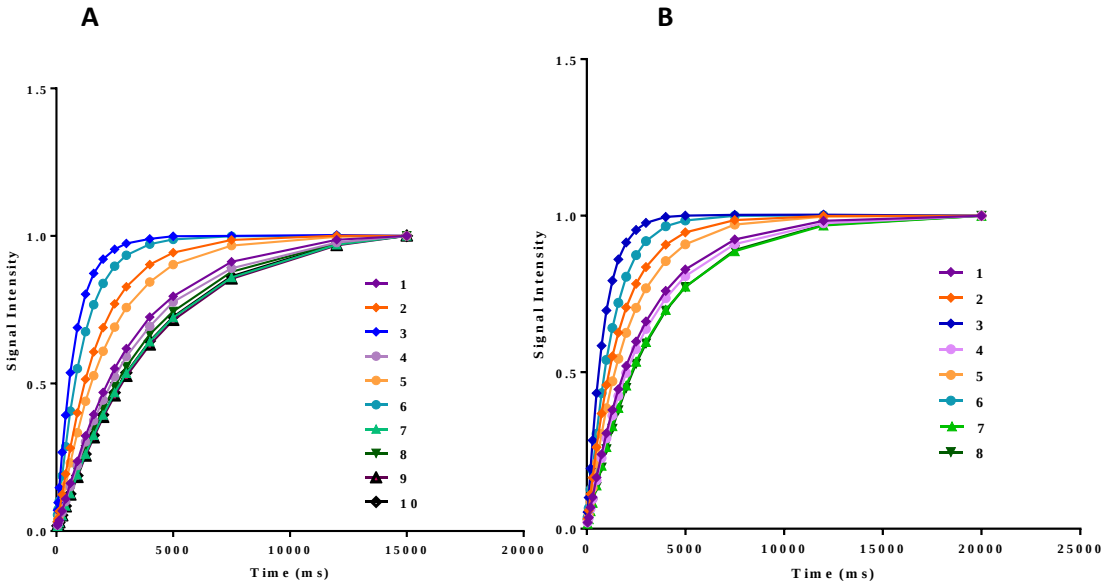

Figure I.5.5. Relaxation rates of constructs **Gd-24** and **Gd-26** at different field strengths. A) 4.7 T at 37 °C and B) 7.0 T at 37° C; 1: **Gd-26** 10 µM + dL5; 2: **Gd-26** 50 µM + dL5; 3: **Gd-26** 150 µM + dL5; 4: **Gd-24** 10 µM + dL5; 5: **Gd-24** 50 µM + dL5; 6: **Gd-24** 150 µM + dL5; 7: MG-2p 5 µM + dL5; 8: MG-2p 20 µM + dL5; 9: dL5 20 µL; 10: PBS 1x.

The fluorescence of the new constructs was investigated in live cells. The constructs were incubated with living Chinese hamster cells (CHO) and immediately imaged using CMU's specialized fluorometer stage and camera. The constructs fluorescence was poor compared with that of the control MG-2p, Figure I.5.6. The less than impressive fluorescence could be caused by accelerated dynamic quenching[13] by the negatively charged Gd(III) imaging agents. There was also evidence of cell death while imaging for all samples. The cell deaths might be due to the relatively large amount of

MG-2p dye (300 nM with respect to MG-2p) which has been known to cause cell death (private communication). Although the fluorescence properties of these new constructs are no as impressive as those of the control, the fact remains that they still fluoresce and could have bimodal applications.

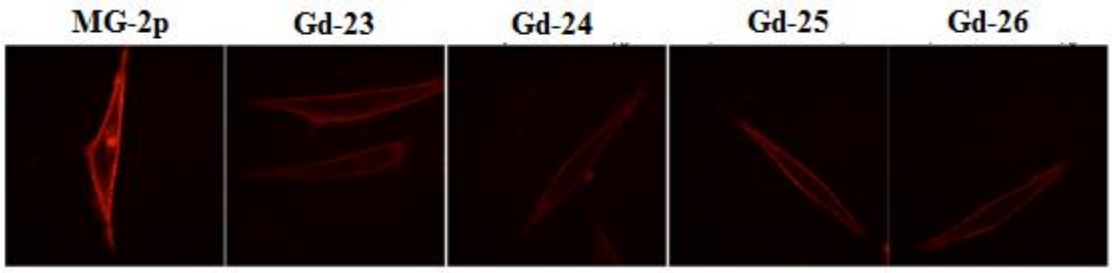

Figure I.5.6. Fluorescence imaging: 100nM on Chinese Hamster Ovary cells (CHO) 100nM of Gd = 300nM of MG on CHO.

The new construct **Gd-24** was taken forward for T_1 measurements with living yeast cells that express dL5 protein on the surface of the cell membrane. The T_1 and T_2 measurements were taken on the Minispec 0.47 T instrument at CMU. At first, the Minispec was being saturated by the cell density which led us to dilute the samples. However, diluting the samples greatly reduced the relaxation signal, so by trial and error, a concentration had to be found between sufficient dilution and enough construct. As expected, the relaxation times decreased with increasing concentration of constructs, Table I.5.4. The cells were quite green from the MG-2p part of the dye. The cells were purposely saturated with the construct in ensure binding to all dL5 proteins on the surface of the cells. The cells were washed by spinning down the cells, removing the supernatant and resuspending the cell pellet with PBS. Relaxation measurements were retaken revealing values that were similar to background relaxation times (T_2 values not shown), Table I.5.3.

It appeared that the construct did not influence the relaxation times. To further investigate this phenomenon, relaxation measurements were taken of the cells with just MG-2p (no Gd(III) imaging agent), Table I.5.5. The T_1 relaxation times decreased (T_2 also decreased, not shown) with increasing MG-2p dye (20 to 100 μM). It can be concluded that the cells contribute to the relaxation times, which is known.[14] The data also suggested that MG-2p dye also contributed to the relaxation times, but it was unclear by how much.

Table I.5.4. T_1 measurements of yeast cells on Minispec, 0.47 T.

	100μM per Gd or 33.3μM MG-2p dye	**50μM per Gd or 16.7μM MG-2p dye**	**20μM per Gd or 6.67μM MG-2p dye**
Total volume 200 μL (PBS)	94μL cells with dL5	94μL cells with dL5	94μL cells with dL5
T_1 37°C (ms)	580 ± 30	790 ± 50	990 ± 70
Treatment	Wash	Wash	Wash
T_1 37°C (ms)	890 ± 70	920 ± 80	990 ± 90

The data collected at CMU indicated that the biomodal constructs synthesized might still have some optimization in respect to design. Further investigations into the contribution of MG-2p to relaxation times might be of interest for future applications of the MG-2p dye in MR imaging.

Table I.5.5. Unexpected T_1 contributions from cells on Minispec, 0.47 T.

Controls	**Cells without dL5**	**Cells with dL5**	**Cells with dL5 + MG-2p (no Gd)**		
Total volume 200 µL (PBS)	94µL cells	94µL cells	94µL cells	94µL cells	94µL cells
MG-2p dye	-	-	73 µL dye (100 µM)	36.4 µL dye (50 µM)	14.6 µL dye (20 µM)
Treatment			Not washed	Not washed	Not washed
T_1 37°C (ms)	1100 ± 100	1100 ± 100	550 ± 40	780 ± 50	1110 ± 90

I.5.4. Conclusion

I initiated the proposed project to combine our MRI contrast agent with our collaborators' fluorescence dye to perform key experiments that would lay the foundation for other experiments involving more specific cell types, such as cancerous cells and even animal models. We made four new bimodal MRI-fluorescence imaging agents that show improved relaxivities. Fluorescence imaging using these constructs does not appear promising. Because of the concentration need for MR imaging (10-50 µM) is too high for fluorescence imaging. These bimodal imaging could still by used a MRI CAs with MG-2p acting as a targeting molecule (pM affinity to dL5).

The significance of this project has far reaching implications in the field of imaging agents. The results obtained from this study will contribute not only to the syntheses of dual modality imaging agents but also to adding another effective imaging

tool in the diagnostic tool box for medicinal applications.

I.5.5. Acknowledgements

I would like to thank our collaborators at Carnegie Mellon University, Brigitte, Marcel Bruchez, Yi Wang, Alan Waggner, Erik Wiener. Kevin Hitchens. I thank Virgil Simplaceanu and Kevin Hitchens for their helpful advice and the Pittsburgh NMR Center for Biomedical Research.

I.5.6. References

[1] (a) Hüber, M. M.; Staubli, A. B.; Kustedjo, K.; Gray, M. H. B; Shih, J.; Fraser, S. E.; Jacobs, R. E.; Meade, T. J. *Bioconjugate Chem.* **1998,** *9,* 242; (b) Ta, R.; Suchy, M.; Tam, J. H. K.; Li, A. X.; Martinez-Santiesteban , F. S.; Scholl, T. J.; Robert H.E. Hudson, R. H. E.; Bartha, R. & Pasternak, S. *Contrast Media Mol. Imaging* **2013**, *8* 127.

[2] (a) Chen, X.; Conti, P.S.; Moats, R.A. *Cancer Res.* **2004**, *64*, 8009; (b) Kim, S.; Lim, Y.T.; Soltesz, E.G.; De Grand, A.M.; Lee, J.; Nakayama, A.; et al. *Nat. Biotechnol.* **2004**, *22*, 93.

[3] (a) Colak SB, van der Mark MB, Hooft GW, Hoogengraad JH, van der Linden EW, Kuijpers FA. *IEEE J, Sel, Top, Quantum Electron*, **1999**, *5*, 1143; (b) Weissleder R, Ntziachristos V. *Nat. Med.* **2003**, *9*, 123.

[4] Hüber, M. M.; Staubli, A. B.; Kustedjo, K.; Gray, M. H. B.; Shih, J.; Fraser, S. E.; Jacobs, R. E.; Meade, T. J. *Bioconjugate Chem.* **1998,** *9,* 242.

[5] Suchý, M.; Ta, R.; Li, A. X.; Wojciechowski, F.; Pasternak, S. H.; Bartha, R.; Hudson, R. H. E. *Org. Biomol. Chem.* **2010**, 8, 2560.

[6] Manning, H. C.; Goebel,T.; Thompson, R. C.; Price, R. R.; Lee, H.; Bornhop, D. J. *Bioconjugate Chem*. **2004,** *15*, 1488.

[7] Weissleder, R.; Pitter, M. *Nature*. **2008**, *452*, 580.

[8] Zhang, Y.-H.; Gao, Z.-X.; Zhong, C.-L.; Zhou, H.-B.; Chen, L.; Wu, W.-M.; Peng, X.-J. & Yao, Z.-J. *Tetrahedron* **2007**, *63*, 6813.

[9] Szent-Gyorgyi, C.; Stanfield, R. L.; Andreko, S.; Dempsey, A.; Ahmed, M.; Capek, S.; Waggoner, A. S.; Wilson, I. A.; Bruchez, M. P. *J. Mol. Biol*. **2013**, *425*, 4595; Szent-Gyorgyi, C.; Schmidt, B. A.; Creeger, Y.; Fisher, G. W.; Zakel, K. L.; Adler, S.;

Fitzpatrick, J. A. J.; Woolford, C. A.; Yan, Q.; Vasilev, K. V.; et al *Nat. Biotechn*. **2008**, *26*, 235.

[10] Yan, Q.; Schwartz, S. L.; Maji, S.; Huang, F.; Szent-Gyorgyi, C.; Lidke, D. S.; Lidke, K.A.; Bruchez, M. P. *Chem. Phys. Chem.* **2014**, 15, 687.

[11] Meyer, D.; Schaefer, M.; Doucet, D. *Invest. Radiol. (Suppl. 1)* **1992**, *25*, S53.

[12] Ranganathan, R. S.; Raju, N.; Fan, H.; Zhang, X.; Tweedle, M. F.; Desreux, J. F.; Jacques, V. *Inorg. Chem.* **2002**, *41*, 6856.

[13] Xiangzhao, A.; Qiang, M.; Xingguang, S. *Microchimica Acta* **2013**, *180*, 269.

[14] (a) Belfi, C.A.; Medendorp, S.V.; Ngo, F.Q.; *Magn. Reson. Med.* **1999**, *22*, 379; (b) Ling, G.N. & Tucker, M. *J. Natl. Cancer Inst.* **1980**, *64*, 1199; (c) K. V. R. Chary & G. Govil (**2008**) *NMR in Biological Systems: From Molecules to Humans*. Dordrecht, Netherlands: Springer.

I.6. Gd(III)-based MRI CA Dendrimers

I.6.1. Introduction

In the quest for optimized Gd(III)-based MRI contrast agents (CAs), many groups have investigated methods to reduce the longitudinal relaxation time (T_1) of surrounding water molecules which increases the signal intensity of MR images.[1,2] Gd(III)-based CAs are not as sensitive as other imaging techniques such as positron emission tomography[3] and light microscopy.[4] One method of optimizing the sensitivity and increasing the relaxivity is to increasing the rotational relaxation time (τ_R)[1] by making the Gd(III)-based CA part of a macromolecular structure.[5,6] Another approach to increasing the sensitivity is by loading a macromolecular structure with several MRI CAs,[7] this potentially lowers the dosage and prevents dilution upon administration.

Click chemistry[8] has been used to couple MRI CAs to a variety of macromolecular structures. Dendrimers are synthetically controlled macromolecular structures that have shown great versatility as a delivery scaffold for drugs[9] and imaging agents.[10,11] If a triazole linker formed from a click coupling reaction is relatively rigid hindering local rotation, which makes intuitive sense, for the clicked Gd(III)-based CAs, the decreased local rotation could be expected to factor into the rotational relaxation time to increase the relaxivity.[12]

Using click chemistry and the newly synthesized Gd(III)-based MRI CAs (**Gd-12** and **Gd-17**), dendrimers loaded with three Gd(III)-based CAs (**Gd-27** and **Gd-28**) were designed to optimize MRI CAs, Figure I.6.1. The multi-CA dendrimer is expected to have higher relaxivity per Gd than the individual CAs. The DOTMA dendrimer (**Gd-28**)

is also predicted to show higher relaxivity based on previous studies (see section I.4).

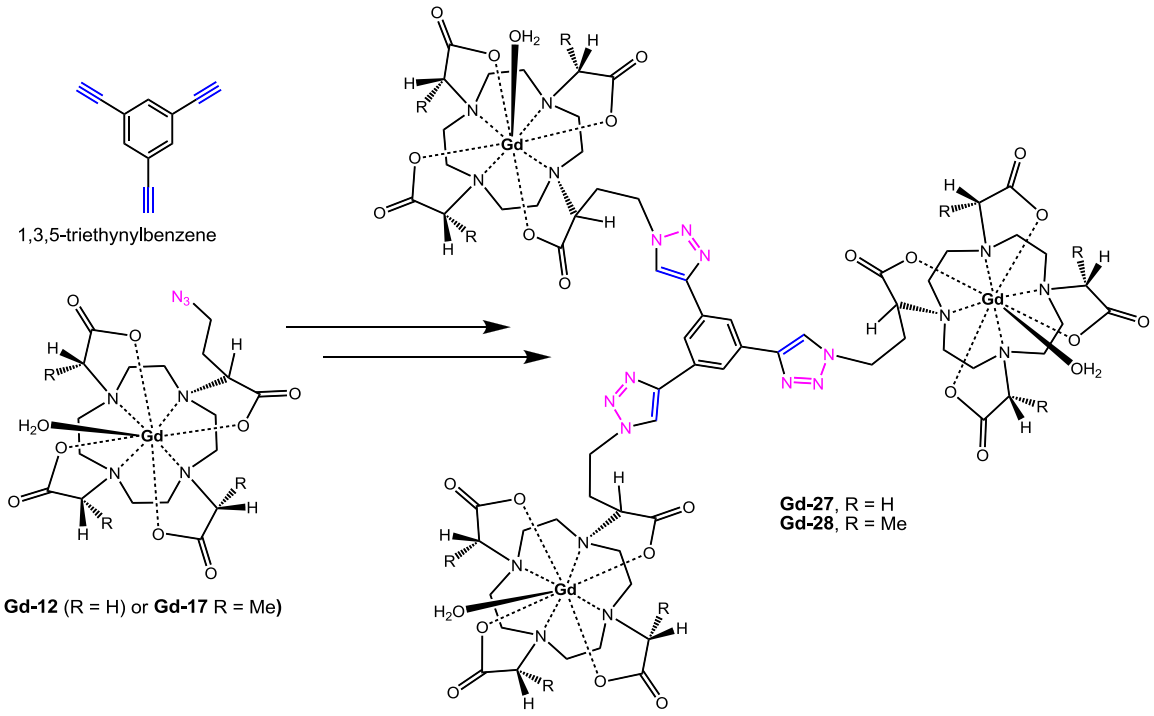

Figure I.6.1. Synthetic scheme to make first generation dendrimers, **Gd-27** and **Gd-28**.

In addition, a different type of dendrimer was designed for optimized Gd(III)-based MRI CAs. This dendrimer type includes an MRI CA as the core, Figure I.6.2. The rational for having a CA as the core of the dendrimer is to determine the affect on relaxivity of a virtually non-rotating Gd(III)-based CA as well as comparing the dendrimers made from DOTA and DOTMA CAs (**Gd-28** versus **Gd-29**).

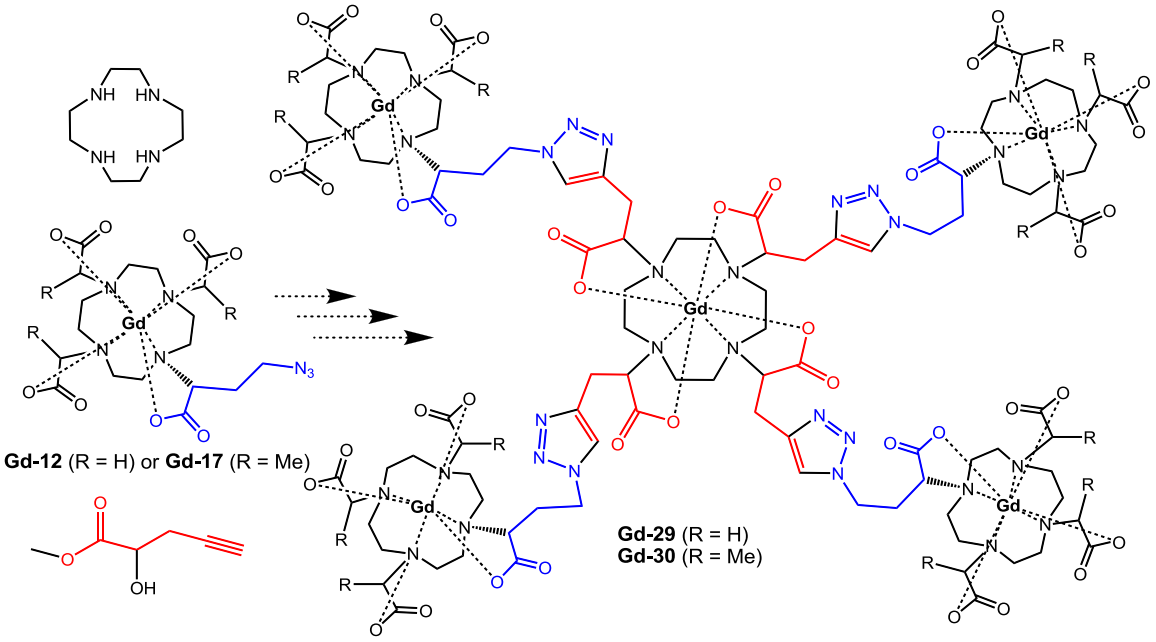

Figure I.6.2. Tetra- Gd(III)-based dendrimer with Gd(III)-based CA core, **Gd-29** and **Gd-30**.

The synthesis, purification and characterization of these dendrimers was not trivial. Dendrimers **Gd-27** and **Gd-28** were successfully made but optimization involved a significant amount of trial and error. The synthesis of dendrimers **Gd-29** and **Gd-30** were unfortunately not completed due to synthetic challenges confronted while making the alkyne coupling arm.

I.6.2. Experimental section

General method for the synthesis of complexes **Gd-12** and **Gd-17**, see Section I.4.

The 1,3,5-triethynylbenzene core

Using modified procedures from literature,[13] a Sonogashira coupling[14] was done with 1,3,5-tribromobenzene and trimethylsilylacetylene in the presence of a palladium catalyst[15] and copper iodide. To an oven dried flask TEA (3.0 mL) was added along with 1,3,5-tribromobenzene (1.0032 g, 3.176 mmol). To reaction mixture was added copper

iodide (0.0607 g, 0.3177 mmol), trimethylsilylacetylene (1.032g, 10.48 mmol), $PdCl_2(PPh_3)_2$ (0.1118 g, 0.1588 mmol), and additional TEA (15.0 mL). The reaction was put in a 50 °C oil bath for 47 h and monitored by TLC (4:1 hexanes/ ethyl acetate) using a UV lamp to see a product spot with a R_f = 0.26. Upon reaction completion, the mixture was filtered through a Celite pad which was washed with Et_2O (2 x 40 mL). The filtrate was then washed with NH_4Cl solution (1 x 75 mL). The organic layer was then extracted with deionized water (4 x 50 mL). The organic layers were combined and washed with Et_2O (50 mL), and dried over Na_2SO_4, filtered and concentrated under vacuum. The crude product was purified by silica gel chromatography (100% pentanes) affording red oil (1.0746 g, 91.9%). ^{1}H NMR (CD_2Cl_2, 499.9 MHz): δ 7.46 (s, 3H), 0.24 (s, 27H).

The TMS protected benzene (2.9852 g, 8.140 mmol) was dissolved in DCM (8.0 mL) and MeOH (17.0 mL). A 1M solution of NaOH (0.2 mL, 0.0163 mmol) was added dropwise to the reaction solution at room temperature. The reaction stirred at room temperature for 3 hours. Aliquots were taken to monitor the reaction by proton NMR and TLC (4:1 hexanes/ ethyl acetate) using a UV lamp to see a product spot with a R_f = 0.62. The reaction mixture was concentrated under vacuum and then redissolved in Et_2O (100 mL). The reaction was washed with deionized water (2 x 100 mL) and extracted with Et_2O (100 mL) and the ether phases dried over $MgSO_4$, filtered and concentrated under vacuum. The crude product was an off-white solid (1.1019 g, 90.1%). ^{1}H NMR ($CDCl_3$, 499.9 MHz): δ 7.58 (s, 3H), 3.11 (s, 3H).

*Dendrimer **Gd-27**.*

To a dry 100 mL round bottom flask containing hydrolyzed **Gd-12** NaTfO

(3.3986 mmol, crude from previous reaction, 4.5 equiv) was added DIH_2O (7 mL) and *t*BuOH (7 mL). To this solution was added 1,3,5-triethynylbenzene (0.7624 mmol, 0.1145 g, 1.0 equiv), sodium ascorbate (10.6320 mmol, 2.1063 g, 13.9 equiv), and $CuSO_4{\cdot}5H_2O$ (0.2844 mmol, 0.0710 g, 0.37 equiv). The sides of the flask were rinsed with DIH_2O (3.5 mL) and *t*BuOH (3.5 mL). The flask was capped with a septum with a nitrogen inlet and stirred in a 60 °C oil bath for 2 days. The reaction was monitored by ESI-MS (negative mode). The reaction was put into a tared Falcon tube and frozen at -80 °C, after which it was lyophilized to concentrate the reaction mixture. The dried reaction mixture was redissolved in a minimum about of DI water and put into SpectraPor MWCO 1000 tubing and dialyzed against DIH_2O (3 x 1L), changing water every 3 hours. The solution in the tubing was put into a tared Falcon tube, frozen and lyophilized to give a beige foam solid (0.2088 g, 94.1%). MALDI- TOF, see Appendix Figure A.2.

*Dendrimer **Gd-28**.*

To a dry 100 mL round bottom flask containing hydrolyzed **Gd-17** NaTfO (0.3210 mmol, crude from previous reaction, 32.1 equiv) was added DIH_2O (6.5 mL) and tBuOH (6.5 mL). To this solution was added 1,3,5-triethynylbenzene (0.0100 mmol, 0.0015 g, 1.0 equiv), sodium ascorbate (0.1661 mmol, 0.0329 g, 16.6 equiv), and $CuSO_4{\cdot}5H_2O$ (0.0382 mmol, 0.0095 g, 3.8 equiv). The sides of the flask were rinsed with DIH_2O (2 mL) and tBuOH (2 mL). The flask was capped with a septum with a nitrogen inlet and stirred in a 60 °C oil bath for 2 days. The reaction was monitored by ESI-MS (negative mode). The reaction was put into a tared Falcon tube and frozen at -80 °C, after which it was lyophilized to concentrate the reaction mixture. The dried reaction mixture was redissolved in a minimum about of DI water and put into SpectraPor MWCO 1000

tubing and dialyzed against DIH_2O (3 x 1L), changing water every 3 hours. The solution in the tubing was put into a tared Falcon tube, frozen and lyophilized to give a beige foamy solid (0.1247 g, 62.8%). MALDI- TOF, see Appendix Figure A.3.

The tetra-azide cyclen core

To a dry flask equipped with stir bar in the glovebox was added cyclen monohydrate (0.0338 g, 0.174 mmol), freshly made compound **6a** (0.2226 g, 0.764 mmol), DIPEA (0.2295 g, 1.737 mmol) dissolved in DCM (4.0 mL). The reaction stirred in the glovebox for 16 h at room temperature. Aliquots were taken to monitor the reaction progression by proton NMR. The reaction was extracted with deionized water (2 x 2 mL) and DCM (2 x 2 mL) and dried over Na_2SO_4, filtered and concentrated under vacuum. The crude product was purified by silica gel chromatography (10% MeOH/$CHCl_3$) affording an amber yellow oil (0.0611 g, 39.6%). ^{1}H NMR ($CDCl_3$, 499.9 MHz): δ 3.70 (s, 12H), 3.51-3.44 (m, 4H), 3.43-3.40 (m, 4H), 3.39-3.34, (m, 4H), 2.88-2.79 (m, 8H), 2.65-2.55 (m, 8H), 2.02-1.95 (dddd, J_{HH}= 6.4, 6.6, 7.3, 13.8 Hz, 4H), 1.84-1.76 (dddd, J_{HH}= 6.4, 6.6, 7.1, 13.7 Hz, 2H). ^{13}C NMR ($CDCl_3$, 125.7 MHz): δ 172.7, 60.66, 51.29, 50.83, 48.61, 28.77. ^{23}Na NMR ($CDCl_3$, 132.2 MHz): δ -0.0 (s), -3.4 (s). ^{19}F NMR ($CDCl_3$, 470.3 MHz): δ -78.6 (s).

Alkyne ester synthesis

The Ni-BPB-glycine complex synthesized following literature[16] procedures. BPB was made by Douglas Grotjahn. To a dry flask was added BPB (0.2530 g, 0.658 mmol), $Ni(NO_3)_2$. $6H_2O$ (0.3878 g, 1.316 mmol), glycine (0.2482 g, 3.290 mmol) and MeOH

(4.0 mL). A solution of KOH (0.2801 g, 4.992 mmol) and MeOH (4.0 mL) was prepared separately and then added dropwise to the reaction mixture. The reaction was under nitrogen and placed in a 55 °C oil bath for 24 hours. Aliquots were taken to monitor the reaction by TLC (4:1 DCM/ acetone) and (3:1 hexanes/ ethyl acetate) using a UV lamp to see a product spot with a R_f = 0.28 and 0.13, respectively. The reaction was quenched by adding acetic acid (0.29 mL, 4.992 mmol) and deionized water (60 mL) to give a red-orange precipitate, which was collected by filtration through a Buchner funnel. The red solid was dried to give product (0.1872 g, 57.1%). ^{1}H NMR ($CDCl_3$, 499.9 MHz): δ 8.25-8.22 (m, 3H), 7.55-7.54 (m, 2H), 7.53-7.51 (m, 2H), 7.48-7.44 (m, 2H), 7.35-7.32 (m, 1H), 7.19-7.11 (m, 2H), 7.41-6.98 (m, 1H), 6.82-6.80 (dd, J_{HH}= 1.5, 8.5, 1H), 4.36 (d, J_{HH}= 13.0, 1H), 3.71-3.70 (b, 1H), 3.64-3.59 (m, 2H), 3.43-3.40 (m, 1H), 3.35-3.24 (m, 1H), 2.55-2.53 (m, 1H), 2.48-2.39 (m, 1H), 2.24-2.17 (m, 1H), 2.21-2.04 (m, 1H). ESI-MS *m*/*z* 469.9 (*M* + H), (calculated for $C_{27}H_{24}N_3NiO_3$ = 496.12).

The glycine-BPB-Ni complex (0.1872 g, 0.376 mmol) was dissolved in ACN (2.0 mL) and the flask put in an ice bath. Propargyl bromide (0.1490 g, 1.253 mmol), KOH (0.0212 g, 0.378 mmol), and tert-butyl ammonium bromide (0.0044g, 0.0136 mmol) were added to the reaction solution. The reaction was kept under nitrogen and allowed to warm to room temperature for 4.5 hours. Aliquots were taken to monitor the reaction by proton NMR and TLC (4:1 DCM/ acetone) using a UV lamp to see a product spot with a R_f = 0.45. The reaction mixture was concentrated under vacuum and the residue purified by silica gel chromatography (20% acetone/ DCM) affording a red solid (0.1168 g, 58.1%). ESI-MS *m*/*z* 536.3 (*M* + H), (calculated for $C_{30}H_{26}N_3NiO_3$ = 535.24). ^{1}H NMR ($CDCl_3$,

499.9 MHz): δ 8.04-8.03 (m, 2H), 7.50-7.49 (m, 2H), 7.47-7.42 (m, 1H), 7.35-7.32 (m, 2H), 7.25-7.22 (m, 1H), 7.20-7.17 (m, 1H), 7.15-7.11 (m, 1H), 6.90-6.97 (m, 1H), 6.66-6.62 (m, 2H), 4.41 (d, J_{HH}= 13.0, 1H), 4.02-3.96 (m, 1H), 3.63 (s, 1H), 3.61-3.57 (m, 1H), 3.45-3.41 (dd, J_{HH}= 10.5, 16.5, 1H), 2.81-2.75 (m, 1H), 2.64-2.60 (m, 1H), 2.54-2.53 (m, 1H), 2.51-2.44 (m, 1H), 2.27-2.21 (ddd, J_{HH}= 2.5, 7.0, 17.0, 1H), 2.14 (s, 1H) 2.09-2.00 (m, 2H).

The propargylglycine-Ni complex (0.0798 g, 0.149 mmol) was dissolved in THF (12.0 mL). Concentrated 6 M HCl (12.0 mL) was added dropwise to the mixture. The reaction mixture changed from a red solution to yellow to a clear solution after the acid was added. The reaction was placed in a 55 C oil bath for 1 hour. Aliquots were taken to monitor the reaction by TLC (4:1 DCM/ acetone). The product was not successfully recovered from the reaction.

I.6.3. Results and discussion

There has been some difficulty in finding a method for the complete deprotection of the methyl esters of compound **12**. The proton NMR spectrums of the reactions were not clear, so IR and TLC were used to confirm product formation. In IR, the peak at ~2100 cm^{-1} for the azide, the carbonyl stretch at ~1733 cm^{-1}, and the carboxylate stretch at ~1600 cm^{-1} were closely observed. TLC conditions were 50% H_2O/MeOH visualized with potassium permanganate stain, starting material R_f = ~0.42 and product R_f = ~ 0.55. Several conditions were tried to find the optimal deprotection conditions for the chelate, Table I.6.1.

Reactions of entries 1 and 2 of Table I.6.1 were done to determine the completion

time when using LiOH. The reaction did not go to completion even after 2 days under those reaction conditions. In an attempt to keep the number of different cations to minimum, NaOH was used as the base and at greater equivalence (5.23 equiv compared to ~3.2 equiv) that yielded product but took 6 days! Entries 4 and 5 used different batches of starting material with all other factors being equal (entry 4 workup with Li_2CO_3 and entry 5 workup with Cs_2CO_3) to see if other ions affected the product (sodium ion present in macrocyclic product) (Appendix Figure A.4).

Table I.6.1. Optimizing of methyl ester deprotection of compound **12**.

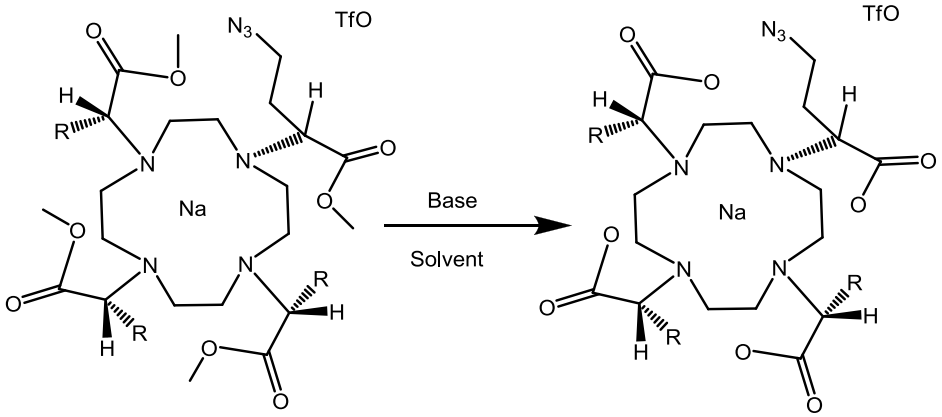

12, R = H
17, R = Me

carbo-12, R = H
carbo-17, R = Me

Entry	Temperature	Base (eq.)	THF/H2O	Time	Results
1	RT	LiOH (3.1)	10/1	27 h	SM + product
2	RT	LiOH (3.4)	10/1	2 d	SM + product
3	RT	NaOH (5.2)	2/1	6 d	Product
4	0°C -> RT	LiOH (6.4)	6/1	24 h	Product
5	0°C -> RT	LiOH (6.0)	6/1	24 h	Product
6	0°C -> RT	LiOH (5.8)	6/1	3 d	Product
7	RT	LiOH (6.0)	6/1	30 min.	Product

There seemed to be no difference between entries 4 and 5 suggesting that other cations present do not affect product formation and both were done within 24 hours.

Entry 6 took longer than expected but looked good by TLC and IR. Several parameters were found to form product cleanly such as using ~ 6.0 equiv of LiOH. While optimizing temperature, the fastest reaction was found to be 30 min. at room temperature, entry 7. The conditions used for Entry 7 were used to for all future deprotection of methyl esters on similar chelates like compound **17**.

The 1,3,5-triethynylbenzene core was chosen to create a rigid core for the first generation of these types of dendrimers (**Gd-27** and **Gd-28**). The central benzene ring and added triazole rings form a conjugated system which forms a planar rigid structure. The 1,3,5-triethynylbenzene core was made by following literature procedures.[14] The synthesis was relative straightforward and each step has been optimized to give at least 90% yield, Figure I.6.3.

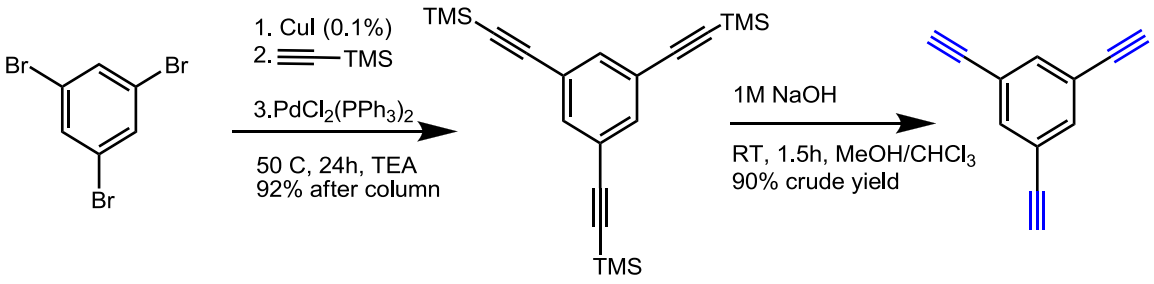

Figure I.6.3. Synthesis of 1,3,5-triethynylbenzene.

The copper(I) catalyzed azide alkyne cycloaddition (CuAAC)[17] was used to couple the Gd(III)-based MRI CAs to the 1,3,5-triethynylbenzene. Several test reactions were done with compound **5** (see Section I.3) and phenylacetylene to find the most efficient combination of solvent, copper(I) source, temperature, time, and additives (data not shown). Another challenge confronted while synthesizing these dendrimers was the purification and characterization steps. Once the Gd(III)-based MRI CAs are used, the

products are almost strictly water soluble. Reverse phase chromatography and size exclusion purification techniques were used to obtain the desired products. The presence of paramagnetic metal Gd(III) precluded the use of characterization by NMR. Mass spectroscopy was mainly for used characterization because of the unique isotopic pattern from the Gd(III) ions in the dendrimers (see Appendix Figure A.2-A.3).

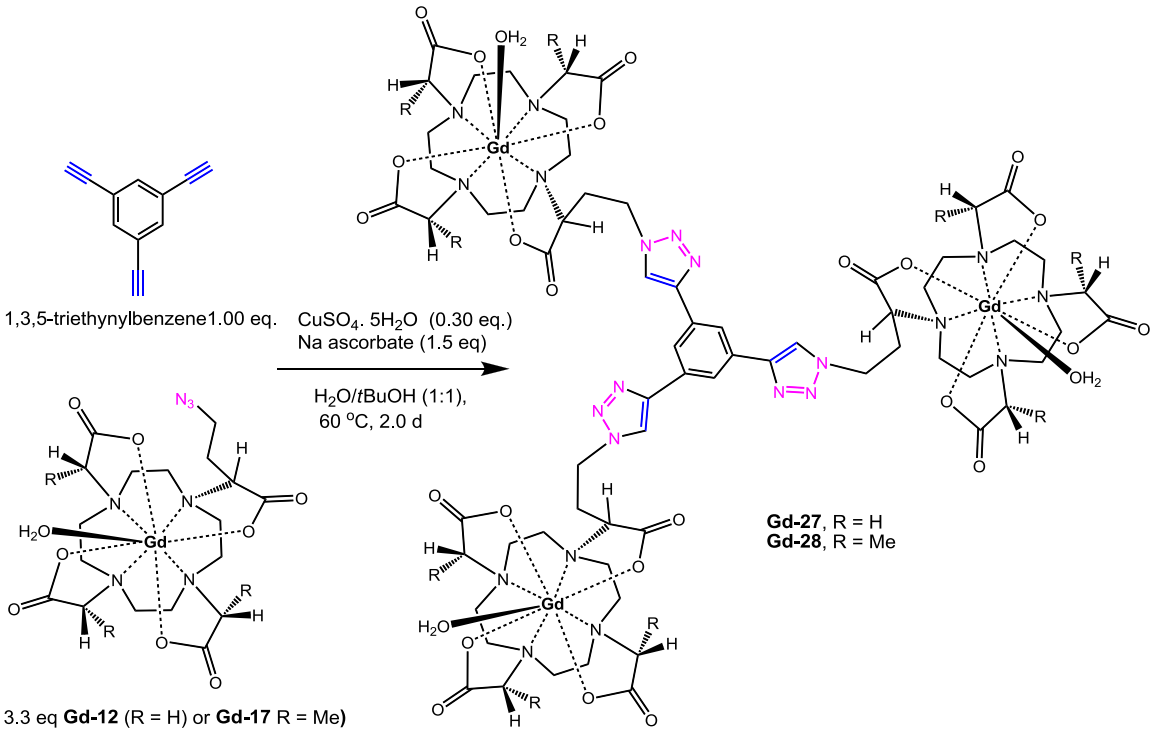

Figure I.6.4. Scheme for synthesis of **Gd-27** and **Gd-28.**

Efficient CuAAC reactions depend on several factors, for example solubility of starting material and reagents and catalyst amount. For the synthesis of **Gd-27** and **Gd-28**, it was found that the following conditions were ideal: 1.0 molar equiv. of triyne, 3.3 molar equiv. of azide, at least 0.10 molar equiv. of Cu(I), at least 0.50 molar equiv. of Na ascorbate, minimal amount of solvent, 60 °C, under nitrogen, and stirring for about 2

days, Figure I.6.4. Unfortunately, an extremely similar dendrimer had been published[18] at the time by Thomas Meade's group. Although their synthetic design was comparable to dendrimers **Gd-27** and **Gd-28**, they only studied the DOTA version of their MRI CA.

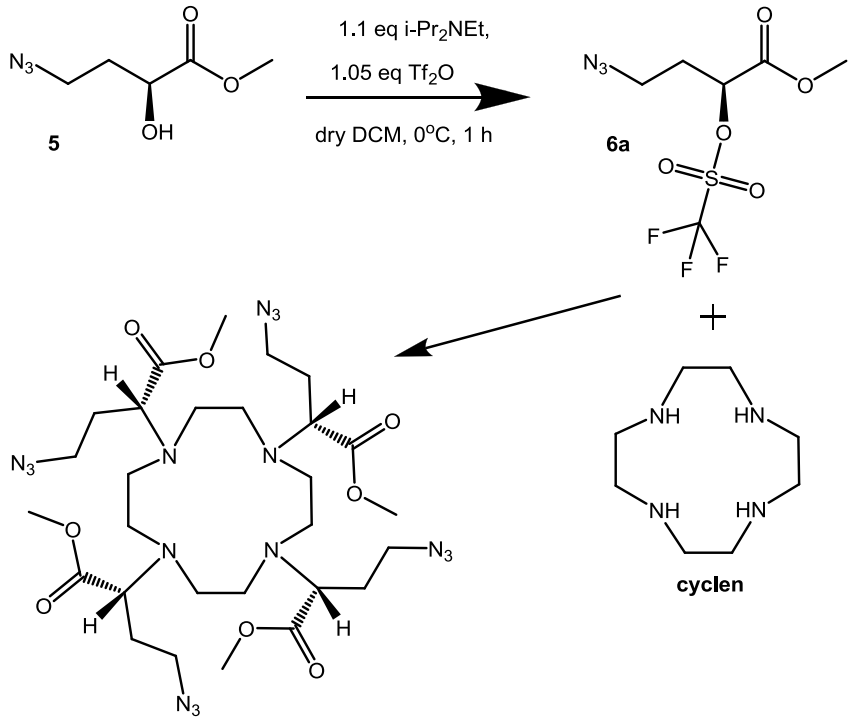

Figure I.6.5. Synthesis of tetra-azide cyclen core.

The synthesis of the tetra-azide core was quite straight forward, Figure I.6.5. Using excess alkylating agent **6a** gave the desired product in good yields. After purification, crystals were not able to be grown for X-ray diffraction (XRD). Full characterization was done on the tetra-azide cyclen core.

Synthesizing (*S*)-propargylglycine needed for the click reaction to make the **Gd-29** and **Gd-30** dendrimers was found to be challenging, Figure I.6.7. The (*S*)-propargylglycine synthesis was adapted from literature procedures.[13] The hydrolysis of the Ni-BPB-alkyne to give (*S*)-propargylglycine was difficult to identify and separate

from the reaction mixture. The synthesis proved more complex than initially proposed and thus will be investigated in the future.

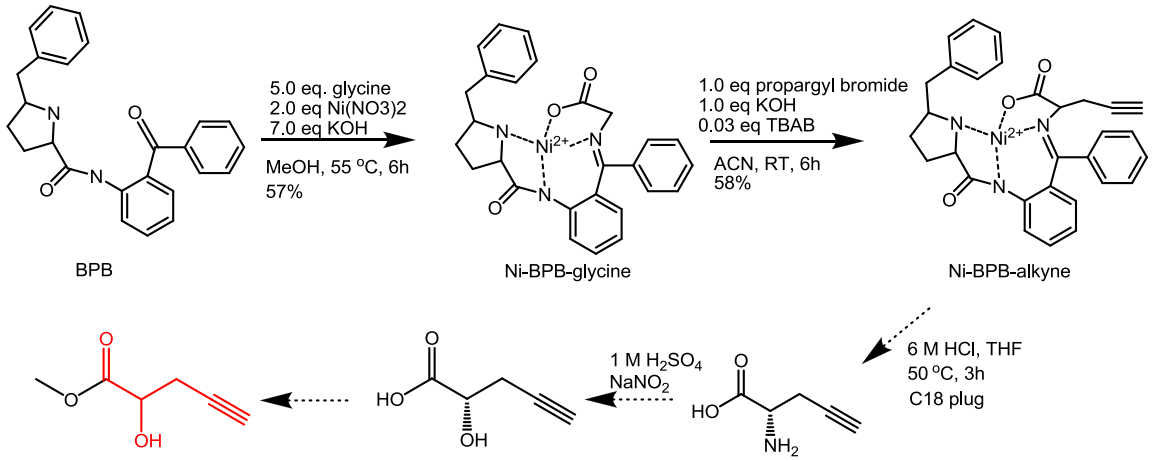

Figure I.6.6. Synthesis of alkyne moiety.

I.6.4. Conclusions

Bifunctional Gd-based MRI contrast agents (**12** and **17**) were synthesized and analyzed by MALDI-TOF. The desired conformers of the Gd- complexes **Gd-12** and **Gd-17** were observed by synthesizing the europium analogs (compound **Eu-12** and **Eu-17**). The first generation of dendrimers were made (**Gd-27** and **Gd-28**) using click chemistry to couple the contrast agents to a core (have been sent to our collaborator to relaxivity studies). Comparative study of the T_1 of these dendrimers with the MG-2p constructs (**Gd-25** and **Gd-26**, Section I.5) would be of interest.

I.6.5 Acknowledgements

I would like to thank all the members of our lab's dendrimer subgroup for helpful conversations related to this project.

I.6.6. References

[1] Merbach, A. E., Toth, I. (**2001**) *The Chemistry of Contrast Agents in Medical Magnetic Resonance Imaging*, (1st ed.). Wiley: New York.

[2] Kurtkoti, J.; Snow, T.; Hiremagalur, B. *Nephrology* **2008**, *13*, 235–241. (b) Dillman, J. R.; Ellis, J. H.; Cohan, R. H.; Strouse, P. J.; Jan, S. C. *Am. J. Roentgenol.* **2007**, *189*, 1533.

[3] Sharma, V.; Luker Gary, D.; Piwnica-Worms, D. *J. Magn. Reson. Imaging* **2002**, *16*, 336.

[4] Zhang, J.; Campbell, R. E.; Ting, A. Y.; Tsien, R. Y. *Nat. Rev*. *Mol. Cell Biol.* **2002**, *3*, 906.

[5] Nobuhisa Ozaki, N.; Sankar, A. U. R. S.; Yamashita, M. et al. *Bioorg. & Med. Chem. Let.* **2010**, *20*, 932.

[6] De León-Rodríguez, L. M.; Lubag, A.; Udugamasooriya, D. G.; Proneth, B.; Brekken, R. A.; Sun, X.; Kodadek, T.; Sherry, A. D. *J. Am. Chem. Soc.* **2010**, *132*, 12829.

[7] Bryson, J. M.; Chu, W.-J.; Lee, J.-H.; Reineke, T. M. *Bioconjugate Chem.*, **2008**, *19*, 1505.

[8] (a) Binder, W. H. & Sachsenhofer, R. Macromol. *Rapid Commun.* **2007**, *28*, 15; (b) Fernandez-Megia, E.; Correa, J.; Riguera, R. *Biomacromolecules*, **2006**, *7*, 3104; (c) Moses, J. E. & Moorhouse, A. D. *Chem. Soc. Rev.*, **2007**, *36*, 1249; (d) Hein, J. E. & Fokin, V. V. *Chem. Soc. Rev*., **2010**, *39*, 1302.

[9] Tathagata Dutta, T.& Jain, N. K. *Biochimica & Biophysica Acta* **2007**, *1770*, 681.

[10] Xu, H.; Regino, C.A.S.; Koyama, Y.; Hama, Y.; Gunn, A. J.; Bernardo, M.; Kobayashi, H.; Choyke, P. L. & Brechbiel, M. W. *Bioconjugate Chem*. **2007,** *18*, 1474.

[11] Villaraza, A. J. L.; Bumb, A. & Brechbiel, M. W. *Chem. Rev.* **2010,** *110*, 2921.

[12] (a) Zhang, Z.; Greenfield, M. T.; Spiller, M.; Mcmurry, T. J.; Lauffer, R. B.; Caravan, P. *Angew. Chem., Int. Ed.* **2005**, *44*, 6766; (b) Nicolle, G. M.; Toth, E.; Schmitt-Willich, H.; Raduchel, B.; Merbach, A. E. *Chem.—Eur. J.* **2002**, *8*, 1040.

[13] (a) Belokon, Y. N.; Bulychev, A. G.; Vitt, S. V.; Struchkov, Yu. T.; Batsanov, A. S.; Timofeeva, T. V.; Tsyryapkin, V. A.; Ryzhov, M. G.; Lysova, L. A.; et al. *J. Am. Chem. Soc.* **1985**, *107*, 4252; (b) Belokon, Y. N.; Maleev, V. I.; Savelèva, T. F.; Moskalenko, M.

A.; Pripadchev, D. A.; Khrustalev, V. N.; Saghiyan, A. S. *Amino Acids* **2010**, *39*, 1171; (c) Belokon, Y. N.; Gugkaeva, Z. T.; Hakobyan, K. V.; Maleev, V. I.; Moskalenko, M. A.; Khrustalev, V. N.; Saghyan, A. S.; Tsaloev, A. T.; Babievsky, K. K. *Amino Acids* **2012**, *43*, 299; (d) Linderberg, M. T.; Moge, M.; Sivadasan, S. *Org. Process Res. Dev.* **2006**, *10*, 838.

[14] Kuroda, T.; Sakurai, Y.; Suzuki, Y.; Nakamura, A. O.; Kuwahara, M.; Ozaki, H.; Sawai, H. *Chem.- Asian J.* **2006**, 1, 575.

[15] Montilla, F.; Galindo, A.; Rosa, V.; Aviles, T. F. M. et al *Dalton Trans.* **2004**, 2588.

[16] Belokon, Y. N.; Tararov, V. I.; Maleev, V. I.; Savelèva, T. F.; Ryzhov, M. G. *Tetrahedron: Asymmetry* **1998**, *9*, 4249.

[17] (a) Huisgen, R. *Angew. Chem.* **1963**, *2*, 565; (b) *Angew. Chem.* **1963**, *2*, 633.; (c) Kolb, H.; Sharpless, B. *DDT.* **2003**, *8*, 1128; (d) Empting M., et al. *Angew. Chem. Int. Ed.* **2011**, *50*, 5207; (e) Rostovtsev, V. et al. *Angew. Chem. Int. Ed.* **2002**, *41*, 2596; (f) Rostovtsev, V. et al. *Angew Chem.* **2002**, *114*, 2708; (g) Tornøe, C. et al. *J. Org.Chem.* **2002**, *67*, 3057; (h) Meldal, M.; Tornøe, C. *Chem. Rev.* **2008**, *108*, 2952.

[18] Mastarone, D. J.; Harrison, V. S. R.; Eckermann, A. L.; Parigi, G.; Luchinat, C.; Meade, T. J. *J. Am. Chem. Soc.* **2011**, *133*, 14, 5329.

CHAPTER II

Bifunctional Imaging agents for Positron Emission Tomography (PET)

II.1 PET Introduction

II.1.1. PET Background

Positron emission tomography (PET) is a nuclear medicine imaging technique for reconstructing 2D and 3D images of biological processes *in vivo* using positron-emitting radiopharmaceuticals. Physiologic and biochemical processes such as blood flow, oxygen, glucose, and free fatty acid metabolism, amino acid transport and neuroreceptor density can be imaged using such radionuclides as carbon-11, nitrogen-13, oxygen-15, and fluorine-18. A few examples of diagnostic uses of PET include Alzheimer's disease, Parkinson's disease, dementia, for epilepsy, and other neurodevelopmental disorders.[1,2]

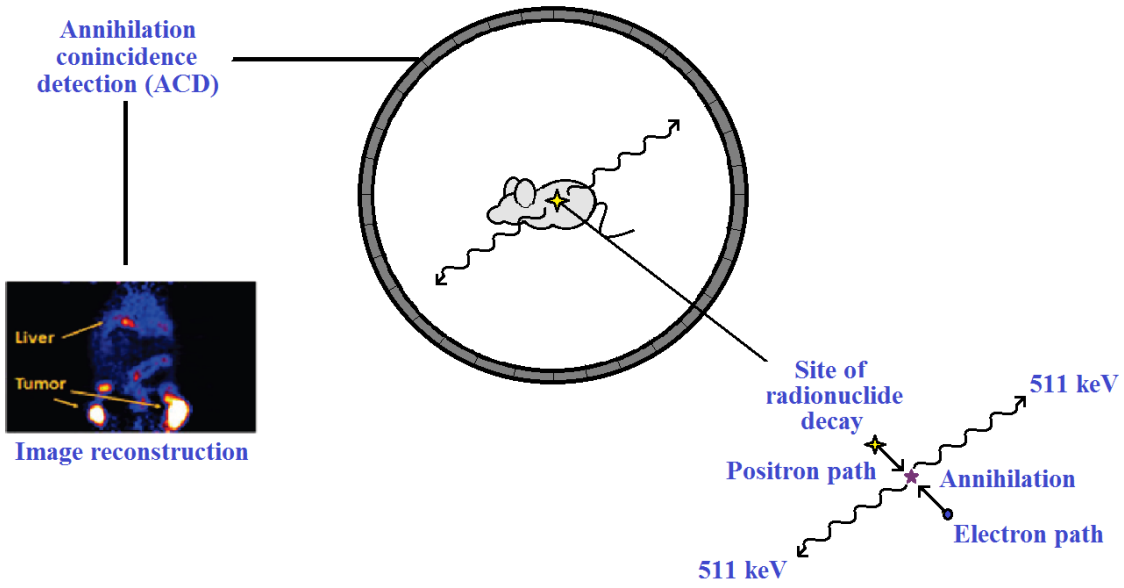

Figure II.1.1. Annihilation coincidence detection for PET.

PET is based on annihilation coincidence detection (ACD) of photons generated from an annihilation event between a positron and electron. A radiopharmaceutical is usually injected into a patient/animal model. The radiopharmaceutical is processed by the body, and the radionuclide, which is part of the radiopharmaceutical, decays emitting a positron. The positron travels a short distance (a few millimeters) from the radionuclide

before its kinetic energy is transferred to a free electron in the surrounding tissue and a mutual annihilation event occurs. This annihilation event results in two 511 keV photons emitted simultaneously "back-to-back" at 180-degrees from each other, known as a true coincidence, Figure II.1.1.

Positron decay:

$$p \rightarrow n + \beta^+ + \nu + \text{energy}$$

where *p* is a proton, *n* is a neutron, β^+ is a positron, and ν is a neutrino.

Mutual annihilation:

$$\beta^+ + \beta^- \rightarrow \gamma + \gamma$$

where β^+ is a positron, β^- is an electron, and γ is gamma/photon (511 keV).

The pair of photons can be located by a circular array of detectors during a specified coincidence timing window (usually 6-12 nanoseconds). PET detector electronics can estimate the density of positron annihilation events in a specific voxel by ACD. Because radioactive decay is a random process, when there are enough radionuclides and annihilation events have occurred, the density of the original radiopharmaceutical can be measured for that voxel typically with a resolution ~1-2 mm.[3] Commonly, PET images are fused with other modalities such as X-ray computed tomography (CT) or magnetic resonance (MR) that have better resolution.

II.1.2. PET tracers

Radiopharmaceuticals are radioactive medicinal compounds for diagnosis and/or treatment of diseases. The use of radiopharmaceuticals for diagnostic imaging will be discussed, but their use for treatment is beyond the scope of this work. Radioactive isotopes are routinely incorporated into biologically active molecules, which in their

entirety, are known as tracers. Positron emitting radionuclides are generally used for PET imaging. A prominent PET tracer currently used clinically is ^{18}F-fluorodeoxyglucose (FDG) (Figure II.1.2).

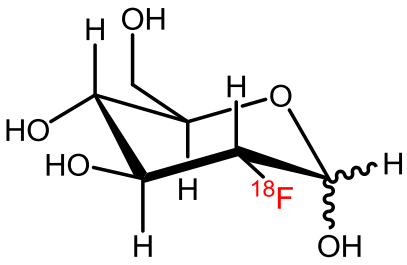

Figure II.1.2. Common PET tracers: ^{18}F-fluorodeoxyglucose (FDG).

The uptake and metabolism of FDG indicates glucose metabolism in tissues which can be used to monitor pathological conditions such as stages of cancer. As discussed in the previous section, carbon-11, nitrogen-13, oxygen-15, or fluorine-18 can be incorporated into tracers for various biomedical applications (Table II.1.1.).

One main characteristic taken into account for PET radiotracers is the half-life of the radionuclide. The common radionuclides mentioned previously have short half-lives (carbon-11, 20 min; nitrogen-13, 10 min; oxygen-15, 2 min; fluorine-18, 110 min). The half-life of the radionuclide needs to be long enough to synthesize the radiopharmaceutical and to image the desired target location as well as allow clearance through untargeted tissue. Other factors that influence the choice of radionuclides are the mode of decay positron emitting (β^+), electron capture (EC), beta-emitting (β^- and cost and availability of the isotope.

Table II.1.1. Positron emitting radiotracers and examples of their biomedical applications.

PET Radiotracer	Biomedical applications
[^{11}C]SCH23390	dopamine DI receptor
[^{11}C]Ro151788	central benzodiazepine receptor
[^{11}C]PK11195	peripheral benzodiazepine receptor
[^{11}C]PIB	amyloid plaque: Alzheimer's disease
[^{11}C]AG1478	EGF receptors
[^{11}C]choline	biosynthesis of phospholipids
[^{13}N]ammonia	blood flow
[^{15}O]oxygen	oxygen metabolism
[^{15}O]carbon monoxide	blood volume
[^{15}O]carbon dioxide	blood flow
[^{15}O]water	blood flow
[^{18}F]FDG	glucose metabolism
[^{18}F]FMISO	hypoxic tissue
[^{18}F]MPPF	serotonin $5HT_{1A}$ receptors
[^{18}F]A85380	nicotinic acetylcholine receptors
[^{18}F]FLT	DNA proliferation

*Table adapted from the Centre of Positron Emission Tomography's website, Austin Hospital, Melbourne Australia.

There are a handful of positron emitting radionuclides that have attracted the attention of researchers for use as PET tracers. These include but are not limited to isotopes of cobalt, copper, gallium, rubidium, and yttrium (Table II.1.2).

Table II.1.2. Positron emitting radionuclides.

Isotope	Half-life	Method of production	Decay mode	$E_{\beta+}$ (keV)	Ref.
^{55}Co	17.5 h	cyclotron, ^{54}Fe(d,n)^{55}Co	β+ (77%) EC (23%)	1513, 1037	4,5
^{60}Cu	24 min.	cyclotron, ^{60}Ni(p,n)^{60}Cu	β+ (93%) EC (7%)	3920, 3000 2000	4,6,7
^{61}Cu	3.3 h	cyclotron, ^{61}Ni(p,n)^{61}Cu	β+ (62%) EC (38%)	1220, 1150 940, 560	4,6,7
^{62}Cu	9.74 min.	^{62}Zn/^{62}Cu generator	β+ (98%) EC (2%)	2910	4,7
^{64}Cu	12.7 h	cyclotron, ^{64}Ni(p,n)^{64}Cu	β+ (19%) EC (41%) β$^-$ (40%)	656	4,7,8
^{66}Ga	9.5 h	cyclotron, ^{63}Cu(α,nγ)^{66}Ga	β+ (56%) EC (44%)	4150, 935	4
^{68}Ga	1.1 h	^{68}Ge/^{68}Ga generator	β+ (90%) EC (10%)	1880, 770	4,9
^{82}Rb	78 sec.	^{82}Sr/^{82}Rb generator	β+ (96%) EC (4%)	3150	4
^{86}Y	14.7 h	cyclotron, ^{86}Sr(p,n)^{86}Y	β+ (33%) EC (66%)	2335, 2019 1603, 1248, 1043	4,10

*Table adapted from ref.[11]

II.1.3 Copper radionuclides and chelators for copper

Although there appears to be a diverse selection of radionuclides from which to choose, the cost of production and half-lives severely limit the choices. Copper is widely used for labeling proteins, peptides, monoclonal antibodies and other targeting agents. Copper radiopharmaceuticals can be classified into two groups, those with shorter half-lives and those with longer half-lives (Table II.1.3). Short-lived copper radionuclides are generally stable enough to localized in either heart, brain, kidney or tumors upon first pass through the circulatory system for imaging.[12,13] Longer-lived copper radionuclides

are employed for targeting biomolecules that take longer to get to their intended destination.

Table II.1.3. Comparison of half-lives of copper and other selected isotopes.

Isotope	Half-life
^{11}C	20.3 minutes
^{18}F	109 minutes
^{60}Cu	23.4 minutes
^{61}Cu	3.32 hours
^{62}Cu	9.76 minutes
^{64}Cu	12.7 hours
^{67}Cu	62.0 hours

One challenge for copper PET tracers has been finding copper chelators with optimal characteristics for desired targeting biomolecules. The lipophilicity and overall charge of a tracer affects the tracer's biodistribution, accumulation and removal from the body. It is known that negatively charged tracers clear through the kidneys, whereas positively charged tracers tend to accumulate in the heart, and neutral tracers are required to cross the blood brain barrier. It has also been shown that negatively charged copper tracers are cleared through the body significantly more quickly than are positively charged tracers.

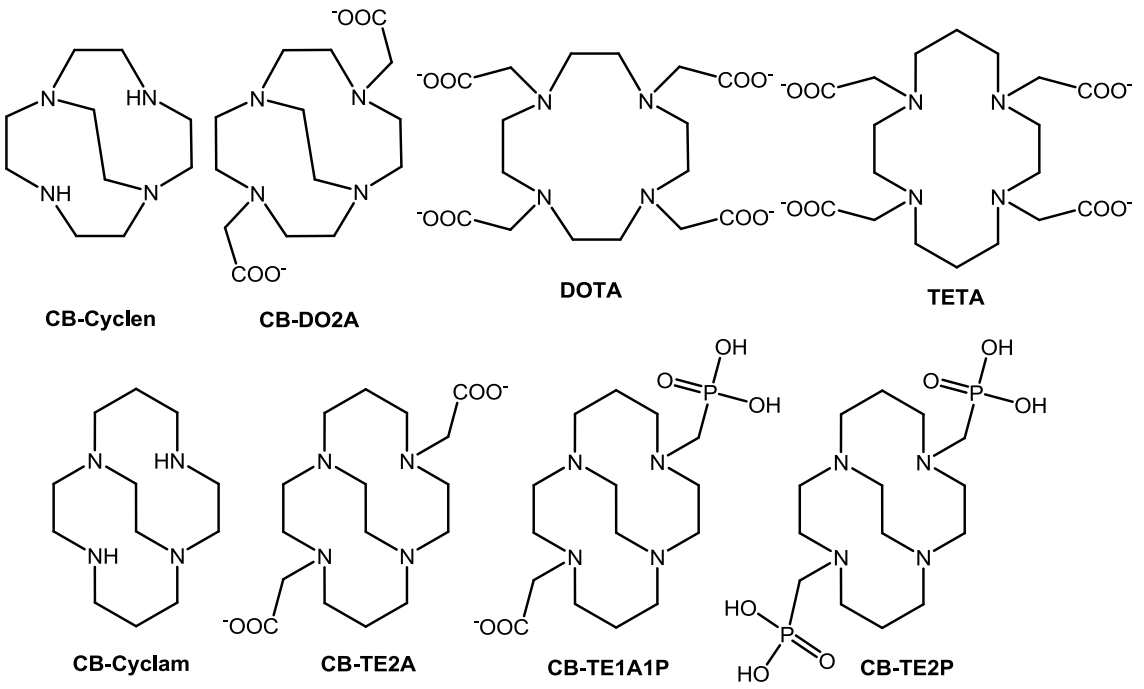

Figure II.1.3. Chelates used for copper to make PET tracers.

Moi, et al. have shown that kinetic inertness is more important than thermodynamic stability for copper chelators, Figure II.1.3.[14] There is evidence showing that kinetic inertness roughly corresponds to *in vivo* stability, which is more prominent for macrocycles than linear polyamino-polycarboxylate chelators.[15,16] The optimal design for a bifunctional chelator (BFC) for copper PET embodies a chelate that strongly binds six-coordinate copper as well as a coupling moiety to attach targeting biomolecules. The kind of BFCs chosen greatly influences the pharmacokinetics, biodistribution and metabolism of the radiopharmaceutical.[17,18]

Macrocycles like 1,4,8,11-tetraazacyclotetradecane-1,4,8,11-tetraacetic acid (TETA) were initially studied for their potential use as PET tracers for copper. The tracer (^{64}Cu-TETA) was coupled to octreotide, a mimic of a natural somatostatin hormone, which inhibited growth of somatostatin -receptor positive tumors in rats, but was also

found to undergo transchelation by liver superoxide dismutase.[19] Investigations into a series of macrocycles for ^{64}Cu PET tracers (Figure II.1.4.) found that CB-TE2A had the most desirable *in vivo* clearance and resistance to transchelation.[20,21] These favorable results for CB-TE2A are likely due to the coordination number of the chelate in combination with the overall neutral charge of the resulting Cu(II) complex.

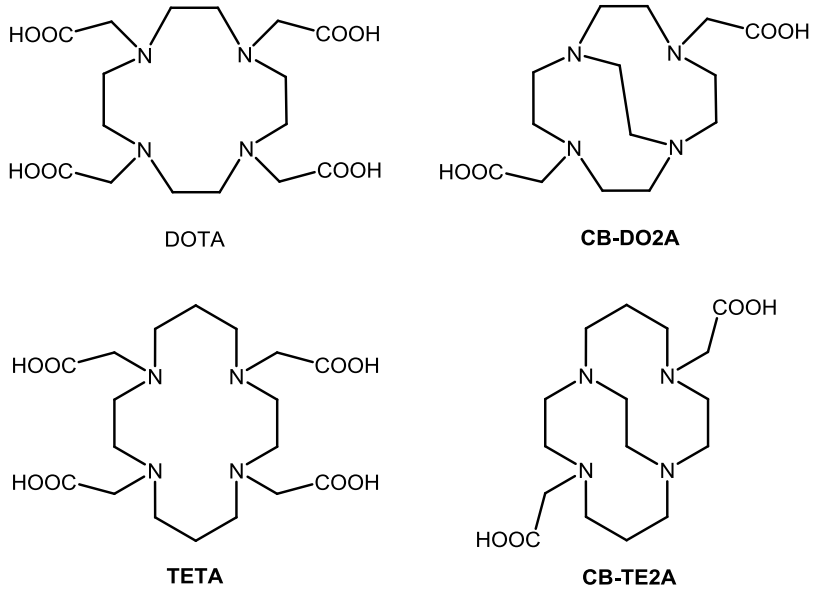

Figure II.1.4. TETA, DOTA, CB-DO2A, CB-TE2A chelators for copper for PET tracers.

II. 2 Bifunctional PET tracers for ^{64}Cu

II.2.1 Introduction

Bifunctional macrocycles for 64-copper (^{64}Cu) PET are known. Several groups have used either the CB-cyclam scaffold to build a chelator for copper while retaining a moiety for further coupling to biomolecules.[22] Some biomolecules tested with ^{64}Cu have been octreotide and its derivatives (mimicking a natural somatostatin) and sst2ANT (somatostatin subtype 2 antagonist).[23,24] Unfortunately, to make these types of bifunctional PET tracers, one of the coordinating carboxylates is sacrificed to attach

their alkylating moiety that couples to their biomolecule (Figure II.2.1). This reduces the binding affinity for Cu(II) to the macrocycle because of only one negatively charged coordinating ligand.

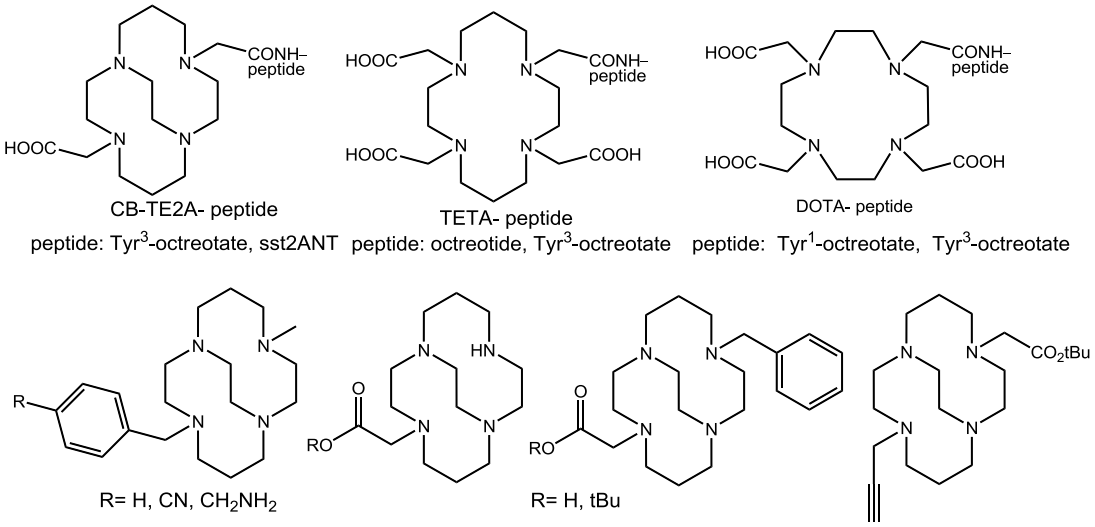

Figure II.2.1. Examples of bifunctional macrocyclic chelators for ^{64}Cu. sst2ANT = somatostatin subtype 2 antagonist.

There are a handful of examples where the macrocyclic chelator does provide coordinative saturation of copper while still possessing a coupling moiety (Figure II.2.2) to attach a biomarker or other biologically active molecule. Lewis and coworkers used the carbon chain on CB-TE2A to attach groups like isothiocyanate to couple to biomolecules of interest, **I**.[28,29] Other bifunctional CB-TE2A tracers alkylate with one or two alkylating agents that contain a carboxylate group for coordinating to copper and a succinimidyl ester to couple biomolecules, **II** and **III**.[30,31] Bifunctional tracers that are divalent like chelate **C** in Figure II.2.2 have been shown to have prolonged biological retention and enhanced specific binding in tissues expressing target receptors.[25-29] The disadvantages of most of examples in Figure II.2.2 are the long syntheses of the desired macrocycles and the presence of multiple stereoisomers of the product.

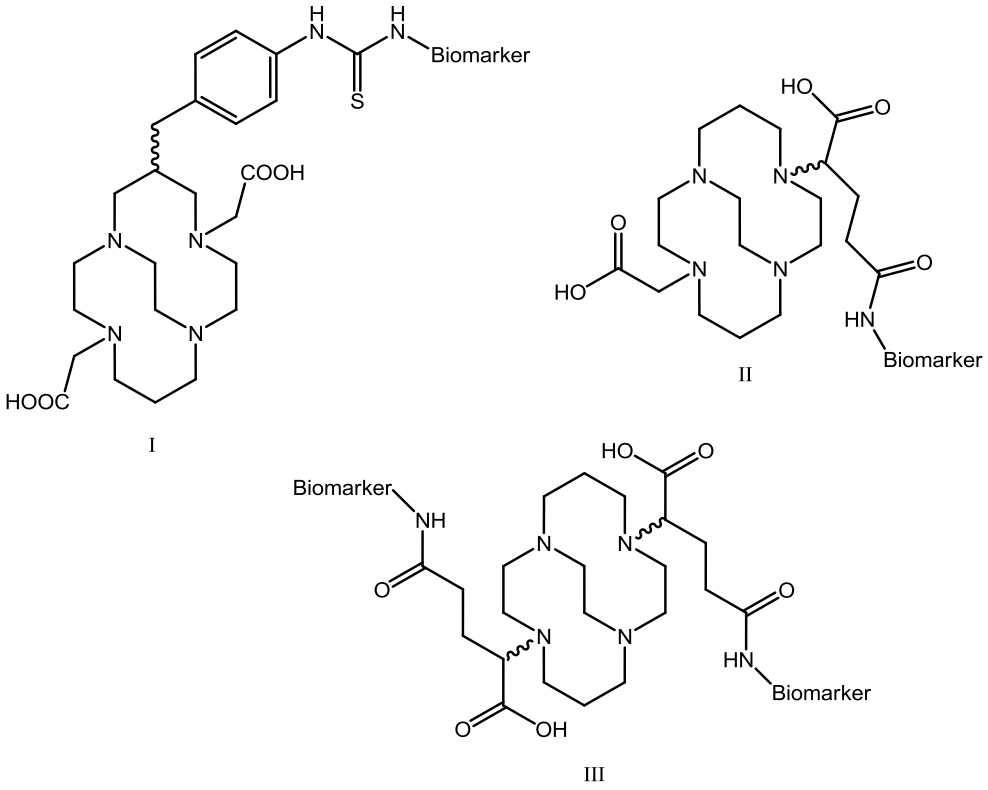

Figure II.2.2. Examples of CB-cyclam that retain six coordinating ligands for copper while maintaining a coupling moiety for biomarkers.

In collaboration with Erik Wiener at UPMC and Carolyn J. Anderson and her group at the University of Pittsburgh, Pennsylvania, we set out to make a cross-bridged cyclam (CB-cyclam) macrocycle scaffold for ^{64}Cu complexation with functionalizable moieties for coupling various targeting biomolecules for minimally invasive PET tracers, Figure II.2.3. The functionalized CB-cyclam with two identical azide-bearing moieties provides several advantages with respect to PET applications: (1) click chemistry can be used to couple alkynyl biomolecules, (2) the azides can be reduced to amines for peptide coupling, (3) the synthesis of the azide-bearing moiety has been optimized,[30] and (4) the tracer can increase its affinity of the biomolecule by allowing two attachments points for biomolecules.

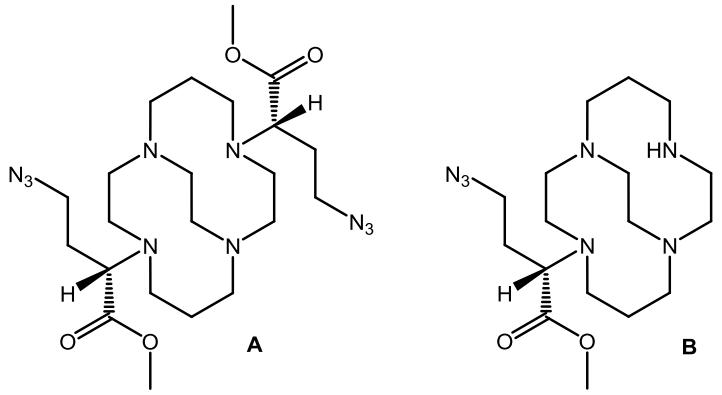

Figure II.2.3. Synthetic design of CB-cyclam:dialkylated A and monoalkylated B desired PET tracers.

By using CB-cyclam as a scaffold, the proposed chelator was expected to tightly coordinate copper-64 preventing it from becoming unbound and causing false signals and/or unwanted toxicity. The azide moiety can be coupled, through azide-alkyne cycloaddition (click chemistry) or peptide coupling, to a disease-related molecule, using more than one coupling site. Possible applications of this tracer include but not limited to tumor receptors in cancer such as integrins, somatostatin, and bombesin, with high affinity peptides.

II.2.2 Experimental Section

For general experimental considerations not detailed here, see section I.2.2. CB-cyclam was supplied by Professor Anderson and her group.[31]

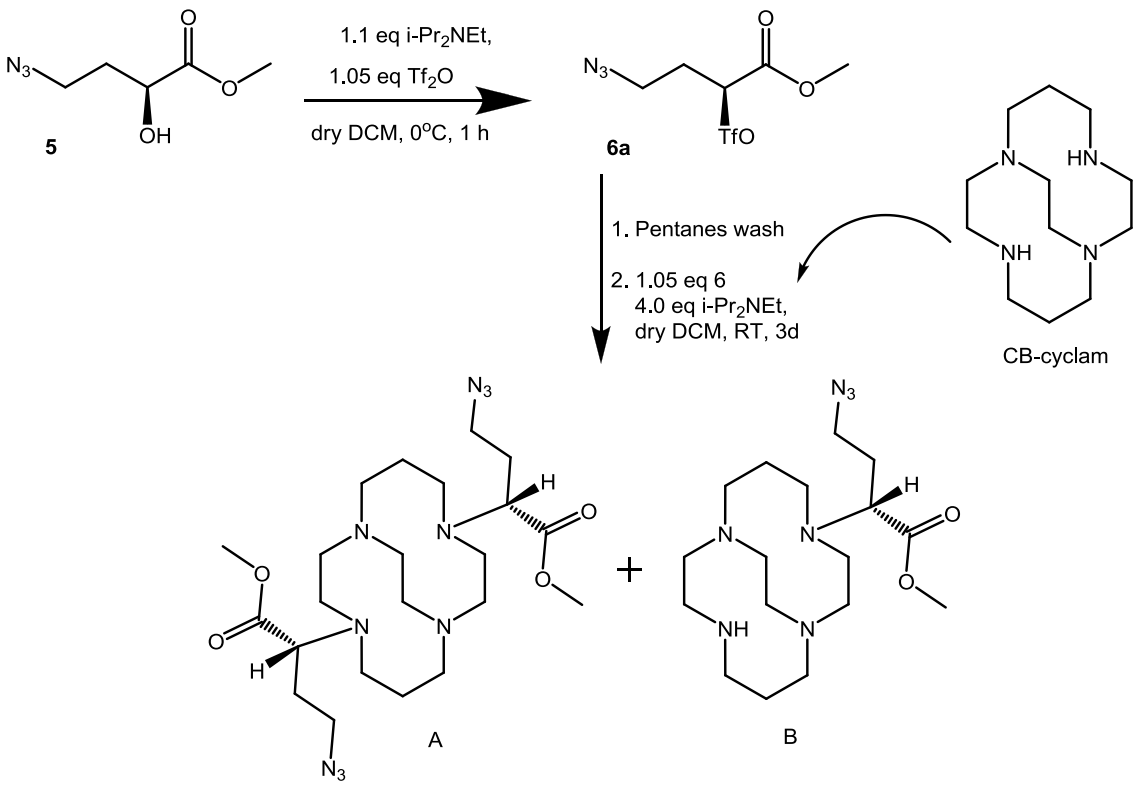

Figure II.2.4. Synthesis of chelate **A** and **B** from racemic CB-cyclam.The hydrated CB-cyclam was dried over molecular sieves and over P_2O_5 in a dessicator.

*Synthesis of compound **5** and **6a** (see Chapter I, MRI chapter).*

*Synthesis of dialkylated CB-cyclam, (**A**). (Figure II.2.4).*

Several attempts to dialkylated CB-cyclam were performed (see Table II.2.1) with varying amounts of alkylating agents, reaction time, temperature, and equivalents of base. The general procedure of synthesis is as follows.

Run **1**

To a dry J. Young NMR tube was added CB-cyclam (0.0490 g, 0.184 mmol) and dry deuterated DCM (0.6 mL). Dry DIPEA (0.16 mL, 0.92 mmol) was added dropwise to the tube. The alkylating agent compound **6a** (0.40 mL. 0.37 mmol) was added dropwise and left for 2 days at room temperature. The reaction was monitored by proton and fluorine NMR spectroscopies.

Run **2**

To a dry J. Young tube was added CB-cyclam (0.0436 g, 0.1662 mmol) and dry deuterated DCM (0.6 mL). Dry DIPEA (0.15 mL, 0.86 mmol) was added dropwise to the tube. The alkylating agent compound **6a** (0.19 mL. 0.17 mmol) was added dropwise and left for 3 days at room temperature. The reaction was monitored by proton and fluorine NMR spectroscopies . ^{1}H NMR (CD_2Cl_2, 399.7 MHz): δ 4.28-4.25 (dd, *J* = 4.4, 8.0, 2H), 3.79-3.75 (m, 2H), 3.73 (s, 6H), 3.61-3.62.62 (m, 11H, peaks overlap extensively), 2.18-2.01 (m, 4H), 1.91-1.76 (m, 4H), 1.74-1.64 (m, 2H), 1.62-1.51 (m, 2H).

Run **3**

To an oven-dried flask was added CB-cyclam (0.0784 g, 0.343 mmol) and dry DCM (5.0 mL). Dry DIPEA (0.360 mL, 2.07 mmol) was added dropwise to the solution. The reaction flask was placed in an ice bath and compound **6a** (2.68 mL, 6.0 eq) was added dropwise. The reaction mixture was let warm to room temperature and stirred under nitrogen for 16 hours. Aliquots were taken and check for completion by proton and fluorine NMR spectroscopies. The reaction was extracted with DCM (2 x 7 mL) and deionized water (3 x 7 mL) and dried over Na_2SO_4, filtered and concentrated under vacuum. The crude product (0.0167 g) was purified by Biotage silica gel chromatography (ethyl acetate/DCM, 0.5/0.5) to afford no product.

Run **4**

To an oven-dried flask was added CB-cyclam (0.1308 g, 0.5782 mmol) and dry DCM (4.0 mL). Dry DIPEA (0.2791 g, 2.159 mmol) was added dropwise to the solution. The reaction flask was placed in an ice bath and compound **6a** (0.3681 g, 1.264 mmol, 2.2 equiv) was added to reaction flask via cannula transfer and DCM (4 x 3 mL). The

reaction mixture was let warm to room temperature and stirred under nitrogen for 17 hours then placed in a 50 ^{o}C oil bath for 5 days. Aliquots were taken and checked for completion by proton and fluorine NMR and mass spectrometry. The reaction was washed with 1 N NaOH (15 mL) and deionized water (2 x 15 mL), the organic phase was dried over Na_2SO_4, filtered, and the filtrate concentrated under vacuum. The crude product (0.2928 g) was purified by silica gel chromatography (ACN/DCM, 0.4/1) and C18 chromatography (water/ACN, 0.1/1) affording an amber oil (0.0284g, 9.7% yield of **A**). ESI-MS *m*/*z* 509.3 (*M* + H), (calculated for $C_{22}H_{40}N_{10}O_4$ = 508.62). Proton NMR spectrum similar to that of run 2.

Run **5**

To a dry J. Young tube was added CB-cyclam (0.0260 g, 0.12 mmol) and dry deuterated DCM (0.6 mL). Dry DIPEA (100 µL, 0.574 mmol) was added dropwise to the tube. The alkylating agent compound **6a** was added in increments every hour (0.25 equiv, 0.5 equiv, 1.0 equiv, 2.0 equiv, 2.7 equiv) (total: 2.27 mmol, 2.7 equiv) and monitored by proton and fluorine NMR spectroscopies. Proton NMR spectrum similar to that of run 2.

Run **6a** and **6b**

To an oven-dried flask was added dried CB-cyclam (0.0600 g, 0.26 mmol) and dry DCM (5.0 mL). Dry DIPEA (0.1027 g, 0.7946 mmol) was added dropwise to the solution. The reaction flask was placed in an ice bath and compound **6a** (0.1595 g, 0.5481 mmol, 2.01 equiv) was added to the reaction flask using DCM (2 x 1.0 mL). The reaction mixture was stirred under nitrogen for 38 hours at room temperature. More compound **6a** (total 0.3158 g, 1.0845 mmol) and DIPEA (total 0.2734 g) were added and the mixture was stirred for an additional 37 hours at room temperature. Aliquots were taken and

checked for completion by proton and fluorine NMR and mass spectrometry. The reaction was concentrated under vacuum. Proton NMR spectrum similar to that of run 2. The crude product (0.3040 g, amber oil) was sent to our collaborators for purification by HPLC. ESI-TOF MS *m*/*z* 509.7 (*M* + H), (calculated for $C_{22}H_{40}N_{10}O_4$ = 508.62).

Run **7a** and **7b**

To an oven-dried flask was added dried CB-cyclam (0.6321 g, 2.7924 mmol) and dry DCM (3.0 mL). Dry DIPEA (0.1214 g, 0.9393 mmol) was added dropwise to the solution. The reaction flask was placed in an ice bath and compound **6a** (0.6111 g, 2.098 mmol) was added to reaction flask and DCM (2 x 5.0 mL). The reaction mixture stirred under nitrogen 12 days. More compound **6** (2.8713 g, total 9.860 mmol) and DIPEA (0.6124 g, total 5.6774 mmol) were added and the mixture stirred for an additional 10 days at 30 ^{o}C. Aliquots were taken and checked for completion by proton and fluorine NMR. The reaction was extracted with DCM (3 x 10 mL) and deionized water (3 x 5 mL) and dried over Na_2SO_4, filtered and concentrated under vacuum. Proton NMR spectrum similar to that of run 2. The crude product (0.2336 g, amber oil) was sent to our collaborators for purification by HPLC. ESI-TOF MS *m*/*z* 509.33 (*M* + H), (calculated for $C_{22}H_{40}N_{10}O_4$ = 508.62).

Run **8**

To an oven-dried flask was added CB-cyclam (0.0495 g, 0.1887 mmol) and dry DCM (3.0 mL). Dry DIPEA (0.15 mL, 0.86 mmol) was added dropwise to the solution. The reaction flask was placed in an ice bath and compound **6a** (0.2209 g, 0.7586 mmol) was added to reaction flask and DCM (4 x 1 mL). The reaction mixture stirred under nitrogen in the glovebox for 3 days. More CB-cyclam (total 0.0564 g, 0.2149 mmol) was

added and allowed to stir for 21 hours. Aliquots were taken and checked for completion by proton and fluorine NMR and mass spectrometry. The solvent of the reaction mixture was left to slowly evaporate to form $DIPEAH^+$ TfO^- crystals (confirmed by XRD). The yellow/amber solution was separated from the crystals and concentrated under vacuum. After several weeks at room temperature, the crude product (0.2243 g, amber oil) was sent to our collaborators for purification by HPLC, but sample appeared to have decomposed.

Run **9**

To an oven-dried flask was added CB-cyclam (0.0628 g, 0.239 mmol) and dry DCM (4.0 mL). Dry DIPEA (0.9 mL, 5.2 mmol) was added dropwise to the solution. The reaction flask was placed in an ice bath and compound **6a** (0.1316 g, 0.4519 mmol) was added to reaction flask via cannula transfer and DCM (2 x 1 mL). The reaction mixture was warmed to room temperature and stirred under nitrogen in a 60 ^oC oil bath for 16 hours. Aliquots were taken and checked for completion by proton and fluorine NMR and TLC. The reaction was extracted with DCM (2 x 10 mL) and deionized water (2 x 5 mL) and dried over Na_2SO_4, filtered and concentrated under vacuum. The crude product was purified by silica gel chromatography (ACN/DCM, 0.4/1) affording an amber oil (0.0725 g, 59.5%). Proton NMR spectrum similar to that of run 2.

Run **10**

To an oven-dried flask was added CB-cyclam (0.0729 g, 0.278 mmol) and dry DCM (4.0 mL). Dry DIPEA (0.10 mL, 0.57 mmol) was added dropwise to the solution. The reaction flask was placed in an ice bath and compound **6a** (0.0742 g, 0.574 mmol) was added to reaction flask via cannula transfer and DCM (2 x 1 mL). The reaction

mixture was warmed to room temperature and K_2CO_3 (0.3470 g, 2.250 mmol) was added. The reaction was stirred under nitrogen in a 55 ^oC oil bath for 16 hours. Aliquots were taken and checked for completion by proton and fluorine NMR and TLC. The reaction was extracted with DCM (2 x 10 mL) and deionized water (2 x 5 mL) and dried over Na_2SO_4, filtered and concentrated under vacuum. Proton NMR spectrum similar to that of run 2. The crude product was purified by silica gel chromatography (ACN/DCM, 0.4/1) affording an amber oil (0.0375 g, 26.5%). ESI-MS *m*/*z* 509.35 (*M* + H), (calculated for $C_{22}H_{40}N_{10}O_4$ = 508.62).

Separation of dialkylated diastereomers.

Possible diastereomers of dialkylated CB-cyclam were separated by TLC (ACN/DCM, 0.4/1) and visualized by UV-lamp giving two spots with R_f = 0.45 and R_f = 0.31. The crude product from run **10** was heavily spotted on TLC plates and not stained. The spots were scratched off the developed TLC, respectively. The silica gel scratched from each spot was transferred to a Whatman 2 (42.5mm) filter paper in a Buchner funnel with DCM (5.0 mL) and ACN (5.0 mL), and the filtrate was concentrated under vacuum. The concentrated spots resulted in yellow oils (0.0062 g and 0.0057 g, respectively) which were used for copper complexation (see Synthesis of **C** and **D**).

*Synthesis of mono-alkylated CB-cyclam, **B**.*

To an oven-dried flask was added CB-cyclam (0.1052g, 0.4009 mmol) and dry DCM (3.0 mL). To this solution was added fresh compound **6a** dropwise at room temperature. The reaction was let stir in the glovebox for 3 days. Reaction was monitored by proton and fluorine NMR. The reaction solution was washed with 3M NaOH (2 x 70 mL), DCM (1 x 70 mL) and dried over Na_2SO_4 and concentrated under vacuum to give a

crude yellow/ amber oil (0.1247g). The crude product was purified by silica gel chromatography (MeOH/$CHCl_3$/TEA, 1/1/0.08), affording a clear light yellow oil (0.0121g, 0.03293 mmol, 8.2%). The proton NMR spectrum is quite complex since there are two enantiomers possible for the mono-alkylated CB-cyclam. ^{1}H NMR ($CDCl_3$, 499.9 MHz): δ 4.97-4.73 (m, 1H), 4.36-3.76 (m, 1H), 3.72 (s, 3H), 3.69-3.62 (m, 2H), 3.48-3.27 (m, 6H), 3.24-3.02 (m, 2H), 2.98-2.41 (m, 14H), 1.95-1.71 (m, 4H). ^{23}Na NMR ($CDCl_3$, 132.2 MHz): δ -0.0 (s). ^{15}N NMR ($CDCl_3$, 50.7 MHz): δ -36.86, -200.0 , -251.29. ESI-MS *m*/*z* 368.28 (*M* + H), (calculated for $C_{17}H_{33}N_7O_2$ = 367.27), see Appendix Figure A.4.

*Synthesis of **C**.*

To a vial was added compound **Aa** (0.0062 g, 0.012 mmol) and THF (1.0 mL). To this solution was added 1 M LiOH (37.0 µL, 3.0 equiv) and deionized water (0.15 mL). The reaction stirred at room temperature for 2 hours before placing under vacuum. The crude solid was used in the next step without purification.

To a vial was added compound **Ab** (0.0057 g, 0.011 mmol) and THF (1.0 mL). To this solution was added 1 M LiOH (34.0 µL, 3.0 equiv) and deionized water (0.15 mL). The reaction stirred at room temperature for 2 hours before placing under vacuum. The crude solid was used in the next step without purification.

*Synthesis of **D**.*

To crude product **Ca** was added $CuCl_2.2H_2O$ (0.0024 g, 0.014 mmol) and MeOH (1.0 mL). The complexation reaction was stirred at room temperature over 14 hours. The reaction developed a white precipitate which was separated from the green/blue solution. The solution was then placed under vacuum and redissolved in deionized water (1.5 mL). Excess salts were removed from the crude product by running the product through a Bio-

Rad P-2 Gel column using deionized water as the eluent. Colored fractions were setup for recrystallization by slow evaporation. Crystals (goldenrod color) formed and were sent for XRD.

To crude product **Cb** was added $CuCl_2.2H_2O$ (0.0019g, 0.01121 mmol) and MeOH (1.0 mL). The complexation reaction was stirred at room temperature over 14 hours. The mixture developed a white precipitate which was separated from the green/blue solution. The solution was then placed under vacuum and diluted with deionized water (1.5 mL). Excess salts were removed from the crude product by running the product through a Bio-Rad P-2 Gel column using deionized water as the eluent. Colored fractions were setup for recrystallization by slow evaporation. Crystals (shamrock green color) formed and were sent for XRD.

II.2.3. Results and Discussion

After initial efforts to synthesize the dialkylated CB-cyclam macrocycle, we realized the significance of the fact that the starting CB-cyclam was racemic: homochiral alkylating agent **6a** could produce a mixture of product diastereomers. Whatever the cause, the proton NMR spectra of alkylation mixtures proved to be quite difficult to interpret, with one example shown in Figure II.2.5. The reaction was conducted in deuterated methylene chloride and ^{1}H and ^{19}F NMR spectroscopies were used. Even with an internal standard, $C(Si(CH_3)_3)_4$, to help calculate the amount of starting materials and products, the spectra were difficult to analyze.

The reaction progression was monitored by NMR, mass spectrometry and TLC. There are characteristic peaks that could be followed by NMR such as the methoxy and methine protons, Figure II.2.6. Positive mode MS aided in confirming presence of the product: calculated for $M = C_{22}H_{40}N_{10}O_4$, 508.62; found: m/z 509.6 ($M + H^+$).

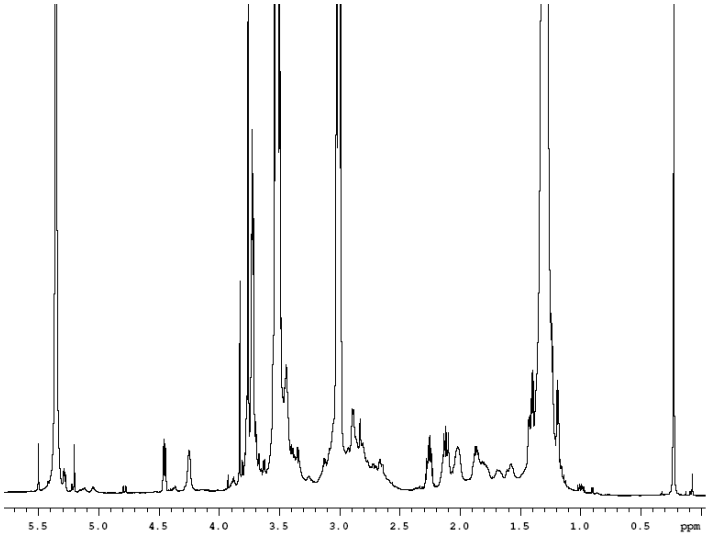

Figure II.2.5. Proton NMR spectrum of reaction mixture to synthesize **A**.

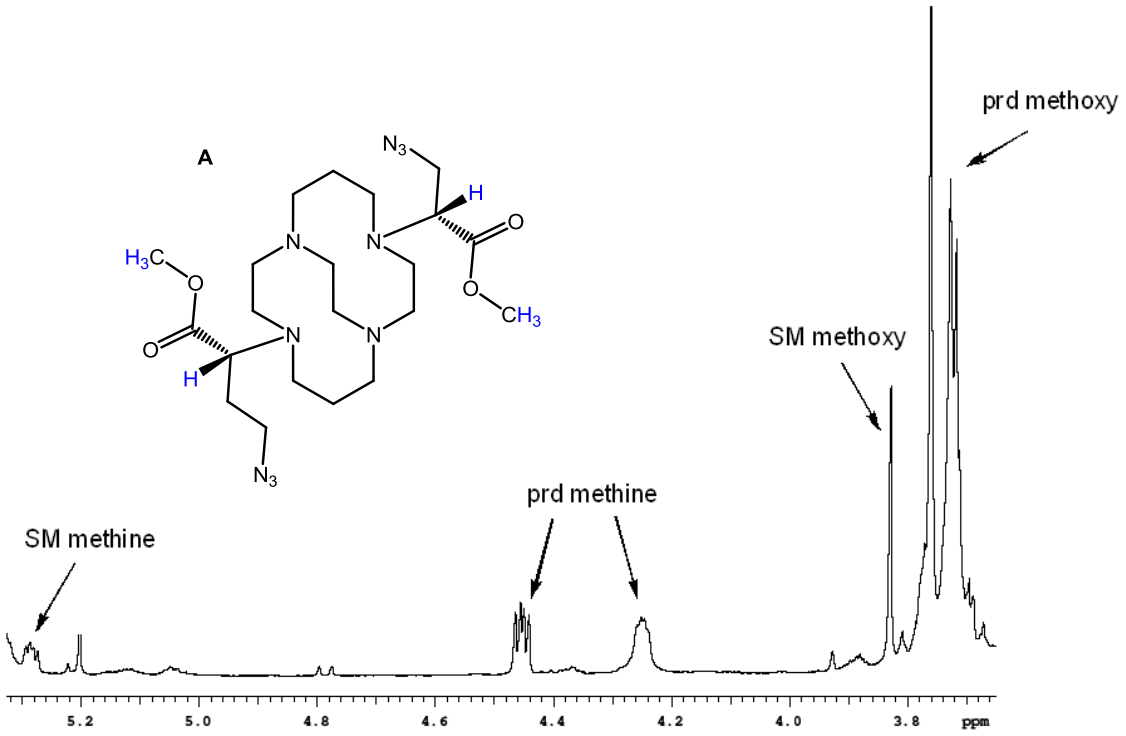

Figure II.2.6. Proton NMR spectra of synthesis of **A** with annotation for key proton assignments.

Several attempts were made to optimize the dialkylation of CB-cyclam. Entries 1, 2 and 3 in Table II.2.1. were J. Young tube reactions that were preliminary tests to gauge the degree of product formation. Based these observations, later experiments and consulting experts in the field, it is known that the first alkylation occurs relatively quickly, but the second alkylation is notoriously more difficult.

Table II.2.1. Optimization of reaction conditions for the dialkylation of CB-cyclam, **A**.

Run	CB-cyclam	Alkylating agent 6 (equiv)*	DIPEA added (equiv)	Time	Solvent	Temp.	Outcome/ Comments
1	$2H_2O$	2.0	5.0	2 h	CD_2Cl_2	RT	mostly monoalkylated & SM
2	$2H_2O$	1.0	5.0	3 d	CD_2Cl_2	RT	mostly mono alkylated & some dialkylated with SM
3	$2H_2O$	2.7[a]	3.0	5 d	CD_2Cl_2	RT	Not isolated (accidently threw away)
4	$2H_2O$	2.0	6.0	16 h	dry CH_2Cl_2	RT	9.6 % isolated yield
5	$2H_2O$	2.2	3.0	5 d	dry DCM	RT to 50 ^{0}C	9.7 % isolated yield
6a	[b]	2.01	3.0	2 d	dry DCM	RT	see 6b
6b	$2H_2O$	2.05	2.2	5 d	dry DCM	RT	0.3040g crude, sent to Pittsburgh
7a	[c]	0.75	2.2	2 d	dry DCM	30 ^{0}C	see 7b
7b	[c]	1.03	2.03	10 d	dry DCM	30 ^{0}C	0.2336g crude, sent to Pittsburgh
8	$2H_2O$	3.95	3.5	23 d	dry DCM	RT	0.2243g crude, sent to Pittsburgh
9	$2H_2O$	2.0	2.2	12 h	dry DCM	60 ^{0}C	59.5% purified
10	$2H_2O$	2.0	2.2 + K_2CO_3	12 h	dry DCM	55 ^{0}C	26.5% purified

* Alkylating agent was made fresh for each reaction.
[a]: stepwise addition 0.25 equiv, 0.5 equiv, 1.0 equiv, 2.0 equiv, total 2.7 equiv.
[b]: dried over molecular sieves , filtered & lyophilized CB-cyclam.[32]
[c]: dried over molecular sieves and put in desiccator with P_2O_5.

We suspected the CB-cyclam from our collaborators might be "wet." We sent a sample for elemental analysis to determine the amount of water molecules associated with the macrocycle, Table II.2.2. From elemental analysis (Found: C% 57.99, H% 11.36, N% 21.93), the CB-cyclam appeared to be a monohydrate.

Table II.2.1. Calculated and experimental values for elemental analysis of CB-cyclam from collaborator.

# of water molecules	C %	H %	N %
0	63.67	11.58	24.75
1	58.98	11.55	22.93
2	54.93	11.52	21.35
3	51.40	11.50	19.98
experimental	57.99	11.36	21.93

The amount of base required to push the reaction forward was assumed to be at least 3.0 equivalents, since the two secondary amines and the water from the CB-cyclam hydrate need to be deprotonated. In Run 4, freshly made alkylating agent **6a** was used unpurified and a large excess of *N*,*N*-diisopropylamine (DIPEA) was used, yet only a meager amount of dialkylated product was isolated. In Run 5, the alkylating agent was washed with pentanes to remove protonated DIPEA and heated in intervals over 5 days but still did not yield much product.

The main hurdle was the hydrated CB-cyclam starting material. The water could and mostly likely did act as a nucleophile and reacted with compound **6a** reverting it back to compound **5**, removing the alkylating agent from the reaction. Reaction conditions always used dry CH_2Cl_2 solvent and were set up using Schlenk line techniques and/or the glovebox. For runs 6 and 7, attempts were made to dry the CB-cyclam hydrate before alkylation by either drying the starting material over molecular sieves (which worked

well for us in the alkylation of formylcyclen hydrate, see Chapter I) and either lyophilizing or drying over phosphorous pentoxide, respectively. Both yielded monoalkylated and dialkylated products which were sent to our collaborators at the University of Pittsburgh (U. Pitt.) for further purification. Upon analysis with HPLC and TOF MS-ES at U. Pitt., the dialkylated product isolated was not as clean as previously sent samples (see Appendix Figure A.4). In run 8, more freshly made dialkylating agent was used (~ 4 equiv) to drive the reaction forward and left unheated for fear of racemization. The crude products were sent to University of Pittsburgh, where our collaborators were able to purify clean dialkylated product (see Appendix Figure A.5).

Because the previous drying methods did not yield the desired results, a comparative study was done using higher temperatures and another drying agent, K_2CO_3 (runs 9 and 10). Dialkylated products were formed in both reactions, confirmed by NMR and MS, but run 9 gave more than twice the product yield than run 10 with K_2CO_3. Optimizing this reaction has been tricky. It appears the physical presence of a drying agent during the reaction seems to interfere with clean alkylations. Perhaps the minute amount of water present might aid in stabilized the protonated DIPEA from becoming deprotonated from the ring amine, but this explanation is only speculative. In any case, the yield of dialkylated CB-cyclam (**A**) was successfully increased from ~10% to ~60%, which was deemed a significant success.

It is interesting to note that the CB-cyclam from our collaborators was racemic about the nitrogens. During the purification of the dialkylated product (**A**), the TLC showed two spots that were somewhat separated from each other (R_f: 0.45 & 0.31 in 40% ACN/DCM). These two spots were found to both be dialkylated product (**A**) by MS. This

led us to conclude that they might be the diastereomers of **A**. Since during the column purification these two spots were not separated, an unconventional method was used to isolate each spot on the TLC. After heavily spotting and developing the TLC, the spots were scratched off the TLC plate and isolated from the silica by washing with dichloromethane.

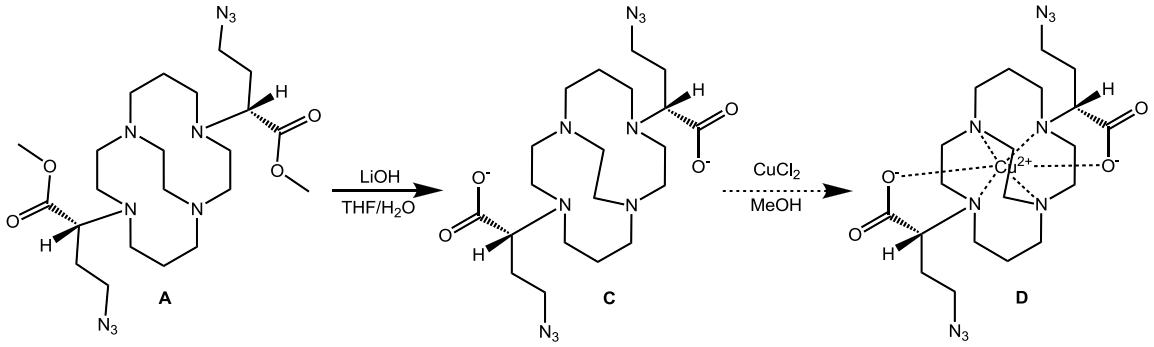

Figure II.2.7. Synthetic scheme for copper complexation of compound **A**.

In an effort to confirm the structure and presence of stereoisomers, the spot extracts were treated with base to deprotect the methyl esters and complexed with cold copper to crystallize. Each potentially diastereomeric copper complex appeared to have formed different colored crystals (golden rod yellow and shamrock green). We sent the crystals to UCSD small molecule X-ray facility for analysis, but unfortunately, the crystals were just copper chloride, the copper source for complexation. The complexation can be optimized by heating and using copper perchlorate as a copper source.

II.2.4. Conclusions

We have made two novel PET tracer chelates, compounds **A** and **B**, that are currently being used as ^{64}Cu PET tracers by our collaborators. Our chelates offer ligands that can saturatively coordinate copper and coupling arm/s to link to molecules of

interest. The dialkylation of CB-cyclam with our homochiral linker proved to be challenging and puzzling, yet we were able to significantly increase the product yield. We were able to separate possible diastereomers of the dialkylated product (**A**) from TLC spots. And although we were not able to crystallize the copper complexes, the project is primed to efficiently make more compound **A** and **B** as well as try other copper complexation and crystallization methods.

II.2.5. Acknowledgements

I would like to thank our collaborators at the University of Pittsburgh: Erik Wiener and Carolyn Anderson for the opportunity to work on this project, and Dexing Zeng for his patience, guidance and starting material for this project. I especially thank Josh Swider for mass spectrometry analysis of some key samples.

II.2.6. References

[1] Prince, J. L. & Links, J. M. (**2006**) *Medical Imaging Signals and Systems*. Upper Saddle River, NJ: Pearson Prentice Hall.

[2] Cherry, S. R., Sorensen, J. A., & Phelps, M. E. (**2003**) *Physics in Nuclear Medicine* (3rd ed.). Philadelphia, PA: Saunders.

[3] Rudin, M. ; Weissleder, R. *Rev. Drug. Discov*. **2003**, *2*, 123.

[4] *Table of Isotopes*, 7th ed.; John Wiley & Sons: New York, 1978; Vol. 7.

[5] Zaman, M. R.; Qaim, S. M. *Radiochim. Acta* **1996**, *75*, 59.

[6] Bass, L. A.; McCarthy, D. W.; Jones, L. A.; Cutler, P. D.; Shefer, R. E.; Klinkowstein, R. E.; Schwarz, S. W.; Cutler, C. S.; Lewis, J. S.; Anderson, C. J.; Welch, M. J. *J. Labelled Compd. Radiopharm.* **1997**, *40*, 325.

[7] Blower, P. J.; Lewis, J. S.; Zweit, J. *Nucl. Med. Biol.* **1996**, *23*, 957.

[8] McCarthy, D. W.; Shefer, R. E.; Klinkowstein, R. E.; Bass, L. A.; Margeneau, W. H.; Cutler, C. S.; Anderson, C. J.; Welch, M. J. *Nucl. Med. Biol.* **1997**, *24*, 35.

[9] Loćh, C.; Mazie`re´, B.; Comar, D. *J. Nucl. Med.* **1979**, *21*, 171.

[10] Rösch, F.; Qaim, S. M.; Stöcklin, G. *Radiochim. Acta* **1993**, *61*, 1.

[11] Anderson, C. J. and Welch, M. J. *Chem. Rev.* **1999**, *99*, 2219-2234.

[12] Petering, D. H. *Bioinorg. Chem.* **1972**, *1*, 255.

[13] Green, M. A. *Nucl. Med. Biol.* **1987**, *14*, 59.

[14] Moi, M. K.; Meares, C. F.; McCall, M. J.; Cole, W. C.; DeNardo, S. J. *Anal. Biochem.* **1985**, *148*, 249.

[15] Cole, W. C.; DeNardo, S. J.; Meares, C. F.; McCall, M. J.; DeNardo, G. L.; Epstein, A.L.; O'Brien, H. A.; Moi, M. K. *Int. J. Radiat. Appl. Instrum. Part B Nucl. Med. Biol.* **1986**, *13*, 363.

[16] Kukis, D. L.; Diril, H.; Greiner, D. P.; DeNardo, S. J.; DeNardo, G. L.; Salako, Q, A.; Meares, C. F. *Cancer* **1994**, *73*, 779.

[17] Anderson, C. J.; Rocque, P. A.; Weinheimer, C. J.; Welch, M. J. *Nucl. Med. Biol.* **1993**, *20*, 461.

[18] Rogers, B. E.; Anderson, C. J.; Connett, J. M.; Guo, L. W.; Edwards, W. B.; Sherman, E. L. C.; Zinn, K. R.; Welch, M. J. *Bioconjugate Chem.* **1996**, *7*, 511.

[19] Bass, L. A.; Wang, M.; Welch, M. J.; Anderson, C. J. *Bioconjugate Chem.* **2000**, *11*, 527.

[20] Boswell, C. A.; Sun, X.; Niu, W.; Weisman, G. R.; Wong, E. H.; Rheingold, A. L.; Anderson, C. J. *J. Med. Chem.* **2004**, *47*, 1465.

[21] Pandya, D. N.; Kim, J. K.; Park, J. C.; Hochun Lee, H.; Phapale, P. B.; Kwak, W.; Choi, T. H.; Cheon, G. J.; Yoon, Y.-R.; Yoo, J. *Chem. Commun.* **2010**, *46*, 3517.

[22] (a) de Jong, M.; Bakker, W. H.; Krenning, E. P.; Breeman, W. A. P.; van der Pluijm, M. E.; Bernard, B. F.; Visser, T. J.; Jermann, E.; Béhé, M.; Powell, P.; Mäcke, H. R. *Eur. J. Nucl. Med.* **1997**, *24*, 368, (b) Li, W. P.; Lewis, J. S.; Kim, J.; Bugaj, J. E.; Johnson, M. A.; Erion, J. E.; Anderson, C. J. *Bioconjugate Chem.* **2003**, *13*, 721; (c) Shokeen, M.; Anderson, C. J. *Accts. Chem. Res.* **2009**, *42*, 832; (d) Silversides, J. D.; Smith, R.; Archibald, S. J. *Dalton Trans*. **2011**, *40*, 6289; (e) Lebedev, A. Y.; Holland, J. P.; Lewis, J. S. *Chem. Commun.* **2010**, *46*, 1706.

[23] Wang, M.; Caruano, A. L.; Lewis, M. R.; Meyer, L. A., VanderWaal, R. P.; Anderson, C. J. *Cancer Res.* **2003**, *63*, 6864.

[24] Sprague, J. E.; Peng, Y.; Sun, X.; Weisman, G. R.; Wong, E. H.; Achilefu, S.; Anderson, C. J. *Clin. Cancer Res*. **2004**, *10*, 8674.

[25] (a) C. M. Perkins (Procter&Gamble Company), *US Pat.*, 6,627,176, **2003**; (b) J. B. Brogan (General Electric Company), *US Pat.*, 7,306,785, **2007**.

[26] Lewis, E. A.; Boyle, R. W.; Archibald, S. J. *Chem. Commun.* **2004**, *19*, 2212.

[27] Lewis, E. A.; Allan,C. C.; Boyle, R. W.; Archibald, S. J. *Tetrahedron Lett.* **2004**, *45*, 3059.

[28] Boswell, C. A.; Regino, C. A. S.; Baidoo, K. E.; Wong, K. J.; Bumb, A.; Xu, H.; Milenic, D. E.; Kelley, J. A.; Lai, C. C.; Brechbeil, M. W. *Bioconj. Chem.* **2008**, *19*, 1476.

[29] Liu, W.; Hao, G.; Long, M. A.; Anthony, T.; Hsieh, J.T.; Sun, X. *Angew. Chem. Int. Ed.* **2009**, *48*, 7346.

[30] Huang, Z.; Raghvendra, S.; Nigam, A.; Abadjian, M.-C.; Potter, D. M.; Grotjahn, D.B.; Wiener, E. C. *Invest. Radiol.* **2010**, *45*, 641.

[31] Sun, X.; Wuest, M.; Weisman, G. R., et al. *J. Med. Chem.* **2002,** *45*, 469.

[32] Wong, E. H.; Weisman, G. R.; Hill, D. C.; Reed, D. P.; Rogers, M. E.; Condon, J. S.; Fagan, M. A.; Calabrese, J. C.; Lam, K.-C.; Guzei, I. A.; et al *J. Am. Chem. Soc.* **2000**, *122*, 10561.

CHAPTER III

Study of Iridium-based Catalysts for Water Oxidation with Ceric Ammonium Nitrate showing Evidence of Iridium Nanoparticles

III.1 Introduction to Water Oxidation Catalysts (WOC)

Current concerns revolving around global warming and using non-renewable energy sources have propelled the search for alternative fuels. In Nature, photosystem II, found in green plants and algae, converts water to oxygen using sunlight. By analogy, if we could make a photocatalyst for oxidizing water, but use the electrons to reduce water and make hydrogen, we would achieve sunlight-driven water splitting (eq 1). Harnessing such a conversion for commercial uses would provide an alternative to fossil fuels as a viable, clean (carbon neutral) and relatively cheap energy source.[1,2] Photosystem II is comprised of a multi-metallic ($CaMn_4O_5$) core, which has inspired research into multimetallic water splitting cataysts, yet research has shown that single metal site complexes can also achieve oxidation of water to O_2 (eq. 1b).[3] Other complexes such as Fe- or Co-based catalysts[4] provide precedence that other metals besides Ru or Mn can catalyze water oxidation.

Water splitting can be thought of as the sum of two half-reactions, the water oxidation reaction (1a) and the proton reduction reaction (eq. 1b). Ideally, catalyst(s) would be able to perform these reactions in series to give energy and non-greenhouse gases. Of the two half-reactions, water oxidation (see eq. 1a) is considered the most challenging,[5,6] so our group decided to approach this half-reaction.

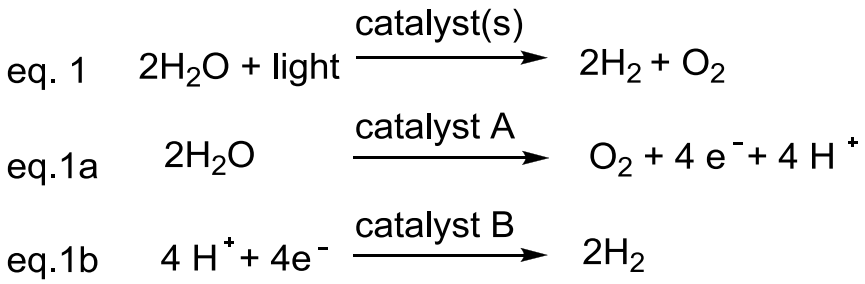

In 2008, Bernhard's group reported the first iridium-based WOC.[4] Therefore, in 2008-2009, like other groups searching for competent catalysts, our group focused on finding an iridium-based catalysts while using a sacrificial oxidant to remove electrons. Throughout water oxidation literature, ceric ammonium nitrate (CAN) is a commonly used oxidant used to test catalysts.[7] Typical reaction CAN/catalyst ratios are 100-10,000 (very acidic conditions) and CAN concentrations range from ~0.01 M to more than 1 M. The ability of CAN to oxidize organic compounds is well-known, so perhaps in hindsight the results of the Grotjahn group's research are not surprising, but in the years 2008-2011, many people were assuming that molecular iridium-based WOC were robust when driven by CAN, when in fact the oxidant was causing numerous changes to the catalysts. Publication of the Grotjahn lab's paper in late 2011 helped redirect the field, and culminated the work of 13 people; the project was risky enough that no one person based their thesis research on it, with the work in the Grotjahn lab on Ir-based WOC being divided among 9 students (4 Ph.D., 3 M.S., one undergraduate), and one visiting professor and the PI.

Since 1982,[8a] Ru has been the most common metal used to make catalysts for water oxidation,[8] but other metals have been shown to be active (e.g. Mn, Fe, Co).[9] The report of Bernhard's group in 2008 showcased the first discrete Ir-based water oxidation

catalyst **1** and analogs.[10] Other Ir-based catalysts followed: Cp*Ir-based systems **2a**,**b**[11] as well as simpler complexes such as **5** and **6**,[12,13] carbonyl analog **8**,[13] chelating carbene complexes **3a** and **4a**,[14] unidentate carbene complex **9**,[15] a chelating carbene complex related to both **2a** and **9** (not shown),[16] and binuclear (COD)Ir system **7**.[17] Since iridium is a precious metal, large-scale application would only be possible if a robust catalyst is made.[18] Our group's interest in Cp*Ir chemistry[19] exemplified by complexes such as **10**[20] has led us to explore such complexes as WOC.

III.2 Study of the destiny of Ir-based WOC during cerium (IV) oxidations

The preliminary findings of others in the research group were that iridium-rich nanoparticles (NPs) were forming from complexes **1-10** (Figure III.2.1.). Under strongly oxidizing conditions, it seemed reasonable that iridium-rich NPs would be oxides, typically of the formula IrO_x or IrO_2 which are known, efficient catalysts for water oxidation.[21] The possibility that some iridium-based organometallic catalysts[11,12,15,17] (Figure III.2.1.) could be forming NPs was considered, but without any direct evidence. On the contrary, there was even negative evidence in some studies.[12]

This section starts by summarizing data from others on the project that pointed toward changes in molecular iridium catalysts, followed by what I contributed to the project in order to get the paper published. Data shown in Figures III.2.2 to III.2.7 and III.2.9 to III.2.13 were obtained by other co-authors on the published paper. Data shown in Figure III.2.8 and Table III.2.1 entries 1-2 were obtained by Dr. Douglas Grotjahn and Jessica Martin. Data shown in Table III.2.1 entries 3-16 were obtained by Jessica Martin and Marie-Caline Abadjian.

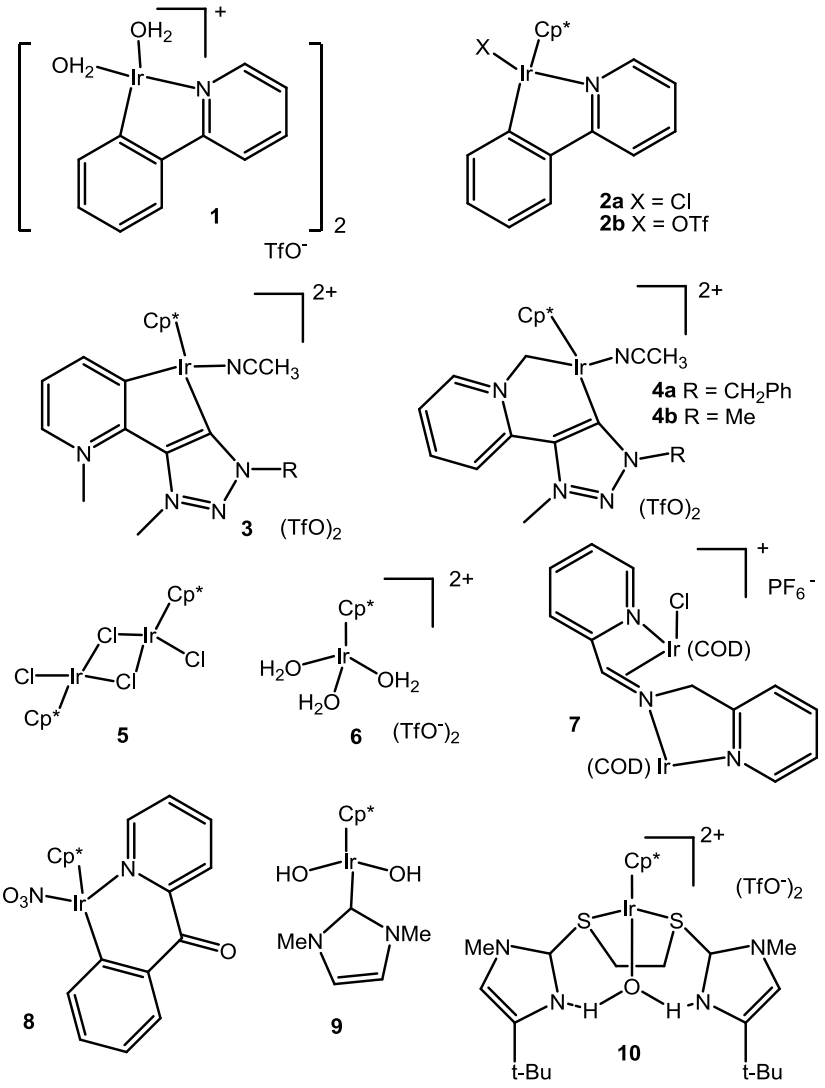

Figure III.2.1. Organometallic water oxidation catalysts of iridium.

As discussed above, ultimately one wants to use efficient catalysis of water oxidation driven by sunlight, altogether a major scientific and technical challenge. However, using sacrificial oxidant as a start, our group (like others) added catalysts in a minimal amount of water, acetonitrile or water-acetonitrile mixtures to aqueous CAN (ceric ammonium nitrate) at the same initial concentrations used by previous studies (78 mM[9] or 172 mM[10]).

Oxygen production from the various Ir-based catalysts tested was monitored by

several methods. In addition, color changes were observed from the initial vibrant orange of CAN to various shades of pale violet, blues, or olive greens as the reactants mixed depending on the catalyst used and progression of the reaction. Since aqueous Ce(IV) is a bright orange and Ce(III) is colorless,[22] it was postulated that the color changes involved the catalysts somehow. According to literature,[21b,21c,21f] colors described as "blue", "purple" or "blue-gray" were associated with IrO_2 or IrO_x NP. Distinctive UV-vis absorption spectra with a maximum between 550 – 700 nm had been observed depending on additive and perhaps NP size or aggregation.[21a,21c,21f] In our lab, water oxidation reaction mixtures with a variety of Ir-based catalysts showed growth of UV-vis absorbances between 550 – 650 nm (Figure III.2.2.) which agreed with recorded ranges of absorption maxima for IrO_2 or IrO_x NPs.[21b,21c,21f] Even when $IrCl_3$ was used as a catalyst, similar results as **6** and **9** were observed: an initial rise in absorbance around 560 nm then decline and rise of another absorption around 610-620 nm. The changes in absorbance over the reaction time suggested the formation of NPs in the reaction mixture. Control experiments were done before oxidation to verify that the catalysts did not absorb in the 550 -700 nm range.

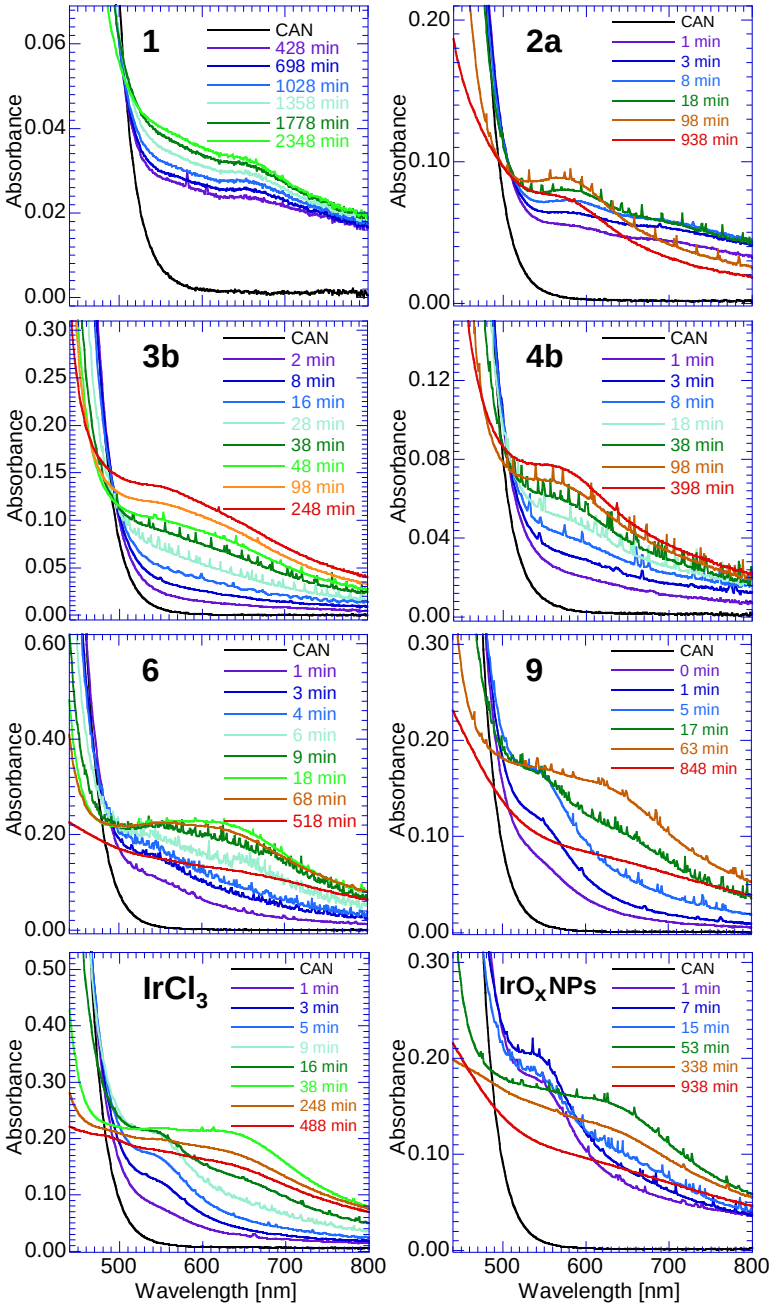

Figure III.2.2. UV-vis absorption spectra obtained at various times after the catalyst indicated was added to freshly prepared aqueous solutions of CAN ($[CAN]_0$ = 75.8-78.9 mM). The amount of catalyst added was such that $[catalyst]_0$ ~ 0.05 mM (range 0.050 – 0.053 mM), $[CAN]_0$ / $[catalyst]_0$ = 1560. The absorbances with maxima between 550 and 650 nm are ascribed to IrO_x NPs. Small spikes on the traces are caused by gas bubbles (O_2, as detected in separate experiments, not shown).

To further explore the role of initial concentration of catalyst, another set of experiments were designed. A sufficient amount of **2a** was added to a CAN aqueous solution (78 mM) in CH_3CN/H_2O (85:15) to make mixtures with $[\mathbf{2a}]_0$ = 1.35, 0.45, 0.15, 0.05, and 0.0157 mM. From the series of dilutions, even at the most dilute concentration of catalyst **2a** (0.0157 mM), gave detectable growth of a peak near 580 nm in the UV-vis spectrum (Figure II.2.2.). The maximal absorbance at this wavelength was about proportional to the concentration of **2a** (compare Figure III.2.2.a-c also see Figure III.2.2.d). The conditions under which Figure III.2.2.c (lower left) were generated are within range of concentrations used by the Crabtree group for water oxidation reaction (using [**2a**] = 0.001-0.020 mM, typically 0.005 mM). At a lower concentration ([**2a**] = 0.0052 mM), it could not be determined whether there was a distinct peak at 580 nm. From Figure III.2.2.d, the data for this experiment (lower left point) fit a trend over a 30-fold range in catalyst **2a** concentrations. A detectable absorbance peak at 580 nm was seen within minutes of adding sufficient catalyst, $[\mathbf{2a}]_0$ = 0.05 mM (Figure III.2.2.b). The greatest intensity of the absorbance at 580 nm was reached within 3 hours but then slowly diminished (over hours). Complex **1** was the slowest to develop an absorbance peak between 600 – 650 nm as well as the slowest of the tested catalysts. Production of O_2 by catalysts **1-9** was previously shown occur over at least one hour and then taper off over time.[21] Catalyst **6** at various concentrations (0.050 to 0.005 mM) showed very similar results shown in Figure III.2.2. Savini et al. had found that this simple catalyst (**6**)[13] to be 2-3 times faster than **2a** or **9**[21d] at forming oxygen.

To provide further evidence of the presence of IrOx NPs, scanning transmission electron microscopy (STEM) and powder X-ray diffraction were used. The powder X-ray

diffraction (PXRD) data were obtained from water oxidation samples ($[CAN]_0$ = 78 mM, $[\mathbf{2a}]_0$ = 0.45 mM) where aliquots were removed after 15, 45, 115, and 120 minutes (procedure: frozen in dry ice-acetone and then lyophilized overnight). Both the aliquots removed and the yellowish solids left after removing water showed the 580 nm absorption. The intensity of the absorption was somewhat reduced after lyophilization. Data from powder XRD of the residual solids were assigned to IrO_2, of which greater signal intensities arose from aliquots that were removed later in the water oxidation process. Peaks for Ce_2O_3 were also seen in samples.

Another experiment was done using 10% as much cerium ($[CAN]_0$ = 7.8 mM) with the same initial concentration of **2a** to decrease the amount of CAN-derived peaks, so as to make IrO_2 peaks more evident. It is possible that not all iridium was in the form crystalline IrO_2, but perhaps significant amounts might be in the form of IrO_x NP, which would not show up as IrO_2 peaks.

III. 2.2 Experimental Section

2.2.1 STEM and EDX

To assess the formation of nanoparticles from our reactions, scanning transmission electron microscopy (STEM) and energy dispersive X-ray spectroscopy (EDX) were used. Our collaboration at UCSD with Dr. Kenneth Vecchio enabled access to a Hitachi HD2000 STEM equipped with a cold cathode field emission electron source and a turbo-pumped main chamber. Samples were prepared by adding the reaction solution (1-2 drops) directly onto a carbon film coated with a copper grid. The samples were allowed to air dry for 1-2 minutes and then coated with a thin amorphous carbon film by evaporation to provide a uncharged surface coating.

Characterization of the samples used STEM for morphology and structure and EDX for elemental identification. STEM images were scanned beam images, using the secondary electron signal, which provides surface topology, the direct transmitted electron beam (unscattered electrons) or the diffracted transmission electrons collected on an annular dark field detector.

2a + CAN after 15 min (see Figure III.2.3)

A solution was made with CAN (216.1 mg, 0.394 mmol) and water (4.67 mL) to which was added sufficient nitric acid to reach pH = 1. A second solution was made from **2a** (20.9 mg, 0.0405 mmol) in acetonitrile (1.7 mL) and water (0.3 mL) ([**2a**] = 20.2 mM). To the freshly made CAN solution was added **2a** solution (0.333 mL, enough to make $[\mathbf{2a}]_0$ = 1.35 mM and $[CAN]_0$ = 78.8 mM). The color of the mixture became dark forest green. After 15 min, a sample was plated on a grid, and the sample was carbon coated and mounted into the STEM. Nanoparticles rich in cerium and iridium were found.

2a + CAN after 4h (see Figure III.2.4)

A solution was made with CAN (262.0 mg, 0.478 mmol) and water (5.0 mL). A second solution was made from **2a** (20.7 mg, 0.0400 mmol) and water (5.0 mL). To a sample of the CAN solution (2.9 mL, containing 0.277 mmol, enough to make $[CAN]_0$ = 79.2 mM) was added to a sample of the **2a** solution (0.60 mL, enough to make $[\mathbf{2a}]_0$ = 1.37 mM). The mixture turned brownish-yellow, then greenish-yellow. After 3 and 4 h total reaction time, the mixture was green and slightly cloudy. Samples were plated and mounted into the STEM at the 4 h time point.

1 + CAN after 6.3 h (see Figure III.2.5)

A solution was made with CAN (85.4 mg, 0.156 mmol) and water (1.778 mL). A second solution was made from **1** (9.7 mg, 0.0141 mmol) and water (1.00 mL) ([**1**] = 14.1 mM). To the freshly made CAN solution was added a sample of the **1** solution (0.222 mL, enough to make $[\mathbf{1}]_0$ = 1.57 mM and $[CAN]_0$ = 78.0 mM). The color of the mixture became pinkish-purple, then a grayish-brown. After 6.3 h, a sample was plated on a grid and carbon coated. The STEM-EDX showed nanoparticles rich in cerium and iridium.

3b + CAN after 16 min (see Figure III.2.6)

A solution was made with CAN (128.5 mg, 0.234 mmol) and water (2.31 mL) to which was added sufficient nitric acid to reach pH = 1. A second solution was made from **3b** (5.0 mg, 0.0058 mmol) in water (1.0 mL) ([**3b**] = 5.8 mM). To the freshly made CAN solution was added the **3b** solution (0.69 mL, enough to make $[\mathbf{3b}]_0$ = 1.35 mM and $[CAN]_0$ = 78.0 mM). After 11 min, the mixture was dark purple and clear. After mixing (16 minutes), a sample was plated on a grid, and within another 16 min had been carbon-coated, and was then mounted into the STEM.

6 + CAN after 15 min (see Figure III.2.7)

A solution of **6** was prepared with $[Cp^*Ir(\mu\text{-}Cl)Cl]_2$ (10.3 mg, 0.0129 mmol) and AgOTf (13.4 mg, 0.0522 mmol) in water (0.7 mL) to give **6** in water ([**6**] = 36.9 mM) according to amounts of reactants used). A fresh solution was made from CAN (128.4 mg, 0.234 mmol) and water (2.89 mL). To the freshly made CAN solution was added the **6** solution (110 µL, enough to make $[\mathbf{6}]_0$ = 1.35 mM and $[CAN]_0$ = 78.1 mM). The mixture became intense purple color. After 15 min, a sample was plated on a grid, and within another 10 min had been carbon coated, and was then mounted into the STEM.

IrO_x NP + CAN after 1 min and 15 min (see Figure III.2.8.)

Two separate but essentially identical preparations were made, differing only in the time point that the sample was removed for analysis. A fresh solution was made with CAN (21.2 mg, 0.0387 mmol) and water (161 μL). To the solution (made 15 min earlier) was added a preparation of IrO_x NP (335 L of 2.0 mM, intended to give $[IrO_x]_0$ = 1.34 mM and $[CAN]_0$ = 77.4 mM. The mixture retained the purple color of the IrO_x NP. Within a minute a sample was plated on a grid, and within another 10 min had been carbon-coated, and was then mounted into the STEM. The second reaction was prepared in nearly identical fashion as the first, but the sample was removed after 15 min of mixing. Nanoparticles appear to be present, but they are associated within a Ce-rich matrix. From UV-vis experiments (see Figure III.2.2), the cerium is reduced to Ce(III) material since, the Ce(IV) species CAN is gone after only 1 min.

$IrCl_3$ + CAN after 3.5 h (see Figure III.2.9. and III.2.10.)

A solution was made from CAN (84.1 mg, 0.153 mmol) in deoxygenated water (7 mL; $[CAN]_0$ = 21.9 mM). After 5 min, to this solution was added a solution of $IrCl_3$ x H_2O [0.50 mL of a solution made from $IrCl_3$ x H_2O (9.9 mg, 0.0283 mmol) and water (0.92 mL), 0.0307 M, or 0.0154 mmol]. The mixture color became greenish on mixing. After 3.5 h, the green color became darker. At this point samples were plated on a grid and carbon-coated, and then mounted into the STEM. Nanoparticles rich in cerium and iridium were found.

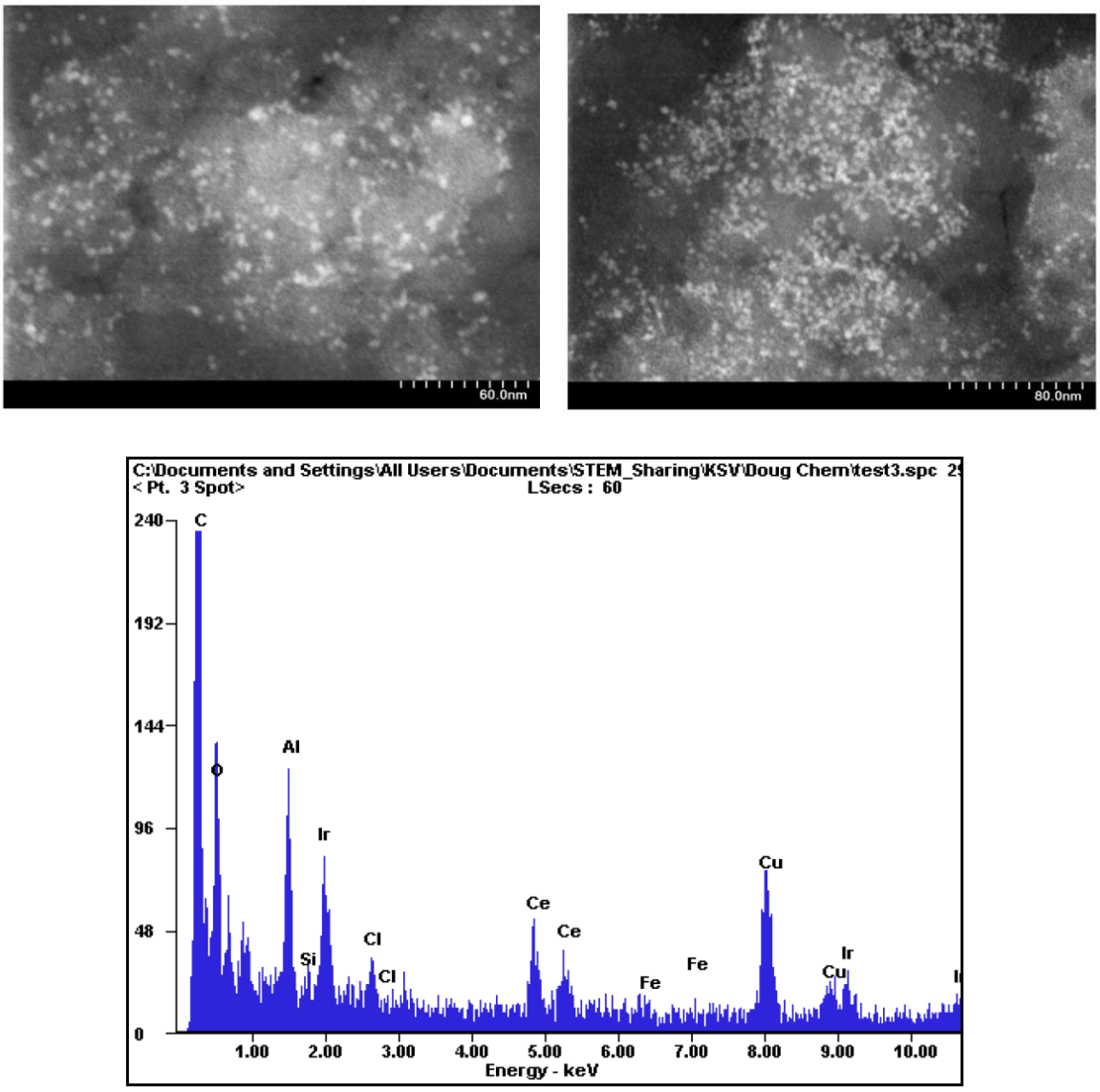

Figure III.2.3. Sample removed 15 min after **2a** was added to CAN. UV-vis data (see Figure III.2.2) from an identical but separate experiment show that within 15 min, a strong UV-vis absorption near 580 nm develops under these conditions. Above: STEM images. Below: EDX data showing Ir, Ce, O, and Cl present in the samples. The Cu and Al peaks are derived from the sample grid and X-ray detector, respectively. Carbon is present in the sample itself, the plate, and the coating.

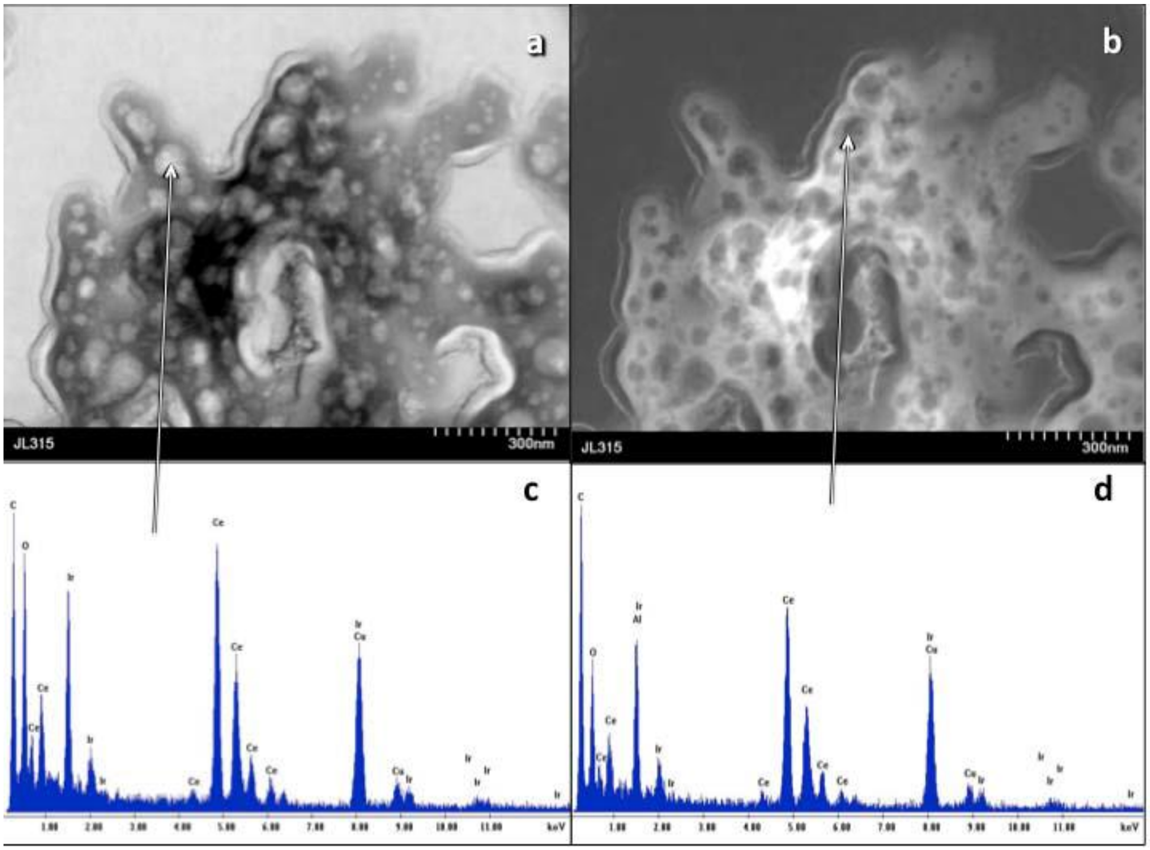

Figure III.2.4. Bright-field (a) and dark-field (b) images of Ce- and Ir-rich material from mixing **2a** and CAN after 4 h. (c, d) EDX spectra showing Ir, Ce, and O present in the samples. The Cu and Al peaks are derived from the sample grid and X-ray detector, respectively. Carbon is present in the sample itself, the plate, and the coating.

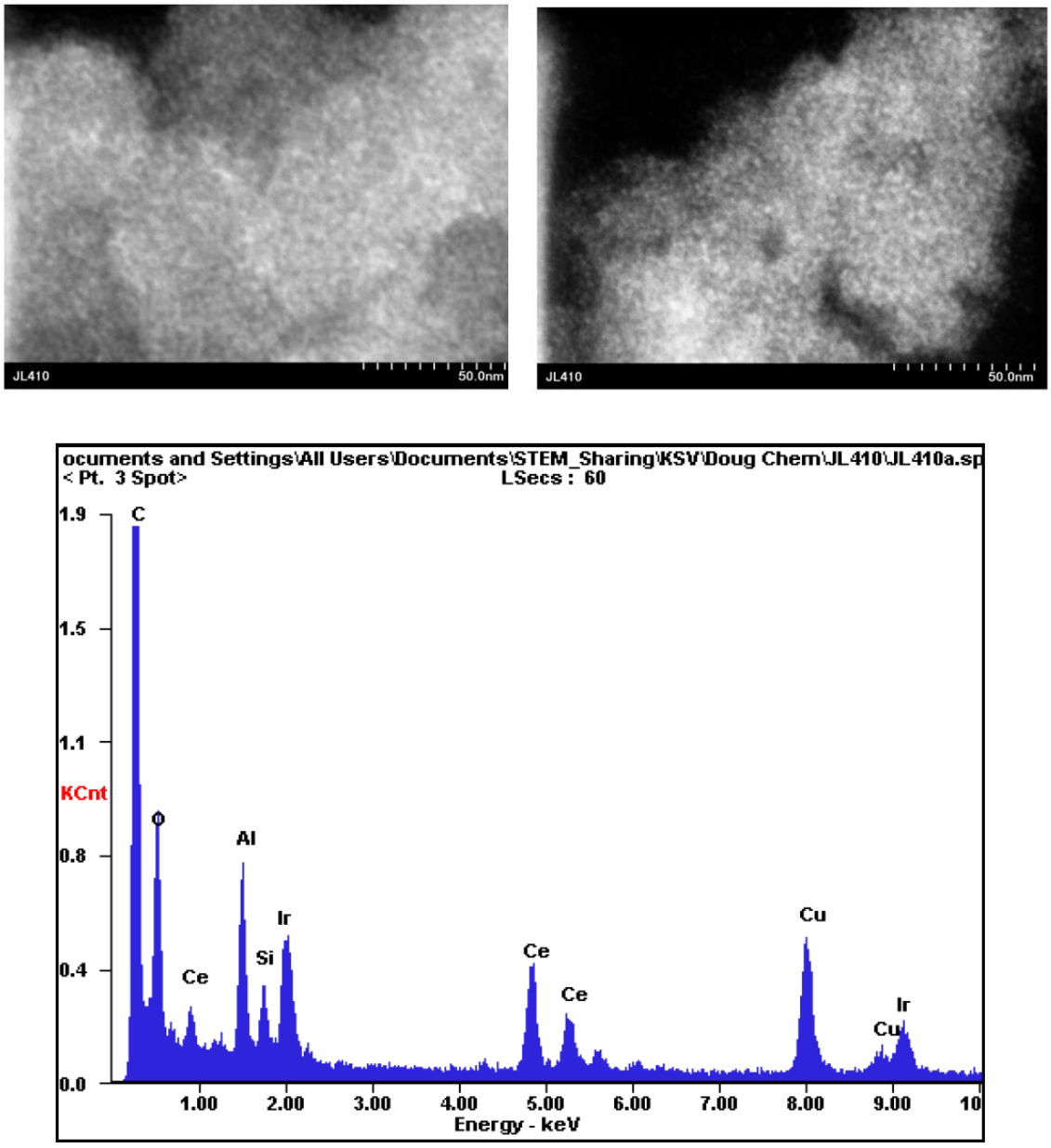

Figure III.2.5. Sample removed 6.3 h after adding **1** to CAN. Above: STEM images. Below: EDX data showing Ir, Ce, O, and Cl present in the samples. The Cu and Al peaks are derived from the sample grid and x-ray detector, respectively. Carbon is present in the sample itself, the plate, and the coating.

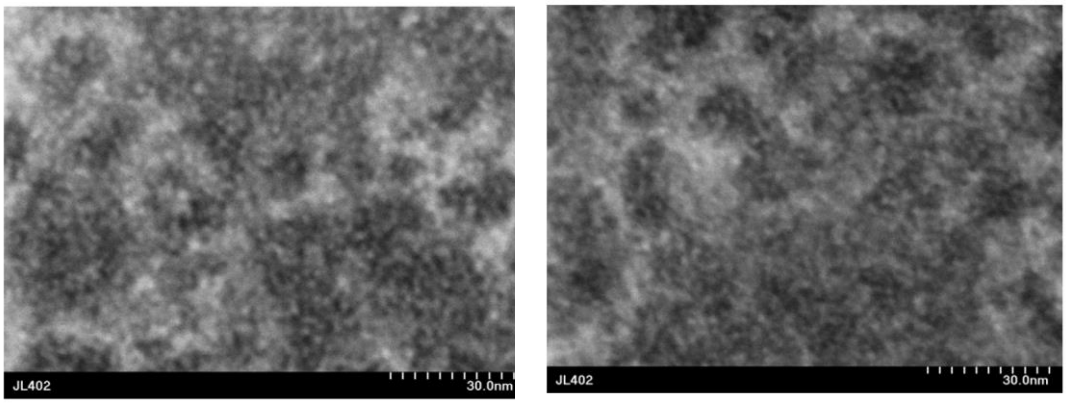

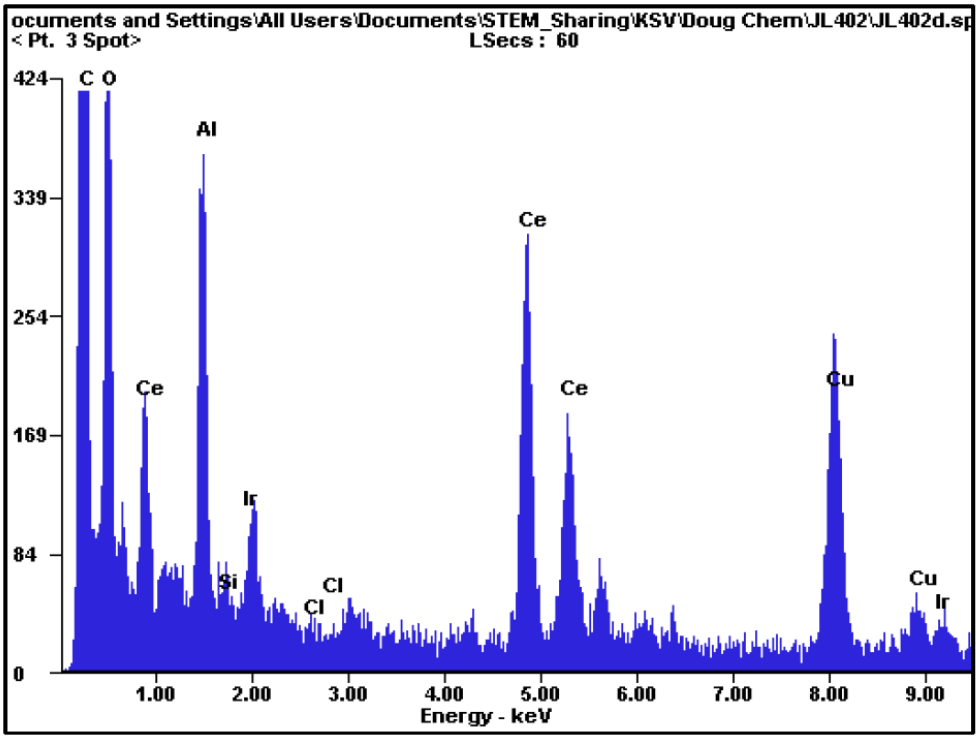

Figure III.2.6. Sample removed 15 min after **3b** was added to CAN. UV-vis data (see Figure III.2.2) from an identical but separate experiment show that within 15 min, a strong UV-vis absorption near 580 nm develops under these conditions. Data from yet another separate but identical experiment on **3b** (not shown) show that the 580-nm absorption is only slightly diminished in intensity after lyophilization or evaporation under oil-pump vacuum, showing that whatever gives rise to the 580 nm absorption is present both before and after concentration, hence would be expected to be visible in this Figure also. Above: STEM images. Below: EDX data showing Ir, Ce, O, and Cl present in the samples. The Cu and Al peaks are derived from the sample grid and X-ray detector, respectively. Carbon is present in the sample itself, the plate, and the coating.

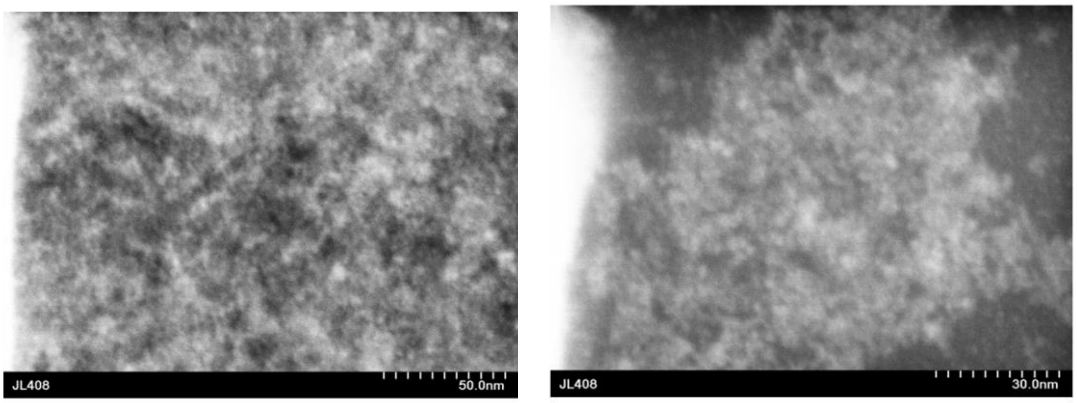

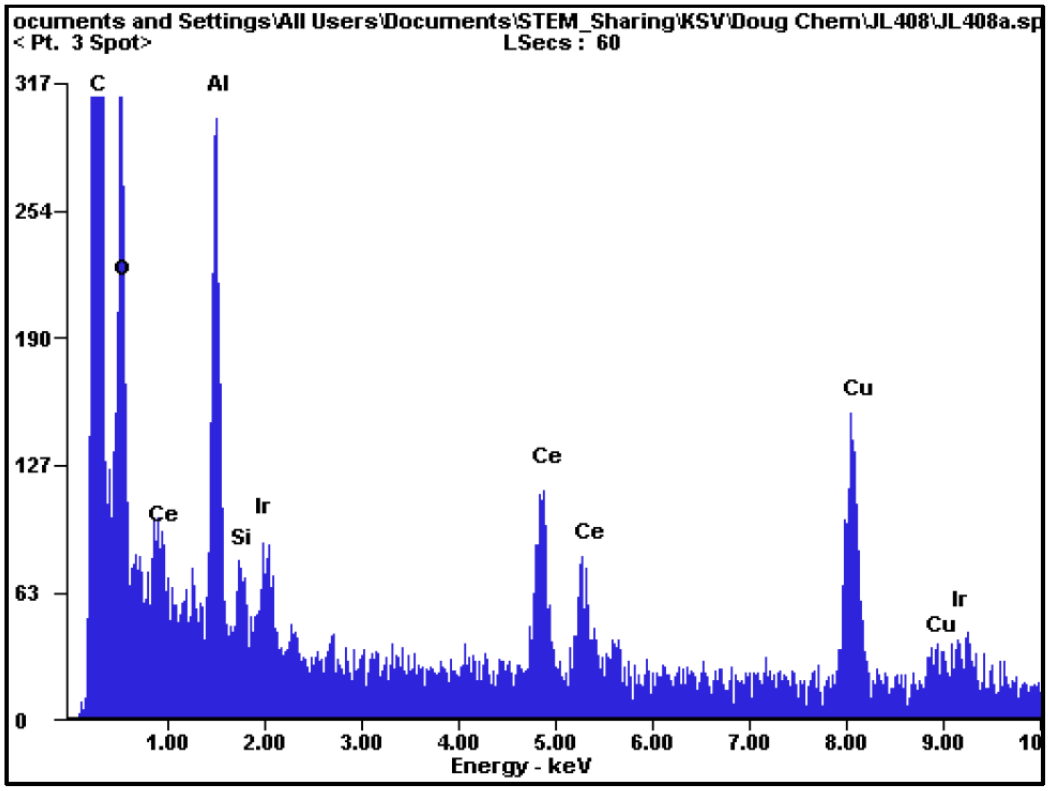

Figure III.2.7. Sample removed 15 min after **6** was added to CAN. Above: STEM images. Below: EDX data showing Ir, Ce, O, and Cl present in the samples. The Cu and Al peaks are derived from the sample grid and X-ray detector, respectively. Carbon is present in the sample itself, the plate, and the coating.

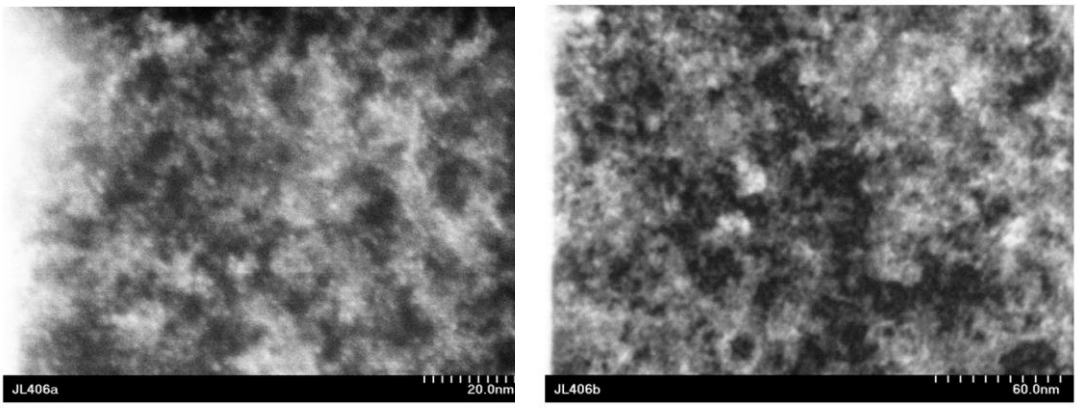

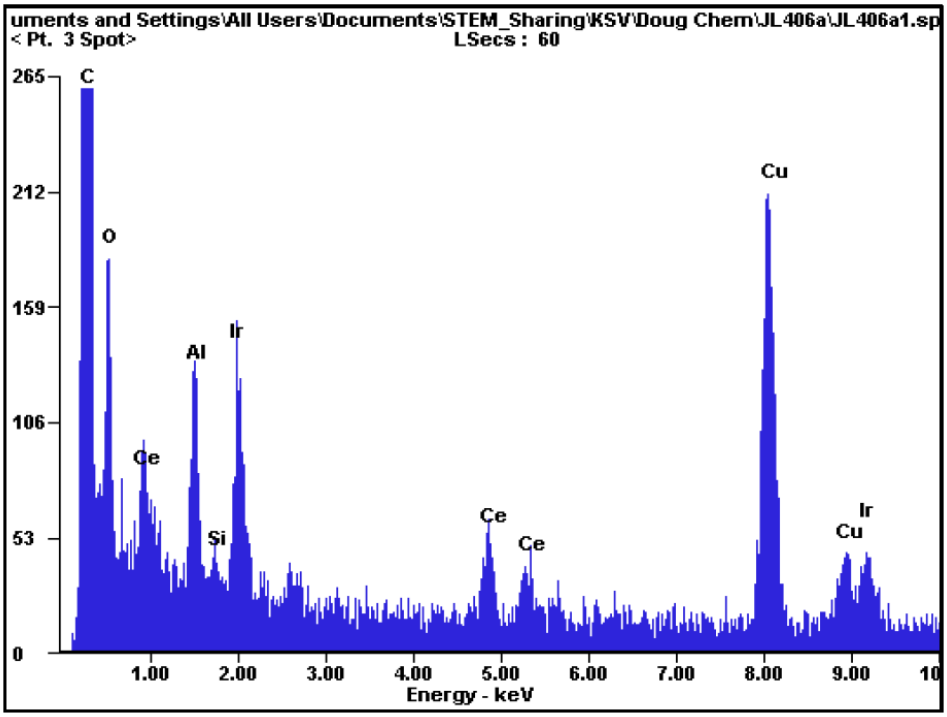

Figure III.2.8. Sample removed <1 and 15 min after IrO_x NP were added to CAN. Above left: STEM image of sample removed within 1 min. UV-vis data (see Figure III.2.2) from an identical but separate experiment show that all Ce(IV) is consumed by this point, and that the original UV-vis absorption near 580 nm for IrO_x NP has shifted to about 550 nm and is joined by one just above 600 nm. Above right: STEM image from sample removed after 15 min. Below: EDX data showing Ir, Ce, O, and Cl present in the samples. The Cu and Al peaks are derived from the sample grid and X-ray detector, respectively. Carbon is present in the sample itself, the plate, and the coating.

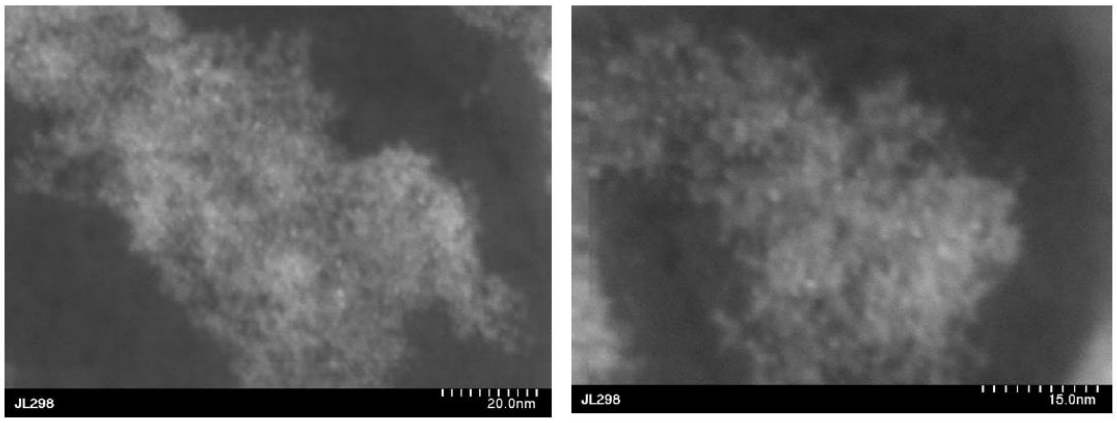

Figure III.2.9. STEM images of sample removed 15 min after $IrCl_3$ was added to CAN.

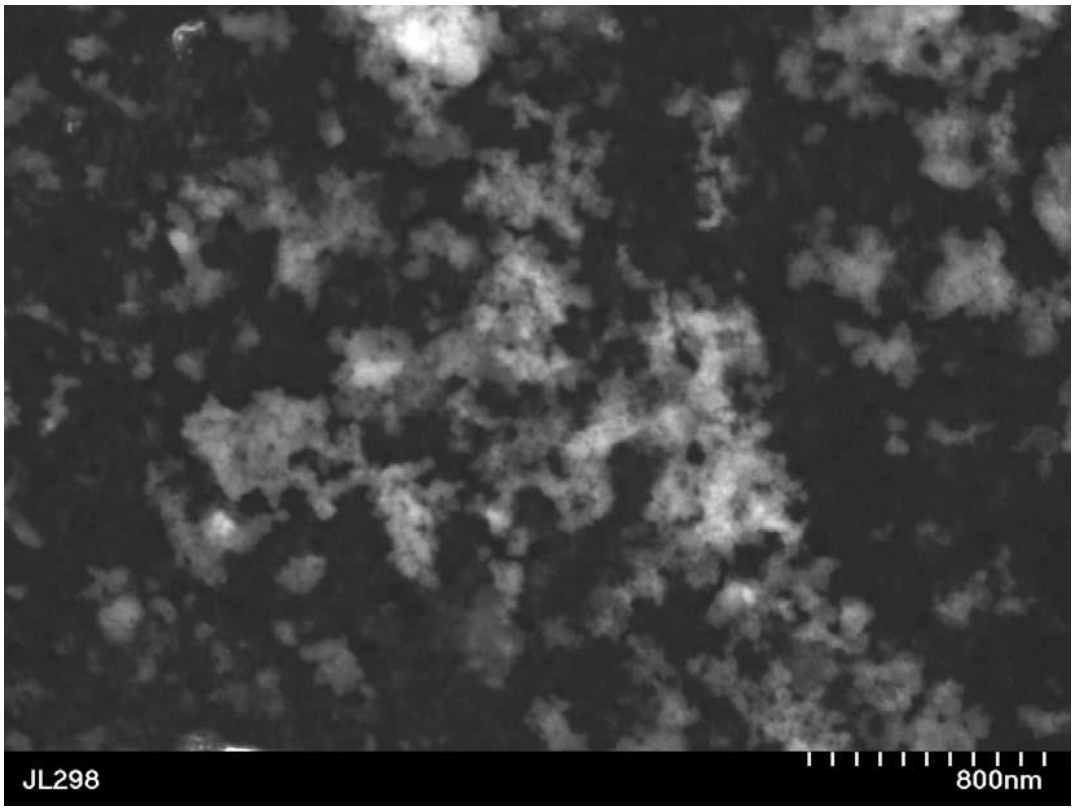

Figure III.2.10A. STEM image of 3.5 h after $IrCl_3$ was added to CAN.

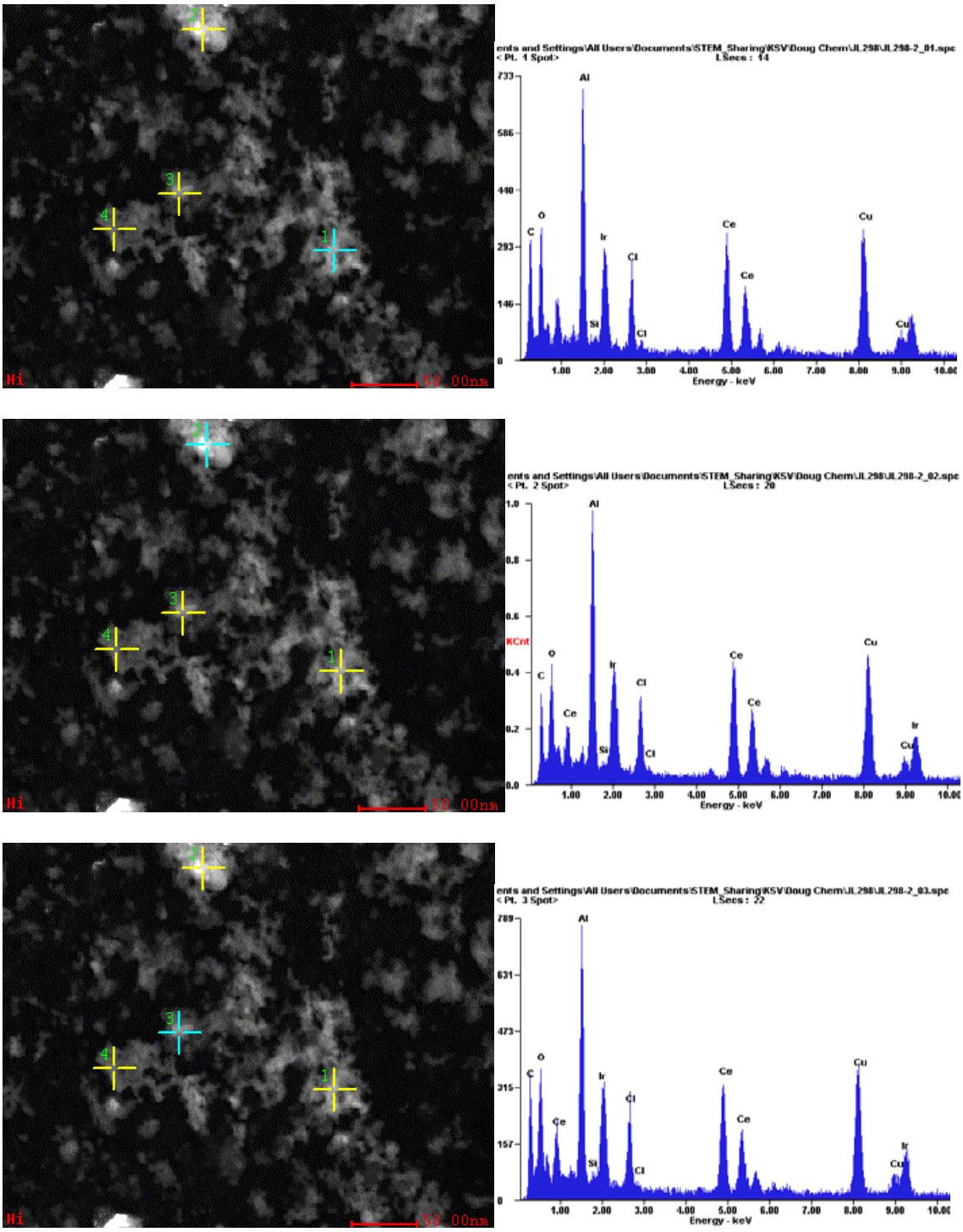

Figure III.2.10B EDX data of same field,figure III.2.10A showing Ir, Ce, O, and Cl present in the samples. The Cu and Al peaks are derived from the sample grid and X-ray detector, respectively. Carbon is present in the sample itself, the plate, and the coating.

2.2.2 UV-vis Absoprtion

UV-vis absorbance spectra were collected using a quartz cuvette with 0.1 or 1 cm optical path in a Cary Varian Bio 50 spectrophotometer. For the experiments shown discussed 2.8 mL of a freshly prepared 78-80 mM aqueous solution of CAN was placed in the 1 cm cuvette. UV-vis scans with 1 min interval were initiated using Cary Varian Scanning Kinetics software. After two scans, 0.020 - 0.090 mL of 1.3-5.0 mM aqueous (**1**, **3b**, **4b**, **6**, **9**, $IrCl_3$, IrO_x NP) or H_2O-CH_3CN (**2a**, **7**, **10**) solutions of various catalysts were added to the cuvette in order to obtain a solution containing $[CAN]_0$ 77.5-78 mM and $[catalyst]_0$ = 0.05 mM. The cuvette was shaken and promptly placed back in the spectrophotometer for continuing the scanning. The Teflon stopper was loosened to let the oxygen escape as it formed. For the experiments shown in Figure III.2.11., the conditions were adjusted such that $[CAN]_0$ 77.5-78 mM and [catalyst]0 = 1.38 mM. The scans were acquired with 1 min interval for the initial 20 min, then with 5 min interval for the next 80 min, and with 30 min interval for the next 14 h. A solvent background spectrum was subtracted from every recorded spectrum.

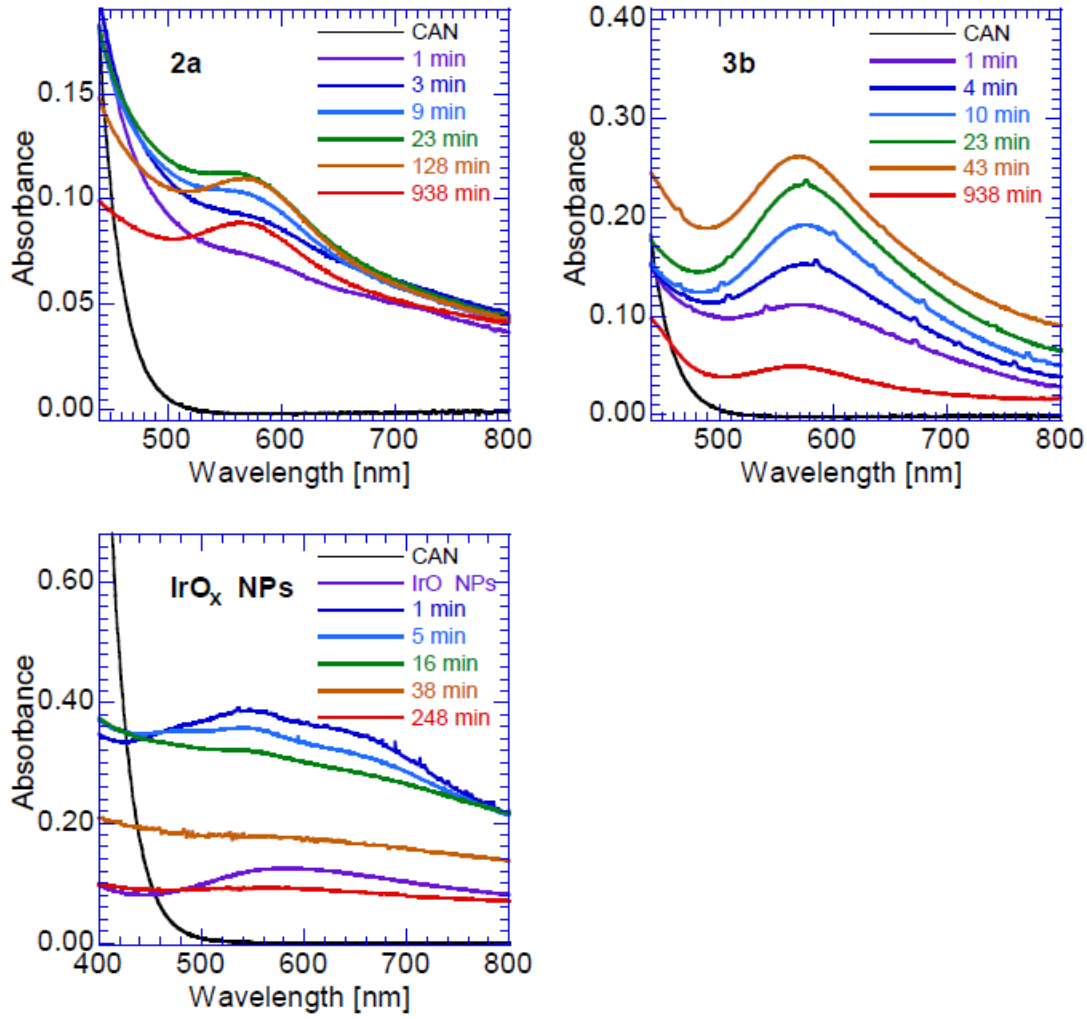

Figure III.2.11. UV-vis absorption spectra obtained from reaction mixtures with $[CAN]_o$ = near 78 mM in water, at various times after addition of catalysts under conditions such that $[catalyst]_o$ = 1.38 mM.

These concentrations are the same ones used to obtain STEM and EDX data (figure III.2.3-10). Note that for molecular catalysts **2a** and **3b**, close to maximal absorbance near 580 nm develops within 15-30 minutes whereas for Ir_xO NPs, the first minute the 580 nm absorbance is accompanied by one near 640-660 nm. Separate experiments on **3b** after 15-30 minutes reaction time were performed, where a known reaction volume (300 µL or 400 µL) was subjected to evaporation under oil pump

vacuum or lyophilization. After 3 to 5 hours, the purplish residues were reconstituted with the same amount of water (300 µL or 400 µL). The UV-vis spectra were essentially the same, with a lowering of absorbance at 580 nm to ½ or 2/3 that seen in the original sample. Similar results are shown for **2a**, showing that the material absorbing near 580 nm is present in the original reaction mixture and after concentrations.

III.2.3 Results and Discussion

STEM images of 2-10 nm succinate-stabilized IrO_2 NPs[21c] were obtained in collaboration with Prof. Kenneth Vecchio at UCSD. Energy dispersive X-ray (EDX) of the NPs confirmed the presence of iridium. Using STEM and EDX for water oxidation mixtures ($[CAN]_0$ = 173 mM, $[\mathbf{2a}]_0$ = 1.5 mM or ($[CAN]_0$ = 22 mM, $[IrCl_3]_0$ = 2.0 mM), the images revealed larger particles containing Ce and some Ir (Table III.2.1) (working in collaboration with Jessica Martin). Entry 1 and 2 were done to determine the limit of detection of nanoparticles using IrO_x NPs as a model. It was found that 0.15 mM IrO_x NPs was near the limit of detection. Entries 3, 4, and 5 were also limit of detection experiments to find the concentration of catalyst (~1.34 mM) required to observe the nanoparticles formed by STEM. To investigate the effect of concentrating the reaction mixture by different methods (under high vacuum, lyophilization or ultracentrifugation at 80,000 rpm (data not shown)), entry 6 and 7 determined that both manipulations resulted in different morphologies of the nanoparticles than previously observed. Entries 8 through 16 were tests with the different catalysts and CAN to detect the presence or absence of nanoparticles forming from the reactions. Interestingly, all the catalysts formed Ir and Ce rich nanoparticles that could be detected by STEM and EDX.

Table III.2.1. Experiments to determine limits of detection of Ir-rich NP by STEM as well as effects of reaction mixture processing by various means.

Entry	$[IrO_x\ NP]_0$ (mM)	$[cat.]_0$ (mM)	$[CAN]_0$ (mM)	STEM IrOx	STEM [cat.]	Manipulation
1	2.0	.		yes	.	none
2	0.15	.		no	.	none
3	.	0.15 (**2a**)	77.8	no	0.15 mM	10 min. aliquot
4	.	0.15 (**2a**)	77.8	no	0.15 mM	25 min. aliquot
5	.	1.34 (**2a**)	78.8	yes	1.34 mM	15 min. aliquot
6	0.15	.	.	no	1.33 mM	highvac
7	0.15	.	.	yes	1.36 mM	lyophilization
8	.	0.05 (**2a**)	78.0	no	1.35 mM	lyophilization
9	.	0.48 (**2a**)	3.15	yes	1.35 mM	lyophilization
10	.	1.35 (**3b**)	78.1	yes	1.35 mM	15 min. aliquot
11	.	0.05 (**2a**)	2.98	yes	1.35 mM	lyophilization
12	.	0.05 (**3b**)	2.98	yes	1.35 mM	lyophilization
13	.	1.35 (**9**)	78.0	yes	1.35 mM	15 min. aliquot
14	.	1.35 (**6**)	78.0	yes	1.35 mM	15 min. aliquot
15	.	1.35 (**1**)	78.0	yes	1.35 mM	~8 h aliquot
16	.	1.35 (**11**)	78.0	yes	1.35 mM	15 min. aliquot

There was no evidence of small Ir-rich NPs. We hypothesized that Ir and Ce were aggregating under our reaction conditions, forming species somewhat different from IrO_2 and IrO_x NP made under other conditions[21b,21c,21f] and different from bulk IrO_2 NP. Such aggregates could have formed, because Ce(III) and Ce(IV) ions form dimers in solution[23b-23e] and solid state[23f] by oxide or hydroxide bridging ligands. Another route that

could form these aggregates would be an Ir-Ce association during electron transfer.[11] Others have suggested an interaction forming Ce-OH-Ru,[24] but in light of various references, it does seem likely that there could be Ce-Ce and Ce-Ir interactions during catalysis. The typical CAN/catalyst ratios used for water oxidation reactions are 100-10,000, where the catalyst is added to an aqueous CAN solution.

To study the fate of the catalyst, a series of experiments were performed where the catalyst was added to limited amounts of CAN (5 mol/ mol of catalyst) followed by increases in 5 mol increments of CAN, to see the extent of delayed oxygen production.

There are several modes of measuring oxygen production as the reaction progresses; using an electrode,[8k,11,12] pressure,[10] volumetric,[12,17] or fluorescence-based assays.[12] Dissolved O_2 in the reaction mixture have been measured by others within the first minutes of the reaction,[11,12] yet most record the O_2 present in the headspace of the reaction.[8k,10,14] In our studies, we chose to record the oxygen levels in the aqueous phase (~ 7 mL) as well as the headspace (~7.9 mL) with a custom-made reaction cell with a Clark electrode in each phase (Figure III.2.12.). This enabled us to observe oxygen formation as it occurred in the first few seconds in the reaction mixture as well as over time (minutes) as oxygen diffused to the headspace, Figure III.2.13. The solubility of oxygen gas in water is ~ 1 mM. In our experiments, it appears that it takes ~ 15 minutes for equilibration of the oxygen to occur under typical laboratory conditions (magnetic stirring).

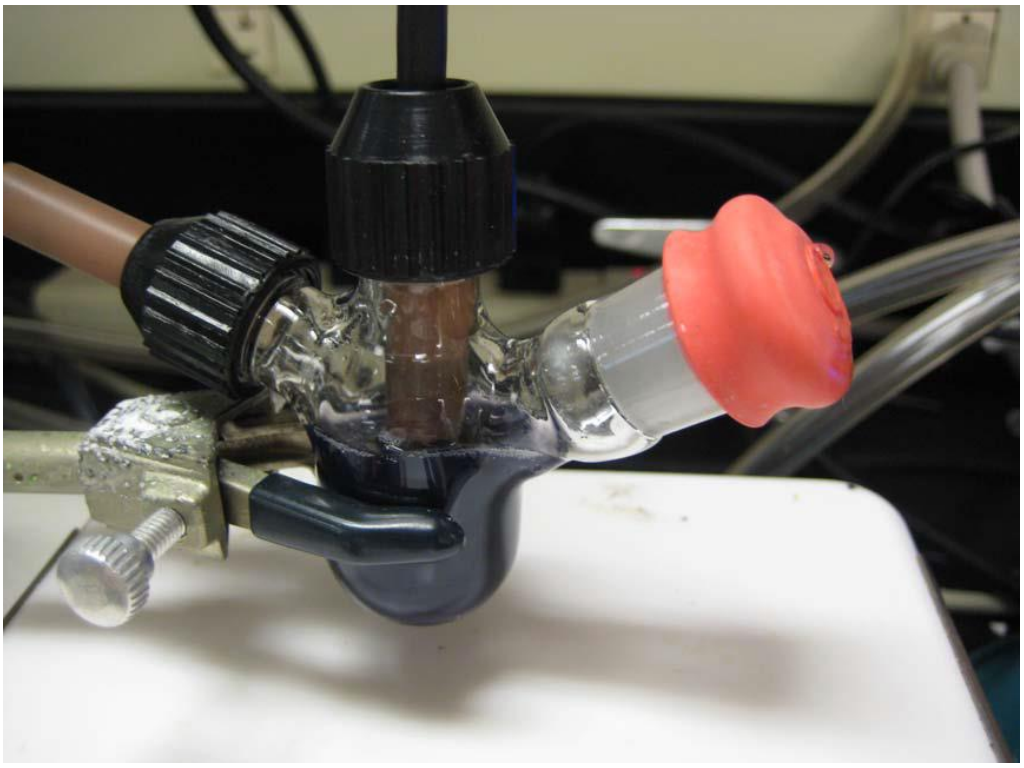

Figure III.2.12. Custom made reaction cell for measuring oxygen levels (Randy Hansen at SC Glass Tech.). A Clark electrode is submerged in reaction mixture and another electrode from the side measures the headspace. The catalyst solution is injected through septum and puncture sealed with grease. Image from ref.[27]

The data show that several equivalents of oxidant (CAN) are needed to prepare the Ir-based catalysts for water oxidation. The number of moles of oxidant tends to increase as the number of carbon-containing ligands increases. For instance, $IrCl_3 \cdot xH_2O$ (15 μmol) was added to CAN (78.4 μmol) and almost no oxygen was formed. This is consistent with previous work[12,17] indicating that some oxidant is required to form the actual water-oxidizing catalyst. When more equivalent of CAN were added (75.7 – 81.0 μmol), there was an instantaneous formation of oxygen in the liquid after each addition. An analogous experiment with **6** (15.6 μmol) needed several equivalent of CAN (totaling ~ 15 mol CAN per mol Ir) for significant amounts of O_2 to form after each addition. However, an experiment with **10** required as much as 30 mol CAN per mol Ir, and **2a**

showed similar results.

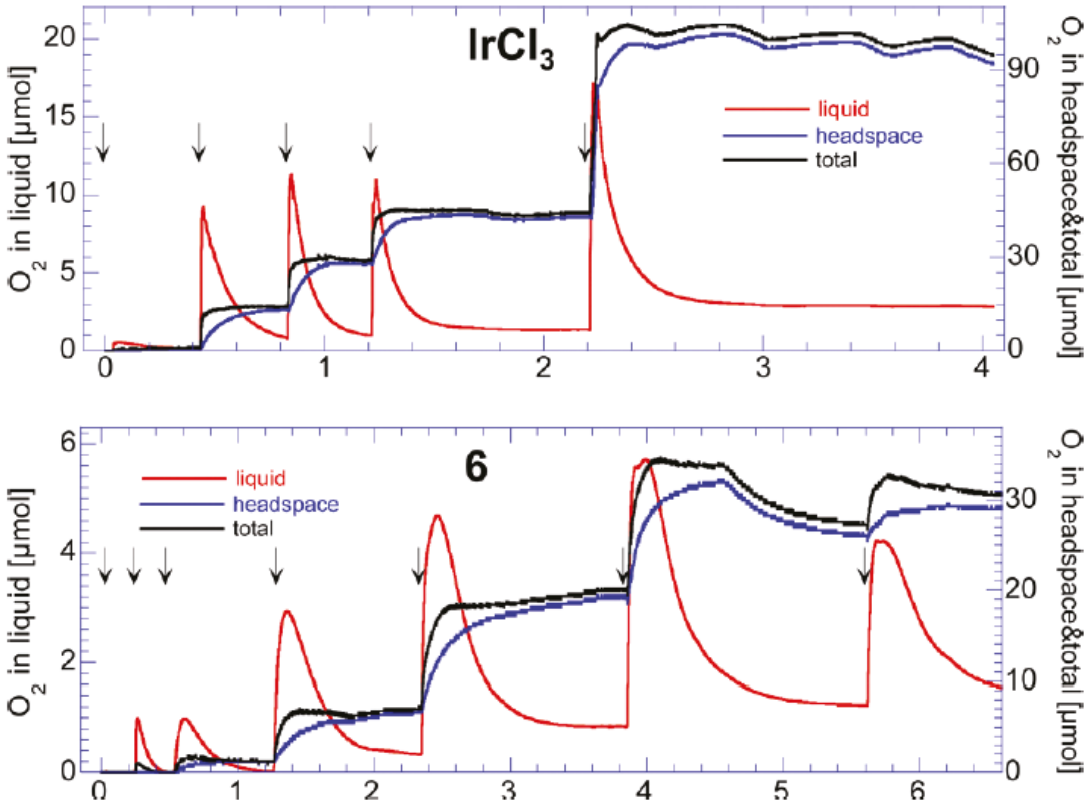

Figure III.2.13. Effects of stepwise reactions of ca. 5 mol of CAN per mole of Ir catalyst. O_2 amounts in liquid and headspace were measured using two Clark electrodes. Arrows point to times at which more CAN was added. (a, top) To CAN (78.4 μmol) in water (7.0 mL) was added $IrCl_3$ (15 μmol) in water (0.5 mL) at time 0.0 min; <1 μmol of O_2 was seen. In contrast, at t = 26, 50, and 73 min, more CAN (75.7 – 81.0 μmol) produced close to theoretical amounts of O_2 within 5 min each time. The need to consider diffusion of freshly formed O_2 from liquid to headspace over ca. 15 min is apparent. A final addition at t = 133 min of CAN (237.1 μmol) is also shown. Conclusion: only about 5 mol of Ce(IV) per mole of Ir is needed to generate active catalyst. (b, bottom) A similar experiment with 6 (15.6 μmol) shows very little O_2 (<10% of theory) after additions at 2 and 15 min, slightly more at 32 min, and ca. 50, 80, and 100% of theoretical O_2 after 76, 141, and 232 min.

Approximately 15 mol of Ce(IV) is needed per mole of Ir to generate active WOC, suggesting that Cp* ligand consumes some Ce(IV). Similar experiments with **2a**, **3b**, **4b**, and **9** showed no or little O_2 until 20-30 equiv of Ce(IV), suggesting that added

organic ligand consumes oxidant.

For comparison, acidified IrO_x NP[21f] were used, oxygen was formed after the first 5 mol of CAN added. Our data suggests that Cp* and other organic ligands consume CAN to promote the formation of the active water oxidation catalyst. Interestingly, not only in our hands but also those of others, bulk IrO_2 is inactive as a water oxidation catalyst, which led others to discount the possibility that Ir oxides were acting as WOC.[11,12,14] In our experiments, succinate-stabilized IrO_x NP[21e] showed an initial high rate of O_2 production, only for a short time, ultimately giving only tens of turnovers. Our studies with acidified IrO_x NP[21f] showed much higher activity, but in any case bulk IrO_2 is not a suitable comparison.

Finally, we note that our group contributed extensive NMR evidence for oxidation of the Cp* ligand by as little as 1 to 15 equiv of CAN. These data will not be discussed in detail here, but the Macchioni group and later the Crabtree group have also reported NMR studies of the oxidative transformation and complete removal of the Cp* ligand by strong oxidants, forming small organic acids and CO_2.

III.2.4. Conclusion

Our preliminary data shows that in water oxidation reactions using CAN and iridium-based catalysts, iridium-based nanoparticulate catalysts may be forming even early-on in the course of reaction. We suggested that UV-vis spectroscopy is one sensitive method for detecting and identifying nanoparticulate material from low initial concentrations of iridium-based catalysts, but subsequent work by Crabtree[25] and others[26] on Ir-based WOC and periodate as terminal oxidant provide evidence for formation of

colored Ir(IV) species with similar UV absorptions as what we saw. Moreover, from our NMR data as well as those of other groups, it became clear that 1 to 15 equiv of oxidant (CAN or periodate) are enough to fully transform and remove the Cp* ligand from Ir. To directly see nanoparticles or use powder diffraction patterns (data not shown), higher concentrations were used and data supporting iridium-cerium agglomerations or association were collected. Our data do not discount the role for molecular catalysis of water oxidation at the early stages of the reaction progress, but there seems to be a concern for long term stability of the iridium-cased catalysts studied.

Since our groups' paper[27] with these data, other researchers have found similar outcomes of their molecular water oxidation catalysts when using CAN as an oxidant.[28,29] The acidic conditions of CAN along with an unknown rate-determining step has fueled research into exploring the mechanistic aspects of molecular catalysts for water oxidation and possibly using other oxidants like sodium periodate ($NaIO_4$).[30-33] The causes of whether molecular iridium catalysts remain homogeneous or form nanoparticles or colloids still eludes researchers.[29,32,34] Yet new results show that on molecular iridium catalysts, Cp* or another hydrocarbon ligand can be a sacrificial placeholder to a more reactive species.[31,35.36]

Although iridium oxides are excellent catalysts for water oxidation, the drive to develop a robust and stable molecular catalytic system is worth pursuing for a more cost efficient and tunable system that can incorporate a light-harvesting component. Water oxidation is an important part in schemes to harness solar energy as an alternative fuel source.

III.2.5. Acknowledgments

Synthesis of catalysts and testing was done by several members of our group, who are named as co-authors on our joint publication. In particular: synthesis of catalysts, NMR studies of reactions, powder X-ray diffraction, oxygen measurements, and some UV-vis measurements were done by these colleagues.

III.2.6. References

[1] Sala, X.; Maji, S.; Bofill, R.; García-Antón, J.; Escriche, L.; Llobet, A. *Acc. Chem. Res.* **2014**, *47*, 504.

[2] Lewis, N. S.; Nocera, D. G. *Proc. Nat. Acad. Sci. USA* **2006**, *103*, 15729.

[3] Wasylenko, D.J.; Palmer, R.D.; Berlinguette, C.P. Chem. Commun. **2013**, *499*, 218.

[4] (a) Ellis, W. C.; McDaniel, N. D.; Bernhard, S.; Collins, T. J. *J. Am. Chem. Soc.* **2010**, *132*, 10990; (b) Yin, Q.; Tan, J. M.; Besson, C.; Geletii, Y. V.; Musaev, D. G.; (c) Kuznetsov, A. E.; Luo, Z.; Hardcastle, K. I.; Hill, C. L. *Science* **2010**, *328*, 342.

[5] Sala, X.; Romero, I.; Rodriguez, M.; Escriche, L.; Llobet, A. *Angew. Chem. Int. Ed.* **2009**, *48*, 2842.

[6] Brimblecombe, R.; Dismukes, G. C.; Swiegers, G. F.; Spiccia, L. *Dalton Trans.* **2009**, 9374.

[7] (a) Nair, V.; Deepthi, A. *Chem. Rev.* **2007**, *107*, 1862; (b) Binnemans, K; Gschneider, K. A., Bünzli, J.-C. G., Pecharsky, V. K. (**2006**) *Handbook on the Physics and Chemistry of Rare Earths*, (ed.). Amsterdam, Elsevier.

[8] (a) Gersten, S. W.; Samuels, G. J.; Meyer, T. J. *J. Am. Chem. Soc.* **1982**, *104*, 4029. (b) Bozoglian, F.; Romain, S.; Ertem, M. Z.; Todorova, T. K.; Sens, C.; Mola, J.; Rodriguez, M.; Romero, I.; Benet-Buchholz, J.; Fontrodona, X.; Cramer, C. J.; Gagliardi, L.; Llobet, A. *J. Am. Chem. Soc.* **2009**, *131*, 15176. (c) Sartorel, A.; Miro, P.; Salvadori, E.; Romain, S.; Carraro, M.; Scorrano, G.; Di Valentin, M.; Llobet, A.; Bo, C.; Bonchio, M. *J. Am. Chem. Soc.* **2009**, *131*, 16051. (d) Chen, Z.; Concepcion, J. J.; Jurss, J. W.; Meyer, T. J. *J. Am. Chem. Soc.* **2009**, *131*, 15580. (e) Duan, L.-L.; Xu, Y.-H.; Zhang, P.; Wang, M.; Sun, L.-C. *Inorg. Chem.* **2010**, *49*, 209. (f) Geletii, Y. V.; Huang, Z.; Hou, Y.; Musaev, D. G.; Lian, T.; Hill, C. L. *J. Am. Chem. Soc.* **2009**, *131*, 7522. (g) Xu, Y.; Aakermark, T.; Gyollai, V.; Zou, D.; Eriksson, L.; Duan, L.; Zhang, R.; Aakermark, B.; Sun, L. *Inorg.*

Chem. **2009**, *48*, 2717. (h) Deng, Z.; Tseng, H.-W.; Zong, R.; Wang, D.; Thummel, R. P. *Inorg. Chem.* **2008**, *47*, 1835. (i) Hurst, J. K.; Cape, J. L.; Clark, A. E.; Das, S.; Qin, C. *Inorg. Chem.* **2008**, *47*, 1753. (j) Romero, I.; Rodriguez, M.; Sens, C.; Mola, J.; Kollipara, M. R.; Francas, L.; Mas-Marza, E.; Escriche, L.; Llobet, A. *Inorg. Chem.* **2008**, *47*, 1824. (k) Zong, R.; Thummel, R. P. *J. Am. Chem. Soc.* **2005**, *127*, 12802. (l) Sens, C.; Romero, I.; Rodriguez, M.; Llobet, A.; Parella, T.; Benet-Buchholz, J. *J. Am. Chem. Soc.* **2004**, *126*, 7798.

[9] (a) Brimblecombe, R.; Kolling, D. R. J.; Bond, A. M.; Dismukes, G. C.; Swiegers, G. F.; Spiccia, L. *Inorg. Chem.* **2009**, *48*, 7269. (b) Poulsen, A. K.; Rompel, A.; McKenzie, C. J. *Angew. Chem. Int. Ed.* **2005**, *44*, 6916. (c) Tagore, R.; Chen, H.; Zhang, H.; Crabtree, R. H.; Brudvig, G. W. *Inorg. Chim. Acta* **2007**, *360*, 2983. (d) Ramaraj, R.; Kira, A.; Kaneko, M. *Chem. Lett.* **1987**, 261.

[10] McDaniel, N. D.; Coughlin, F. J.; Tinker, L. L.; Bernhard, S. *J. Am. Chem. Soc.* **2008**, *130*, 210.

[11] Hull, J. F.; Balcells, D.; Blakemore, J. D.; Incarvito, C. D.; Eisenstein, O.; Brudvig, G. W.; Crabtree, R. H. *J. Am. Chem. Soc.* **2009**, *131*, 8730.

[12] Blakemore, J. D.; Schley, N. D.; Balcells, D.; Hull, J. F.; Olack, G. W.; Incarvito, C. D.; Eisenstein, O.; Brudvig, G. W.; Crabtree, R. H. *J. Am. Chem. Soc.* **2010**, *132*, 16017.

[13] Savini, A.; Bellachioma, G.; Ciancaleoni, G.; Zuccaccia, C.; Zuccaccia, D.;Macchioni, A. *Chem. Commun. (Cambridge, UK)* **2010**, *46*, 9218.

[14] Lalrempuia, R.; McDaniel, N. D.; Müller-Bunz, H.; Bernhard, S.; Albrecht, M. *Angew. Chem., Int. Ed.* **2010**, *49*, 9765.

[15] Hetterscheid, D. G. H.; Reek, J. N. H. *Chem. Commun. (Cambridge, UK)* **2011**, *47*, 2712.

[16] Brewster, T. P.; Blakemore, J. D.; Schley, N. D.; Incarvito, C. D.; Hazari, N.; Brudvig, G. W.; Crabtree, R. H. *Organometallics* **2011**, *30*, 965.

[17] Dzik, W. I.; Calvo, S. E.; Reek, J. N. H.; Lutz, M.; Ciriano, M. A.; Tejel, C.; Hetterscheid, D. G. H.; de Bruin, B. *Organometallics* **2011**, *30*, 372.

[18] McDaniel, N. D.; Bernhard, S. *Dalton Trans.* **2010**, *39*, 10021.

[19] (a) Grotjahn, D. B.; Groy, T. L. *J. Am. Chem. Soc.* **1994**, *116*, 6969. (b) Amouri, H.; Vaissermann, J.; Rager, M. N.; Grotjahn, D. B. *Organometallics* **2000**, *19*, 1740. (c) Miranda-Soto, V.; Grotjahn, D. B.; DiPasquale, A. G.; Rheingold, A. L. *J. Am. Chem. Soc.* **2008**, *130*, 13200. (d) Grotjahn, D. B.; Kraus, J. E.; Amouri, H.; Rager, M.-N.; Cortes-Llamas, S. A.; Mallari, A. A.; DiPasquale, A. G.; Liable-Sands, L. M.; Golen, J.

A.; Zakharov, L. N.; Moore, C.; Rheingold, A. L. *J. Am. Chem. Soc.* **2010**, *132*, 7919.

[20] Miranda-Soto, V.; Parra-Hake, M.; Morales-Morales, D.; Toscano, R. A.; Boldt, G.; Koch, A.; Grotjahn, D. B. *Organometallics* **2005**, *24*, 5569.

[21] (a) Nahor, G. S.; Hapiot, P.; Neta, P.; Harriman, A. *J. Phys. Chem.* **1991**, *95*, 616. (b) Nakagawa, T.; Beasley, C. A.; Murray, R. W. *J. Phys. Chem. C* **2009**, *113*, 12958. (c) Hoertz, P. G.; Kim, Y.-I.; Youngblood, W. J.; Mallouk, T. E. *J. Phys. Chem. B* **2007**, *111*, 6845. (d) Nakagawa, T.; Bjorge, N. S.; Murray, R. W. *J. Am. Chem. Soc.* **2009**, *131*, 15578. (e) Yagi, M.; Tomita, E.; Sakita, S.; Kuwabara, T.; Nagai, K. *J. Phys. Chem. B* **2005**, *109*, 21489. (f) Zhao, Y.; Hernandez-Pagan, E. A.; Vargas-Barbosa, N. M.; Dysart, J. L.; Mallouk, T. E. *J. Phys. Chem. Lett.* **2011**, *2*, 402.

[22] Heidt, L. J.; Berestecki, J. *J. Am. Chem. Soc.* **1955**, *77*, 2049.

[23] (a) Heidt, L. J.; Berestecki, J. *J. Am. Chem. Soc.* **1955**, *77*, 2049. (b) Hardwick, T. J.; Robertson, E. *Can. J. Chem.* **1951**, *29*, 818. (c) Hayes, S. A.; Yu, P.; O'Keefe, T. J.; O'Keefe, M. J.; Stoffer, J. O. *J. Electrochem. Soc.* **2002**, *149*, C623. (d) Yu, P.; Hayes, S. A.; O'Keefe, T. J.; O'Keefe, M. J.; Stoffer, J. O. *J. Electrochem. Soc.* **2006**, *153*, C74. (e) Yu, P.; O'Keefe, T. J. *J. Electrochem. Soc.* **2006**, *153*, C80. (f) Guillou, N.; Auffrédic, J. P.; Louër, D. *J. Solid State Chem.* **1994**, *112*, 45.

[24] Yoshida, M.; Masaoka, S.; Abe, J.; Sakai, K. *Chem. Asian J.* **2010**, *5*, 2369.

[25] (a) Parent, A. R.; Crabtree, R. H.; Brudvig, G. W. *Chem. Soc. Rev.* **2013**, *42*, 2247; (b) Parent, A. R.; Brewster, T. P.; De Wolf, W.; Crabtree, R. H.; Brudvig, G. W. *Inorg. Chem.* **2012**, *51*, 6147.

[26] Zuccaccia, C.; Bellachioma, G.; Bortolini, O.; Bucci, A.; Savini, A.; Macchioni, A. *Chem. - A Eur. J.* **2014**, *20*, 3446.

[27] Grotjahn, D. B.; Brown, D. B.; Martin, J. K.; Marelius, D. C.; Abadjian, M.-C.; Tran, H. N.; Kalyuzhny, G.; Vecchio, K. S.; Specht, Z. G.; Cortes-Llamas, S. A. *J. Am. Chem. Soc.* **2011**, *133*, 19024.

[28] Savini, A.; Belanzoni, P.; Bellachioma, G.; Zuccaccia, C.; Zuccaccia, D.; Macchioni, A. *Green Chem.* **2011**, *13*, 3360.

[29] Junge, H.; Marquet, N.; Kammer, A.; Denurra, S.; Bauer, M.; Wohlrab, S.; Gaertner, F.; Pohl, M.-M.; Spannenberg, A.; Gladiali, S.; et al *Chem. - A Eur. J.* **2012**, *18*, 12749, S12749/1-S12749/19.

[30] Parent, A. R.; Crabtree, R. H.; Brudvig, G. W. *Chem. Soc. Rev.* **2013**, *42*, 2247.

[31] Ingram, A. J.; Wolk, A. B.; Flender, C.; Zhang, J.; Johnson, C. J.; Hintermair, U.;

Crabtree, R. H.; Johnson, M. A.; Zare, R. N. *Inorg. Chem.* **2014**, *53*, 423.

[32] Codola, Z.; Cardoso, J. M. S.; Royo, B.; Costas, M.; Lloret-Fillol, J. *Chem. - A Eur. J.* **2013**, *19*, 7203.

[33] Savini, A.; Bucci, A.; Bellachioma, G.; Rocchigiani, L.; Zuccaccia, C.; Llobet, A.; Macchioni, A. *Eur. J. Inorg. Chem.* **2014**, *2014*, 690.

[34] Schley, N. D.; Blakemore, J. D.; Subbaiyan, N. K.; Incarvito, C. D.; D'Souza, F.; Crabtree, R. H.; Brudvig, G. W. *J. Am. Chem. Soc.* **2011**, *133*, 10473.

[35] Huang, J.; Blakemore, J. D.; Fazi, D.; Kokhan, O.; Schley, N. D.; Crabtree, R. H.; Brudvig, G. W.; Tiede, D. M. *Phys. Chem. Chem. Phys.* **2014**, *16*, 1814.

[36] Hintermair, U.; Stafford, S. W.; Parent, A. R.; Ess, D. H.; Richens, D. T.; Vaccaro, P. H.; Brudvig, G. W. and Crabtree, R. H. *J. Am. Chem. Soc.* **2013**, *135*, 10837.

Appendix

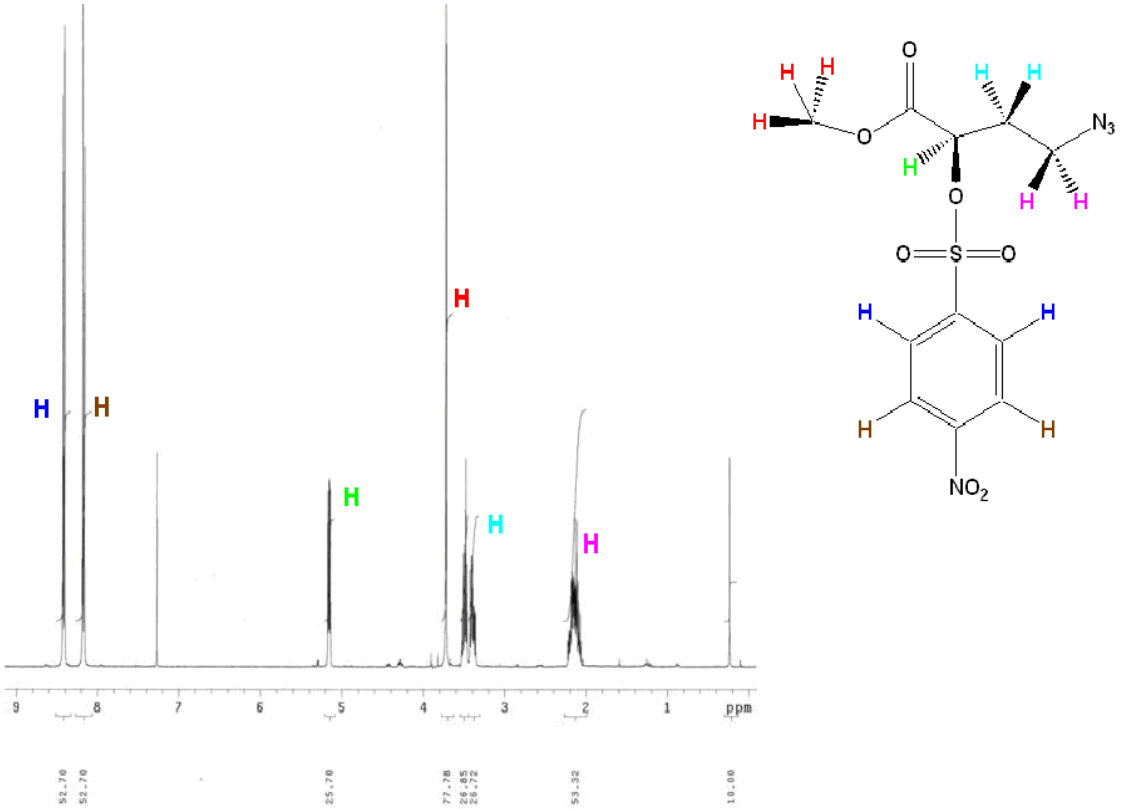

Figure A.1. Proton spectrum of purified compound **6b** ($CDCl_3$, 399.8 MHz), peaks assigned.

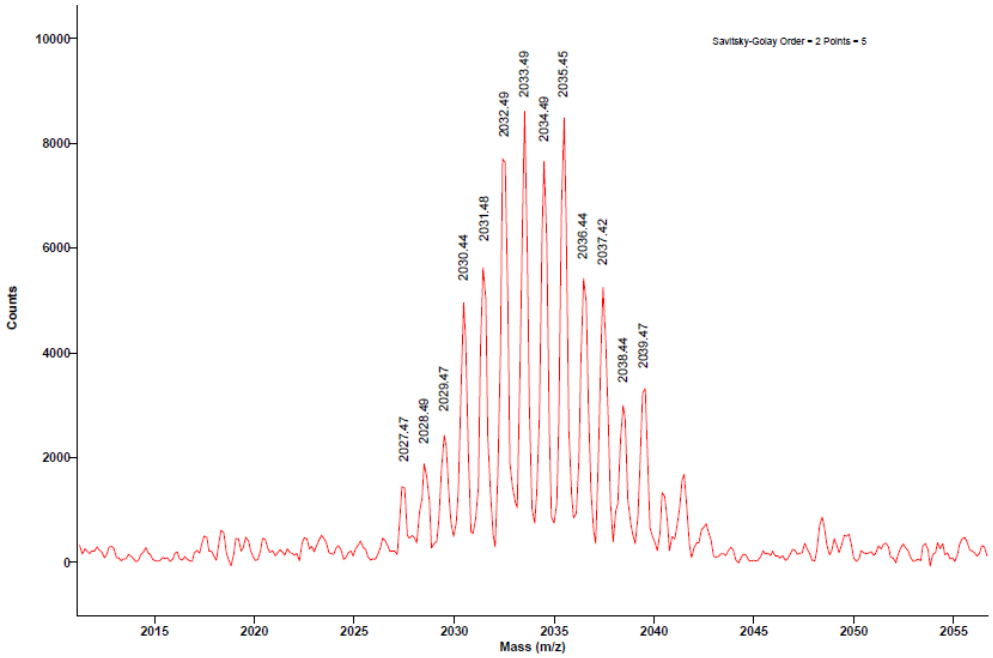

Figure A.2. MALDI-TOF of dendrimer **Gd-27**.

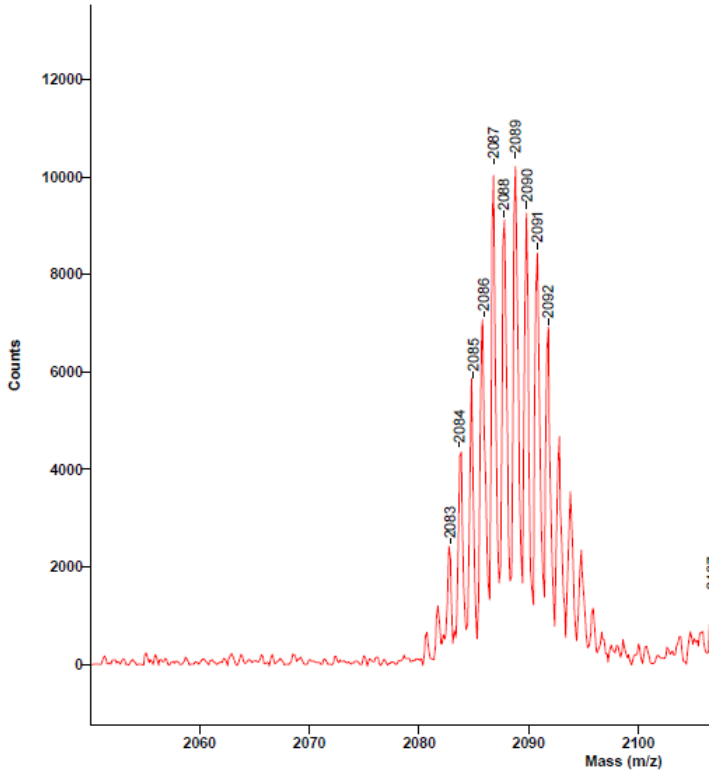

Figure A.3. MALDI-TOF of dendrimer **Gd-28.**

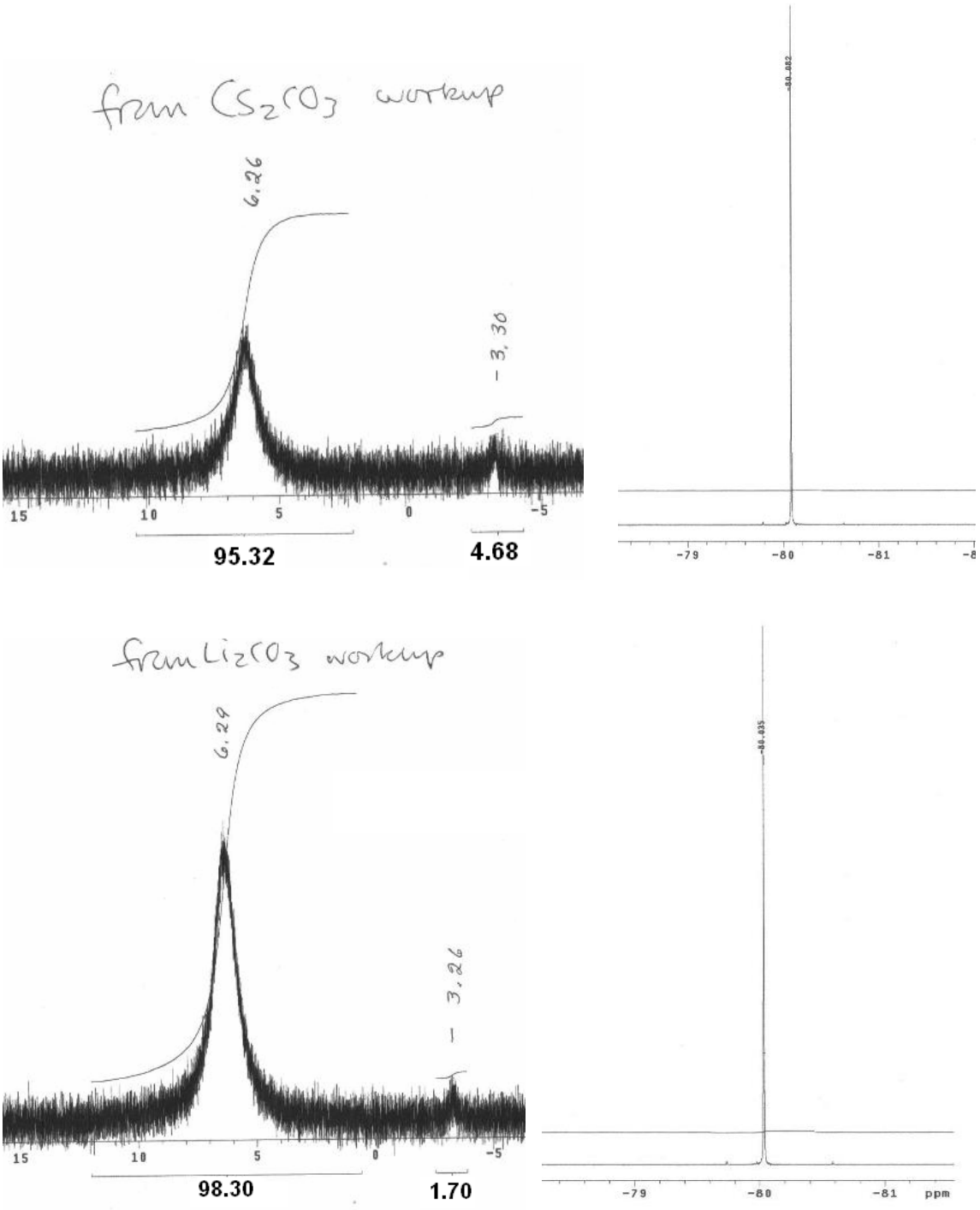

Figure A.4. ^{19}F and ^{23}Na NMR spectrum of different workup of compound **12**.F NMR peak -80.035 ppm assigned to triflate ion and Na NMR peak ~ 3 ppm assigned to sodium triflate, ~6.3 ppm assigned to sodium chelated in center of chelate.

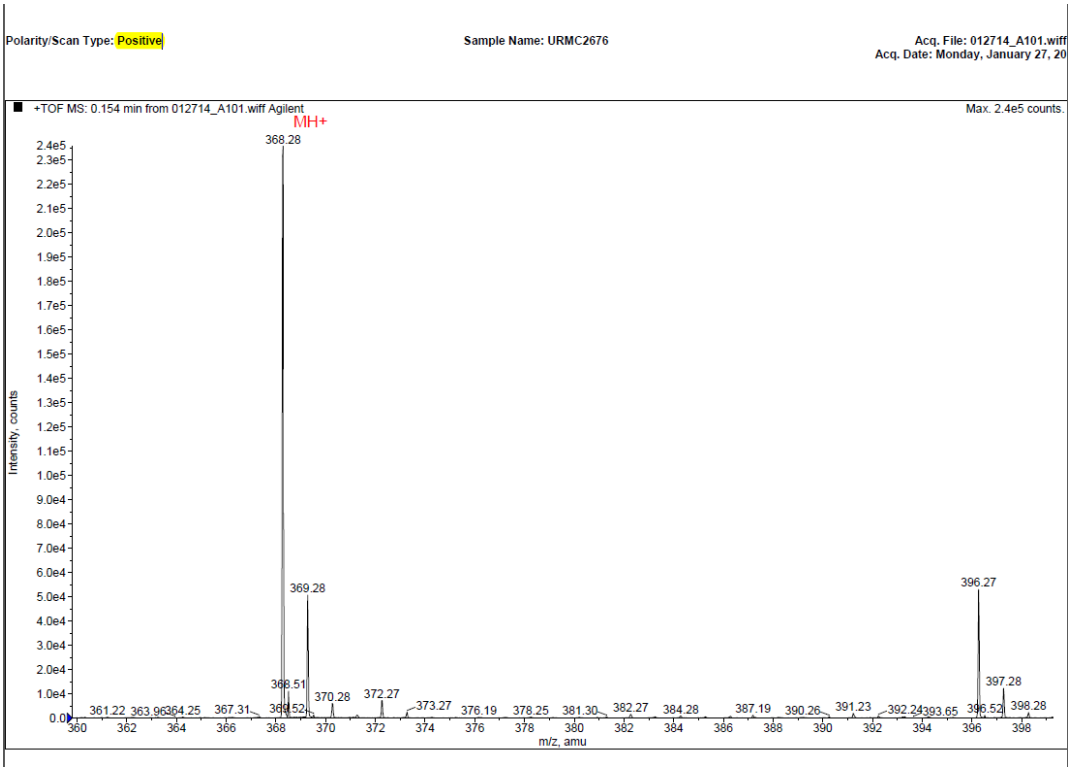

Figure A.5. Mass spectrum of compound **B**.

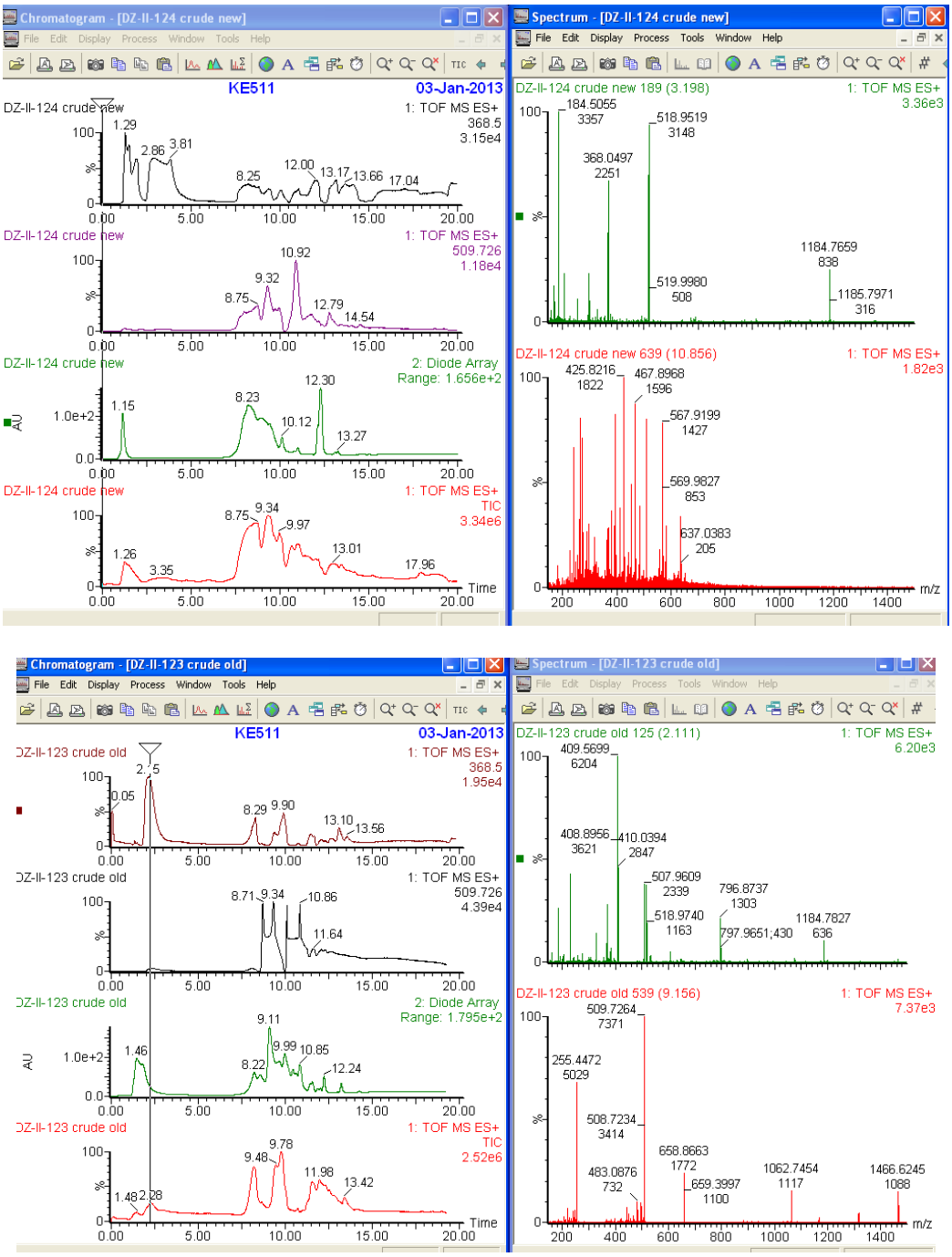

Figure A.6. Chromatogram of purification of compound **A** with MS-ES spectrum.

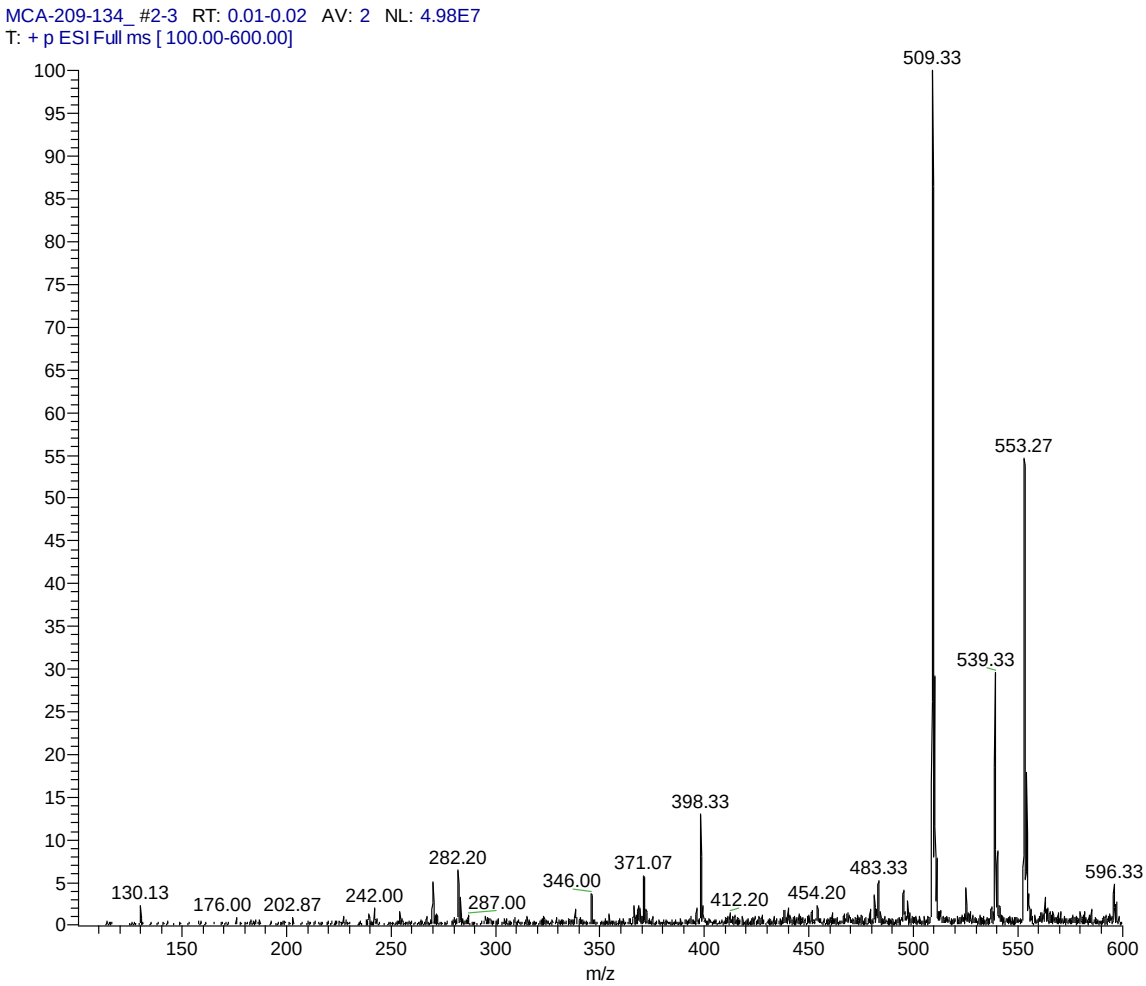

Figure A.7. Mass spectrum of compound **A**. All runs on a Thermo Finnigan LCQ Deca.

Table A.1. Crystal data and structure refinement for **12-NaTfO**.

Identification code	MCA-2-219	
Empirical formula	C_{23} H_{39} F_3 N_7 Na O_{11} S	
Formula weight	701.66	
Temperature	100(2) K	
Wavelength	1.54184 Å	
Crystal system	Monoclinic	
Space group	P2(1)	
Unit cell dimensions	a = 10.5760(8) Å	α= 90°.
	b = 13.0209(9) Å	β= 100.771(6)°.
	c = 24.2852(17) Å	γ = 90°.
Volume	3285.4(4) $Å^3$	
Z	4	
Density (calculated)	1.419 Mg/m^3	
Absorption coefficient	1.735 mm^{-1}	
F(000)	1472	
Crystal size	0.25 x 0.25 x 0.02 mm^3	
Theta range for data collection	3.87 to 65.93°.	
Index ranges	-11<=h<=12, -13<=k<=14, -18<=l<=28	
Reflections collected	15638	
Independent reflections	8623 [R(int) = 0.1224]	
Completeness to theta = 25.00°	90.7 %	
Absorption correction	Multi-scan	
Max. and min. transmission	0.9661 and 0.6709	
Refinement method	Full-matrix least-squares on F^2	
Data / restraints / parameters	8623 / 1 / 838	
Goodness-of-fit on F^2	1.019	
Final R indices [I>2sigma(I)]	R1 = 0.0831, wR2 = 0.2064	
R indices (all data)	R1 = 0.1490, wR2 = 0.2504	
Absolute structure parameter	-0.02(5)	
Extinction coefficient	0.0004(2)	
Largest diff. peak and hole	1.363 and -0.346 e.$Å^{-3}$	

Table A.2. Atomic coordinates (x 10^4) and equivalent isotropic displacement parameters (Å^{2}x 10^3) for **12-NaTfO**. U(eq) is defined as one third of the trace of the orthogonalized U^{ij} tensor.

	x	y	z	U(eq)
C(1)	4915(9)	4004(8)	3484(4)	46(2)
C(2)	5243(10)	5053(8)	3766(5)	53(3)
C(3)	4357(9)	6635(8)	4055(4)	53(3)
C(4)	3951(9)	6413(7)	4610(4)	44(2)
C(5)	2400(12)	5531(7)	5047(4)	56(3)
C(6)	2852(10)	4434(7)	5065(4)	49(2)
C(7)	3020(9)	2899(7)	4508(4)	41(2)
C(8)	4151(10)	3121(7)	4236(4)	48(3)
C(9)	3196(9)	2757(7)	3258(4)	44(2)
C(10)	4102(10)	1923(7)	3089(4)	49(3)
C(11)	3327(14)	908(8)	2863(5)	72(4)
C(12)	2408(11)	3288(9)	2759(4)	55(3)
C(13)	1160(20)	3056(12)	1859(7)	181(12)
C(14)	4048(10)	6197(8)	3079(4)	51(3)
C(15)	2725(13)	6717(7)	2908(4)	54(3)
C(16)	1568(14)	7940(11)	2325(6)	106(6)
C(17)	1730(9)	6965(7)	4432(4)	42(2)
C(18)	414(9)	6611(7)	4146(3)	36(2)
C(19)	-1724(10)	7193(8)	3796(5)	58(3)
C(20)	935(10)	3538(7)	4606(4)	50(3)
C(21)	213(9)	3243(7)	4060(5)	44(2)
C(22)	-1636(12)	2383(11)	3622(7)	89(4)
C(23)	1668(12)	10197(8)	4524(5)	59(3)
C(1')	5053(12)	7319(13)	1440(6)	83(4)
C(2')	5007(13)	8438(15)	1302(7)	104(5)
C(3')	6179(12)	9952(11)	1196(6)	80(4)
C(4')	6357(14)	9886(12)	634(6)	93(5)
C(5')	7669(14)	9039(11)	29(5)	85(4)
C(6')	7066(17)	7982(13)	-83(5)	105(5)

Table A.2. Atomic coordinates (x 10^4) and equivalent isotropic displacement parameters (Å^{2}x 10^3) for **12-NaTfO**. U(eq) is defined as one third of the trace of the orthogonalized U^{ij} tensor contd.

	x	y	z	U(eq)
C(7')	6756(16)	6353(12)	322(5)	91(5)
C(8')	5649(12)	6506(12)	614(5)	79(4)
C(9')	6458(11)	5786(10)	1498(5)	65(3)
C(10')	5371(12)	5113(10)	1647(5)	72(3)
C(11')	5714(18)	4067(13)	1805(10)	129(7)
C(12')	7510(13)	6040(10)	2030(5)	69(3)
C(13')	9121(15)	5300(10)	2679(6)	106(6)
C(14')	6500(15)	9133(13)	2105(6)	95(5)
C(15')	7809(15)	9225(13)	2330(4)	82(4)
C(16')	9400(20)	9443(18)	3178(6)	154(9)
C(17')	8649(10)	10216(9)	733(5)	62(3)
C(18')	9925(12)	9706(10)	926(4)	60(3)
C(19')	12165(13)	10027(13)	1151(6)	99(5)
C(20')	8900(20)	6880(12)	256(7)	105(6)
C(21')	9639(13)	6451(10)	793(7)	76(4)
C(22')	11589(16)	5685(19)	1232(11)	190(14)
C(23')	8600(12)	3535(11)	630(5)	75(4)
F(1)	847(8)	9444(5)	4602(4)	90(2)
F(2)	1960(8)	10695(5)	5011(3)	91(2)
F(3)	1002(6)	10845(5)	4150(3)	76(2)
F(1')	8797(6)	4108(5)	1075(3)	74(2)
F(2')	8840(9)	4140(9)	188(4)	123(3)
F(3')	9558(7)	2812(6)	685(3)	87(2)
N(1)	3821(7)	3537(5)	3668(3)	38(2)
N(2)	4186(7)	5820(5)	3646(3)	40(2)
N(3)	2622(7)	6083(5)	4546(3)	40(2)
N(4)	2270(8)	3821(5)	4570(3)	40(2)
N(5)	4276(13)	120(8)	2746(4)	89(4)
N(6)	4914(13)	-334(9)	3173(5)	87(3)

Table A.2. Atomic coordinates (x 10^4) and equivalent isotropic displacement parameters (Å^{2}x 10^3) for **12-NaTfO**. U(eq) is defined as one third of the trace of the orthogonalized U^{ij} tensor contd.

	x	y	z	U(eq)
N(7)	5489(12)	-881(10)	3471(5)	101(4)
N(1')	6058(9)	6742(9)	1214(4)	69(3)
N(2')	6190(9)	9013(9)	1482(4)	69(3)
N(3')	7661(8)	9454(7)	581(4)	61(2)
N(4')	7601(11)	7208(9)	326(4)	77(3)
N(5')	4560(20)	3545(12)	1894(9)	149(7)
N(6')	4347(13)	2712(12)	1676(5)	91(4)
N(7')	4106(19)	1918(18)	1521(7)	151(7)
Na(1)	2067(3)	4917(2)	3688(1)	33(1)
Na(1')	8056(3)	7986(3)	1288(1)	49(1)
O(1)	2167(7)	4190(5)	2731(2)	50(2)
O(2)	1821(7)	6560(5)	3119(3)	44(2)
O(3)	131(6)	5766(5)	3961(2)	43(2)
O(4)	475(6)	3421(5)	3595(3)	49(2)
O(5)	1986(12)	2639(6)	2366(4)	127(5)
O(6)	2782(8)	7373(6)	2489(3)	70(2)
O(7)	-419(6)	7384(4)	4113(3)	44(2)
O(8)	-859(7)	2730(6)	4102(4)	67(2)
O(1')	7676(11)	6846(7)	2233(4)	101(3)
O(2')	8725(9)	9118(7)	2079(3)	78(2)
O(3')	10076(7)	8807(6)	1043(3)	63(2)
O(4')	9389(8)	6527(6)	1244(4)	72(2)
O(5')	8159(8)	5190(6)	2191(3)	71(2)
O(6')	8029(12)	9428(9)	2878(4)	117(4)
O(7')	10870(8)	10370(6)	954(3)	73(2)
O(8')	10742(10)	6003(11)	714(6)	143(6)
O(1S)	3653(8)	9055(5)	4754(3)	68(2)
O(2S)	3781(7)	10609(5)	4232(3)	51(2)
O(3S)	2531(6)	9153(5)	3795(3)	46(2)

Table A.2. Atomic coordinates (x 10^4) and equivalent isotropic displacement parameters ($Å^2$x 10^3) for **12-NaTfO**. U(eq) is defined as one third of the trace of the orthogonalized U^{ij} tensor contd.

	x	y	z	U(eq)
O(1S')	6233(9)	3845(8)	372(6)	127(5)
O(2S')	7199(14)	2435(10)	-73(6)	175(7)
O(3S')	7057(11)	2368(7)	981(5)	110(4)
S(1)	3074(2)	9699(2)	4297(1)	41(1)
S(2)	7047(4)	2990(3)	475(2)	117(2)

Table A.3. Bond lengths [Å] and angles [°] for **12-NaTfO**.

C(1)-N(1)	1.449(12)	C(21)-O(8)	1.337(12)
C(1)-C(2)	1.537(15)	C(22)-O(8)	1.372(16)
C(2)-N(2)	1.486(12)	C(23)-F(2)	1.333(12)
C(3)-N(2)	1.442(12)	C(23)-F(3)	1.340(14)
C(3)-C(4)	1.517(14)	C(23)-F(1)	1.346(12)
C(4)-N(3)	1.450(12)	C(23)-S(1)	1.800(12)
C(5)-N(3)	1.469(12)	C(1')-N(1')	1.487(17)
C(5)-C(6)	1.505(14)	C(1')-C(2')	1.49(2)
C(6)-N(4)	1.477(12)	C(2')-N(2')	1.45(2)
C(7)-N(4)	1.463(12)	C(3')-N(2')	1.405(17)
C(7)-C(8)	1.500(14)	C(3')-C(4')	1.416(18)
C(8)-N(1)	1.462(11)	C(4')-N(3')	1.517(17)
C(9)-N(1)	1.488(12)	C(5')-N(3')	1.448(14)
C(9)-C(12)	1.504(15)	C(5')-C(6')	1.52(2)
C(9)-C(10)	1.552(13)	C(6')-N(4')	1.453(19)
C(10)-C(11)	1.598(17)	C(7')-N(4')	1.427(17)
C(11)-N(5)	1.500(15)	C(7')-C(8')	1.491(19)
C(12)-O(1)	1.200(12)	C(8')-N(1')	1.474(14)
C(12)-O(5)	1.291(13)	C(9')-N(1')	1.447(16)
C(13)-O(5)	1.474(15)	C(9')-C(10')	1.542(17)
C(14)-N(2)	1.442(12)	C(9')-C(12')	1.574(16)
C(14)-C(15)	1.540(16)	C(10')-C(11')	1.44(2)
C(15)-O(2)	1.182(13)	C(11')-N(5')	1.45(2)
C(15)-O(6)	1.339(12)	C(12')-O(1')	1.159(13)
C(16)-O(6)	1.470(15)	C(12')-O(5')	1.322(13)
C(17)-N(3)	1.480(12)	C(13')-O(5')	1.417(13)
C(17)-C(18)	1.507(13)	C(14')-C(15')	1.40(2)
C(18)-O(3)	1.205(10)	C(14')-N(2')	1.496(17)
C(18)-O(7)	1.330(11)	C(15')-O(2')	1.245(15)
C(19)-O(7)	1.470(12)	C(15')-O(6')	1.334(14)
C(20)-C(21)	1.454(15)	C(15')-Na(1')	3.052(13)
C(20)-N(4)	1.477(13)	C(16')-O(6')	1.49(2)
C(21)-O(4)	1.233(11)	C(17')-N(3')	1.439(15)

Table A.3. Bond lengths [Å] and angles [°] for **12-NaTfO** contd.

C(17')-C(18')	1.499(16)	Na(1')-O(1')	2.823(11)
C(18')-O(3')	1.208(13)	O(1S)-S(1)	1.433(7)
C(18')-O(7')	1.314(14)	O(2S)-S(1)	1.426(6)
C(19')-O(7')	1.435(14)	O(3S)-S(1)	1.436(6)
C(20')-N(4')	1.47(2)	O(1S')-S(2)	1.401(10)
C(20')-C(21')	1.50(2)	O(2S')-S(2)	1.550(14)
C(21')-O(4')	1.178(15)	O(3S')-S(2)	1.471(12)
C(21')-O(8')	1.350(17)	N(1)-C(1)-C(2)	111.2(8)
C(21')-Na(1')	3.000(13)	N(2)-C(2)-C(1)	114.3(8)
C(22')-O(8')	1.46(3)	N(2)-C(3)-C(4)	116.9(8)
C(23')-F(1')	1.298(13)	N(3)-C(4)-C(3)	113.0(7)
C(23')-F(3')	1.370(14)	N(3)-C(5)-C(6)	112.9(8)
C(23')-F(2')	1.392(16)	N(4)-C(6)-C(5)	114.0(8)
C(23')-S(2)	1.764(14)	N(4)-C(7)-C(8)	112.3(7)
N(1)-Na(1)	2.590(7)	N(1)-C(8)-C(7)	114.7(8)
N(2)-Na(1)	2.550(8)	N(1)-C(9)-C(12)	109.5(7)
N(3)-Na(1)	2.555(7)	N(1)-C(9)-C(10)	115.7(8)
N(4)-Na(1)	2.549(7)	C(12)-C(9)-C(10)	112.7(8)
N(5)-N(6)	1.274(16)	C(9)-C(10)-C(11)	111.5(8)
N(6)-N(7)	1.112(14)	N(5)-C(11)-C(10)	108.2(11)
N(1')-Na(1')	2.642(11)	O(1)-C(12)-O(5)	124.0(9)
N(2')-Na(1')	2.500(10)	O(1)-C(12)-C(9)	125.1(9)
N(3')-Na(1')	2.551(9)	O(5)-C(12)-C(9)	110.9(9)
N(4')-Na(1')	2.511(10)	N(2)-C(14)-C(15)	109.4(8)
N(5')-N(6')	1.21(2)	O(2)-C(15)-O(6)	126.4(10)
N(6')-N(7')	1.11(2)	O(2)-C(15)-C(14)	125.1(8)
Na(1)-O(3)	2.521(7)	O(6)-C(15)-C(14)	108.5(11)
Na(1)-O(1)	2.530(7)	N(3)-C(17)-C(18)	110.5(7)
Na(1)-O(2)	2.535(7)	O(3)-C(18)-O(7)	123.6(8)
Na(1)-O(4)	2.557(7)	O(3)-C(18)-C(17)	126.5(8)
Na(1')-O(4')	2.380(9)	O(7)-C(18)-C(17)	109.9(7)
Na(1')-O(2')	2.419(8)	C(21)-C(20)-N(4)	110.9(8)
Na(1')-O(3')	2.557(9)	O(4)-C(21)-O(8)	120.3(10)

Table A.3. Bond lengths [Å] and angles [°] for **12-NaTfO** contd.

O(4)-C(21)-C(20)	128.0(9)	O(3')-C(18')-C(17')	125.1(12)
O(8)-C(21)-C(20)	111.7(9)	O(7')-C(18')-C(17')	110.9(10)
F(2)-C(23)-F(3)	107.5(9)	N(4')-C(20')-C(21')	110.7(11)
F(2)-C(23)-F(1)	106.2(9)	O(4')-C(21')-O(8')	121.2(16)
F(3)-C(23)-F(1)	106.4(10)	O(4')-C(21')-C(20')	127.3(13)
F(2)-C(23)-S(1)	112.3(9)	O(8')-C(21')-C(20')	111.3(14)
F(3)-C(23)-S(1)	112.3(8)	O(4')-C(21')-Na(1')	48.1(6)
F(1)-C(23)-S(1)	111.8(7)	O(8')-C(21')-Na(1')	155.1(9)
N(1')-C(1')-C(2')	113.9(12)	C(20')-C(21')-Na(1')	82.0(8)
N(2')-C(2')-C(1')	116.4(12)	F(1')-C(23')-F(3')	108.1(9)
N(2')-C(3')-C(4')	115.7(12)	F(1')-C(23')-F(2')	107.0(12)
C(3')-C(4')-N(3')	112.9(9)	F(3')-C(23')-F(2')	103.1(10)
N(3')-C(5')-C(6')	115.4(12)	F(1')-C(23')-S(2)	113.9(10)
N(4')-C(6')-C(5')	114.2(11)	F(3')-C(23')-S(2)	112.8(10)
N(4')-C(7')-C(8')	116.0(12)	F(2')-C(23')-S(2)	111.1(8)
N(1')-C(8')-C(7')	112.8(10)	C(1)-N(1)-C(8)	112.5(7)
N(1')-C(9')-C(10')	115.9(10)	C(1)-N(1)-C(9)	111.2(7)
N(1')-C(9')-C(12')	108.0(9)	C(8)-N(1)-C(9)	112.0(7)
C(10')-C(9')-C(12')	111.7(9)	C(1)-N(1)-Na(1)	109.3(5)
C(11')-C(10')-C(9')	116.0(12)	C(8)-N(1)-Na(1)	106.5(5)
C(10')-C(11')-N(5')	107.8(15)	C(9)-N(1)-Na(1)	104.8(5)
O(1')-C(12')-O(5')	127.1(11)	C(14)-N(2)-C(3)	112.6(7)
O(1')-C(12')-C(9')	124.5(11)	C(14)-N(2)-C(2)	110.8(8)
O(5')-C(12')-C(9')	108.4(10)	C(3)-N(2)-C(2)	111.5(7)
C(15')-C(14')-N(2')	114.7(10)	C(14)-N(2)-Na(1)	105.2(6)
O(2')-C(15')-O(6')	120.2(13)	C(3)-N(2)-Na(1)	108.0(6)
O(2')-C(15')-C(14')	127.3(11)	C(2)-N(2)-Na(1)	108.5(5)
O(6')-C(15')-C(14')	112.5(13)	C(4)-N(3)-C(5)	110.9(7)
O(2')-C(15')-Na(1')	48.7(6)	C(4)-N(3)-C(17)	111.2(6)
O(6')-C(15')-Na(1')	154.9(11)	C(5)-N(3)-C(17)	109.8(8)
C(14')-C(15')-Na(1')	82.1(7)	C(4)-N(3)-Na(1)	109.6(5)
N(3')-C(17')-C(18')	110.0(10)	C(5)-N(3)-Na(1)	109.7(5)
O(3')-C(18')-O(7')	124.0(11)	C(17)-N(3)-Na(1)	105.6(5)

Table A.3. Bond lengths [Å] and angles [°] for **12-NaTfO** contd.

C(7)-N(4)-C(6)	112.1(7)	N(7')-N(6')-N(5')	173.1(18)
C(7)-N(4)-C(20)	110.1(7)	O(3)-Na(1)-O(1)	125.5(2)
C(6)-N(4)-C(20)	110.1(7)	O(3)-Na(1)-O(2)	76.6(2)
C(7)-N(4)-Na(1)	109.6(5)	O(1)-Na(1)-O(2)	80.3(2)
C(6)-N(4)-Na(1)	109.8(5)	O(3)-Na(1)-N(4)	88.3(2)
C(20)-N(4)-Na(1)	105.0(5)	O(1)-Na(1)-N(4)	123.4(2)
N(6)-N(5)-C(11)	115.7(9)	O(2)-Na(1)-N(4)	156.2(3)
N(7)-N(6)-N(5)	165.9(12)	O(3)-Na(1)-N(2)	124.8(2)
C(9')-N(1')-C(8')	107.3(10)	O(1)-Na(1)-N(2)	87.0(3)
C(9')-N(1')-C(1')	115.2(10)	O(2)-Na(1)-N(2)	65.8(2)
C(8')-N(1')-C(1')	111.9(10)	N(4)-Na(1)-N(2)	110.8(3)
C(9')-N(1')-Na(1')	109.6(6)	O(3)-Na(1)-N(3)	66.4(2)
C(8')-N(1')-Na(1')	106.1(7)	O(1)-Na(1)-N(3)	158.2(3)
C(1')-N(1')-Na(1')	106.4(8)	O(2)-Na(1)-N(3)	85.8(2)
C(3')-N(2')-C(2')	111.9(11)	N(4)-Na(1)-N(3)	71.2(2)
C(3')-N(2')-C(14')	112.9(11)	N(2)-Na(1)-N(3)	71.9(3)
C(2')-N(2')-C(14')	111.9(12)	O(3)-Na(1)-O(4)	78.7(2)
C(3')-N(2')-Na(1')	107.8(7)	O(1)-Na(1)-O(4)	76.9(2)
C(2')-N(2')-Na(1')	109.5(9)	O(2)-Na(1)-O(4)	126.6(2)
C(14')-N(2')-Na(1')	102.4(7)	N(4)-Na(1)-O(4)	66.3(2)
C(17')-N(3')-C(5')	111.4(10)	N(2)-Na(1)-O(4)	156.5(3)
C(17')-N(3')-C(4')	110.5(10)	N(3)-Na(1)-O(4)	124.9(3)
C(5')-N(3')-C(4')	112.2(9)	O(3)-Na(1)-N(1)	158.3(2)
C(17')-N(3')-Na(1')	109.0(6)	O(1)-Na(1)-N(1)	64.5(2)
C(5')-N(3')-Na(1')	108.4(7)	O(2)-Na(1)-N(1)	125.1(3)
C(4')-N(3')-Na(1')	105.0(7)	N(4)-Na(1)-N(1)	71.3(3)
C(7')-N(4')-C(6')	111.9(11)	N(2)-Na(1)-N(1)	71.4(2)
C(7')-N(4')-C(20')	111.6(12)	N(3)-Na(1)-N(1)	111.8(3)
C(6')-N(4')-C(20')	111.9(12)	O(4)-Na(1)-N(1)	86.1(2)
C(7')-N(4')-Na(1')	109.4(8)	O(4')-Na(1')-O(2')	115.8(3)
C(6')-N(4')-Na(1')	109.8(8)	O(4')-Na(1')-N(2')	158.5(4)
C(20')-N(4')-Na(1')	101.8(8)	O(2')-Na(1')-N(2')	69.5(3)
N(6')-N(5')-C(11')	116.7(17)	O(4')-Na(1')-N(4')	69.4(4)

Table A.3. Bond lengths [Å] and angles [°] for **12-NaTfO** contd.

O(2')-Na(1')-N(4')	164.1(4)	O(2')-Na(1')-C(15')	22.7(3)
N(2')-Na(1')-N(4')	111.7(4)	N(2')-Na(1')-C(15')	50.9(4)
O(4')-Na(1')-N(3')	126.2(3)	N(4')-Na(1')-C(15')	162.5(4)
O(2')-Na(1')-N(3')	93.7(3)	N(3')-Na(1')-C(15')	97.7(4)
N(2')-Na(1')-N(3')	72.0(3)	O(3')-Na(1')-C(15')	100.2(4)
N(4')-Na(1')-N(3')	72.3(4)	N(1')-Na(1')-C(15')	100.9(4)
O(4')-Na(1')-O(3')	78.2(3)	O(1')-Na(1')-C(15')	63.7(4)
O(2')-Na(1')-O(3')	78.3(3)	C(21')-Na(1')-C(15')	145.6(4)
N(2')-Na(1')-O(3')	122.9(4)	C(12)-O(1)-Na(1)	111.0(6)
N(4')-Na(1')-O(3')	88.5(3)	C(15)-O(2)-Na(1)	111.9(6)
N(3')-Na(1')-O(3')	64.5(3)	C(18)-O(3)-Na(1)	110.0(6)
O(4')-Na(1')-N(1')	88.9(3)	C(21)-O(4)-Na(1)	108.6(6)
O(2')-Na(1')-N(1')	122.6(4)	C(12)-O(5)-C(13)	116.5(9)
N(2')-Na(1')-N(1')	72.0(4)	C(15)-O(6)-C(16)	111.4(10)
N(4')-Na(1')-N(1')	71.2(4)	C(18)-O(7)-C(19)	116.7(7)
N(3')-Na(1')-N(1')	112.7(3)	C(21)-O(8)-C(22)	118.7(10)
O(3')-Na(1')-N(1')	158.9(3)	C(12')-O(1')-Na(1')	99.4(9)
O(4')-Na(1')-O(1')	78.0(3)	C(15')-O(2')-Na(1')	108.5(8)
O(2')-Na(1')-O(1')	75.0(3)	C(18')-O(3')-Na(1')	112.3(8)
N(2')-Na(1')-O(1')	83.8(4)	C(21')-O(4')-Na(1')	110.3(9)
N(4')-Na(1')-O(1')	120.8(4)	C(12')-O(5')-C(13')	114.5(9)
N(3')-Na(1')-O(1')	155.6(3)	C(15')-O(6')-C(16')	117.6(13)
O(3')-Na(1')-O(1')	131.4(3)	C(18')-O(7')-C(19')	118.9(9)
N(1')-Na(1')-O(1')	60.0(3)	C(21')-O(8')-C(22')	114.0(14)
O(4')-Na(1')-C(21')	21.6(4)	O(2S)-S(1)-O(1S)	114.5(4)
O(2')-Na(1')-C(21')	128.5(4)	O(2S)-S(1)-O(3S)	116.9(4)
N(2')-Na(1')-C(21')	162.0(4)	O(1S)-S(1)-O(3S)	114.5(4)
N(4')-Na(1')-C(21')	51.8(4)	O(2S)-S(1)-C(23)	102.4(4)
N(3')-Na(1')-C(21')	105.2(4)	O(1S)-S(1)-C(23)	103.4(6)
O(3')-Na(1')-C(21')	68.4(3)	O(3S)-S(1)-C(23)	102.5(5)
N(1')-Na(1')-C(21')	93.6(4)	O(1S')-S(2)-O(3S')	119.7(8)
O(1')-Na(1')-C(21')	98.7(4)	O(1S')-S(2)-O(2S')	112.0(8)
O(4')-Na(1')-C(15')	127.1(4)	O(3S')-S(2)-O(2S')	118.4(8)

Table A.3. Bond lengths [Å] and angles [°] for **12-NaTfO** contd.

O(1S')-S(2)-C(23')	103.6(6)
O(3S')-S(2)-C(23')	100.6(7)
O(2S')-S(2)-C(23')	97.4(8)

Table A.4. Anisotropic displacement parameters ($Å^2 x\ 10^3$) for **12-NaTfO**. The anisotropic displacement factor exponent takes the form: $-2\pi^2[\ h^2\ a^{*2}U^{11} + ... + 2\ h\ k\ a^*\ b^*\ U^{12}\ ]$.

	U^{11}	U^{22}	U^{33}	U^{23}	U^{13}	U^{12}
C(1)	38(5)	50(6)	54(6)	5(5)	19(5)	4(5)
C(2)	36(6)	49(6)	75(7)	10(5)	10(5)	0(5)
C(3)	33(5)	50(6)	67(7)	-1(5)	-19(5)	-5(5)
C(4)	54(6)	31(5)	39(5)	0(4)	-11(5)	0(4)
C(5)	99(9)	37(5)	30(5)	-3(4)	9(5)	-1(5)
C(6)	60(6)	52(6)	35(5)	1(4)	7(4)	-8(5)
C(7)	50(6)	32(5)	39(5)	5(4)	-2(4)	10(4)
C(8)	59(7)	36(5)	42(5)	13(4)	-6(5)	11(5)
C(9)	52(6)	31(5)	52(6)	-4(4)	12(5)	9(4)
C(10)	60(7)	41(5)	53(6)	12(4)	23(5)	18(5)
C(11)	115(11)	41(6)	67(7)	-5(5)	34(7)	27(7)
C(12)	65(7)	47(7)	49(6)	-4(5)	2(5)	9(5)
C(13)	280(30)	88(11)	105(12)	-50(10)	-130(15)	97(15)
C(14)	59(7)	41(5)	59(6)	12(5)	22(5)	3(5)
C(15)	86(9)	33(6)	37(5)	12(4)	-3(6)	10(6)
C(16)	107(11)	79(9)	111(11)	69(9)	-35(9)	13(8)
C(17)	59(6)	26(4)	37(5)	-14(4)	0(4)	-16(4)
C(18)	40(5)	32(5)	34(5)	2(4)	3(4)	-3(4)
C(19)	49(7)	55(6)	67(7)	-17(5)	4(5)	10(5)
C(20)	70(7)	34(5)	52(6)	-2(4)	25(5)	3(5)
C(21)	34(6)	30(5)	72(8)	4(5)	19(5)	10(4)
C(22)	47(7)	83(9)	125(12)	-3(8)	-13(8)	-8(7)
C(23)	75(8)	41(6)	71(7)	-24(6)	36(6)	-12(6)
C(1')	42(7)	124(13)	85(9)	0(8)	17(6)	2(8)
C(2')	49(9)	143(15)	122(13)	36(11)	20(8)	35(9)
C(3')	51(7)	84(9)	109(11)	15(8)	24(7)	38(7)
C(4')	88(10)	90(10)	80(9)	1(8)	-36(8)	17(8)
C(5')	102(10)	102(10)	41(6)	-11(7)	-11(6)	14(9)
C(6')	139(14)	119(13)	48(7)	-7(8)	-8(8)	-28(11)

Table A.4. Anisotropic displacement parameters ($Å^2 x\ 10^3$) for **12-NaTfO**. The anisotropic displacement factor exponent takes the form: $-2\pi^2[\ h^2\ a^{*2}U^{11} + ... + 2\ h\ k\ a^*\ b^*\ U^{12}\ ]$ contd.

	U^{11}	U^{22}	U^{33}	U^{23}	U^{13}	U^{12}
C(7')	126(13)	96(10)	48(7)	-24(7)	9(8)	-41(10)
C(8')	69(8)	111(10)	45(6)	-13(7)	-18(6)	-8(8)
C(9')	62(7)	80(8)	58(7)	-16(6)	25(6)	-15(7)
C(10')	65(8)	88(9)	57(7)	12(6)	-4(6)	-6(7)
C(11')	113(13)	84(11)	210(20)	28(13)	76(14)	-11(11)
C(12')	87(9)	57(8)	52(7)	-10(6)	-13(6)	13(7)
C(13')	121(12)	61(7)	102(10)	-15(7)	-70(10)	40(8)
C(14')	111(13)	97(10)	92(10)	-13(8)	55(10)	18(9)
C(15')	80(10)	131(12)	33(6)	-19(7)	7(6)	1(9)
C(16')	200(20)	190(20)	58(8)	-43(11)	-4(11)	-89(18)
C(17')	48(7)	59(7)	77(8)	14(6)	4(6)	11(6)
C(18')	68(8)	62(8)	51(6)	7(6)	12(5)	15(7)
C(19')	65(9)	123(12)	101(10)	59(9)	-1(7)	30(9)
C(20')	170(18)	75(10)	89(11)	-36(8)	76(12)	-21(10)
C(21')	72(9)	62(8)	103(12)	-39(8)	39(9)	-6(7)
C(22')	49(10)	200(20)	300(30)	-170(20)	-26(15)	31(12)
C(23')	57(8)	91(9)	67(8)	-20(7)	-14(6)	18(7)
F(1)	109(6)	51(4)	134(6)	-15(4)	83(5)	-28(4)
F(2)	139(7)	67(4)	84(5)	-33(4)	65(5)	-24(4)
F(3)	44(4)	40(3)	142(6)	-12(4)	13(4)	4(3)
F(1')	71(4)	78(4)	63(4)	-19(3)	-10(3)	12(3)
F(2')	130(7)	151(8)	99(6)	30(6)	51(6)	0(6)
F(3')	69(4)	105(5)	86(5)	-14(4)	10(4)	24(4)
N(1)	37(4)	33(4)	45(4)	8(3)	6(4)	15(3)
N(2)	39(5)	27(4)	52(5)	16(3)	1(4)	5(3)
N(3)	50(5)	31(4)	34(4)	-3(3)	-3(3)	-1(4)
N(4)	52(5)	29(4)	41(4)	9(3)	11(4)	1(3)
N(5)	160(11)	59(6)	60(6)	18(5)	51(7)	60(7)
N(6)	128(10)	71(7)	75(7)	6(7)	57(7)	50(8)

Table A.4. Anisotropic displacement parameters ($Å^2 x\ 10^3$) for **12-NaTfO**. The anisotropic displacement factor exponent takes the form: $-2\pi^2[\ h^2\ a^{*2}U^{11} + ... + 2\ h\ k\ a^*\ b^*\ U^{12}\ ]$ contd.

	U^{11}	U^{22}	U^{33}	U^{23}	U^{13}	U^{12}
N(7)	106(9)	106(9)	104(9)	64(8)	54(7)	67(8)
N(1')	48(6)	102(8)	52(5)	21(5)	-5(4)	12(5)
N(2')	42(6)	93(8)	71(6)	-16(6)	6(4)	17(5)
N(3')	50(5)	74(6)	54(5)	11(4)	-1(4)	14(5)
N(4')	80(8)	90(8)	58(6)	-33(6)	9(5)	-8(6)
N(5')	210(19)	78(9)	180(16)	-25(10)	91(14)	-55(11)
N(6')	117(10)	93(10)	62(7)	-7(7)	16(6)	-35(8)
N(7')	156(15)	179(18)	123(13)	-67(13)	37(11)	-41(14)
Na(1)	39(2)	24(2)	33(2)	-2(1)	3(1)	5(1)
Na(1')	40(2)	56(2)	47(2)	-8(2)	-1(2)	4(2)
O(1)	69(5)	38(4)	43(4)	3(3)	7(3)	14(3)
O(2)	49(4)	33(3)	48(4)	6(3)	2(3)	7(3)
O(3)	44(4)	36(4)	47(4)	-12(3)	0(3)	-7(3)
O(4)	46(4)	36(3)	61(5)	-5(3)	-2(3)	4(3)
O(5)	188(11)	54(5)	97(7)	-30(5)	-85(7)	50(6)
O(6)	90(6)	57(4)	59(5)	25(4)	3(4)	10(4)
O(7)	48(4)	36(3)	49(4)	-4(3)	7(3)	5(3)
O(8)	53(5)	50(4)	104(6)	-1(4)	27(4)	-10(4)
O(1')	137(9)	55(5)	83(6)	-7(5)	-51(6)	8(5)
O(2')	90(6)	85(6)	55(5)	-15(4)	4(5)	12(5)
O(3')	64(5)	65(5)	61(5)	12(4)	8(4)	16(4)
O(4')	61(5)	52(4)	108(7)	5(5)	29(5)	9(4)
O(5')	88(6)	54(4)	57(4)	4(3)	-21(4)	15(4)
O(6')	159(10)	130(9)	64(6)	-26(6)	30(7)	0(8)
O(7')	61(5)	71(5)	80(5)	35(4)	-5(4)	9(5)
O(8')	53(6)	172(12)	215(14)	-138(11)	53(8)	-39(7)
O(1S)	80(5)	49(4)	60(4)	22(3)	-23(4)	2(4)
O(2S)	59(4)	32(3)	61(4)	-3(3)	12(3)	-13(3)
O(3S)	50(4)	39(3)	47(4)	-17(3)	7(3)	-8(3)

Table A.4. Anisotropic displacement parameters ($Å^2 x\ 10^3$) for **12-NaTfO**. The anisotropic displacement factor exponent takes the form: $-2\pi^2[\ h^2\ a^{*2}U^{11} + ... + 2\ h\ k\ a^*\ b^*\ U^{12}\ ]$ contd.

	U^{11}	U^{22}	U^{33}	U^{23}	U^{13}	U^{12}
O(1S')	48(5)	89(7)	218(13)	-8(7)	-45(6)	21(5)
O(2S')	196(14)	129(10)	146(10)	-72(8)	-109(10)	1(9)
O(3S')	119(9)	54(5)	160(10)	26(6)	34(7)	13(5)
S(1)	47(1)	31(1)	43(1)	1(1)	3(1)	0(1)
S(2)	69(2)	92(3)	169(4)	-23(3)	-32(3)	11(2)

Table A.5. Hydrogen coordinates (x 10^4) and isotropic displacement parameters ($Å^2$x 10^3) for **12-NaTfO**.

	x	y	z	U(eq)
H(1A)	4719	4094	3072	55
H(1B)	5670	3544	3577	55
H(2A)	5470	4951	4176	64
H(2B)	6010	5335	3639	64
H(3A)	3868	7240	3885	64
H(3B)	5279	6827	4133	64
H(4A)	4515	5871	4810	53
H(4B)	4071	7040	4844	53
H(5A)	1468	5543	5056	67
H(5B)	2855	5894	5385	67
H(6A)	3799	4428	5097	59
H(6B)	2651	4103	5405	59
H(7A)	2458	2388	4280	50
H(7B)	3330	2594	4882	50
H(8A)	4721	3616	4472	57
H(8B)	4645	2478	4223	57
H(9)	2568	2384	3446	53
H(10A)	4771	1749	3419	59
H(10B)	4538	2200	2794	59
H(11A)	2850	644	3148	86
H(11B)	2700	1062	2517	86
H(13A)	255	2939	1879	271
H(13B)	1362	2711	1527	271
H(13C)	1318	3795	1834	271
H(14A)	4123	5621	2822	62
H(14B)	4739	6698	3054	62
H(16A)	843	7483	2347	159
H(16B)	1497	8190	1940	159
H(16C)	1556	8524	2578	159

Table A.5. Hydrogen coordinates (x 10^4) and isotropic displacement parameters ($Å^2$x 10^3) for **12-NaTfO** contd.

	x	y	z	U(eq)
H(17A)	2069	7467	4190	51
H(17B)	1667	7311	4789	51
H(19A)	-1681	7032	3406	87
H(19B)	-2254	7807	3807	87
H(19C)	-2107	6614	3963	87
H(20A)	947	2959	4871	60
H(20B)	507	4128	4752	60
H(22A)	-2004	2971	3395	134
H(22B)	-2333	1965	3720	134
H(22C)	-1128	1966	3407	134
H(1'1)	5214	7240	1853	100
H(1'2)	4203	7012	1290	100
H(2'1)	4751	8511	890	125
H(2'2)	4323	8758	1472	125
H(3'1)	6865	10394	1406	96
H(3'2)	5346	10296	1200	96
H(4'1)	6264	10580	464	111
H(4'2)	5675	9445	420	111
H(5'1)	8571	9003	-27	102
H(5'2)	7206	9523	-253	102
H(6'1)	6130	8038	-89	126
H(6'2)	7180	7751	-459	126
H(7'1)	7266	5761	497	109
H(7'2)	6411	6168	-73	109
H(8'1)	5108	7076	431	95
H(8'2)	5115	5876	574	95
H(9')	6892	5374	1240	78
H(10C)	5046	5444	1960	87
H(10D)	4654	5100	1321	87

Table A.5. Hydrogen coordinates (x 10^4) and isotropic displacement parameters (Å^{2}x 10^3) for **12-NaTfO** contd.

	x	y	z	U(eq)
H(11C)	6373	4055	2153	155
H(11D)	6071	3722	1505	155
H(13D)	9718	5847	2620	160
H(13E)	9593	4653	2755	160
H(13F)	8716	5476	2998	160
H(14C)	6051	9751	2209	114
H(14D)	6155	8532	2279	114
H(16D)	9792	8774	3137	232
H(16E)	9424	9587	3576	232
H(16F)	9867	9979	3017	232
H(17C)	8439	10655	1037	75
H(17D)	8691	10660	406	75
H(19D)	12385	10110	1558	148
H(19E)	12757	10436	973	148
H(19F)	12238	9301	1054	148
H(20C)	9365	7474	138	126
H(20D)	8819	6351	-41	126
H(22D)	12101	6274	1397	285
H(22E)	12164	5140	1150	285
H(22F)	11069	5429	1497	285

Table A.6. ^{1}H and ^{19}F NMR ratios to calculate ratio of triflate per compound **12**.

Ratio	MCA-39-70	MCA-40-70	MCA-41-71	Average	STD
Fluorobenzene to 12	1.45 : 1.00	1.26 : 1.00	1.67 : 1.00	-	-
Fluorobenzene to triflate	1.00 : 1.76	1.00 : 0.96	1.00 : 0.63	-	-
12 to triflate	1.00 : 0.85	1.00 : 1.17	1.00 : 1.06	1.03	0.16

Table A.7. Crystal data and structure refinement for **17-NaTfO**.

Identification code	grot337_0m	
Empirical formula	C_{26} H_{45} F_3 N_7 Na O_{11} S	
Formula weight	743.74	
Temperature	100(2) K	
Wavelength	1.54178 Å	
Crystal system	Monoclinic	
Space group	P2(1)	
Unit cell dimensions	a = 19.499(5) Å	α= 90°.
	b = 13.546(3) Å	β= 108.526(15)°.
	c = 28.385(5) Å	γ = 90°.
Volume	7109(3) $Å^3$	
Z	8	
Density (calculated)	1.390 Mg/m^3	
Absorption coefficient	1.635 mm^{-1}	
F(000)	3136	
Crystal size	0.35 x 0.15 x 0.05 mm^3	
Theta range for data collection	3.30 to 50.00°.	
Index ranges	-19<=h<=19, -13<=k<=13, -28<=l<=27	
Reflections collected	33482	
Independent reflections	13239 [R(int) = 0.0560]	
Completeness to theta = 50.00°	98.7 %	
Absorption correction	None	
Max. and min. transmission	0.9227 and 0.5985	
Refinement method	Full-matrix least-squares on F^2	
Data / restraints / parameters	13239 / 1253 / 1815	
Goodness-of-fit on F^2	1.056	
Final R indices [I>2sigma(I)]	R1 = 0.0986, wR2 = 0.2673	
R indices (all data)	R1 = 0.1064, wR2 = 0.2850	
Absolute structure parameter	-0.02(4)	
Largest diff. peak and hole	0.949 and -0.740 e.$Å^{-3}$	

Table A.8. Atomic coordinates (x 10^4) and equivalent isotropic displacement parameters ($Å^2$x 10^3) for **17-NaTfO**. U(eq) is defined as one third of the trace of the orthogonalized U^{ij} tensor.

	x	y	z	U(eq)
Na(1)	241(2)	8239(2)	-1391(1)	44(1)
O(1)	-709(3)	9527(5)	-1900(2)	61(2)
O(2)	759(3)	8978(5)	-1978(2)	51(2)
O(3)	627(3)	6689(5)	-1738(2)	51(2)
O(4)	-848(4)	7197(5)	-1637(2)	61(2)
O(5)	-427(5)	10884(5)	-2276(3)	85(2)
O(6)	1718(4)	8823(9)	-2232(2)	92(3)
O(7)	364(4)	5088(5)	-1714(2)	68(2)
O(8)	-2015(5)	7392(7)	-1749(3)	95(3)
N(1)	332(4)	9989(5)	-1011(3)	59(2)
N(2)	1590(3)	8686(5)	-1006(2)	51(2)
N(3)	803(4)	6938(5)	-748(2)	54(2)
N(4)	-453(4)	8244(5)	-764(2)	56(2)
N(5)	1152(10)	12583(13)	-1263(8)	152(7)
N(6)	1451(9)	12794(12)	-854(6)	122(6)
N(7)	1811(11)	12913(14)	-485(6)	145(6)
C(1)	1075(5)	10094(8)	-660(3)	65(3)
C(2)	1655(4)	9741(7)	-859(3)	53(2)
C(3)	1876(5)	8076(7)	-555(3)	54(2)
C(4)	1591(5)	7024(7)	-626(4)	59(3)
C(5)	570(6)	7138(8)	-309(3)	67(3)
C(6)	-233(6)	7354(8)	-455(3)	69(3)
C(7)	-258(6)	9147(8)	-462(4)	68(3)
C(8)	-207(6)	10049(8)	-752(4)	72(3)
C(9)	189(5)	10705(6)	-1422(3)	64(3)
C(10)	-1(8)	11762(8)	-1290(6)	97(4)
C(11)	307(11)	12573(14)	-1446(9)	159(9)
C(12)	-372(5)	10282(6)	-1883(3)	59(3)
C(13)	-873(9)	10530(11)	-2765(4)	97(4)

Table A.8. Atomic coordinates (x 10^4) and equivalent isotropic displacement parameters (Å^{2}x 10^3) for **17-NaTfO**. U(eq) is defined as one third of the trace of the orthogonalized U^{ij} tensor contd.

	x	y	z	U(eq)
C(17)	1246(7)	9091(18)	-2730(3)	127(8)
C(14)	1901(4)	8441(8)	-1391(3)	64(3)
C(15)	2679(5)	8795(11)	-1303(4)	76(3)
C(16)	1393(5)	8808(7)	-1890(3)	61(3)
C(18)	562(6)	5969(7)	-970(3)	59(3)
C(19)	962(7)	5088(7)	-688(4)	70(3)
C(20)	524(5)	5984(6)	-1519(3)	48(2)
C(21)	300(10)	4998(10)	-2239(4)	99(5)
C(22)	-1221(5)	8225(10)	-1064(4)	74(3)
C(23)	-1760(7)	8008(15)	-785(6)	112(5)
C(24)	-1325(5)	7538(8)	-1504(4)	68(3)
C(25)	-2161(9)	6727(13)	-2185(4)	114(5)
Na(2)	4647(2)	6294(3)	1366(1)	57(1)
O(9)	5296(4)	7823(7)	1811(3)	87(3)
O(10)	3886(3)	6880(5)	1855(2)	62(2)
O(11)	4396(4)	4705(5)	1753(2)	60(2)
O(12)	5885(3)	5668(7)	1750(2)	77(2)
O(13)	4934(8)	9205(9)	2065(5)	143(5)
O(14)	2924(4)	6450(7)	2069(3)	83(2)
O(15)	4609(5)	3082(6)	1803(2)	85(3)
O(16)	7010(4)	6251(9)	1937(4)	107(3)
N(8)	4313(4)	7941(6)	887(3)	72(3)
N(9)	3280(4)	6254(6)	901(3)	80(3)
N(10)	4420(5)	4792(6)	808(3)	82(3)
N(11)	5451(5)	6473(7)	817(3)	94(4)
N(12)	3551(12)	11369(15)	904(8)	184(8)
N(13)	3053(12)	11270(20)	525(9)	180(8)
N(14)	2724(15)	11260(20)	156(8)	196(9)
C(26)	3586(6)	7811(10)	517(4)	94(4)

Table A.8. Atomic coordinates (x 10^4) and equivalent isotropic displacement parameters (Å^{2}x 10^3) for **17-NaTfO**. U(eq) is defined as one third of the trace of the orthogonalized U^{ij} tensor contd.

	x	y	z	U(eq)
C(27)	3070(6)	7264(9)	721(4)	87(4)
C(28)	3182(9)	5562(9)	478(4)	103(5)
C(29)	3637(7)	4615(9)	612(4)	95(4)
C(30)	4733(9)	5011(11)	408(4)	114(6)
C(31)	5457(9)	5524(10)	581(5)	111(6)
C(32)	5121(9)	7257(10)	450(4)	106(5)
C(33)	4872(8)	8146(9)	660(5)	98(4)
C(34)	4279(7)	8710(8)	1247(4)	90(4)
C(35)	4222(13)	9780(10)	1065(9)	153(9)
C(36)	3791(15)	10442(17)	1246(9)	175(11)
C(37)	4889(6)	8513(9)	1722(4)	82(4)
C(38)	5493(13)	9100(20)	2537(7)	193(13)
C(39)	2950(5)	5937(8)	1271(3)	64(3)
C(40)	2126(5)	6026(12)	1102(6)	104(5)
C(41)	3299(5)	6490(8)	1751(3)	67(3)
C(42)	3269(7)	6872(11)	2555(4)	89(4)
C(43)	4813(8)	3959(8)	1118(4)	86(4)
C(44)	4751(15)	2963(10)	877(5)	152(9)
C(45)	4580(5)	3980(7)	1587(3)	57(3)
C(46)	4379(9)	3017(11)	2240(4)	95(4)
C(47)	6168(6)	6741(11)	1154(5)	109(6)
C(48)	6809(9)	6743(15)	946(7)	125(7)
C(49)	6325(5)	6142(10)	1639(4)	87(4)
C(50)	7179(6)	5698(13)	2404(4)	97(4)
Na(3)	82(1)	9727(2)	3619(1)	36(1)
O(17)	-1150(3)	10232(5)	3093(2)	46(2)
O(18)	254(3)	11364(4)	3296(2)	40(1)
O(19)	1131(3)	9352(5)	3312(2)	58(2)
O(20)	-326(3)	8208(4)	3106(2)	42(1)

Table A.8. Atomic coordinates (x 10^4) and equivalent isotropic displacement parameters ($Å^2$x 10^3) for **17-NaTfO**. U(eq) is defined as one third of the trace of the orthogonalized U^{ij} tensor contd.

	x	y	z	U(eq)
O(21)	-1715(4)	11655(6)	2893(3)	75(2)
O(22)	1159(3)	12337(5)	3266(3)	61(2)
O(23)	1577(5)	7933(6)	3125(4)	96(3)
O(24)	-1354(4)	7377(7)	2800(3)	87(3)
N(15)	-653(3)	10691(5)	4081(2)	40(2)
N(16)	953(3)	10841(5)	4267(2)	44(2)
N(17)	1065(3)	8646(5)	4194(3)	56(2)
N(18)	-548(3)	8465(4)	4007(2)	41(2)
N(19)	-2129(9)	13470(15)	4126(7)	151(4)
N(20)	-2206(10)	14145(16)	3842(8)	151(4)
N(21)	-2394(13)	14588(19)	3527(9)	189(9)
C(51)	-139(5)	11105(7)	4537(3)	54(2)
C(52)	532(4)	11552(6)	4461(3)	46(2)
C(53)	1395(5)	10205(7)	4664(3)	67(3)
C(54)	1659(4)	9266(7)	4489(4)	68(3)
C(55)	724(5)	8113(8)	4522(3)	69(3)
C(56)	-9(5)	7703(7)	4248(3)	57(3)
C(57)	-811(5)	8991(7)	4372(3)	57(3)
C(58)	-1155(5)	9992(6)	4194(3)	48(2)
C(59)	-1028(4)	11458(6)	3733(3)	48(2)
C(60)	-1657(8)	12003(12)	3831(7)	125(5)
C(61)	-1480(8)	12759(12)	4165(8)	125(5)
C(62)	-1293(4)	11020(7)	3214(3)	40(2)
C(63)	-1983(6)	11351(12)	2381(4)	100(5)
C(64)	1371(4)	11314(6)	3981(3)	51(2)
C(65)	1892(5)	12117(9)	4263(5)	82(4)
C(66)	856(4)	11673(6)	3484(3)	39(2)
C(67)	694(8)	12744(10)	2805(4)	88(4)
C(68)	1305(5)	7969(7)	3880(3)	63(3)

Table A.8. Atomic coordinates (x 10^4) and equivalent isotropic displacement parameters ($Å^2$x 10^3) for **17-NaTfO**. U(eq) is defined as one third of the trace of the orthogonalized U^{ij} tensor contd.

	x	y	z	U(eq)
C(69)	2024(6)	7414(10)	4129(6)	90(4)
C(70)	1323(5)	8510(7)	3416(4)	70(3)
C(71)	1588(10)	8387(14)	2671(6)	135(8)
C(72)	-1143(4)	8081(6)	3598(3)	45(2)
C(73)	-1538(6)	7175(8)	3713(4)	69(3)
C(74)	-876(5)	7883(7)	3158(3)	50(2)
C(75)	-1176(10)	7256(17)	2344(5)	133(8)
Na(4)	4782(1)	12908(2)	3610(1)	40(1)
O(25)	5774(4)	12537(6)	3258(3)	79(2)
O(26)	4342(3)	11310(5)	3120(2)	54(2)
O(27)	3539(3)	13370(4)	3115(2)	44(1)
O(28)	4955(3)	14562(5)	3277(2)	50(2)
O(29)	6302(6)	11237(9)	3068(5)	129(4)
O(30)	3386(3)	10291(5)	2910(2)	61(2)
O(31)	2864(4)	14695(6)	2936(3)	87(2)
O(32)	5842(3)	15597(5)	3249(2)	56(2)
N(22)	5804(3)	11775(6)	4150(3)	72(3)
N(23)	4209(3)	11619(5)	4038(2)	48(2)
N(24)	4104(4)	13847(6)	4098(2)	57(2)
N(25)	5696(4)	14012(6)	4232(2)	61(2)
N(26)	7234(13)	8718(19)	3846(10)	212(6)
N(27)	7256(14)	8190(20)	4185(11)	212(6)
N(28)	7235(14)	8160(20)	4554(11)	212(6)
C(76)	5496(5)	11237(10)	4493(4)	88(4)
C(77)	4749(4)	10836(7)	4242(4)	62(3)
C(78)	3992(6)	12155(8)	4414(4)	72(3)
C(79)	3632(6)	13150(8)	4239(4)	77(4)
C(80)	4647(6)	14291(10)	4542(4)	82(4)
C(81)	5293(5)	14719(9)	4429(3)	83(4)

Table A.8. Atomic coordinates (x 10^4) and equivalent isotropic displacement parameters (Å^{2}x 10^3) for **17-NaTfO**. U(eq) is defined as one third of the trace of the orthogonalized U^{ij} tensor contd.

	x	y	z	U(eq)
C(82)	6168(6)	13324(10)	4610(4)	103(6)
C(83)	6393(5)	12406(9)	4406(5)	83(4)
C(84)	5993(5)	11102(8)	3796(4)	72(3)
C(85)	6655(8)	10409(13)	3989(9)	160(7)
C(86)	6624(8)	9515(13)	3728(9)	160(7)
C(87)	6002(7)	11731(9)	3352(5)	97(5)
C(88)	6298(13)	11720(20)	2610(8)	173(11)
C(89)	3588(4)	11227(7)	3648(3)	51(2)
C(90)	3185(8)	10415(11)	3827(6)	101(5)
C(91)	3815(4)	10945(6)	3204(3)	45(2)
C(92)	3574(8)	9929(10)	2491(4)	91(4)
C(93)	3670(5)	14597(7)	3759(4)	69(3)
C(94)	3102(8)	15166(11)	3908(7)	108(5)
C(95)	3367(4)	14150(7)	3241(3)	54(3)
C(96)	2559(7)	14320(12)	2433(5)	115(6)
C(97)	6088(5)	14540(8)	3950(3)	61(3)
C(98)	6579(8)	15378(14)	4227(5)	141(9)
C(99)	5553(4)	14893(7)	3456(3)	51(2)
C(100)	5366(6)	15980(9)	2779(3)	67(3)
S(1)	-5(2)	4631(2)	3975(1)	72(1)
F(1)	1045(5)	5717(5)	4513(3)	96(2)
F(2)	1231(4)	4165(5)	4636(2)	86(2)
F(3)	1304(5)	4813(8)	3959(4)	126(3)
O(1A)	-209(6)	5423(6)	3617(3)	92(3)
O(2A)	-292(5)	4696(9)	4376(3)	105(3)
O(3A)	-32(6)	3668(6)	3755(3)	96(3)
C(1A)	893(7)	4848(7)	4264(4)	83(4)
S(4)	4886(7)	7997(9)	3904(5)	117(4)
F(10)	3602(14)	7500(30)	3622(5)	260(30)

Table A.8. Atomic coordinates (x 10^4) and equivalent isotropic displacement parameters (Å^{2}x 10^3) for **17-NaTfO**. U(eq) is defined as one third of the trace of the orthogonalized U^{ij} tensor contd.

	x	y	z	U(eq)
F(11)	3937(11)	8489(13)	4274(6)	126(7)
F(12)	4290(20)	6923(16)	4367(8)	250(20)
O(10A)	4670(20)	8810(20)	3533(12)	153(13)
O(11A)	4982(18)	7177(16)	3624(10)	155(12)
O(12A)	5353(13)	8268(18)	4374(7)	153(9)
C(4A)	4146(10)	7687(15)	4039(7)	117(4)
S(2)	3570(2)	6003(3)	-1003(1)	102(1)
F(4)	2347(5)	5237(10)	-1345(3)	137(4)
F(5)	3234(10)	4383(12)	-1472(4)	218(9)
F(6)	3110(8)	4411(9)	-727(4)	169(5)
O(4A)	3309(6)	6511(9)	-654(3)	112(3)
O(5A)	4286(5)	5661(11)	-771(4)	132(5)
O(6A)	3493(5)	6458(10)	-1472(3)	118(4)
C(2A)	3047(6)	5003(10)	-1125(4)	102(1)
S(3)	1647(3)	9676(4)	860(2)	105(2)
F(7)	1147(9)	9338(17)	1526(5)	174(7)
F(8)	2220(9)	8634(16)	1545(7)	177(8)
F(9)	1142(10)	8135(11)	957(9)	217(11)
O(7A)	912(7)	10053(11)	587(5)	118(5)
O(8A)	2014(10)	10507(10)	1146(6)	140(6)
O(9A)	2052(8)	9185(12)	588(5)	123(6)
C(3A)	1516(8)	8881(11)	1249(5)	105(2)
S(5)	4601(7)	7721(9)	3897(5)	117(4)
F(13)	5648(12)	8744(12)	4277(6)	125(6)
F(14)	5761(14)	7656(18)	3721(7)	186(10)
F(15)	5811(16)	7156(16)	4458(7)	186(10)
O(13A)	4468(19)	6735(12)	3704(9)	144(12)
O(14A)	4338(15)	7930(17)	4282(9)	153(9)
O(15A)	4460(20)	8480(20)	3494(12)	153(13)

Table A.8. Atomic coordinates (x 10^4) and equivalent isotropic displacement parameters ($Å^2$x 10^3) for **17-NaTfO**. U(eq) is defined as one third of the trace of the orthogonalized U^{ij} tensor contd.

	x	y	z	U(eq)
C(5A)	5488(10)	7832(13)	4113(7)	117(4)
S(6)	1164(8)	9250(12)	886(5)	105(2)
F(16)	1940(30)	8240(30)	1565(10)	260(60)
F(17)	1280(30)	9430(40)	1777(12)	174(7)
F(18)	2216(19)	9860(30)	1508(14)	177(8)
O(33)	1540(20)	8670(30)	620(12)	123(6)
O(34)	518(14)	8750(30)	858(13)	105(2)
O(35)	1170(20)	10310(16)	826(13)	118(5)
C(6A)	1698(16)	9170(20)	1474(8)	105(2)

Table A.9. Bond lengths [Å] and angles [°] for **17-NaTfO**.

Na(1)-O(2)	2.423(6)	N(5)-N(6)	1.158(18)
Na(1)-O(4)	2.459(7)	N(5)-C(11)	1.56(2)
Na(1)-N(3)	2.523(7)	N(6)-N(7)	1.071(16)
Na(1)-O(3)	2.533(6)	C(1)-C(2)	1.495(12)
Na(1)-N(4)	2.554(7)	C(1)-H(1A)	0.9900
Na(1)-N(2)	2.579(7)	C(1)-H(1B)	0.9900
Na(1)-N(1)	2.587(7)	C(2)-H(2A)	0.9900
Na(1)-O(1)	2.620(7)	C(2)-H(2B)	0.9900
Na(1)-C(16)	3.109(9)	C(3)-C(4)	1.519(12)
Na(1)-C(24)	3.116(9)	C(3)-H(3A)	0.9900
O(1)-C(12)	1.209(10)	C(3)-H(3B)	0.9900
O(2)-C(16)	1.203(9)	C(4)-H(4A)	0.9900
O(3)-C(20)	1.192(9)	C(4)-H(4B)	0.9900
O(4)-C(24)	1.200(10)	C(5)-C(6)	1.516(13)
O(5)-C(12)	1.358(11)	C(5)-H(5A)	0.9900
O(5)-C(13)	1.464(13)	C(5)-H(5B)	0.9900
O(6)-C(16)	1.317(10)	C(6)-H(6A)	0.9900
O(6)-C(17)	1.467(12)	C(6)-H(6B)	0.9900
O(7)-C(20)	1.329(10)	C(7)-C(8)	1.495(13)
O(7)-C(21)	1.459(12)	C(7)-H(7A)	0.9900
O(8)-C(24)	1.318(11)	C(7)-H(7B)	0.9900
O(8)-C(25)	1.483(14)	C(8)-H(8A)	0.9900
N(1)-C(8)	1.465(11)	C(8)-H(8B)	0.9900
N(1)-C(9)	1.473(11)	C(9)-C(12)	1.525(12)
N(1)-C(1)	1.481(11)	C(9)-C(10)	1.555(13)
N(2)-C(14)	1.446(11)	C(9)-H(9)	1.0000
N(2)-C(3)	1.475(10)	C(10)-C(11)	1.391(18)
N(2)-C(2)	1.483(11)	C(10)-H(10D)	0.9900
N(3)-C(18)	1.468(11)	C(10)-H(10E)	0.9900
N(3)-C(4)	1.468(11)	C(11)-H(11A)	0.9900
N(3)-C(5)	1.479(11)	C(11)-H(11B)	0.9900
N(4)-C(22)	1.469(11)	C(13)-H(13A)	0.9800
N(4)-C(7)	1.473(11)	C(13)-H(13B)	0.9800
N(4)-C(6)	1.473(12)	C(13)-H(13C)	0.9800

Table A.9. Bond lengths [Å] and angles [°] for **17-NaTfO** contd.

C(14)-C(16)	1.531(12)	Na(2)-N(8)	2.587(8)
C(14)-C(15)	1.534(12)	Na(2)-C(49)	3.121(10)
C(14)-H(14)	1.0000	O(9)-C(37)	1.200(12)
C(15)-H(15A)	0.9800	O(10)-C(41)	1.209(10)
C(15)-H(15B)	0.9800	O(11)-C(45)	1.193(10)
C(15)-H(15C)	0.9800	O(12)-C(49)	1.192(11)
C(17)-H(17A)	0.9800	O(13)-C(37)	1.334(13)
C(17)-H(17B)	0.9800	O(13)-C(38)	1.441(17)
C(17)-H(17C)	0.9800	O(14)-C(41)	1.329(11)
C(18)-C(19)	1.509(13)	O(14)-C(42)	1.448(12)
C(18)-C(20)	1.537(11)	O(15)-C(45)	1.354(11)
C(18)-H(18)	1.0000	O(15)-C(46)	1.449(12)
C(19)-H(19A)	0.9800	O(16)-C(49)	1.343(12)
C(19)-H(19B)	0.9800	O(16)-C(50)	1.466(13)
C(19)-H(19C)	0.9800	N(8)-C(33)	1.458(13)
C(21)-H(21A)	0.9800	N(8)-C(34)	1.475(13)
C(21)-H(21B)	0.9800	N(8)-C(26)	1.484(12)
C(21)-H(21C)	0.9800	N(9)-C(39)	1.458(11)
C(22)-C(24)	1.519(13)	N(9)-C(27)	1.472(12)
C(22)-C(23)	1.532(14)	N(9)-C(28)	1.488(12)
C(22)-H(22)	1.0000	N(10)-C(29)	1.469(13)
C(23)-H(23A)	0.9800	N(10)-C(30)	1.480(13)
C(23)-H(23B)	0.9800	N(10)-C(43)	1.485(13)
C(23)-H(23C)	0.9800	N(11)-C(31)	1.451(14)
C(25)-H(25A)	0.9800	N(11)-C(47)	1.467(13)
C(25)-H(25B)	0.9800	N(11)-C(32)	1.484(13)
C(25)-H(25C)	0.9800	N(12)-N(13)	1.204(19)
Na(2)-O(12)	2.462(7)	N(12)-C(36)	1.57(2)
Na(2)-O(10)	2.463(7)	N(13)-N(14)	1.042(17)
Na(2)-N(10)	2.530(8)	C(26)-C(27)	1.504(14)
Na(2)-O(11)	2.533(7)	C(26)-H(26A)	0.9900
Na(2)-O(9)	2.545(8)	C(26)-H(26B)	0.9900
Na(2)-N(11)	2.550(8)	C(27)-H(27A)	0.9900
Na(2)-N(9)	2.573(8)	C(27)-H(27B)	0.9900

Table A.9. Bond lengths [Å] and angles [°] for **17-NaTfO** contd.

C(28)-C(29)	1.537(14)	C(42)-H(42B)	0.9800
C(28)-H(28A)	0.9900	C(42)-H(42C)	0.9800
C(28)-H(28B)	0.9900	C(43)-C(44)	1.501(15)
C(29)-H(29A)	0.9900	C(43)-C(45)	1.537(12)
C(29)-H(29B)	0.9900	C(43)-H(43)	1.0000
C(30)-C(31)	1.510(16)	C(44)-H(44A)	0.9800
C(30)-H(30A)	0.9900	C(44)-H(44B)	0.9800
C(30)-H(30B)	0.9900	C(44)-H(44C)	0.9800
C(31)-H(31A)	0.9900	C(46)-H(46A)	0.9800
C(31)-H(31B)	0.9900	C(46)-H(46B)	0.9800
C(32)-C(33)	1.491(15)	C(46)-H(46C)	0.9800
C(32)-H(32A)	0.9900	C(47)-C(48)	1.542(14)
C(32)-H(32B)	0.9900	C(47)-C(49)	1.543(14)
C(33)-H(33A)	0.9900	C(47)-H(47)	1.0000
C(33)-H(33B)	0.9900	C(48)-H(48A)	0.9800
C(34)-C(37)	1.513(14)	C(48)-H(48B)	0.9800
C(34)-C(35)	1.531(15)	C(48)-H(48C)	0.9800
C(34)-H(34)	1.0000	C(50)-H(50A)	0.9800
C(35)-C(36)	1.430(19)	C(50)-H(50B)	0.9800
C(35)-H(35A)	0.9900	C(50)-H(50C)	0.9800
C(35)-H(35B)	0.9900	Na(3)-O(18)	2.464(6)
C(36)-H(36A)	0.9900	Na(3)-O(17)	2.486(6)
C(36)-H(36B)	0.9900	Na(3)-O(20)	2.499(6)
C(38)-H(38A)	0.9800	Na(3)-O(19)	2.517(6)
C(38)-H(38B)	0.9800	Na(3)-N(17)	2.549(6)
C(38)-H(38C)	0.9800	Na(3)-N(18)	2.550(6)
C(39)-C(41)	1.514(12)	Na(3)-N(16)	2.561(6)
C(39)-C(40)	1.528(13)	Na(3)-N(15)	2.584(7)
C(39)-H(39)	1.0000	Na(3)-C(62)	3.100(8)
C(40)-H(40A)	0.9800	Na(3)-C(66)	3.121(8)
C(40)-H(40B)	0.9800	Na(3)-C(70)	3.129(9)
C(40)-H(40C)	0.9800	O(17)-C(62)	1.182(9)
C(42)-H(42A)	0.9800	O(18)-C(66)	1.200(8)

Table A.9. Bond lengths [Å] and angles [°] for **17-NaTfO** contd.

O(19)-C(70)	1.207(10)	C(54)-H(54B)	0.9900
O(20)-C(74)	1.211(9)	C(55)-C(56)	1.500(12)
O(21)-C(62)	1.330(10)	C(55)-H(55A)	0.9900
O(21)-C(63)	1.441(14)	C(55)-H(55B)	0.9900
O(22)-C(66)	1.332(9)	C(56)-H(56A)	0.9900
O(22)-C(67)	1.443(12)	C(56)-H(56B)	0.9900
O(23)-C(70)	1.341(11)	C(57)-C(58)	1.526(12)
O(23)-C(71)	1.434(16)	C(57)-H(57A)	0.9900
O(24)-C(74)	1.330(10)	C(57)-H(57B)	0.9900
O(24)-C(75)	1.452(13)	C(58)-H(58A)	0.9900
N(15)-C(59)	1.459(10)	C(58)-H(58B)	0.9900
N(15)-C(58)	1.467(10)	C(59)-C(62)	1.519(11)
N(15)-C(51)	1.473(10)	C(59)-C(60)	1.531(13)
N(16)-C(53)	1.464(10)	C(59)-H(59)	1.0000
N(16)-C(64)	1.466(10)	C(60)-C(61)	1.363(18)
N(16)-C(52)	1.479(10)	C(60)-H(60A)	0.9900
N(17)-C(68)	1.457(11)	C(60)-H(60B)	0.9900
N(17)-C(54)	1.459(11)	C(61)-H(61A)	0.9900
N(17)-C(55)	1.492(11)	C(61)-H(61B)	0.9900
N(18)-C(72)	1.453(9)	C(63)-H(63A)	0.9800
N(18)-C(57)	1.476(11)	C(63)-H(63B)	0.9800
N(18)-C(56)	1.476(11)	C(63)-H(63C)	0.9800
N(19)-N(20)	1.196(18)	C(64)-C(66)	1.528(11)
N(19)-C(61)	1.566(18)	C(64)-C(65)	1.529(12)
N(20)-N(21)	1.042(17)	C(64)-H(64)	1.0000
C(51)-C(52)	1.518(11)	C(65)-H(65A)	0.9800
C(51)-H(51A)	0.9900	C(65)-H(65B)	0.9800
C(51)-H(51B)	0.9900	C(65)-H(65C)	0.9800
C(52)-H(52A)	0.9900	C(67)-H(67A)	0.9800
C(52)-H(52B)	0.9900	C(67)-H(67B)	0.9800
C(53)-C(54)	1.514(13)	C(67)-H(67C)	0.9800
C(53)-H(53A)	0.9900	C(68)-C(70)	1.516(13)
C(53)-H(53B)	0.9900	C(68)-C(69)	1.550(12)
C(54)-H(54A)	0.9900	C(68)-H(68)	1.0000

Table A.9. Bond lengths [Å] and angles [°] for **17-NaTfO** contd.

C(69)-H(69A)	0.9800	O(32)-C(99)	1.336(10)
C(69)-H(69B)	0.9800	O(32)-C(100)	1.457(11)
C(69)-H(69C)	0.9800	N(22)-C(83)	1.432(12)
C(71)-H(71A)	0.9800	N(22)-C(84)	1.487(12)
C(71)-H(71B)	0.9800	N(22)-C(76)	1.488(11)
C(71)-H(71C)	0.9800	N(23)-C(89)	1.457(10)
C(72)-C(74)	1.523(11)	N(23)-C(78)	1.460(11)
C(72)-C(73)	1.538(12)	N(23)-C(77)	1.477(11)
C(72)-H(72)	1.0000	N(24)-C(79)	1.461(11)
C(73)-H(73A)	0.9800	N(24)-C(93)	1.469(12)
C(73)-H(73B)	0.9800	N(24)-C(80)	1.490(11)
C(73)-H(73C)	0.9800	N(25)-C(81)	1.458(12)
C(75)-H(75A)	0.9800	N(25)-C(97)	1.458(11)
C(75)-H(75B)	0.9800	N(25)-C(82)	1.496(12)
C(75)-H(75C)	0.9800	N(26)-N(27)	1.19(2)
Na(4)-O(27)	2.465(5)	N(26)-C(86)	1.56(2)
Na(4)-O(25)	2.495(7)	N(27)-N(28)	1.061(19)
Na(4)-O(28)	2.496(6)	C(76)-C(77)	1.505(12)
Na(4)-N(24)	2.537(7)	C(76)-H(76A)	0.9900
Na(4)-N(25)	2.555(7)	C(76)-H(76B)	0.9900
Na(4)-O(26)	2.570(7)	C(77)-H(77A)	0.9900
Na(4)-N(23)	2.575(7)	C(77)-H(77B)	0.9900
Na(4)-N(22)	2.594(7)	C(78)-C(79)	1.528(14)
Na(4)-C(95)	3.115(8)	C(78)-H(78A)	0.9900
O(25)-C(87)	1.177(12)	C(78)-H(78B)	0.9900
O(26)-C(91)	1.230(9)	C(79)-H(79A)	0.9900
O(27)-C(95)	1.197(9)	C(79)-H(79B)	0.9900
O(28)-C(99)	1.201(9)	C(80)-C(81)	1.511(13)
O(29)-C(87)	1.320(13)	C(80)-H(80A)	0.9900
O(29)-C(88)	1.454(16)	C(80)-H(80B)	0.9900
O(30)-C(91)	1.319(10)	C(81)-H(81A)	0.9900
O(30)-C(92)	1.437(12)	C(81)-H(81B)	0.9900
O(31)-C(95)	1.310(10)	C(82)-C(83)	1.494(15)
O(31)-C(96)	1.453(14)	C(82)-H(82A)	0.9900

Table A.9. Bond lengths [Å] and angles [°] for **17-NaTfO** contd.

C(82)-H(82B)	0.9900	C(97)-H(97)	1.0000
C(83)-H(83A)	0.9900	C(98)-H(98A)	0.9800
C(83)-H(83B)	0.9900	C(98)-H(98B)	0.9800
C(84)-C(87)	1.524(13)	C(98)-H(98C)	0.9800
C(84)-C(85)	1.549(14)	C(100)-H(10A)	0.9800
C(84)-H(84)	1.0000	C(100)-H(10B)	0.9800
C(85)-C(86)	1.412(19)	C(100)-H(10C)	0.9800
C(85)-H(85A)	0.9900	S(1)-O(2A)	1.422(9)
C(85)-H(85B)	0.9900	S(1)-O(3A)	1.440(8)
C(86)-H(86A)	0.9900	S(1)-O(1A)	1.443(8)
C(86)-H(86B)	0.9900	S(1)-C(1A)	1.706(12)
C(88)-H(88A)	0.9800	F(1)-C(1A)	1.355(11)
C(88)-H(88B)	0.9800	F(2)-C(1A)	1.402(12)
C(88)-H(88C)	0.9800	F(3)-C(1A)	1.357(12)
C(89)-C(91)	1.512(11)	S(4)-O(12A)	1.403(16)
C(89)-C(90)	1.528(13)	S(4)-O(11A)	1.412(15)
C(89)-H(89)	1.0000	S(4)-O(10A)	1.485(15)
C(90)-H(90A)	0.9800	S(4)-C(4A)	1.661(18)
C(90)-H(90B)	0.9800	F(10)-C(4A)	1.339(17)
C(90)-H(90C)	0.9800	F(11)-C(4A)	1.402(18)
C(92)-H(92A)	0.9800	F(12)-C(4A)	1.360(18)
C(92)-H(92B)	0.9800	S(2)-O(5A)	1.419(9)
C(92)-H(92C)	0.9800	S(2)-O(4A)	1.428(8)
C(93)-C(94)	1.516(13)	S(2)-O(6A)	1.430(9)
C(93)-C(95)	1.524(12)	S(2)-C(2A)	1.665(13)
C(93)-H(93)	1.0000	F(4)-C(2A)	1.344(13)
C(94)-H(94A)	0.9800	F(5)-C(2A)	1.428(14)
C(94)-H(94B)	0.9800	F(6)-C(2A)	1.359(13)
C(94)-H(94C)	0.9800	S(3)-O(9A)	1.430(10)
C(96)-H(96A)	0.9800	S(3)-O(8A)	1.439(12)
C(96)-H(96B)	0.9800	S(3)-O(7A)	1.485(11)
C(96)-H(96C)	0.9800	S(3)-C(3A)	1.620(15)
C(97)-C(98)	1.532(14)	F(7)-C(3A)	1.371(16)
C(97)-C(99)	1.533(11)	F(8)-C(3A)	1.404(16)

Table A.9. Bond lengths [Å] and angles [°] for **17-NaTfO** contd.

F(9)-C(3A)	1.362(16)	O(3)-Na(1)-N(1)	158.8(2)
S(5)-O(14A)	1.375(16)	N(4)-Na(1)-N(1)	71.9(2)
S(5)-O(13A)	1.436(14)	N(2)-Na(1)-N(1)	71.5(2)
S(5)-O(15A)	1.492(15)	O(2)-Na(1)-O(1)	73.8(2)
S(5)-C(5A)	1.649(17)	O(4)-Na(1)-O(1)	80.2(2)
F(13)-C(5A)	1.321(17)	N(3)-Na(1)-O(1)	158.8(3)
F(14)-C(5A)	1.400(18)	O(3)-Na(1)-O(1)	125.6(2)
F(15)-C(5A)	1.343(17)	N(4)-Na(1)-O(1)	86.8(2)
S(6)-O(34)	1.410(16)	N(2)-Na(1)-O(1)	121.7(2)
S(6)-O(33)	1.442(16)	N(1)-Na(1)-O(1)	64.1(2)
S(6)-O(35)	1.445(16)	O(2)-Na(1)-C(16)	20.7(2)
S(6)-C(6A)	1.667(18)	O(4)-Na(1)-C(16)	134.2(2)
F(16)-C(6A)	1.330(18)	N(3)-Na(1)-C(16)	107.0(3)
F(17)-C(6A)	1.400(19)	O(3)-Na(1)-C(16)	71.4(2)
F(18)-C(6A)	1.356(18)	N(4)-Na(1)-C(16)	159.4(3)
		N(2)-Na(1)-C(16)	49.3(2)
O(2)-Na(1)-O(4)	123.6(2)	N(1)-Na(1)-C(16)	89.9(3)
O(2)-Na(1)-N(3)	127.3(2)	O(1)-Na(1)-C(16)	94.0(2)
O(4)-Na(1)-N(3)	86.7(2)	O(2)-Na(1)-C(24)	131.6(3)
O(2)-Na(1)-O(3)	80.4(2)	O(4)-Na(1)-C(24)	20.9(2)
O(4)-Na(1)-O(3)	75.5(2)	N(3)-Na(1)-C(24)	92.7(3)
N(3)-Na(1)-O(3)	65.7(2)	O(3)-Na(1)-C(24)	96.3(3)
O(2)-Na(1)-N(4)	155.1(3)	N(4)-Na(1)-C(24)	49.8(2)
O(4)-Na(1)-N(4)	66.3(2)	N(2)-Na(1)-C(24)	161.7(3)
N(3)-Na(1)-N(4)	72.7(2)	N(1)-Na(1)-C(24)	104.9(3)
O(3)-Na(1)-N(4)	124.2(2)	O(1)-Na(1)-C(24)	69.4(3)
O(2)-Na(1)-N(2)	66.6(2)	C(16)-Na(1)-C(24)	148.7(3)
O(4)-Na(1)-N(2)	158.0(3)	C(12)-O(1)-Na(1)	105.1(5)
N(3)-Na(1)-N(2)	73.0(2)	C(16)-O(2)-Na(1)	113.7(5)
O(3)-Na(1)-N(2)	88.3(2)	C(20)-O(3)-Na(1)	109.9(5)
N(4)-Na(1)-N(2)	113.5(2)	C(24)-O(4)-Na(1)	112.1(6)
O(2)-Na(1)-N(1)	85.4(2)	C(12)-O(5)-C(13)	116.8(9)
O(4)-Na(1)-N(1)	125.7(3)	C(16)-O(6)-C(17)	114.4(8)
N(3)-Na(1)-N(1)	112.5(2)	C(20)-O(7)-C(21)	115.8(8)

Table A.9. Bond lengths [Å] and angles [°] for **17-NaTfO** contd.

C(24)-O(8)-C(25)	115.1(10)	N(2)-C(2)-H(2A)	108.7
C(8)-N(1)-C(9)	112.0(8)	C(1)-C(2)-H(2A)	108.7
C(8)-N(1)-C(1)	111.2(7)	N(2)-C(2)-H(2B)	108.7
C(9)-N(1)-C(1)	111.6(7)	C(1)-C(2)-H(2B)	108.7
C(8)-N(1)-Na(1)	107.1(5)	H(2A)-C(2)-H(2B)	107.6
C(9)-N(1)-Na(1)	107.6(5)	N(2)-C(3)-C(4)	112.9(6)
C(1)-N(1)-Na(1)	107.0(5)	N(2)-C(3)-H(3A)	109.0
C(14)-N(2)-C(3)	113.2(7)	C(4)-C(3)-H(3A)	109.0
C(14)-N(2)-C(2)	114.5(7)	N(2)-C(3)-H(3B)	109.0
C(3)-N(2)-C(2)	108.7(6)	C(4)-C(3)-H(3B)	109.0
C(14)-N(2)-Na(1)	104.0(4)	H(3A)-C(3)-H(3B)	107.8
C(3)-N(2)-Na(1)	106.8(5)	N(3)-C(4)-C(3)	114.7(7)
C(2)-N(2)-Na(1)	109.2(5)	N(3)-C(4)-H(4A)	108.6
C(18)-N(3)-C(4)	109.9(7)	C(3)-C(4)-H(4A)	108.6
C(18)-N(3)-C(5)	112.5(7)	N(3)-C(4)-H(4B)	108.6
C(4)-N(3)-C(5)	111.5(7)	C(3)-C(4)-H(4B)	108.6
C(18)-N(3)-Na(1)	107.9(4)	H(4A)-C(4)-H(4B)	107.6
C(4)-N(3)-Na(1)	107.2(5)	N(3)-C(5)-C(6)	111.8(7)
C(5)-N(3)-Na(1)	107.6(5)	N(3)-C(5)-H(5A)	109.2
C(22)-N(4)-C(7)	112.3(8)	C(6)-C(5)-H(5A)	109.2
C(22)-N(4)-C(6)	112.3(8)	N(3)-C(5)-H(5B)	109.2
C(7)-N(4)-C(6)	111.1(7)	C(6)-C(5)-H(5B)	109.2
C(22)-N(4)-Na(1)	105.4(5)	H(5A)-C(5)-H(5B)	107.9
C(7)-N(4)-Na(1)	108.2(5)	N(4)-C(6)-C(5)	113.6(8)
C(6)-N(4)-Na(1)	107.1(5)	N(4)-C(6)-H(6A)	108.8
N(6)-N(5)-C(11)	118.5(18)	C(5)-C(6)-H(6A)	108.8
N(7)-N(6)-N(5)	169(2)	N(4)-C(6)-H(6B)	108.8
N(1)-C(1)-C(2)	114.2(7)	C(5)-C(6)-H(6B)	108.8
N(1)-C(1)-H(1A)	108.7	H(6A)-C(6)-H(6B)	107.7
C(2)-C(1)-H(1A)	108.7	N(4)-C(7)-C(8)	114.0(7)
N(1)-C(1)-H(1B)	108.7	N(4)-C(7)-H(7A)	108.7
C(2)-C(1)-H(1B)	108.7	C(8)-C(7)-H(7A)	108.7
H(1A)-C(1)-H(1B)	107.6	N(4)-C(7)-H(7B)	108.7
N(2)-C(2)-C(1)	114.1(7)	C(8)-C(7)-H(7B)	108.7

Table A.9. Bond lengths [Å] and angles [°] for **17-NaTfO** contd.

H(7A)-C(7)-H(7B)	107.6	N(2)-C(14)-C(16)	108.7(7)
N(1)-C(8)-C(7)	114.6(8)	N(2)-C(14)-C(15)	115.8(8)
N(1)-C(8)-H(8A)	108.6	C(16)-C(14)-C(15)	111.4(8)
C(7)-C(8)-H(8A)	108.6	N(2)-C(14)-H(14)	106.8
N(1)-C(8)-H(8B)	108.6	C(16)-C(14)-H(14)	106.8
C(7)-C(8)-H(8B)	108.6	C(15)-C(14)-H(14)	106.8
H(8A)-C(8)-H(8B)	107.6	C(14)-C(15)-H(15A)	109.5
N(1)-C(9)-C(12)	109.6(7)	C(14)-C(15)-H(15B)	109.5
N(1)-C(9)-C(10)	114.5(9)	H(15A)-C(15)-H(15B)	109.5
C(12)-C(9)-C(10)	113.1(9)	C(14)-C(15)-H(15C)	109.5
N(1)-C(9)-H(9)	106.3	H(15A)-C(15)-H(15C)	109.5
C(12)-C(9)-H(9)	106.3	H(15B)-C(15)-H(15C)	109.5
C(10)-C(9)-H(9)	106.3	O(2)-C(16)-O(6)	123.1(8)
C(11)-C(10)-C(9)	119.3(14)	O(2)-C(16)-C(14)	125.1(8)
C(11)-C(10)-H(10D)	107.5	O(6)-C(16)-C(14)	111.4(7)
C(9)-C(10)-H(10D)	107.5	O(2)-C(16)-Na(1)	45.5(4)
C(11)-C(10)-H(10E)	107.5	O(6)-C(16)-Na(1)	157.8(7)
C(9)-C(10)-H(10E)	107.5	C(14)-C(16)-Na(1)	81.2(5)
H(10D)-C(10)-H(10E)	107.0	O(6)-C(17)-H(17A)	109.5
C(10)-C(11)-N(5)	114.7(14)	O(6)-C(17)-H(17B)	109.5
C(10)-C(11)-H(11A)	108.6	H(17A)-C(17)-H(17B)	109.5
N(5)-C(11)-H(11A)	108.6	O(6)-C(17)-H(17C)	109.5
C(10)-C(11)-H(11B)	108.6	H(17A)-C(17)-H(17C)	109.5
N(5)-C(11)-H(11B)	108.6	H(17B)-C(17)-H(17C)	109.5
H(11A)-C(11)-H(11B)	107.6	N(3)-C(18)-C(19)	116.0(7)
O(1)-C(12)-O(5)	125.1(8)	N(3)-C(18)-C(20)	109.3(7)
O(1)-C(12)-C(9)	125.8(8)	C(19)-C(18)-C(20)	113.5(8)
O(5)-C(12)-C(9)	109.1(8)	N(3)-C(18)-H(18)	105.7
O(5)-C(13)-H(13A)	109.5	C(19)-C(18)-H(18)	105.7
O(5)-C(13)-H(13B)	109.5	C(20)-C(18)-H(18)	105.7
H(13A)-C(13)-H(13B)	109.5	C(18)-C(19)-H(19A)	109.5
O(5)-C(13)-H(13C)	109.5	C(18)-C(19)-H(19B)	109.5
H(13A)-C(13)-H(13C)	109.5	H(19A)-C(19)-H(19B)	109.5
H(13B)-C(13)-H(13C)	109.5	C(18)-C(19)-H(19C)	109.5

Table A.9. Bond lengths [Å] and angles [°] for **17-NaTfO** contd.

H(19A)-C(19)-H(19C)	109.5	H(25B)-C(25)-H(25C)	109.5
H(19B)-C(19)-H(19C)	109.5	O(12)-Na(2)-O(10)	122.9(3)
O(3)-C(20)-O(7)	124.8(7)	O(12)-Na(2)-N(10)	87.3(3)
O(3)-C(20)-C(18)	125.3(7)	O(10)-Na(2)-N(10)	126.5(3)
O(7)-C(20)-C(18)	109.9(7)	O(12)-Na(2)-O(11)	79.2(3)
O(7)-C(21)-H(21A)	109.5	O(10)-Na(2)-O(11)	78.2(2)
O(7)-C(21)-H(21B)	109.5	N(10)-Na(2)-O(11)	64.5(2)
H(21A)-C(21)-H(21B)	109.5	O(12)-Na(2)-O(9)	78.3(3)
O(7)-C(21)-H(21C)	109.5	O(10)-Na(2)-O(9)	75.6(3)
H(21A)-C(21)-H(21C)	109.5	N(10)-Na(2)-O(9)	157.8(3)
H(21B)-C(21)-H(21C)	109.5	O(11)-Na(2)-O(9)	127.6(3)
N(4)-C(22)-C(24)	109.4(7)	O(12)-Na(2)-N(11)	66.2(3)
N(4)-C(22)-C(23)	116.4(9)	O(10)-Na(2)-N(11)	155.7(3)
C(24)-C(22)-C(23)	112.0(9)	N(10)-Na(2)-N(11)	73.3(3)
N(4)-C(22)-H(22)	106.1	O(11)-Na(2)-N(11)	125.9(3)
C(24)-C(22)-H(22)	106.1	O(9)-Na(2)-N(11)	85.4(3)
C(23)-C(22)-H(22)	106.1	O(12)-Na(2)-N(9)	158.5(3)
C(22)-C(23)-H(23A)	109.5	O(10)-Na(2)-N(9)	65.4(2)
C(22)-C(23)-H(23B)	109.5	N(10)-Na(2)-N(9)	73.5(3)
H(23A)-C(23)-H(23B)	109.5	O(11)-Na(2)-N(9)	83.9(3)
C(22)-C(23)-H(23C)	109.5	O(9)-Na(2)-N(9)	122.9(3)
H(23A)-C(23)-H(23C)	109.5	N(11)-Na(2)-N(9)	115.3(3)
H(23B)-C(23)-H(23C)	109.5	O(12)-Na(2)-N(8)	125.3(3)
O(4)-C(24)-O(8)	122.7(9)	O(10)-Na(2)-N(8)	85.5(3)
O(4)-C(24)-C(22)	125.4(8)	N(10)-Na(2)-N(8)	113.5(3)
O(8)-C(24)-C(22)	111.9(9)	O(11)-Na(2)-N(8)	155.5(3)
O(4)-C(24)-Na(1)	47.0(4)	O(9)-Na(2)-N(8)	64.0(3)
O(8)-C(24)-Na(1)	154.6(8)	N(11)-Na(2)-N(8)	72.4(3)
C(22)-C(24)-Na(1)	81.8(5)	N(9)-Na(2)-N(8)	72.6(3)
O(8)-C(25)-H(25A)	109.5	O(12)-Na(2)-C(49)	20.6(3)
O(8)-C(25)-H(25B)	109.5	O(10)-Na(2)-C(49)	130.8(3)
H(25A)-C(25)-H(25B)	109.5	N(10)-Na(2)-C(49)	93.6(4)
O(8)-C(25)-H(25C)	109.5	O(11)-Na(2)-C(49)	99.7(3)
H(25A)-C(25)-H(25C)	109.5	O(9)-Na(2)-C(49)	67.3(3)

Table A.9. Bond lengths [Å] and angles [°] for **17-NaTfO** contd.

N(11)-Na(2)-C(49)	50.0(3)	C(32)-N(11)-Na(2)	106.4(7)
N(9)-Na(2)-C(49)	163.7(3)	N(13)-N(12)-C(36)	118(2)
N(8)-Na(2)-C(49)	104.8(3)	N(14)-N(13)-N(12)	165(3)
C(37)-O(9)-Na(2)	109.8(6)	N(8)-C(26)-C(27)	113.0(8)
C(41)-O(10)-Na(2)	114.5(6)	N(8)-C(26)-H(26A)	109.0
C(45)-O(11)-Na(2)	113.9(6)	C(27)-C(26)-H(26A)	109.0
C(49)-O(12)-Na(2)	112.6(7)	N(8)-C(26)-H(26B)	109.0
C(37)-O(13)-C(38)	117.4(14)	C(27)-C(26)-H(26B)	109.0
C(41)-O(14)-C(42)	116.3(8)	H(26A)-C(26)-H(26B)	107.8
C(45)-O(15)-C(46)	117.4(8)	N(9)-C(27)-C(26)	116.5(10)
C(49)-O(16)-C(50)	113.9(8)	N(9)-C(27)-H(27A)	108.2
C(33)-N(8)-C(34)	112.1(9)	C(26)-C(27)-H(27A)	108.2
C(33)-N(8)-C(26)	113.0(9)	N(9)-C(27)-H(27B)	108.2
C(34)-N(8)-C(26)	109.3(9)	C(26)-C(27)-H(27B)	108.2
C(33)-N(8)-Na(2)	107.3(6)	H(27A)-C(27)-H(27B)	107.3
C(34)-N(8)-Na(2)	107.7(6)	N(9)-C(28)-C(29)	114.2(8)
C(26)-N(8)-Na(2)	107.1(6)	N(9)-C(28)-H(28A)	108.7
C(39)-N(9)-C(27)	112.7(9)	C(29)-C(28)-H(28A)	108.7
C(39)-N(9)-C(28)	115.0(9)	N(9)-C(28)-H(28B)	108.7
C(27)-N(9)-C(28)	110.8(8)	C(29)-C(28)-H(28B)	108.7
C(39)-N(9)-Na(2)	105.0(5)	H(28A)-C(28)-H(28B)	107.6
C(27)-N(9)-Na(2)	106.7(6)	N(10)-C(29)-C(28)	114.0(10)
C(28)-N(9)-Na(2)	105.9(7)	N(10)-C(29)-H(29A)	108.8
C(29)-N(10)-C(30)	111.9(9)	C(28)-C(29)-H(29A)	108.8
C(29)-N(10)-C(43)	112.3(9)	N(10)-C(29)-H(29B)	108.8
C(30)-N(10)-C(43)	110.3(9)	C(28)-C(29)-H(29B)	108.8
C(29)-N(10)-Na(2)	108.8(6)	H(29A)-C(29)-H(29B)	107.6
C(30)-N(10)-Na(2)	106.7(7)	N(10)-C(30)-C(31)	114.4(10)
C(43)-N(10)-Na(2)	106.5(5)	N(10)-C(30)-H(30A)	108.7
C(31)-N(11)-C(47)	112.0(10)	C(31)-C(30)-H(30A)	108.7
C(31)-N(11)-C(32)	112.0(9)	N(10)-C(30)-H(30B)	108.7
C(47)-N(11)-C(32)	113.1(11)	C(31)-C(30)-H(30B)	108.7
C(31)-N(11)-Na(2)	107.2(7)	H(30A)-C(30)-H(30B)	107.6
C(47)-N(11)-Na(2)	105.6(6)	N(11)-C(31)-C(30)	114.5(11)

Table A.9. Bond lengths [Å] and angles [°] for **17-NaTfO** contd.

N(11)-C(31)-H(31A)	108.6	H(36A)-C(36)-H(36B)	107.9
C(30)-C(31)-H(31A)	108.6	O(9)-C(37)-O(13)	120.5(11)
N(11)-C(31)-H(31B)	108.6	O(9)-C(37)-C(34)	127.3(10)
C(30)-C(31)-H(31B)	108.6	O(13)-C(37)-C(34)	112.2(11)
H(31A)-C(31)-H(31B)	107.6	O(13)-C(38)-H(38A)	109.5
N(11)-C(32)-C(33)	114.9(9)	O(13)-C(38)-H(38B)	109.5
N(11)-C(32)-H(32A)	108.5	H(38A)-C(38)-H(38B)	109.5
C(33)-C(32)-H(32A)	108.5	O(13)-C(38)-H(38C)	109.5
N(11)-C(32)-H(32B)	108.5	H(38A)-C(38)-H(38C)	109.5
C(33)-C(32)-H(32B)	108.5	H(38B)-C(38)-H(38C)	109.5
H(32A)-C(32)-H(32B)	107.5	N(9)-C(39)-C(41)	109.1(7)
N(8)-C(33)-C(32)	114.0(11)	N(9)-C(39)-C(40)	114.3(9)
N(8)-C(33)-H(33A)	108.8	C(41)-C(39)-C(40)	111.7(9)
C(32)-C(33)-H(33A)	108.8	N(9)-C(39)-H(39)	107.1
N(8)-C(33)-H(33B)	108.8	C(41)-C(39)-H(39)	107.1
C(32)-C(33)-H(33B)	108.8	C(40)-C(39)-H(39)	107.1
H(33A)-C(33)-H(33B)	107.6	C(39)-C(40)-H(40A)	109.5
N(8)-C(34)-C(37)	107.3(9)	C(39)-C(40)-H(40B)	109.5
N(8)-C(34)-C(35)	116.7(11)	H(40A)-C(40)-H(40B)	109.5
C(37)-C(34)-C(35)	114.8(13)	C(39)-C(40)-H(40C)	109.5
N(8)-C(34)-H(34)	105.7	H(40A)-C(40)-H(40C)	109.5
C(37)-C(34)-H(34)	105.7	H(40B)-C(40)-H(40C)	109.5
C(35)-C(34)-H(34)	105.7	O(10)-C(41)-O(14)	122.2(8)
C(36)-C(35)-C(34)	117.4(15)	O(10)-C(41)-C(39)	123.8(9)
C(36)-C(35)-H(35A)	108.0	O(14)-C(41)-C(39)	113.8(8)
C(34)-C(35)-H(35A)	108.0	O(14)-C(42)-H(42A)	109.5
C(36)-C(35)-H(35B)	108.0	O(14)-C(42)-H(42B)	109.5
C(34)-C(35)-H(35B)	108.0	H(42A)-C(42)-H(42B)	109.5
H(35A)-C(35)-H(35B)	107.2	O(14)-C(42)-H(42C)	109.5
C(35)-C(36)-N(12)	112.0(16)	H(42A)-C(42)-H(42C)	109.5
C(35)-C(36)-H(36A)	109.2	H(42B)-C(42)-H(42C)	109.5
N(12)-C(36)-H(36A)	109.2	N(10)-C(43)-C(44)	117.4(10)
C(35)-C(36)-H(36B)	109.2	N(10)-C(43)-C(45)	105.1(8)
N(12)-C(36)-H(36B)	109.2	C(44)-C(43)-C(45)	114.1(11)

Table A.9. Bond lengths [Å] and angles [°] for **17-NaTfO** contd.

N(10)-C(43)-H(43)	106.5	O(16)-C(49)-Na(2)	154.7(8)
C(44)-C(43)-H(43)	106.5	C(47)-C(49)-Na(2)	81.3(5)
C(45)-C(43)-H(43)	106.5	O(16)-C(50)-H(50A)	109.5
C(43)-C(44)-H(44A)	109.5	O(16)-C(50)-H(50B)	109.5
C(43)-C(44)-H(44B)	109.5	H(50A)-C(50)-H(50B)	109.5
H(44A)-C(44)-H(44B)	109.5	O(16)-C(50)-H(50C)	109.5
C(43)-C(44)-H(44C)	109.5	H(50A)-C(50)-H(50C)	109.5
H(44A)-C(44)-H(44C)	109.5	H(50B)-C(50)-H(50C)	109.5
H(44B)-C(44)-H(44C)	109.5	O(18)-Na(3)-O(17)	75.5(2)
O(11)-C(45)-O(15)	122.4(8)	O(18)-Na(3)-O(20)	125.4(2)
O(11)-C(45)-C(43)	124.4(8)	O(17)-Na(3)-O(20)	79.0(2)
O(15)-C(45)-C(43)	113.1(8)	O(18)-Na(3)-O(19)	80.3(2)
O(15)-C(46)-H(46A)	109.5	O(17)-Na(3)-O(19)	125.7(2)
O(15)-C(46)-H(46B)	109.5	O(20)-Na(3)-O(19)	77.0(2)
H(46A)-C(46)-H(46B)	109.5	O(18)-Na(3)-N(17)	126.3(2)
O(15)-C(46)-H(46C)	109.5	O(17)-Na(3)-N(17)	158.3(2)
H(46A)-C(46)-H(46C)	109.5	O(20)-Na(3)-N(17)	86.3(2)
H(46B)-C(46)-H(46C)	109.5	O(19)-Na(3)-N(17)	65.0(2)
N(11)-C(47)-C(48)	118.1(12)	O(18)-Na(3)-N(18)	154.9(2)
N(11)-C(47)-C(49)	109.2(9)	O(17)-Na(3)-N(18)	86.5(2)
C(48)-C(47)-C(49)	112.8(10)	O(20)-Na(3)-N(18)	66.0(2)
N(11)-C(47)-H(47)	105.2	O(19)-Na(3)-N(18)	124.8(2)
C(48)-C(47)-H(47)	105.2	N(17)-Na(3)-N(18)	72.9(2)
C(49)-C(47)-H(47)	105.2	O(18)-Na(3)-N(16)	66.4(2)
C(47)-C(48)-H(48A)	109.5	O(17)-Na(3)-N(16)	124.2(2)
C(47)-C(48)-H(48B)	109.5	O(20)-Na(3)-N(16)	156.7(2)
H(48A)-C(48)-H(48B)	109.5	O(19)-Na(3)-N(16)	86.6(2)
C(47)-C(48)-H(48C)	109.5	N(17)-Na(3)-N(16)	71.7(2)
H(48A)-C(48)-H(48C)	109.5	N(18)-Na(3)-N(16)	112.6(2)
H(48B)-C(48)-H(48C)	109.5	O(18)-Na(3)-N(15)	84.1(2)
O(12)-C(49)-O(16)	123.3(9)	O(17)-Na(3)-N(15)	65.20(19)
O(12)-C(49)-C(47)	124.3(9)	O(20)-Na(3)-N(15)	125.9(2)
O(16)-C(49)-C(47)	112.3(9)	O(19)-Na(3)-N(15)	157.0(2)
O(12)-C(49)-Na(2)	46.7(5)	N(17)-Na(3)-N(15)	113.0(2)

Table A.9. Bond lengths [Å] and angles [°] for **17-NaTfO** contd.

N(18)-Na(3)-N(15)	72.5(2)	C(66)-O(22)-C(67)	115.8(8)
N(16)-Na(3)-N(15)	71.7(2)	C(70)-O(23)-C(71)	114.7(10)
O(18)-Na(3)-C(62)	63.7(2)	C(74)-O(24)-C(75)	115.5(8)
O(17)-Na(3)-C(62)	20.96(18)	C(59)-N(15)-C(58)	112.4(6)
O(20)-Na(3)-C(62)	99.9(2)	C(59)-N(15)-C(51)	112.3(6)
O(19)-Na(3)-C(62)	133.5(2)	C(58)-N(15)-C(51)	111.7(6)
N(17)-Na(3)-C(62)	161.4(3)	C(59)-N(15)-Na(3)	104.8(4)
N(18)-Na(3)-C(62)	93.5(2)	C(58)-N(15)-Na(3)	107.4(5)
N(16)-Na(3)-C(62)	103.4(2)	C(51)-N(15)-Na(3)	107.8(5)
N(15)-Na(3)-C(62)	49.40(19)	C(53)-N(16)-C(64)	112.8(7)
O(18)-Na(3)-C(66)	20.86(17)	C(53)-N(16)-C(52)	110.9(7)
O(17)-Na(3)-C(66)	96.1(2)	C(64)-N(16)-C(52)	113.1(6)
O(20)-Na(3)-C(66)	134.5(2)	C(53)-N(16)-Na(3)	107.5(5)
O(19)-Na(3)-C(66)	69.5(2)	C(64)-N(16)-Na(3)	102.7(4)
N(17)-Na(3)-C(66)	105.6(2)	C(52)-N(16)-Na(3)	109.4(4)
N(18)-Na(3)-C(66)	159.5(2)	C(68)-N(17)-C(54)	111.3(7)
N(16)-Na(3)-C(66)	49.7(2)	C(68)-N(17)-C(55)	111.8(7)
N(15)-Na(3)-C(66)	90.2(2)	C(54)-N(17)-C(55)	110.6(8)
C(62)-Na(3)-C(66)	82.7(2)	C(68)-N(17)-Na(3)	107.0(5)
O(18)-Na(3)-C(70)	101.6(2)	C(54)-N(17)-Na(3)	109.6(5)
O(17)-Na(3)-C(70)	133.6(3)	C(55)-N(17)-Na(3)	106.5(5)
O(20)-Na(3)-C(70)	65.2(2)	C(72)-N(18)-C(57)	111.4(6)
O(19)-Na(3)-C(70)	21.4(2)	C(72)-N(18)-C(56)	112.9(6)
N(17)-Na(3)-C(70)	49.2(3)	C(57)-N(18)-C(56)	111.6(6)
N(18)-Na(3)-C(70)	103.5(2)	C(72)-N(18)-Na(3)	105.5(4)
N(16)-Na(3)-C(70)	93.9(2)	C(57)-N(18)-Na(3)	107.6(5)
N(15)-Na(3)-C(70)	161.1(2)	C(56)-N(18)-Na(3)	107.5(5)
C(62)-Na(3)-C(70)	149.0(3)	N(20)-N(19)-C(61)	116.3(17)
C(66)-Na(3)-C(70)	89.4(2)	N(21)-N(20)-N(19)	162(3)
C(62)-O(17)-Na(3)	110.2(4)	N(15)-C(51)-C(52)	113.8(6)
C(66)-O(18)-Na(3)	112.2(5)	N(15)-C(51)-H(51A)	108.8
C(70)-O(19)-Na(3)	109.2(5)	C(52)-C(51)-H(51A)	108.8
C(74)-O(20)-Na(3)	111.0(5)	N(15)-C(51)-H(51B)	108.8
C(62)-O(21)-C(63)	117.0(9)	C(52)-C(51)-H(51B)	108.8

Table A.9. Bond lengths [Å] and angles [°] for **17-NaTfO** contd.

H(51A)-C(51)-H(51B)	107.7	N(18)-C(57)-H(57B)	108.7
N(16)-C(52)-C(51)	113.4(7)	C(58)-C(57)-H(57B)	108.7
N(16)-C(52)-H(52A)	108.9	H(57A)-C(57)-H(57B)	107.6
C(51)-C(52)-H(52A)	108.9	N(15)-C(58)-C(57)	113.1(7)
N(16)-C(52)-H(52B)	108.9	N(15)-C(58)-H(58A)	109.0
C(51)-C(52)-H(52B)	108.9	C(57)-C(58)-H(58A)	109.0
H(52A)-C(52)-H(52B)	107.7	N(15)-C(58)-H(58B)	108.9
N(16)-C(53)-C(54)	114.9(7)	C(57)-C(58)-H(58B)	108.9
N(16)-C(53)-H(53A)	108.6	H(58A)-C(58)-H(58B)	107.8
C(54)-C(53)-H(53A)	108.6	N(15)-C(59)-C(62)	108.8(6)
N(16)-C(53)-H(53B)	108.6	N(15)-C(59)-C(60)	118.6(10)
C(54)-C(53)-H(53B)	108.6	C(62)-C(59)-C(60)	108.7(9)
H(53A)-C(53)-H(53B)	107.5	N(15)-C(59)-H(59)	106.8
N(17)-C(54)-C(53)	112.4(7)	C(62)-C(59)-H(59)	106.8
N(17)-C(54)-H(54A)	109.1	C(60)-C(59)-H(59)	106.8
C(53)-C(54)-H(54A)	109.1	C(61)-C(60)-C(59)	116.7(12)
N(17)-C(54)-H(54B)	109.1	C(61)-C(60)-H(60A)	108.1
C(53)-C(54)-H(54B)	109.1	C(59)-C(60)-H(60A)	108.1
H(54A)-C(54)-H(54B)	107.9	C(61)-C(60)-H(60B)	108.1
N(17)-C(55)-C(56)	113.4(7)	C(59)-C(60)-H(60B)	108.1
N(17)-C(55)-H(55A)	108.9	H(60A)-C(60)-H(60B)	107.3
C(56)-C(55)-H(55A)	108.9	C(60)-C(61)-N(19)	113.1(14)
N(17)-C(55)-H(55B)	108.9	C(60)-C(61)-H(61A)	109.0
C(56)-C(55)-H(55B)	108.9	N(19)-C(61)-H(61A)	109.0
H(55A)-C(55)-H(55B)	107.7	C(60)-C(61)-H(61B)	109.0
N(18)-C(56)-C(55)	113.6(7)	N(19)-C(61)-H(61B)	109.0
N(18)-C(56)-H(56A)	108.8	H(61A)-C(61)-H(61B)	107.8
C(55)-C(56)-H(56A)	108.8	O(17)-C(62)-O(21)	122.5(7)
N(18)-C(56)-H(56B)	108.8	O(17)-C(62)-C(59)	126.6(7)
C(55)-C(56)-H(56B)	108.8	O(21)-C(62)-C(59)	110.9(7)
H(56A)-C(56)-H(56B)	107.7	O(17)-C(62)-Na(3)	48.8(4)
N(18)-C(57)-C(58)	114.3(7)	O(21)-C(62)-Na(3)	153.2(6)
N(18)-C(57)-H(57A)	108.7	C(59)-C(62)-Na(3)	82.8(4)
C(58)-C(57)-H(57A)	108.7	O(21)-C(63)-H(63A)	109.5

Table A.9. Bond lengths [Å] and angles [°] for **17-NaTfO** contd.

O(21)-C(63)-H(63B)	109.5	C(69)-C(68)-H(68)	106.4
H(63A)-C(63)-H(63B)	109.5	C(68)-C(69)-H(69A)	109.5
O(21)-C(63)-H(63C)	109.5	C(68)-C(69)-H(69B)	109.5
H(63A)-C(63)-H(63C)	109.5	H(69A)-C(69)-H(69B)	109.5
H(63B)-C(63)-H(63C)	109.5	C(68)-C(69)-H(69C)	109.5
N(16)-C(64)-C(66)	109.4(6)	H(69A)-C(69)-H(69C)	109.5
N(16)-C(64)-C(65)	114.6(8)	H(69B)-C(69)-H(69C)	109.5
C(66)-C(64)-C(65)	112.8(8)	O(19)-C(70)-O(23)	123.2(10)
N(16)-C(64)-H(64)	106.5	O(19)-C(70)-C(68)	125.3(8)
C(66)-C(64)-H(64)	106.5	O(23)-C(70)-C(68)	111.5(9)
C(65)-C(64)-H(64)	106.5	O(19)-C(70)-Na(3)	49.4(4)
C(64)-C(65)-H(65A)	109.5	O(23)-C(70)-Na(3)	151.6(7)
C(64)-C(65)-H(65B)	109.5	C(68)-C(70)-Na(3)	82.1(5)
H(65A)-C(65)-H(65B)	109.5	O(23)-C(71)-H(71A)	109.5
C(64)-C(65)-H(65C)	109.5	O(23)-C(71)-H(71B)	109.5
H(65A)-C(65)-H(65C)	109.5	H(71A)-C(71)-H(71B)	109.5
H(65B)-C(65)-H(65C)	109.5	O(23)-C(71)-H(71C)	109.5
O(18)-C(66)-O(22)	122.9(7)	H(71A)-C(71)-H(71C)	109.5
O(18)-C(66)-C(64)	124.3(7)	H(71B)-C(71)-H(71C)	109.5
O(22)-C(66)-C(64)	112.7(6)	N(18)-C(72)-C(74)	108.9(6)
O(18)-C(66)-Na(3)	47.0(4)	N(18)-C(72)-C(73)	116.3(7)
O(22)-C(66)-Na(3)	158.5(6)	C(74)-C(72)-C(73)	111.0(7)
C(64)-C(66)-Na(3)	79.6(4)	N(18)-C(72)-H(72)	106.7
O(22)-C(67)-H(67A)	109.5	C(74)-C(72)-H(72)	106.7
O(22)-C(67)-H(67B)	109.5	C(73)-C(72)-H(72)	106.7
H(67A)-C(67)-H(67B)	109.5	C(72)-C(73)-H(73A)	109.5
O(22)-C(67)-H(67C)	109.5	C(72)-C(73)-H(73B)	109.5
H(67A)-C(67)-H(67C)	109.5	H(73A)-C(73)-H(73B)	109.5
H(67B)-C(67)-H(67C)	109.5	C(72)-C(73)-H(73C)	109.5
N(17)-C(68)-C(70)	109.1(7)	H(73A)-C(73)-H(73C)	109.5
N(17)-C(68)-C(69)	116.4(9)	H(73B)-C(73)-H(73C)	109.5
C(70)-C(68)-C(69)	111.4(9)	O(20)-C(74)-O(24)	121.8(7)
N(17)-C(68)-H(68)	106.4	O(20)-C(74)-C(72)	125.7(7)
C(70)-C(68)-H(68)	106.4	O(24)-C(74)-C(72)	112.2(7)

Table A.9. Bond lengths [Å] and angles [°] for **17-NaTfO** contd.

O(24)-C(75)-H(75A)	109.5	O(27)-Na(4)-C(95)	20.91(19)
O(24)-C(75)-H(75B)	109.5	O(25)-Na(4)-C(95)	133.7(3)
H(75A)-C(75)-H(75B)	109.5	O(28)-Na(4)-C(95)	66.4(2)
O(24)-C(75)-H(75C)	109.5	N(24)-Na(4)-C(95)	49.8(2)
H(75A)-C(75)-H(75C)	109.5	N(25)-Na(4)-C(95)	105.4(3)
H(75B)-C(75)-H(75C)	109.5	O(26)-Na(4)-C(95)	99.5(2)
O(27)-Na(4)-O(25)	124.7(3)	N(23)-Na(4)-C(95)	93.1(2)
O(27)-Na(4)-O(28)	77.47(19)	N(22)-Na(4)-C(95)	161.9(3)
O(25)-Na(4)-O(28)	79.2(2)	C(87)-O(25)-Na(4)	112.4(6)
O(27)-Na(4)-N(24)	66.2(2)	C(91)-O(26)-Na(4)	112.8(5)
O(25)-Na(4)-N(24)	157.5(3)	C(95)-O(27)-Na(4)	111.8(4)
O(28)-Na(4)-N(24)	85.0(2)	C(99)-O(28)-Na(4)	113.9(5)
O(27)-Na(4)-N(25)	126.1(3)	C(87)-O(29)-C(88)	116.1(12)
O(25)-Na(4)-N(25)	86.2(3)	C(91)-O(30)-C(92)	118.3(8)
O(28)-Na(4)-N(25)	65.6(2)	C(95)-O(31)-C(96)	116.0(9)
N(24)-Na(4)-N(25)	72.6(2)	C(99)-O(32)-C(100)	114.9(7)
O(27)-Na(4)-O(26)	78.8(2)	C(83)-N(22)-C(84)	112.2(8)
O(25)-Na(4)-O(26)	77.3(3)	C(83)-N(22)-C(76)	112.6(8)
O(28)-Na(4)-O(26)	127.8(2)	C(84)-N(22)-C(76)	112.4(9)
N(24)-Na(4)-O(26)	125.2(2)	C(83)-N(22)-Na(4)	106.8(6)
N(25)-Na(4)-O(26)	155.0(3)	C(84)-N(22)-Na(4)	105.9(5)
O(27)-Na(4)-N(23)	86.9(2)	C(76)-N(22)-Na(4)	106.4(5)
O(25)-Na(4)-N(23)	124.0(3)	C(89)-N(23)-C(78)	111.9(7)
O(28)-Na(4)-N(23)	156.7(2)	C(89)-N(23)-C(77)	110.7(7)
N(24)-Na(4)-N(23)	72.8(2)	C(78)-N(23)-C(77)	113.9(7)
N(25)-Na(4)-N(23)	112.6(2)	C(89)-N(23)-Na(4)	105.6(5)
O(26)-Na(4)-N(23)	64.2(2)	C(78)-N(23)-Na(4)	106.1(5)
O(27)-Na(4)-N(22)	156.7(2)	C(77)-N(23)-Na(4)	108.0(5)
O(25)-Na(4)-N(22)	64.5(3)	C(79)-N(24)-C(93)	110.2(8)
O(28)-Na(4)-N(22)	125.7(2)	C(79)-N(24)-C(80)	111.7(7)
N(24)-Na(4)-N(22)	114.2(3)	C(93)-N(24)-C(80)	112.5(8)
N(25)-Na(4)-N(22)	72.7(3)	C(79)-N(24)-Na(4)	107.9(5)
O(26)-Na(4)-N(22)	83.3(2)	C(93)-N(24)-Na(4)	106.3(5)
N(23)-Na(4)-N(22)	71.8(2)	C(80)-N(24)-Na(4)	108.1(6)

Table A.9. Bond lengths [Å] and angles [°] for **17-NaTfO** contd.

C(81)-N(25)-C(97)	109.2(8)	C(81)-C(80)-H(80A)	109.0
C(81)-N(25)-C(82)	114.7(8)	N(24)-C(80)-H(80B)	109.0
C(97)-N(25)-C(82)	112.9(8)	C(81)-C(80)-H(80B)	109.0
C(81)-N(25)-Na(4)	107.8(5)	H(80A)-C(80)-H(80B)	107.8
C(97)-N(25)-Na(4)	106.3(5)	N(25)-C(81)-C(80)	114.6(9)
C(82)-N(25)-Na(4)	105.4(6)	N(25)-C(81)-H(81A)	108.6
N(27)-N(26)-C(86)	115(2)	C(80)-C(81)-H(81A)	108.6
N(28)-N(27)-N(26)	145(4)	N(25)-C(81)-H(81B)	108.6
N(22)-C(76)-C(77)	113.4(7)	C(80)-C(81)-H(81B)	108.6
N(22)-C(76)-H(76A)	108.9	H(81A)-C(81)-H(81B)	107.6
C(77)-C(76)-H(76A)	108.9	C(83)-C(82)-N(25)	115.5(9)
N(22)-C(76)-H(76B)	108.9	C(83)-C(82)-H(82A)	108.4
C(77)-C(76)-H(76B)	108.9	N(25)-C(82)-H(82A)	108.4
H(76A)-C(76)-H(76B)	107.7	C(83)-C(82)-H(82B)	108.4
N(23)-C(77)-C(76)	112.9(8)	N(25)-C(82)-H(82B)	108.4
N(23)-C(77)-H(77A)	109.0	H(82A)-C(82)-H(82B)	107.5
C(76)-C(77)-H(77A)	109.0	N(22)-C(83)-C(82)	114.0(9)
N(23)-C(77)-H(77B)	109.0	N(22)-C(83)-H(83A)	108.7
C(76)-C(77)-H(77B)	109.0	C(82)-C(83)-H(83A)	108.7
H(77A)-C(77)-H(77B)	107.8	N(22)-C(83)-H(83B)	108.7
N(23)-C(78)-C(79)	114.2(8)	C(82)-C(83)-H(83B)	108.7
N(23)-C(78)-H(78A)	108.7	H(83A)-C(83)-H(83B)	107.6
C(79)-C(78)-H(78A)	108.7	N(22)-C(84)-C(87)	106.6(8)
N(23)-C(78)-H(78B)	108.7	N(22)-C(84)-C(85)	119.3(11)
C(79)-C(78)-H(78B)	108.7	C(87)-C(84)-C(85)	113.9(11)
H(78A)-C(78)-H(78B)	107.6	N(22)-C(84)-H(84)	105.3
N(24)-C(79)-C(78)	113.3(8)	C(87)-C(84)-H(84)	105.3
N(24)-C(79)-H(79A)	108.9	C(85)-C(84)-H(84)	105.3
C(78)-C(79)-H(79A)	108.9	C(86)-C(85)-C(84)	116.2(14)
N(24)-C(79)-H(79B)	108.9	C(86)-C(85)-H(85A)	108.2
C(78)-C(79)-H(79B)	108.9	C(84)-C(85)-H(85A)	108.2
H(79A)-C(79)-H(79B)	107.7	C(86)-C(85)-H(85B)	108.2
N(24)-C(80)-C(81)	113.0(7)	C(84)-C(85)-H(85B)	108.2
N(24)-C(80)-H(80A)	109.0	H(85A)-C(85)-H(85B)	107.4

Table A.9. Bond lengths [Å] and angles [°] for **17-NaTfO** contd.

C(85)-C(86)-N(26)	125.3(17)	H(92A)-C(92)-H(92C)	109.5
C(85)-C(86)-H(86A)	106.0	H(92B)-C(92)-H(92C)	109.5
N(26)-C(86)-H(86A)	106.0	N(24)-C(93)-C(94)	119.2(10)
C(85)-C(86)-H(86B)	106.0	N(24)-C(93)-C(95)	108.9(7)
N(26)-C(86)-H(86B)	106.0	C(94)-C(93)-C(95)	112.1(10)
H(86A)-C(86)-H(86B)	106.3	N(24)-C(93)-H(93)	105.1
O(25)-C(87)-O(29)	122.7(10)	C(94)-C(93)-H(93)	105.1
O(25)-C(87)-C(84)	127.1(10)	C(95)-C(93)-H(93)	105.1
O(29)-C(87)-C(84)	110.3(10)	C(93)-C(94)-H(94A)	109.5
O(29)-C(88)-H(88A)	109.5	C(93)-C(94)-H(94B)	109.5
O(29)-C(88)-H(88B)	109.5	H(94A)-C(94)-H(94B)	109.5
H(88A)-C(88)-H(88B)	109.5	C(93)-C(94)-H(94C)	109.5
O(29)-C(88)-H(88C)	109.5	H(94A)-C(94)-H(94C)	109.5
H(88A)-C(88)-H(88C)	109.5	H(94B)-C(94)-H(94C)	109.5
H(88B)-C(88)-H(88C)	109.5	O(27)-C(95)-O(31)	121.5(8)
N(23)-C(89)-C(91)	109.4(6)	O(27)-C(95)-C(93)	125.4(7)
N(23)-C(89)-C(90)	113.6(8)	O(31)-C(95)-C(93)	113.1(8)
C(91)-C(89)-C(90)	114.4(9)	O(27)-C(95)-Na(4)	47.3(3)
N(23)-C(89)-H(89)	106.3	O(31)-C(95)-Na(4)	157.5(7)
C(91)-C(89)-H(89)	106.3	C(93)-C(95)-Na(4)	81.9(5)
C(90)-C(89)-H(89)	106.3	O(31)-C(96)-H(96A)	109.5
C(89)-C(90)-H(90A)	109.5	O(31)-C(96)-H(96B)	109.5
C(89)-C(90)-H(90B)	109.5	H(96A)-C(96)-H(96B)	109.5
H(90A)-C(90)-H(90B)	109.5	O(31)-C(96)-H(96C)	109.5
C(89)-C(90)-H(90C)	109.5	H(96A)-C(96)-H(96C)	109.5
H(90A)-C(90)-H(90C)	109.5	H(96B)-C(96)-H(96C)	109.5
H(90B)-C(90)-H(90C)	109.5	N(25)-C(97)-C(98)	115.7(9)
O(26)-C(91)-O(30)	123.3(7)	N(25)-C(97)-C(99)	109.4(6)
O(26)-C(91)-C(89)	123.0(7)	C(98)-C(97)-C(99)	111.8(9)
O(30)-C(91)-C(89)	113.7(7)	N(25)-C(97)-H(97)	106.5
O(30)-C(92)-H(92A)	109.5	C(98)-C(97)-H(97)	106.5
O(30)-C(92)-H(92B)	109.5	C(99)-C(97)-H(97)	106.5
H(92A)-C(92)-H(92B)	109.5	C(97)-C(98)-H(98A)	109.5
O(30)-C(92)-H(92C)	109.5	C(97)-C(98)-H(98B)	109.5

Table A.9. Bond lengths [Å] and angles [°] for **17-NaTfO** contd.

H(98A)-C(98)-H(98B)	109.5	F(10)-C(4A)-S(4)	110.2(17)
C(97)-C(98)-H(98C)	109.5	F(12)-C(4A)-S(4)	109.9(18)
H(98A)-C(98)-H(98C)	109.5	F(11)-C(4A)-S(4)	108.6(14)
H(98B)-C(98)-H(98C)	109.5	O(5A)-S(2)-O(4A)	110.5(7)
O(28)-C(99)-O(32)	124.7(7)	O(5A)-S(2)-O(6A)	111.7(7)
O(28)-C(99)-C(97)	123.8(7)	O(4A)-S(2)-O(6A)	118.9(8)
O(32)-C(99)-C(97)	111.4(7)	O(5A)-S(2)-C(2A)	106.2(8)
O(32)-C(100)-H(10A)	109.5	O(4A)-S(2)-C(2A)	101.9(7)
O(32)-C(100)-H(10B)	109.5	O(6A)-S(2)-C(2A)	106.3(7)
H(10A)-C(100)-H(10B)	109.5	F(4)-C(2A)-F(6)	109.6(11)
O(32)-C(100)-H(10C)	109.5	F(4)-C(2A)-F(5)	105.3(11)
H(10A)-C(100)-H(10C)	109.5	F(6)-C(2A)-F(5)	104.5(12)
H(10B)-C(100)-H(10C)	109.5	F(4)-C(2A)-S(2)	111.7(10)
O(2A)-S(1)-O(3A)	115.7(6)	F(6)-C(2A)-S(2)	114.8(10)
O(2A)-S(1)-O(1A)	115.3(6)	F(5)-C(2A)-S(2)	110.3(11)
O(3A)-S(1)-O(1A)	113.8(4)	O(9A)-S(3)-O(8A)	114.0(11)
O(2A)-S(1)-C(1A)	102.0(5)	O(9A)-S(3)-O(7A)	119.1(8)
O(3A)-S(1)-C(1A)	104.8(6)	O(8A)-S(3)-O(7A)	104.5(10)
O(1A)-S(1)-C(1A)	102.9(5)	O(9A)-S(3)-C(3A)	107.0(9)
F(1)-C(1A)-F(3)	106.6(9)	O(8A)-S(3)-C(3A)	107.0(9)
F(1)-C(1A)-F(2)	102.1(8)	O(7A)-S(3)-C(3A)	104.4(9)
F(3)-C(1A)-F(2)	103.0(9)	F(9)-C(3A)-F(7)	114.0(15)
F(1)-C(1A)-S(1)	115.0(8)	F(9)-C(3A)-F(8)	114.8(16)
F(3)-C(1A)-S(1)	114.2(8)	F(7)-C(3A)-F(8)	110.9(15)
F(2)-C(1A)-S(1)	114.5(7)	F(9)-C(3A)-S(3)	104.3(13)
O(12A)-S(4)-O(11A)	125.4(19)	F(7)-C(3A)-S(3)	108.5(13)
O(12A)-S(4)-O(10A)	115.8(18)	F(8)-C(3A)-S(3)	103.3(12)
O(11A)-S(4)-O(10A)	103.9(17)	O(14A)-S(5)-O(13A)	115.3(17)
O(12A)-S(4)-C(4A)	101.3(14)	O(14A)-S(5)-O(15A)	116.3(18)
O(11A)-S(4)-C(4A)	102.2(14)	O(13A)-S(5)-O(15A)	112.2(18)
O(10A)-S(4)-C(4A)	105.9(18)	O(14A)-S(5)-C(5A)	107.3(14)
F(10)-C(4A)-F(12)	113(2)	O(13A)-S(5)-C(5A)	105.5(15)
F(10)-C(4A)-F(11)	107.5(19)	O(15A)-S(5)-C(5A)	97.9(17)
F(12)-C(4A)-F(11)	107.1(17)	F(13)-C(5A)-F(15)	112.2(17)

Table A.9. Bond lengths [Å] and angles [°] for **17-NaTfO** contd.

F(13)-C(5A)-F(14)	109.4(18)	O(33)-S(6)-C(6A)	103.1(16)
F(15)-C(5A)-F(14)	104.7(17)	O(35)-S(6)-C(6A)	99.0(15)
F(13)-C(5A)-S(5)	108.6(15)	F(16)-C(6A)-F(18)	115(2)
F(15)-C(5A)-S(5)	113.8(18)	F(16)-C(6A)-F(17)	111(2)
F(14)-C(5A)-S(5)	107.9(16)	F(18)-C(6A)-F(17)	110(2)
O(34)-S(6)-O(33)	107.7(19)	F(16)-C(6A)-S(6)	109.0(19)
O(34)-S(6)-O(35)	121(2)	F(18)-C(6A)-S(6)	103.8(17)
O(33)-S(6)-O(35)	117(2)	F(17)-C(6A)-S(6)	107.4(19)
O(34)-S(6)-C(6A)	106.7(17)		

Symmetry transformations used to generate equivalent atoms:

Table A.10. Anisotropic displacement parameters ($Å^2 x\ 10^3$) for **17-NaTfO**. The anisotropic displacement factor exponent takes the form: $-2\pi^2[\ h^2\ a^{*2}U^{11} + ... + 2\ h\ k\ a^*\ b^*\ U^{12}\ ]$.

	U^{11}	U^{22}	U^{33}	U^{23}	U^{13}	U^{12}
Na(1)	68(2)	39(2)	28(2)	-5(1)	20(1)	2(2)
O(1)	70(4)	53(5)	57(4)	-7(3)	17(3)	-2(4)
O(2)	58(4)	54(4)	40(3)	-2(3)	16(3)	4(3)
O(3)	92(4)	48(4)	20(3)	2(3)	30(3)	1(3)
O(4)	86(5)	52(4)	44(4)	-9(3)	20(3)	-7(4)
O(5)	132(6)	39(4)	69(5)	-3(4)	13(5)	13(4)
O(6)	67(4)	177(10)	35(4)	-6(5)	21(3)	-6(5)
O(7)	111(5)	49(5)	49(4)	-3(3)	32(4)	5(4)
O(8)	111(7)	90(7)	81(5)	-16(5)	26(5)	-37(5)
N(1)	86(5)	50(5)	55(5)	-15(4)	42(5)	3(4)
N(2)	66(4)	47(5)	33(4)	-7(4)	6(3)	-9(4)
N(3)	94(6)	50(5)	22(4)	-6(3)	24(4)	8(4)
N(4)	85(5)	56(5)	36(4)	-21(4)	35(4)	-12(4)
N(5)	184(17)	95(11)	190(20)	-5(12)	71(16)	-47(11)
N(6)	152(12)	103(10)	74(8)	22(8)	-15(8)	-30(9)
N(7)	194(16)	122(13)	119(13)	31(11)	50(13)	32(12)
C(1)	86(7)	58(7)	44(5)	-13(5)	10(5)	-9(5)
C(2)	59(5)	56(6)	43(5)	-12(5)	13(4)	-12(5)
C(3)	68(5)	63(7)	26(4)	-6(4)	7(4)	1(5)
C(4)	74(6)	56(7)	43(5)	0(5)	13(5)	7(5)
C(5)	115(8)	59(7)	32(5)	-8(5)	29(5)	-4(6)
C(6)	112(8)	71(8)	41(5)	-10(6)	46(6)	-17(6)
C(7)	75(6)	87(9)	50(6)	-10(6)	33(5)	-3(6)
C(8)	84(7)	77(9)	60(6)	-38(6)	28(6)	1(6)
C(9)	77(6)	39(6)	80(8)	-18(6)	29(6)	2(5)
C(10)	128(10)	42(7)	131(12)	-10(8)	56(9)	13(7)
C(11)	210(20)	107(17)	170(20)	32(14)	69(19)	21(16)
C(12)	89(7)	29(6)	65(7)	9(5)	33(5)	23(6)
C(13)	141(11)	75(9)	58(7)	17(7)	7(7)	-7(8)

Table A.10. Anisotropic displacement parameters ($Å^2 x\ 10^3$) for **17-NaTfO**. The anisotropic displacement factor exponent takes the form: $-2\pi^2[\ h^2\ a^{*2}U^{11} + ... + 2\ h\ k\ a^*\ b^*\ U^{12}\ ]$ contd.

	U^{11}	U^{22}	U^{33}	U^{23}	U^{13}	U^{12}
C(14)	69(6)	68(7)	52(6)	-11(5)	14(5)	-4(5)
C(15)	68(6)	102(9)	58(6)	6(6)	19(5)	6(6)
C(16)	84(8)	51(7)	48(6)	-13(5)	20(6)	-9(5)
C(17)	86(7)	280(20)	14(5)	22(9)	11(5)	-19(11)
C(18)	102(7)	57(7)	21(4)	9(5)	25(5)	2(6)
C(19)	115(8)	46(7)	57(6)	4(5)	37(6)	-12(6)
C(20)	74(5)	41(6)	32(5)	-6(5)	21(4)	4(4)
C(21)	199(15)	60(8)	53(7)	-30(6)	61(8)	-28(8)
C(22)	71(6)	95(9)	67(7)	-10(7)	40(6)	-14(6)
C(23)	106(9)	135(14)	104(11)	-57(11)	49(8)	-12(9)
C(24)	75(7)	65(7)	64(7)	-8(6)	19(6)	-16(6)
C(25)	138(12)	132(14)	53(7)	-14(8)	5(7)	-43(11)
Na(2)	75(2)	60(2)	33(2)	4(2)	15(2)	5(2)
O(9)	74(5)	116(8)	75(5)	-13(5)	32(4)	-22(5)
O(10)	69(4)	66(5)	59(4)	-1(4)	29(3)	-1(4)
O(11)	90(4)	64(5)	23(3)	5(3)	13(3)	18(4)
O(12)	72(4)	118(7)	45(4)	25(4)	24(3)	5(4)
O(13)	179(11)	101(9)	152(11)	-55(9)	58(10)	-42(8)
O(14)	66(4)	121(7)	72(5)	14(5)	35(4)	14(4)
O(15)	150(7)	60(5)	44(4)	-4(4)	31(4)	30(5)
O(16)	88(6)	126(9)	126(8)	-13(7)	61(6)	-29(6)
N(8)	104(7)	71(7)	51(5)	20(5)	37(5)	-5(5)
N(9)	85(6)	86(7)	43(5)	-16(5)	-17(4)	4(5)
N(10)	159(10)	65(6)	26(4)	2(4)	33(6)	1(6)
N(11)	145(10)	106(9)	64(6)	26(6)	83(7)	28(8)
N(12)	173(11)	182(12)	186(11)	-16(9)	42(9)	-8(9)
N(13)	173(11)	183(12)	177(12)	-4(9)	48(9)	-15(9)
N(14)	229(17)	193(17)	160(14)	6(14)	51(13)	-19(15)
C(26)	141(11)	75(9)	58(7)	25(7)	19(8)	31(8)

Table A.10. Anisotropic displacement parameters ($Å^2 x\ 10^3$) for **17-NaTfO**. The anisotropic displacement factor exponent takes the form: $-2\pi^2[\ h^2\ a^{*2}U^{11} + ... + 2\ h\ k\ a^*\ b^*\ U^{12}\ ]$ contd.

	U^{11}	U^{22}	U^{33}	U^{23}	U^{13}	U^{12}
C(27)	82(7)	101(10)	59(7)	46(7)	-6(6)	6(7)
C(28)	160(13)	76(10)	55(7)	17(7)	10(8)	30(9)
C(29)	165(14)	82(9)	28(5)	-8(6)	18(7)	-13(9)
C(30)	215(19)	94(11)	51(7)	-7(7)	66(10)	15(12)
C(31)	184(16)	107(13)	86(9)	27(9)	105(11)	25(11)
C(32)	180(14)	102(12)	63(7)	48(8)	77(9)	23(10)
vC(33)	145(11)	79(10)	85(9)	39(8)	58(9)	38(9)
C(34)	126(10)	63(8)	95(10)	9(7)	53(9)	-11(7)
C(35)	250(20)	76(12)	190(20)	-1(13)	150(20)	-11(14)
C(36)	220(30)	160(20)	157(19)	62(18)	77(19)	60(20)
C(37)	85(8)	67(9)	110(11)	-15(8)	52(8)	-27(7)
C(38)	177(19)	230(30)	147(19)	-110(20)	15(16)	-30(20)
C(39)	72(6)	78(8)	46(6)	14(5)	24(5)	-8(5)
C(40)	72(7)	101(11)	106(10)	-2(8)	-18(7)	-9(7)
C(41)	60(6)	57(7)	67(7)	26(6)	-5(6)	-2(5)
C(42)	108(8)	87(10)	77(8)	-35(7)	38(7)	-14(7)
C(43)	131(10)	86(10)	51(7)	-6(7)	41(7)	10(8)
C(44)	340(30)	83(12)	58(8)	-10(8)	98(13)	30(15)
C(45)	86(6)	53(7)	31(5)	11(5)	16(5)	19(5)
C(46)	164(12)	82(9)	53(7)	13(6)	52(8)	31(9)
C(47)	104(10)	106(12)	156(15)	47(11)	97(11)	29(9)
C(48)	149(13)	128(14)	140(14)	54(12)	106(12)	45(11)
C(49)	87(8)	124(12)	80(8)	3(8)	67(8)	-16(8)
C(50)	78(7)	140(14)	75(8)	-1(9)	28(6)	-18(8)
Na(3)	44(1)	35(2)	25(1)	3(1)	9(1)	-6(1)
O(17)	57(3)	55(5)	21(3)	3(3)	7(2)	-15(3)
O(18)	56(4)	34(3)	35(3)	0(3)	20(3)	-9(3)
O(19)	64(3)	43(5)	75(4)	-6(3)	35(3)	-4(3)
O(20)	59(3)	37(3)	34(3)	-5(3)	21(2)	-10(3)

Table A.10. Anisotropic displacement parameters ($Å^2 x\ 10^3$) for **17-NaTfO**. The anisotropic displacement factor exponent takes the form: $-2\pi^2[\ h^2\ a^{*2}U^{11} + ... + 2\ h\ k\ a^*\ b^*\ U^{12}\ ]$ contd.

	U^{11}	U^{22}	U^{33}	U^{23}	U^{13}	U^{12}
O(21)	68(4)	83(6)	64(5)	21(4)	7(4)	21(4)
O(22)	75(4)	47(4)	81(5)	-16(4)	55(4)	-18(3)
O(23)	106(6)	57(5)	140(8)	-36(6)	58(6)	6(5)
O(24)	84(4)	117(7)	63(5)	-46(5)	29(4)	-54(5)
N(15)	56(4)	41(4)	19(3)	-6(3)	8(3)	-17(3)
N(16)	43(3)	43(4)	31(4)	-7(3)	-10(3)	-12(3)
N(17)	53(4)	28(4)	69(5)	7(4)	-6(4)	0(3)
N(18)	65(4)	29(4)	31(4)	6(3)	15(3)	-15(3)
N(19)	136(6)	172(8)	162(8)	1(6)	71(6)	-1(6)
N(20)	136(6)	172(8)	162(8)	1(6)	71(6)	-1(6)
N(21)	187(14)	185(16)	188(15)	67(13)	52(12)	77(13)
C(51)	88(6)	47(6)	27(4)	-2(4)	17(4)	-17(5)
C(52)	61(5)	37(5)	28(4)	-16(4)	-2(4)	-4(4)
C(53)	71(6)	47(6)	54(6)	-14(5)	-24(5)	-12(5)
C(54)	49(5)	56(7)	72(7)	3(6)	-19(5)	7(5)
C(55)	95(7)	50(6)	41(5)	25(5)	-10(5)	-1(6)
C(56)	86(6)	39(6)	45(5)	16(4)	17(5)	-22(5)
C(57)	85(6)	56(7)	38(5)	-2(5)	32(5)	-27(5)
C(58)	76(5)	40(6)	42(5)	-4(4)	38(4)	-11(4)
C(59)	45(4)	38(5)	68(6)	6(5)	26(4)	0(4)
C(60)	118(8)	106(10)	183(13)	-34(8)	94(9)	18(7)
C(61)	118(8)	106(10)	183(13)	-34(8)	94(9)	18(7)
C(62)	45(4)	44(6)	31(5)	-2(5)	14(4)	-4(4)
C(63)	74(6)	141(13)	66(8)	64(9)	-4(6)	4(8)
C(64)	46(4)	31(5)	72(6)	-21(5)	14(5)	-16(4)
C(65)	54(5)	68(8)	112(9)	-11(7)	11(6)	-35(5)
C(66)	39(5)	37(5)	47(5)	-5(4)	21(4)	-4(4)
C(67)	151(11)	62(8)	54(7)	12(6)	38(7)	-25(8)
C(68)	60(5)	36(6)	81(7)	-5(6)	6(5)	1(5)

Table A.10. Anisotropic displacement parameters ($Å^2 x\ 10^3$) for **17-NaTfO**. The anisotropic displacement factor exponent takes the form: $-2\pi^2[\ h^2\ a^{*2}U^{11} + ... + 2\ h\ k\ a^*\ b^*\ U^{12}\ ]$ contd.

	U^{11}	U^{22}	U^{33}	U^{23}	U^{13}	U^{12}
C(69)	57(6)	85(10)	121(11)	5(8)	20(6)	25(6)
C(70)	52(5)	49(8)	111(10)	-4(7)	29(6)	-4(5)
C(71)	142(13)	136(16)	169(18)	-71(15)	108(13)	3(11)
C(72)	66(5)	36(5)	34(5)	-3(4)	17(4)	-11(4)
C(73)	70(6)	68(7)	76(7)	-9(6)	33(5)	-28(5)
C(74)	66(6)	47(6)	37(5)	-8(4)	17(5)	-23(5)
C(75)	145(13)	184(19)	76(9)	-71(11)	45(9)	-100(14)
Na(4)	40(1)	52(2)	27(1)	12(1)	10(1)	-1(1)
O(25)	77(4)	81(6)	97(6)	38(5)	53(4)	15(4)
O(26)	69(4)	51(4)	49(4)	6(3)	30(3)	7(3)
O(27)	48(3)	39(4)	37(3)	-4(3)	2(2)	3(3)
O(28)	48(3)	57(4)	36(3)	9(3)	2(3)	-10(3)
O(29)	141(8)	110(9)	180(11)	30(8)	112(9)	73(7)
O(30)	71(4)	59(4)	43(4)	-7(3)	6(3)	-2(4)
O(31)	77(4)	52(5)	116(7)	5(5)	9(5)	10(4)
O(32)	62(3)	59(4)	57(4)	10(3)	34(3)	-9(3)
N(22)	40(4)	84(7)	73(6)	46(6)	-8(4)	-16(4)
N(23)	57(4)	60(5)	33(4)	12(4)	24(3)	-14(4)
N(24)	71(5)	73(6)	29(4)	-20(4)	21(4)	-12(4)
N(25)	62(4)	80(6)	31(4)	-2(4)	1(4)	-20(4)
N(26)	182(7)	223(9)	224(9)	24(7)	53(6)	3(6)
N(27)	182(7)	223(9)	224(9)	24(7)	53(6)	3(6)
N(28)	182(7)	223(9)	224(9)	24(7)	53(6)	3(6)
C(76)	70(6)	110(11)	70(7)	65(8)	2(6)	-14(7)
C(77)	71(6)	67(7)	51(6)	32(5)	25(5)	-7(5)
C(78)	77(6)	89(9)	53(6)	1(6)	28(5)	-29(6)
C(79)	91(7)	109(11)	57(6)	-46(7)	61(6)	-48(8)
C(80)	104(8)	99(10)	47(6)	-35(6)	29(6)	-44(7)
C(81)	102(8)	100(10)	26(5)	-18(6)	-11(5)	-52(8)

Table A.10. Anisotropic displacement parameters ($Å^2 x\ 10^3$) for **17-NaTfO**. The anisotropic displacement factor exponent takes the form: $-2\pi^2[\ h^2\ a^{*2}U^{11} + ...\ + 2\ h\ k\ a^*\ b^*\ U^{12}\ ]$ contd.

	U^{11}	U^{22}	U^{33}	U^{23}	U^{13}	U^{12}
C(82)	74(7)	156(16)	44(6)	37(8)	-29(6)	-49(9)
C(83)	63(6)	81(9)	92(9)	48(8)	6(6)	5(6)
C(84)	49(5)	62(8)	117(10)	22(7)	44(6)	18(5)
C(85)	89(6)	107(10)	260(20)	23(12)	15(9)	39(8)
C(86)	89(6)	107(10)	260(20)	23(12)	15(9)	39(8)
C(87)	81(7)	98(11)	136(12)	77(10)	66(8)	21(8)
C(88)	220(20)	170(20)	210(20)	39(19)	180(20)	20(18)
C(89)	48(5)	51(6)	52(5)	2(5)	13(4)	-7(4)
C(90)	111(9)	95(10)	120(11)	-13(9)	67(9)	-54(8)
C(91)	56(5)	47(6)	37(5)	11(5)	22(4)	9(5)
C(92)	133(10)	62(8)	78(8)	-19(7)	35(8)	2(7)
C(93)	82(6)	56(7)	80(8)	-37(6)	41(6)	-23(6)
C(94)	111(10)	68(9)	173(16)	-34(10)	85(11)	9(7)
C(95)	36(4)	45(7)	75(7)	-12(6)	9(5)	-3(4)
C(96)	79(7)	105(11)	113(11)	28(10)	-40(8)	7(8)
C(97)	59(5)	79(8)	44(5)	7(5)	12(5)	-9(5)
C(98)	105(10)	190(19)	88(9)	58(11)	-23(8)	-102(12)
C(99)	50(5)	51(6)	52(6)	3(5)	13(5)	-6(5)
C(100)	98(7)	60(7)	48(6)	25(5)	30(5)	0(6)
S(1)	139(2)	43(2)	35(1)	-11(1)	28(1)	-8(2)
F(1)	136(6)	57(5)	92(5)	-4(4)	32(4)	-15(4)
F(2)	133(5)	62(4)	60(3)	12(3)	28(4)	27(4)
F(3)	165(8)	129(8)	113(6)	19(6)	85(6)	3(6)
O(1A)	167(8)	51(5)	50(4)	-10(4)	25(5)	5(5)
O(2A)	134(7)	127(9)	63(5)	-20(5)	46(5)	-25(7)
O(3A)	189(9)	47(5)	46(4)	-10(4)	28(5)	-11(5)
C(1A)	186(13)	30(6)	64(7)	-2(6)	84(9)	-4(7)
S(4)	151(11)	71(6)	89(3)	-45(4)	-20(5)	20(6)
F(10)	330(40)	370(50)	45(9)	5(16)	-11(15)	-270(40)

Table A.10. Anisotropic displacement parameters ($Å^2 x\ 10^3$) for **17-NaTfO**. The anisotropic displacement factor exponent takes the form: $-2\pi^2[\ h^2\ a^{*2}U^{11} + ... + 2\ h\ k\ a^*\ b^*\ U^{12}\ ]$ contd.

	U^{11}	U^{22}	U^{33}	U^{23}	U^{13}	U^{12}
F(11)	147(14)	112(15)	110(13)	45(11)	26(11)	38(12)
F(12)	580(80)	117(19)	113(16)	45(14)	180(30)	20(30)
O(10A)	330(30)	50(20)	76(8)	32(12)	61(13)	80(20)
O(11A)	260(40)	80(19)	180(30)	-3(18)	140(30)	70(20)
O(12A)	171(17)	125(17)	180(20)	108(16)	77(14)	2(12)
C(4A)	151(11)	71(6)	89(3)	-45(4)	-20(5)	20(6)
S(2)	107(2)	128(3)	74(2)	26(2)	31(2)	27(2)
F(4)	110(5)	198(11)	101(6)	22(7)	30(5)	8(6)
F(5)	330(20)	207(15)	113(8)	-39(9)	68(10)	122(15)
F(6)	276(15)	130(9)	94(6)	49(6)	47(8)	-21(9)
O(4A)	137(7)	141(9)	83(6)	-21(6)	70(6)	30(7)
O(5A)	81(5)	203(14)	89(6)	5(8)	-3(5)	37(7)
O(6A)	124(7)	185(12)	47(4)	33(6)	29(5)	4(8)
C(2A)	107(2)	128(3)	74(2)	26(2)	31(2)	27(2)
S(3)	101(3)	117(4)	99(3)	-29(3)	33(3)	-11(3)
F(7)	188(12)	270(20)	99(11)	-16(14)	97(12)	1(13)
F(8)	170(11)	146(13)	144(14)	49(10)	-52(10)	23(11)
F(9)	186(15)	98(11)	390(30)	-94(16)	116(19)	-86(11)
O(7A)	151(12)	97(10)	64(8)	10(7)	-27(8)	60(9)
O(8A)	220(18)	66(9)	148(13)	-53(10)	79(13)	-47(10)
O(9A)	167(12)	162(14)	74(6)	-6(8)	85(8)	71(11)
C(3A)	101(3)	117(4)	99(3)	-29(3)	33(3)	-11(3)
S(5)	151(11)	71(6)	89(3)	-45(4)	-20(5)	20(6)
F(13)	200(20)	96(14)	77(10)	11(10)	44(12)	-7(13)
F(14)	300(30)	126(13)	93(9)	7(9)	11(12)	90(16)
F(15)	300(30)	126(13)	93(9)	7(9)	11(12)	90(16)
O(13A)	260(40)	41(12)	120(19)	-21(12)	40(20)	-32(16)
O(14A)	171(17)	125(17)	180(20)	108(16)	77(14)	2(12)
O(15A)	330(30)	50(20)	76(8)	32(12)	61(13)	80(20)

Table A.10. Anisotropic displacement parameters ($Å^2 x\ 10^3$) for **17-NaTfO**. The anisotropic displacement factor exponent takes the form: $-2\pi^2[\ h^2\ a^{*2}U^{11} + ...\ + 2\ h\ k\ a^*\ b^*\ U^{12}\ ]$ contd.

	U^{11}	U^{22}	U^{33}	U^{23}	U^{13}	U^{12}
C(5A)	151(11)	71(6)	89(3)	-45(4)	-20(5)	20(6)
S(6)	101(3)	117(4)	99(3)	-29(3)	33(3)	-11(3)
F(16)	650(160)	120(40)	40(19)	50(20)	140(50)	210(70)
F(17)	188(12)	270(20)	99(11)	-16(14)	97(12)	1(13)
F(18)	170(11)	146(13)	144(14)	49(10)	-52(10)	23(11)
O(33)	167(12)	162(14)	74(6)	-6(8)	85(8)	71(11)
O(34)	101(3)	117(4)	99(3)	-29(3)	33(3)	-11(3)
O(35)	151(12)	97(10)	64(8)	10(7)	-27(8)	60(9)
C(6A)	101(3)	117(4)	99(3)	-29(3)	33(3)	-11(3)

Table A.11. Hydrogen coordinates (x 10^4) and isotropic displacement parameters ($Å^2$x 10^3) for **17-NaTfO**.

	x	y	z	U(eq)
H(1A)	1109	9721	-354	78
H(1B)	1163	10799	-568	78
H(2A)	1643	10146	-1152	64
H(2B)	2131	9846	-603	64
H(3A)	1744	8385	-280	65
H(3B)	2410	8060	-459	65
H(4A)	1736	6713	-896	71
H(4B)	1824	6649	-317	71
H(5A)	843	7710	-125	81
H(5B)	683	6558	-85	81
H(6A)	-504	6780	-640	83
H(6B)	-370	7435	-150	83
H(7A)	213	9042	-202	81
H(7B)	-625	9263	-294	81
H(8A)	-687	10174	-1001	87
H(8B)	-90	10621	-523	87
H(9)	649	10766	-1505	77
H(10D)	-533	11837	-1425	116
H(10E)	130	11801	-923	116
H(11A)	133	13181	-1328	191
H(11B)	135	12589	-1814	191
H(13A)	-836	10993	-3022	146
H(13B)	-1378	10484	-2773	146
H(13C)	-703	9878	-2828	146
H(14)	1909	7704	-1410	77
H(15A)	2682	9513	-1346	114
H(15B)	2876	8476	-1542	114
H(15C)	2978	8623	-964	114
H(17A)	1543	9251	-2941	190

Table A.11. Hydrogen coordinates (x 10^4) and isotropic displacement parameters (Å^{2}x 10^3) for **17-NaTfO** contd.

	x	y	z	U(eq)
H(17B)	954	9667	-2707	190
H(17C)	927	8535	-2874	190
H(18)	51	5897	-971	71
H(19A)	668	4492	-795	106
H(19B)	1054	5188	-331	106
H(19C)	1423	5012	-754	106
H(21A)	-99	5414	-2437	148
H(21B)	203	4308	-2343	148
H(21C)	752	5211	-2289	148
H(22)	-1338	8903	-1206	88
H(23A)	-2253	8129	-1005	167
H(23B)	-1658	8440	-494	167
H(23C)	-1713	7317	-677	167
H(25A)	-2163	7111	-2478	170
H(25B)	-2633	6410	-2245	170
H(25C)	-1784	6219	-2119	170
H(26A)	3634	7446	227	113
H(26B)	3380	8469	400	113
H(27A)	3006	7655	999	105
H(27B)	2594	7233	458	105
H(28A)	3310	5910	211	123
H(28B)	2665	5377	345	123
H(29A)	3486	4244	863	113
H(29B)	3534	4197	312	113
H(30A)	4388	5431	156	137
H(30B)	4786	4384	244	137
H(31A)	5808	5087	818	133
H(31B)	5629	5622	291	133
H(32A)	4702	6972	189	128
H(32B)	5478	7467	289	128

Table A.11. Hydrogen coordinates (x 10^4) and isotropic displacement parameters ($Å^2$x 10^3) for **17-NaTfO** contd.

	x	y	z	U(eq)
H(33A)	5293	8446	912	117
H(33B)	4683	8635	391	117
H(34)	3823	8579	1327	109
H(35A)	4717	10055	1155	184
H(35B)	4025	9773	698	184
H(36A)	4072	10659	1585	210
H(36B)	3356	10089	1265	210
H(38A)	5952	8939	2481	290
H(38B)	5365	8561	2725	290
H(38C)	5544	9714	2724	290
H(39)	3070	5223	1339	77
H(40A)	1990	6711	1139	156
H(40B)	1932	5596	1307	156
H(40C)	1927	5827	753	156
H(42A)	3513	7487	2521	133
H(42B)	3624	6404	2759	133
H(42C)	2902	7009	2716	133
H(43)	5338	4137	1227	104
H(44A)	5185	2574	1042	228
H(44B)	4703	3043	525	228
H(44C)	4324	2620	908	228
H(46A)	3853	2937	2137	143
H(46B)	4517	3622	2437	143
H(46C)	4612	2448	2440	143
H(47)	6120	7441	1251	131
H(48A)	6929	6062	885	187
H(48B)	7230	7053	1187	187
H(48C)	6676	7115	634	187
H(50A)	7067	4998	2331	145
H(50B)	6888	5954	2602	145

Table A.11. Hydrogen coordinates (x 10^4) and isotropic displacement parameters ($Å^2$x 10^3) for **17-NaTfO** contd.

	x	y	z	U(eq)
H(50C)	7693	5772	2591	145
H(51A)	11	10575	4789	65
H(51B)	-388	11619	4670	65
H(52A)	386	12112	4226	55
H(52B)	847	11816	4782	55
H(53A)	1109	10025	4884	81
H(53B)	1821	10586	4866	81
H(54A)	1973	9439	4287	82
H(54B)	1955	8887	4782	82
H(55A)	679	8572	4782	83
H(55B)	1044	7565	4690	83
H(56A)	37	7237	3991	69
H(56B)	-188	7325	4484	69
H(57A)	-401	9088	4680	68
H(57B)	-1172	8570	4454	68
H(58A)	-1576	9896	3892	57
H(58B)	-1333	10280	4454	57
H(59)	-658	11968	3731	58
H(60A)	-1974	12269	3511	150
H(60B)	-1944	11516	3949	150
H(61A)	-1080	13144	4111	150
H(61B)	-1304	12481	4505	150
H(63A)	-2312	11855	2186	150
H(63B)	-2242	10724	2356	150
H(63C)	-1576	11267	2252	150
H(64)	1675	10785	3903	61
H(65A)	2245	12257	4091	123
H(65B)	2145	11891	4601	123
H(65C)	1619	12719	4276	123
H(67A)	514	12210	2564	132

Table A.11. Hydrogen coordinates (x 10^4) and isotropic displacement parameters (Å^{2}x 10^3) for **17-NaTfO** contd.

	x	y	z	U(eq)
H(67B)	967	13217	2674	132
H(67C)	284	13080	2865	132
H(68)	921	7452	3767	76
H(69A)	2145	7008	3881	135
H(69B)	1970	6989	4395	135
H(69C)	2411	7893	4270	135
H(71A)	1376	7935	2393	202
H(71B)	2089	8536	2692	202
H(71C)	1307	9000	2618	202
H(72)	-1510	8622	3495	54
H(73A)	-2060	7245	3548	104
H(73B)	-1442	7125	4073	104
H(73C)	-1365	6577	3593	104
H(75A)	-1325	6598	2207	200
H(75B)	-653	7332	2415	200
H(75C)	-1430	7758	2103	200
H(76A)	5479	11689	4763	105
H(76B)	5822	10682	4646	105
H(77A)	4764	10390	3969	74
H(77B)	4596	10442	4485	74
H(78A)	4426	12267	4707	86
H(78B)	3653	11739	4522	86
H(79A)	3194	13040	3950	92
H(79B)	3477	13444	4508	92
H(80A)	4816	13778	4801	99
H(80B)	4412	14819	4676	99
H(81A)	5125	15261	4185	100
H(81B)	5625	15008	4737	100
H(82A)	6609	13686	4802	123
H(82B)	5908	13131	4844	123

Table A.11. Hydrogen coordinates (x 10^4) and isotropic displacement parameters (Å^{2}x 10^3) for **17-NaTfO** contd.

	x	y	z	U(eq)
H(83A)	6658	12595	4175	100
H(83B)	6730	12032	4683	100
H(84)	5567	10654	3667	86
H(85A)	7091	10775	3983	192
H(85B)	6717	10248	4341	192
H(86A)	6531	9701	3375	192
H(86B)	6184	9169	3742	192
H(88A)	6222	11231	2345	259
H(88B)	6763	12055	2661	259
H(88C)	5908	12211	2515	259
H(89)	3239	11787	3537	61
H(90A)	2751	10226	3555	152
H(90B)	3045	10660	4108	152
H(90C)	3501	9840	3931	152
H(92A)	3694	10487	2311	136
H(92B)	3163	9566	2268	136
H(92C)	3992	9489	2607	136
H(93)	4026	15106	3729	83
H(94A)	2917	15708	3673	162
H(94B)	3318	15436	4243	162
H(94C)	2703	14723	3904	162
H(96A)	2951	14113	2308	173
H(96B)	2275	14841	2219	173
H(96C)	2246	13754	2433	173
H(97)	6410	14045	3864	73
H(98A)	6283	15908	4296	211
H(98B)	6858	15637	4021	211
H(98C)	6911	15127	4540	211
H(10A)	5234	15444	2534	100
H(10B)	5616	16501	2658	100